

Department of Chemical and Environmental
Engineering



**The University of
Nottingham**

**Mineral Transformation, Ash Formation and
Characterisation during Pulverised Fuel
Combustion**

A Thesis Submitted to

The University of Nottingham

By

Laurence Paul Joseph Silvester, MEng

For the degree of

Doctor of Engineering

September 2019

Abstract

Due to the growing concerns about climate change, the power generation sector is increasingly facing pressure to reduce greenhouse gas emissions whilst maintaining energy security and supply. Co-firing biomass with coal is considered an intermediate term solution that can reduce CO₂ emissions from fossil fuel utilisation and maintain use of existing power plant infrastructure. For power generators, ash deposition is still a major cause of reduced boiler efficiency and unscheduled shutdowns on heat transfer surfaces, and historically, less attention has focused on deposition due to biomass co-firing.

In this research, a series of experiments were conducted on a suite of internationally traded coals, biomasses and industrial boiler fly ashes to characterise the particles formed during devolatilisation and char combustion at various residence times using a drop tube furnace (DTF) and mineral liberation analyser (MLA). The mineral transformations, associations and particle parameters determined aid the development of ash formation and erosion models. A unique mineral database using commercial coals, industrial fly ashes and biomasses was developed. This MLA database was used to assess particle parameters which influence erosion potential and determine the ash-deposition related mixed aluminosilicate species which contribute to ash deposit formation. Thermogravimetric analysis of DTF coal chars doped with biomass ashes was performed to investigate the effect of biomass-derived mineral species on the ignition temperature at varying co-firing ratios.

DTF studies suggested that inherent minerals present in the biomass ash enhance the formation of sintered/deposit particles compared to firing only the DTF coal char, and that the deposit particle size increases with residence time in the DTF. Mineral composition data and the development of ternary phase diagrams showed that the DTF coal char has the added benefit of capturing metal fluxing elements such as K and Ca originally present in the biomass ash. MLA can serve as a useful tool to reveal the characteristics or mechanisms of mineral transformations, ash formation and deposition during biomass co-firing.

Acknowledgements

I would like to express my sincere gratitude to the following people for the assistance and help I have been given during this research:

My academic supervisors' Dr Chenggong Sun, Prof Colin Snape, Prof Hao Liu and Dr Ofonime Udoudo for their guidance, financial support and encouragement throughout the duration of the research.

My industrial supervisor Dr William Livingston, Doosan Babcock for his guidance, financial support and supplying the power station fly ashes and coal samples to conduct the research.

Research staff at the University of Nottingham, particularly Dr Elisabeth Steer and Mr David Clift for support with operating and analysing samples on the Mineral Liberation Analyser (MLA) and sample preparation procedures. Adrian Quinn for help with all the analytical equipment in the Energy Technologies Building (ETB).

All those in the Engineering workshop for supporting with the maintenance of the Drop Tube Furnaces and other laboratory equipment.

My family and friends for their moral support, patience and encouragement.

Publications

Poster Presentations

Silvester P.J, L; Sun, C; Liu, H; Snape, C (2015) Characterisation of coal mineral composition and fly ash formation to aid pulverised fuel fly ash modelling using a mineral liberation analyser (SEM-MLA), Summer School June 2015, Harbin Institute of Technology, Harbin, China (presentation and poster).

Silvester P.J, L; Sun, C; Liu, H; Snape, C (2015) Development of a sample preparation procedure and automated SEM-EDX mineral database for pulverised fuels, Energy and Sustainability Poster Competition, March 2015, Nottingham, United Kingdom (poster).

Silvester P.J, L; Sun, C; Liu, H; Snape, C (2014) Impact of biomass co-firing on ash composition and deposition. Summer School June 2014, Pusan National University, Pusan, South Korea (presentation and poster).

Conference Proceedings

Silvester P.J, L; Sun, C; Liu, H; Snape, C (2016) Mineral transformations of pulverised coals using automated SEM-EDX analysis, 33rd Annual International Pittsburgh Coal Conference, August 2016, Cape Town, South Africa.

Silvester P.J, L; Sun, C; Liu, H; Snape, C (2016) A study on the mineral liberation and transformations during pulverised bituminous coal combustion,

11th European Conference on Coal Research and its Applications, September 2016, Sheffield, United Kingdom.

Proposed Publications

Silvester P.J, L; Sun, C; Liu, H; Snape, C, 'Mineral transformations and associations during coal devolatilisation and char burnout in a drop tube furnace' to be submitted to Energy and Fuels.

Silvester P.J, L; Sun, C; Liu, H; Snape, C, 'Advanced mineralogical characterisation of four UK power station fly ashes' to be submitted to Fuel.

Silvester P.J, L; Sun, C; Liu, H; Snape, C, 'Ash deposition-related minerals of co-firing biomass ash and DTF coal char under combustion conditions in a drop tube furnace' to be submitted to Fuel.

Silvester P.J, L; Sun, C; Liu, H; Snape, C, 'The catalytic effect of biomass ash addition on DTF coal char during combustion by thermogravimetric analysis' to be submitted to Fuel.

Table of Contents

Abstract.....	i
Acknowledgements	iii
Publications	iv
Poster Presentations	iv
Conference Proceedings.....	iv
Proposed Publications	v
List of Figures.....	x
List of Tables	xx
Nomenclatures.....	i
Abbreviations	ii
Chapter 1: Introduction	1
1.1 Global Warming and Climate Change.....	4
1.2 Pulverised Fuel Combustion and De-carbonisation	7
1.2.1 Process Overview.....	10
1.2.2 Combustion Systems.....	11
1.3 Motivation for the Research and Research Objectives	15
1.3.1 Motivation for the Project.....	15
1.3.2 Aims of the Project	17
Chapter 2: Literature Review	20
2.1 Fuels for Power Generation	21
2.1.1 Coal.....	21
2.1.2 Biomass and Co-firing	24
2.1.3 Future Trends.....	27
2.2 Factors Influencing Pulverised Fuel Combustion	30
2.2.1 Coal Type and Rank.....	32
2.2.2 Particle Size, Shape and Density.....	33
2.2.3 Heating Rate	35
2.2.4 Macerals.....	36
2.2.5 Char Burnout and Rate Kinetics	38
2.3 Inorganic Constituents of Pulverised Fuels.....	40
2.3.1 Minerals and Transformations	43
2.3.2 Catalytic Influence of Minerals.....	52

2.3.3	Slagging and Fouling.....	54
2.3.4	Ash Formation Modelling.....	62
2.3.5	Impact of Biomass Firing and Co-firing with Coal on Ash Formation and Deposition.....	67
2.4	Erosion in Pulverised Combustion Boilers	70
2.4.1	Mechanism of Particle Impact Erosion.....	72
2.4.2	Measurement of Erosive Wear Rates	74
2.4.3	Fundamentals of Erosion Wear on Boiler Tubes.....	76
2.4.4	Modelling of Erosion Wear Rates on Boiler Tubes.....	82
2.5	Advanced Characterisation Techniques	87
2.5.1	Application of CCSEM to Combustion Studies.....	89
2.5.2	CCSEM Outputs.....	94
2.5.3	MLA vs CCSEM	96
2.6	Impact of Literature Review on Research Direction	101
Chapter 3: Experimental and Theoretical Methods		104
3.1	Samples and Preparation	104
3.1.1	Samples	104
3.1.2	Dry Sieving.....	105
3.1.3	Alpine Jet Sieving	105
3.1.4	Rotary Sample Divider.....	106
3.1.5	Rotary Micro Riffler.....	107
3.2	Experimental and Theoretical Methods.....	108
3.2.1	Proximate Analysis and Ultimate Analysis	108
3.2.2	TGA Loss on Ignition	112
3.2.3	TGA Coal Burnout, Kinetics and Activation Energies.....	115
3.2.4	TGA Burnout of DTF Char	117
3.2.5	TGA Combustion Blends	117
3.2.6	Maceral and Vitrinite Reflectance Analysis	117
3.2.7	Adsorption Isotherms.....	123
3.2.8	X-ray Fluorescence Spectroscopy	126
3.2.9	X-ray Powder Diffraction.....	126
3.2.10	Particle Analysis	128
3.2.11	Drop Tube Furnace	130
3.2.12	Erosion Test Rig.....	144
3.3	Mineral Liberation Analysis – Scanning Electron Microscopy.....	149
3.3.1	Coal and Biomass Sample Preparation	149
3.3.2	Fly Ash Sample Preparation	150
3.3.3	Grinding, Polishing and Coating	152
3.3.4	MLA Setup and Operating Parameters	154

Chapter 4: Automated Mineralogy and Erosion Rate Experimental Results of UK Power Station Fly Ashes from Different PF Combustions

.....	163
4.1 General Introduction	163
4.2 Development of a Mineral Database.....	165
4.3 Erosion Rig Experimental Results of Power Station Fly Ashes and Mineralogical Analysis.....	170
4.3.1 MLA Mineral Compositions of the Power Station Fly Ashes...	180
4.3.2 MLA Coloured Image Analysis of Power Station Fly Ashes ...	183
4.3.3 MLA Assessment of the Tendency for Slagging and Fouling .	188
4.3.4 Influence of the Mineral Grain Particle Size Distributions and Associations and the Relationship with Erosive Wear.....	194
4.3.5 Influence of Mineral Angularities on Erosive Wear.....	200
4.4 Chapter Conclusions	202
Chapter 5: Mineral Transformations and Associations during Coal Devolatilisation and Char Burnout in a Drop Tube Furnace.....	204
5.1 General Introduction	204
5.2 Experimental Matrix.....	205
5.3 DTF and TGA Experimental Study	207
5.3.1 Coal and Biomass Characterisation.....	207
5.3.2 Drop Tube Furnace Conditions.....	208
5.3.3 DTF Devolatilisation and Surface Area	209
5.3.4 TGA Coal Burnout & Reactivity.....	217
5.3.5 DTF Char Firing.....	224
5.4 Mineral Characterisation of Coals, Chars and Ashes	227
5.4.1 DTF and Muffle Furnace Samples	227
5.4.2 Repeatability of the MLA Mineral Characterisation	230
5.4.3 Mineral Transformations and Associations during Devolatilisation and Char Combustion.....	240
5.4.4 MLA Coloured Mosaics of Coal Fractions, DTF Chars, DTF Ashes and Muffle Furnace Ashes.....	262
5.4.5 Evolution of Particle Sizes during Devolatilisation of Coal and Biomass Samples.....	273
5.4.6 Ternary Phase Diagrams during Combustion	280
5.5 Chapter Conclusions	283

Chapter 6: Coal Char Re-firing with Biomass Ash in a Drop Tube Furnace and Characterisation of Associated Mineral Transformations	285
6.1 General Introduction	285
6.2 Experimental Matrix.....	287
6.3 TGA Study of Co-firing Coal Char with Biomass Ash.....	288
6.4 Mineral Transformations and Particle Size Distributions of Co-fired Blends and DTF Ashes	296
6.5 Ternary Phase Diagrams of Biomass Ashes Co-fired with DTF Chars	320
6.6 MLA Coloured Mosaics of 500°C Biomass Muffle Furnace Ashes, Coal Chars and DTF Biomass Co-fired Ashes.....	324
6.7 Mineral Associations of DTF Ash from Co-firing Coal Char with Biomass Ash	333
6.8 Chapter Conclusions	338
Chapter 7: Conclusions and Future Work.....	341
7.1 Automated Mineralogy and Erosion Test Rig Experiments	341
7.2 Drop Tube Furnace Experiments.....	344
7.3 Coal Char Re-firing with Biomass Ash in a Drop Tube Furnace....	346
7.4 Recommendations for Future Work	348
Chapter 8: References.....	349
Chapter 9: Appendices.....	374
Appendix 1: TGA Burnout Profiles of DTF Chars.....	374
Appendix 2: Mineral Transformations during Devolatilisation and Char Combustion.....	376

List of Figures

Figure 1-1: Co-firing biomass with coal options.....	6
Figure 1-2: shows the process of pulverised fuel combustion for electricity generation	10
Figure 2-1: Structure of cellulose[15]	26
Figure 2-2: Structure of hemicellulose - xylan component[15].....	26
Figure 2-3: Structure of hemicellulose - glucomannan component[15].....	27
Figure 2-4: Structure of lignin[15].....	27
Figure 2-5: Variation of vitrinite reflectance with coal type[14].....	39
Figure 2-6: Inorganic constituents in coal and their occurrence[46].....	41
Figure 2-7: Mineral transformation of coal minerals as a function of temperature (modified from [54, 65, 66]).....	46
Figure 2-8: Bituminous coal mineralogy and fly ash composition before and after combustion	46
Figure 2-9: Physical transformations to form ash during coal/biomass combustion	50
Figure 2-10: Catalytic mechanism for the reaction of iron atoms in the char structure[72]	53
Figure 2-11: Catalytic mechanism for reaction of alkali metals[73].....	53
Figure 2-12: Ash formation model showing char fragmentation to ash during burnout from Wilemski and Srinivasachar[119].....	65
Figure 2-13: Cumulative particle size distribution comparison of experimental and model results at different levels of coalescence[128]	66
Figure 2-14: Measured pulverised coal erosion rate versus the hard mineral content of the coals with excluded mineral particles in excess of 25µm in diameter[173].....	80

Figure 2-15: Experimental erosion rates on mild steel as a function of ash particle velocity at an impingement angle of 30°[174]	85
Figure 2-16: Ternary phase diagrams showing mineral phase composition distribution using CCSEM[120]	96
Figure 2-17: Measurement mode flow chart.....	99
Figure 3-1: Rotary sample divider apparatus	106
Figure 3-2: Rotary micro riffler apparatus.....	107
Figure 3-3: Typical proximate analysis graph.....	109
Figure 3-4: Elemental analysis of power station fly ashes	114
Figure 3-5: Coal rank definition diagram[14]	119
Figure 3-6: Coal rank as a function of mean vitrinite reflectance[213]	120
Figure 3-7: Mean random vitrinite reflectance R_o (%).....	122
Figure 3-8: Camsizer P4 setup	129
Figure 3-9: Control panel	131
Figure 3-10: Collection probe with cyclone and control system.....	131
Figure 3-11: Feeding system	132
Figure 3-12 Schematic of the drop tube furnace	136
Figure 3-13: DTF volumetric gas flow analysers	138
Figure 3-14: ABB continuous oxygen gas analyser.....	138
Figure 3-15: Schematic of the erodent test rig apparatus.....	148
Figure 3-16: Epoxy resin, hardener, stirring pot and weighing apparatus....	150
Figure 3-17: Grant PTR-35 rotator apparatus	152

Figure 3-18: Struers rotopol-1 grinder and polisher.....	153
Figure 3-19: FEI Quanta 600 Mineral Liberation Analyser (MLA).....	162
Figure 4-1: Relative erosion rate as a function of the particle impact velocity for the power station fly ashes	171
Figure 4-2: X-ray diffraction of Trimble County fly ash	176
Figure 4-3: X-ray diffraction of Drax fly ash.....	177
Figure 4-4: X-ray diffraction of Ratcliffe fly ash.....	178
Figure 4-5: X-ray diffraction of Longannet fly ash.....	179
Figure 4-6: MLA mineral species legend.....	183
Figure 4-7: Electron micrograph of Trimble County fly ash (USA, Kentucky)	184
Figure 4-8: MLA coloured mosaic of Trimble County fly ash (USA, Kentucky)	184
Figure 4-9: Electron micrograph of Drax fly ash (UK, Yorkshire).....	185
Figure 4-10: MLA coloured mosaic of Drax fly ash (UK, Yorkshire).....	185
Figure 4-11: Electron micrograph of Ratcliffe fly ash (UK, Nottinghamshire).....	186
Figure 4-12: MLA coloured mosaic of Ratcliffe fly ash (UK, Nottinghamshire)	186
Figure 4-13: Electron micrograph of Longannet fly ash (UK, Fife).....	187
Figure 4-14: MLA coloured mosaic of Longannet fly ash (UK, Fife)	187
Figure 4-15: SiO_2 - Al_2O_3 - CaO ternary phase diagram for Ratcliffe fly ash	189
Figure 4-16: SiO_2 - Al_2O_3 - Fe_2O_3 ternary phase diagram for Ratcliffe fly ash	189
Figure 4-17: Comparison of metal oxide compositions from XRF and MLA of the Ratcliffe fly ash	191

Figure 4-18:CaO - Al ₂ O ₃ - SiO ₂ ternary phase diagram[230]	192
Figure 4-19: SiO ₂ - Al ₂ O ₃ - Fe ₂ O ₃ ternary phase diagram[231]	193
Figure 4-20: Particle size distributions of the power station fly ashes.....	195
Figure 4-21: Quartz grain size distributions of the power station fly ashes ..	195
Figure 4-22: Hematite grain size distributions of the power station fly ashes	196
Figure 4-23: Mineral matter distribution and associations in Ratcliffe fly ash	198
Figure 4-24: Mineral matter distribution and associations in Drax fly ash	198
Figure 4-25: Mineral matter distribution and associations in Longannet fly ash	199
Figure 4-26: Mineral matter distribution and associations in Trimble fly ash	199
Figure 5-1: CO ₂ adsorption data showing cumulative pore volume and pore width for the DTF coal and biomass chars	215
Figure 5-2: Char burnout times from TGA isothermal char combustion at different temperatures.....	218
Figure 5-3: Char burnout profiles of TGA char and DTF char at different residence times for South African Koorfontein coal.....	220
Figure 5-4: XRD of muffle furnace coal ashes (500°C, air).....	222
Figure 5-5: XRD of muffle furnace coal ashes (500°C, air) (continued).....	223
Figure 5-6: MLA mineral species legend.....	234
Figure 5-7: Electron micrograph of SA (Koorfontein) coal 0-75 µm fraction	235
Figure 5-8: MLA coloured mosaic of SA (Koorfontein) 0-75 fraction.....	235
Figure 5-9: Electron micrograph of UK (Cumberworth) coal 0-75 µm fraction	236

Figure 5-10: MLA coloured mosaic of UK (Cumberworth) 0-75 fraction	236
Figure 5-11: Electron micrograph of UK (Kellingley) coal 0-75 μm fraction .	237
Figure 5-12: MLA coloured mosaic of UK (Kellingley) 0-75 fraction	237
Figure 5-13: Electron micrograph of USA (Illinois) coal 0-75 μm fraction	238
Figure 5-14: MLA coloured mosaic of USA (Illinois) 0-75 fraction	238
Figure 5-15: Electron micrograph of UK (Roundwood) coal 0-75 μm fraction	239
Figure 5-16: MLA coloured mosaic of UK (Roundwood) 0-75 fraction.....	239
Figure 5-17: Mineral group changes of South African (Koorfontein) Coal during devolatilisation and char combustion	253
Figure 5-18: Mineral group changes of USA Illinois Coal during devolatilisation and char combustion	254
Figure 5-19: Mineral associations of South African (Koorfontein) 53-75 μm coal fraction	257
Figure 5-20: Mineral associations of DTF South African (Koorfontein) Char (1450°C, 200 ms)	258
Figure 5-21: Mineral associations of South African (Koorfontein) muffle furnace ash at 500°C	259
Figure 5-22: Mineral associations of DTF South African (Koorfontein) ash (5% O ₂ , 1450°C, 200 ms).....	260
Figure 5-23: Mineral associations of DTF South African (Koorfontein) ash (5% O ₂ , 1450°C, 600 ms).....	261
Figure 5-24: Cumulative number distribution (%) of the percentage of particles with a circularity between 0.6 - 1.0 within each sample.....	264
Figure 5-25: Electron micrograph of South African (Koorfontein) 53-75 μm fraction.....	265
Figure 5-26: MLA coloured mosaic of South African (Koorfontein) 53-75 μm fraction.....	265

Figure 5-27: Electron micrograph of DTF South African (Koorfontein) Char (1450°C, 200 ms)	266
Figure 5-28: MLA coloured mosaic of DTF South African (Koorfontein) Char (1450°C, 200 ms)	266
Figure 5-29: Electron micrograph of South African (Koorfontein) Ash (500°C muffle furnace).....	267
Figure 5-30: MLA coloured mosaic of South African (Koorfontein) Ash (500°C muffle furnace).....	267
Figure 5-31: Electron micrograph of DTF South African (Koorfontein) Ash (1450°C, 5%O ₂ , 200 ms)	268
Figure 5-32: MLA coloured mosaic of DTF South African (Koorfontein) Ash (1450°C, 5%O ₂ , 200 ms)	268
Figure 5-33: Electron micrograph of DTF South African (Koorfontein) Ash (1450°C, 5%O ₂ , 600 ms).....	269
Figure 5-34: MLA coloured mosaic of DTF South African (Koorfontein) Ash (1450°C, 5%O ₂ , 600 ms)	269
Figure 5-35: Electron micrograph of USA Illinois 53-75 µm coal fraction.....	270
Figure 5-36: MLA coloured mosaic of USA Illinois 53-75 µm coal fraction ..	270
Figure 5-37: Electron micrograph of DTF USA Illinois Char (1450°C, 200 ms)	271
Figure 5-38: MLA coloured mosaic of DTF USA Illinois Char (1450°C, 200 ms)	271
Figure 5-39: Electron micrograph of USA Illinois Ash (500°C muffle furnace)	272
Figure 5-40: MLA coloured mosaic of USA Illinois Ash (500°C muffle furnace)	272
Figure 5-41: Particle size distribution of South African coal and DTF char ..	277
Figure 5-42: Particle size distribution of USA Illinois coal and DTF char	278

Figure 5-43: Particle size distribution of olive cake biomass and DTF char.	279
Figure 5-44: SiO_2 - Al_2O_3 - CaO ternary phase diagram of raw South African coal (53-75 μm)	280
Figure 5-45: SiO_2 - Al_2O_3 - CaO ternary phase diagram of DTF South African char (1450°C, 200 ms, N_2).....	281
Figure 5-46: SiO_2 - Al_2O_3 - CaO ternary phase diagram of DTF South African ash (1450°C, 200 ms, 5% O_2).....	282
Figure 6-1: TGA char burnout profiles of South African Koorfontein DTF Coal Char (1450°C, 200 ms) and 500°C Olive Cake Ash at 5°C min ⁻¹ to 1000°C	291
Figure 6-2: TGA char burnout profiles of South African Koorfontein DTF Coal Char (1450°C, 200 ms) and 500°C Sunflower Ash at 5°C min ⁻¹ to 1000°C	292
Figure 6-3: TGA char burnout profiles of South African Koorfontein DTF Coal Char (1450°C, 200 ms) and 500°C Miscanthus Ash at 5°C min ⁻¹ to 1000°C	293
Figure 6-4: XRD of muffle furnace biomass ashes (500C, air)	294
Figure 6-5: Mineral group changes of DTF South African (Koorfontein) Char (1450°C, N_2 , 200 ms) / Miscanthus 500°C Ash (50:50 weight %) fired at 1450°C, 5% O_2 and 600 ms in a DTF	298
Figure 6-6: Mineral group changes of DTF South African (Koorfontein) Char (1450°C, N_2 , 200 ms) / Sunflower Husk 500°C Ash (50:50 weight %) fired at 1450°C, 5% O_2 and 600 ms in a DTF	299
Figure 6-7: Mineral group changes of DTF South African (Koorfontein) Char (1450°C, N_2 , 200 ms) / Olive Cake 500°C Ash (50:50 weight %) fired at 1450°C, 5% O_2 and 200 ms in a DTF	300
Figure 6-8: Mineral group changes of DTF South African (Koorfontein) Char (1450°C, N_2 , 200 ms) / Olive Cake 500°C Ash (50:50 weight %) fired at 1450°C, 5% O_2 , 600 ms in a DTF	301
Figure 6-9: Electron micrograph of DTF ash of South African (Koorfontein) DTF Char (1450°C, 200 ms) and 500°C Olive Cake ash (50:50 weight %) fired at 1450°C, 5% O_2 and 200 ms	303

Figure 6-10: MLA coloured mosaic of DTF ash of South African (Koorfontein) DTF Char (1450°C, 200 ms) and 500°C Olive Cake ash (50:50 weight %) fired at 1450°C, 5% O ₂ and 200 ms.....	303
Figure 6-11: Electron micrograph of DTF ash of South African Koorfontein DTF Char (1450°C, 200 ms) and 500°C Olive Cake ash (50:50 weight %) fired at 1450°C, 5% O ₂ and 600 ms.....	307
Figure 6-12: MLA coloured mosaic of DTF ash of South African Koorfontein DTF Char (1450°C, 200 ms) and 500°C Olive Cake ash (50:50 weight %) fired at 1450°C, 5% O ₂ and 600 ms.....	307
Figure 6-13: Cumulative particle size distribution of the DTF ash formed from firing DTF South African (Koorfontein) char and olive cake 500°C ash at two residence times.	317
Figure 6-14: Cumulative mineral group size distribution of the DTF ash formed from firing DTF South African (Koorfontein) char and olive cake 500°C ash at 1450°C, 5% O ₂ and 200 ms.....	318
Figure 6-15: Cumulative mineral group size distribution of the DTF ash formed from firing DTF South African (Koorfontein) char and olive cake 500°C ash at 1450°C, 5% O ₂ and 600 ms.....	319
Figure 6-16: Ternary phase diagram of SiO ₂ - Al ₂ O ₃ - K ₂ O[306].....	321
Figure 6-17: SiO ₂ - Al ₂ O ₃ - K ₂ O ternary phase diagram of DTF South African char (1450°C, 200 ms, N ₂).....	321
Figure 6-18: SiO ₂ - Al ₂ O ₃ - K ₂ O ternary phase diagram of muffle furnace olive cake ash (500°C, Air).....	322
Figure 6-19: SiO ₂ - Al ₂ O ₃ - K ₂ O ternary phase diagram of DTF South African (Koorfontein) Char (1450°C, N ₂ , 200 ms) / Olive Cake 500°C Ash (50:50 weight %) fired at 1450°C, 5% O ₂ , 200 ms.....	323
Figure 6-20: SiO ₂ - Al ₂ O ₃ - K ₂ O ternary phase diagram of DTF South African (Koorfontein) Char (1450°C, N ₂ , 200 ms) / Olive Cake 500°C Ash (50:50 weight %) fired at 1450°C, 5% O ₂ , 600 ms.....	323
Figure 6-21: Cumulative number distribution (%) of the percentage of particles with a circularity between 0.6 - 1.0 within each biomass co-fired sample	325
Figure 6-22: Electron micrograph of muffle furnace Miscanthus ash (500°C, air)	326

Figure 6-23: MLA coloured mosaic of muffle furnace Miscanthus ash (500°C, air)	326
Figure 6-24: Electron micrograph of muffle furnace Sunflower ash (500°C, air)	327
Figure 6-25: MLA coloured mosaic of muffle furnace Sunflower ash (500°C, air)	327
Figure 6-26: Electron micrograph of muffle furnace Olive Cake ash (500°C, air)	328
Figure 6-27: MLA coloured mosaic of muffle furnace Olive Cake ash (500°C, air)	328
Figure 6-28: Electron micrograph of DTF South African (Koorfontein) Char (1450°C, N ₂ , 200 ms) / Miscanthus 500°C Ash (50:50 weight %) fired at 1450°C, 5% O ₂ , 600 ms.....	329
Figure 6-29: MLA coloured mosaic of of DTF South African (Koorfontein) Char (1450°C, N ₂ , 200 ms) / Miscanthus 500°C Ash (50:50 weight %) fired at 1450°C, 5% O ₂ , 600 ms.....	329
Figure 6-30: Electron micrograph of DTF South African (Koorfontein) Char (1450°C, N ₂ , 200 ms) / Sunflower Husk 500°C Ash (50:50 weight %) fired at 1450°C, 5% O ₂ , 600 ms.....	330
Figure 6-31: MLA coloured mosaic of DTF South African (Koorfontein) Char (1450°C, N ₂ , 200 ms) / Sunflower Husk 500°C Ash (50:50 weight %) fired at 1450°C, 5% O ₂ , 600 ms.....	330
Figure 6-32: Electron micrograph of DTF South African (Koorfontein) Char (1450°C, N ₂ , 200 ms) / Olive Cake 500°C Ash (50:50 weight %) fired at 1450°C, 5% O ₂ , 200 ms.....	331
Figure 6-33: MLA coloured mosaic of DTF South African (Koorfontein) Char (1450°C, N ₂ , 200 ms) / Olive Cake 500°C Ash (50:50 weight %) fired at 1450°C, 5% O ₂ , 200 ms.....	331
Figure 6-34: Electron micrograph of DTF South African (Koorfontein) Char (1450°C, N ₂ , 200 ms) / Olive Cake 500°C Ash (50:50 weight %) fired at 1450°C, 5% O ₂ , 600 ms.....	332
Figure 6-35: MLA coloured mosaic of DTF South African (Koorfontein) Char (1450°C, N ₂ , 200 ms) / Olive Cake 500°C Ash (50:50 weight %) fired at 1450°C, 5% O ₂ , 600 ms.....	332

Figure 6-36: DTF Ash of DTF South African (Koorfontein) Char (1450°C, 200 ms) / Olive cake 500°C Ash under 1450°C, 5% O ₂ and 200 ms.....	334
Figure 6-37: DTF Ash of DTF South African (Koorfontein) Char (1450°C, 200 ms) / Olive cake 500°C Ash under 1450°C, 5% O ₂ and 600 ms.....	335
Figure 6-38: DTF Ash of DTF South African (Koorfontein) Char (1450°C, 200 ms) / Miscanthus 500°C Ash under 1450°C, 5% O ₂ and 600 ms.....	336
Figure 6-39: DTF Ash of DTF South African (Koorfontein) Char (1450°C, 200 ms) / Sunflower 500°C Ash under 1450°C, 5% O ₂ and 600 ms	337
Figure 9-1: Char burnout profiles of TGA char and DTF char at different residence times for Cumberworth coal.....	374
Figure 9-2: Char burnout profiles of TGA char and DTF char at different residence times for Kellingley coal.....	374
Figure 9-3: Char burnout profiles of TGA char and DTF char at different residence times for USA Illinois coal.....	375
Figure 9-4: Char burnout profiles of TGA char and DTF char at different residence times for Roundwood coal	375
Figure 9-5: Mineral group changes of Kellingley coal during devolatilisation and char combustion	376
Figure 9-6: Mineral group changes of Cumberworth coal during devolatilisation and char combustion	376
Figure 9-7: Mineral group changes of Roundwood coal during devolatilisation and char combustion	377

List of Tables

Table 2-1: Groups and subclassifications of feedstocks.....	25
Table 2-2 Chemical compositions and thermal decomposition reactions of minerals (adapted from [52]).....	48
Table 2-3: Slagging and fouling indices[116]	61
Table 2-4: Coal mineral species and hardness values[173]	79
Table 2-5: Relative erosion rate of two pulverised coals and corresponding fly ashes from a 1 MWth combustion rig after testing in an ambient air jet impactor at an impact velocity of 40 m s ⁻¹ [173].....	81
Table 2-6: Measurement mode descriptions	98
Table 2-7: Institutions worldwide operating CCSEM systems	100
Table 3-1: Proximate and ultimate analysis of samples	111
Table 3-2: Loss on ignition (LOI) of power station fly ashes	112
Table 3-3: Petrographic analysis of the maceral groups	121
Table 3-4: DTF operation settings.....	135
Table 3-5: Ash contents of coals and biomass chars (53-75µm fractions)...	140
Table 3-6: Char yield and collection efficiency for the pyrolysed chars.....	143
Table 3-7: Dynamic epoxy curing settings	151
Table 4-1: Pattern match probability values to assess reliability and classification results.....	166
Table 4-2: Standard Reference Minerals	167
Table 4-3: Elemental compositions of MLA minerals.....	168
Table 4-4: Elemental compositions of MLA minerals (continued).....	169

Table 4-5: Erosion test results for power station fly ashes	172
Table 4-6: Fly ash particle size analysis data by dry sieving	173
Table 4-7: Fly ash particle size distribution by laser light scattering (Malvern)	173
Table 4-8: X-ray fluorescence data of power station fly ashes (conducted by Doosan Babcock)	175
Table 4-9: Mineral compositions of power station fly ashes	181
Table 4-10: Mineral angularities and relative standard deviations (%) of the power station fly ashes	201
Table 4-11: Individual mineral grains and total grains in power station fly ashes	201
Table 5-1: Coal devolatilisation runs and experimental operating conditions conducted on the drop tube furnace	205
Table 5-2: Muffle furnace experiments on DTF coal chars (produced at 1450°C, 200ms)	206
Table 5-3: Coal burnout runs and experimental operating conditions conducted on the drop tube furnace.....	206
Table 5-4: Proximate and DTF volatiles and R factors for coal and biomass chars	211
Table 5-5: Surface area analysis of DTF chars from coal and biomass samples	213
Table 5-6: TGA isothermal coal combustion kinetic parameters	217
Table 5-7: Char burnout kinetic parameters for South African Koornfontein coal	219
Table 5-8: Elemental analysis of DTF chars at 200 and 600 milliseconds...	221
Table 5-9: Re-fired char ash yields and collection efficiencies for South African Koornfontein 200ms char.....	225

Table 5-10: TGA ash contents of the DTF ashes for the South African Koornfontein 200ms char.....	226
Table 5-11: CCSEM/MLA samples with the respective number of particles and x-ray counts.....	229
Table 5-12: SEM-MLA Mineral compositions of raw 0-75 µm coal fractions showing mean and standard deviations for three representative samples (weight percentage % basis).....	231
Table 5-13: Mineral compositions of 53-75 µm raw coal fractions (weight %)	242
Table 5-14: Mineral compositions of DTF coal chars produced at 1450 °C and 200 ms (weight %).....	245
Table 5-15: Mineral compositions of muffle furnace coal ashes produced at 500°C under air (weight %).....	248
Table 5-16: Mineral compositions of the DTF ashes produced from DTF South African Char (1450°C, 200ms, N ₂) (weight %)	250
Table 5-17: XRF data of raw coal samples	252
Table 5-18: Particle size parameters before and after devolatilisation	276
Table 6-1: Coal char and biomass ash combustion study using the drop tube furnace	287
Table 6-2: Muffle furnace experiments on raw biomasses	287
Table 6-3: Ignition temperature as a function of blend ratio.....	289
Table 6-4: XRF data of 500°C biomass ashes	295
Table 6-5: Possible mineral transformations during co-firing of DTF coal char and biomass ashes.....	304
Table 6-6: Mineral compositions of DTF South African (Koornfontein) Char and 500°C biomass ashes.....	308
Table 6-7: Mineral Composition of DTF South African (Koornfontein) coal char and 500°C Biomass Ashes (50:50 weight %) – Calculated	310

Table 6-8: Mineral Composition of DTF Ash from Co-firing Coal Char with Biomass Ash.....	313
--	-----

Nomenclatures

Symbol	Description [SI Units]
A	Pre-exponential factor [s^{-1}]
k	Rate constant [s^{-1}]
E _a	Activation energy [$Jmol^{-1}$]
V	Volume of pores occupied at P/P ₀ [cm^3/g]
V ₀	Total volume of the micropore system [cm^3/g]
B	Constant related to the Gaussian pore distribution width [K^{-2}]
T	Temperature at which the isotherm measured {K}
β	Constant, dependent on adsorbate [dimensionless]
P ₀ /P	inverse relative pressure of the adsorbate [dimensionless]
v	Volume of gas adsorbed [m^3/g]
v _m	Volume of gas adsorbed at the monolayer surface [m^3/g]
p	Equilibrium gas pressure
p ₀	Saturation pressure
c	BET constant
S	Surface area per unit mass [m^2/g]
N	Avogadro's number (of molecules per mole)
A	Cross-sectional surface area of an adsorbed gas molecule
m	mass of materials
R _i	individual reflectance readings
n	number of point analysis measurements per sample
s	sample standard deviation
I _R	reflected perpendicular luminous flux [%]

I_0	incident luminous flux [%]
M_{char}	Mass of char collected after DTF devolatilisation [g]
M_{fuel}	Mass of raw fuel fed into DTF [g]
A_{char}	TGA derived ash content of the DTF char [wt% dry basis]
A_{fue}	TGA derived ash content of the raw fuel [wt% dry basis]
V_r	Gas velocity at a point (r) from the work tube centre [ms^{-1}]
V	Average gas velocity across radius of the work tube (R) [ms^{-1}]
V_0	Velocity of fuel particle passing centre of work tube [ms^{-1}]
t	Residence time of the fuel particle in the furnace [ms]
Q	Volumetric flow rate of gas through DTF [m^3s^{-1}]
A	Cross-sectional area of work tube [m^2]
L	Separation distance between the collector & feeder probes [m]

Abbreviations

CCSEM	Computer controlled scanning electron microscopy
MLA	Mineral liberation analysis
SEM-EDX	Scanning electron microscopy energy dispersive X-ray
XRD	X-ray diffraction
XRF	X-ray fluorescence spectroscopy
ICPMS	Inductively coupled plasma mass spectrometry
TGA	Thermogravimetric analysis
DTF	Drop tube furnace
VM	Volatile matter
FC	Fixed carbon
LHV	Low heating value
HHV	High heating value
MIS	Miscanthus
SUN	Sunflower husk

OC	Olive cake
SAC	South African Coal (Koorfontein)
KC	UK Kellingley Coal
ST	Polish Stefanów Coal
RW	UK Roundwood Coal
CW	UK Cumberworth Coal
CO	USA Illinois Coal (Consul)
GHG	Greenhouse gases
RT	Residence time
T	Temperature
AAEM	Alkali and alkaline earth minerals
CFD	Computational fluid dynamics
CFC	Chlorofluorocarbons
HCFC	Hydrochlorofluorocarbons
OECD	Organisation for Economic Cooperation & Development

Chapter 1: Introduction

The management of ash in pulverised fuel utility boilers is fundamental to the overall performance, integrity and efficiency of power plants. Ash deposition problems are one of the primary causes of reduced boiler efficiency, unscheduled shutdowns, and increased soot-blowing, maintenance and cleaning costs. Ash deposition and related issues costs the global power utility industry billions of dollars annually, mainly because of reduced power generation efficiency and availability, and increased equipment maintenance.

The retention of pulverised fuel ash along the flue gas pathways in a boiler principally occur as slagging and fouling deposits, and over long durations can contribute to the erosive and corrosive wear of internal components. Slag deposits form on the furnace walls in the high temperature radiant section of the boiler, with the mass transfer of particles to the walls occurring mainly due to inertial compaction, and deposit consolidation involving sintering and fusion of the ash particles. Conversely, fouling deposits form in the convective sections of a boiler at lower temperatures, with little or no fusion of the ash particles. The primary mechanism responsible for the consolidation of the deposits is the release of the volatile inorganic species, predominantly alkali metals in the flame, and the subsequent condensation of these species on ash particle surfaces and on the cooler surfaces in the boiler. These species melt at low temperatures and form the bonds between the unfused ash particles. The further consolidation of the deposits can occur by the sulphation of the alkali and alkaline earth metal oxides within the deposit.

Fundamental understanding of these ash deposit growth mechanisms requires a detailed investigation into the mineral matter transformations that occur in pulverised fuel flames to form fly ashes. Boiler manufacturers are continually seeking reliable experimental data to develop computer simulations that can predict the likely ash behaviour based on a variety of feedstocks and operating conditions, with the intention to predict and mitigate against unscheduled maintenance and shutdowns. The high operating and down-time costs of performing industrial-scale boiler studies for ash deposition, and the variability of feedstocks, with various coal and biomass types used daily, makes comparing an initial feedstock to the resultant ash deposit formed practically impossible. Therefore, a reliance on lower cost drop tube furnace studies which simulate the characteristics of industrial-scale boilers, and provide greater control on operating conditions is required to generate the experimental data needed to aid computational fluid dynamic modelling of ash deposition in pulverised fuel combustion.

The major aim of this research was to produce experimental data that can aid the development of ash prediction modelling, principally through detailed characterisation of a number of pulverised fuel and real boiler fly ashes, using both conventional, and advanced techniques. The work programme at the University of Nottingham involved the following types of experiment:

- Devolatilisation experiments in which the pulverised particles were subjected to high temperatures for a range of residence times in a nitrogen atmosphere;

- Char combustion experiments in which char particles, pre-prepared under a range of devolatilisation conditions are burned in nitrogen with oxygen, over a range of residence times;
- Detailed characterisation of a selection of fuels, chars and ashes using a Computer Controlled Scanning Electron Microscope (CCSEM) called a Mineral Liberation Analyser (MLA);
- Analysis of erosion test rig experiments on real boiler fly ashes and subsequent detailed characterisation on the mineral species using MLA.

The intention of this work programme was to investigate the mineral transformations that occur during the devolatilisation and char combustion processes, and generate data on the kinetics of these processes, which are of value in computer modelling work. The emphasis mainly focussed on the final stages of char burnout when the inherent mineral matter is released, and significant coalescence of the fused and partially fused mineral particles can occur. The products from these drop tube furnace tests were characterised in detail to determine the extent of devolatilisation and char burnout, and to determine the nature and distribution of the mineral material, with attention to the mineral associations and interactions. To add further complexity, low temperature biomass ash and coal char was blended together for char combustion studies to investigate the influence that the biomass derived minerals had on the extent of coal char burnout and types of coalescing and agglomerating particles formed during combustion.

1.1 Global Warming and Climate Change

The anthropogenic rise in carbon emissions is widely regarded as the leading cause of global warming and climate change, whereby human activity is detrimentally impacting the climate and ecological systems of the planet. In the most recent IPCC report, significant evidence and projections of the measures required to slow and remediate the consequences of rising temperatures of 1.5°C above pre-industrial levels were presented. There are many gases which are major contributors towards global warming based on their potential to trap the sun's energy in the atmosphere, these include but are not limited to: carbon dioxide (CO₂), carbon monoxide (CO), sulphur oxides (SO_x), nitrous oxides (NO_x), organohalides such as chlorofluorocarbons (CFCs) and hydrochlorofluorocarbons (HCFCs), and ozone (O₃). Throughout the last century, the concentration of these gases has increased in the atmosphere due to burning fossil fuels for power generation to stimulate economic growth.

Coal has remained the main source of energy for the generation of electricity and heat worldwide, contributing around 40% over the last 40 years as generation outputs have grown from 22.3 Exajoules (EJ) in 1971 to 106.6 EJ in 2017[1]. The power sector accounting for nearly two-thirds of global carbon emissions growth, with coal use surpassing 10 Gt CO₂ and coal-fired electricity generation contributing to 30% of global CO₂ emissions[2]. In order to counteract further atmospheric rises, alternative, carbon-neutral technologies are required to halt the persistent global temperature rise, and methods need to be created to reverse the atmospheric carbon emission concentration.

Biomass co-firing with coal is a viable technology for developed and developing countries from an environmental and economic perspective. The addition of biomass with coal reduces the greenhouse gas emissions per unit of energy produced compared to firing coal because burning biomass (e.g. woody biomass and agricultural residues) results in reduced oxide emissions of sulphur (SO_x), nitrogen (NO_x), and fossil-derived carbon dioxide (CO_2)[3, 4]. Furthermore, existing coal fired power plant infrastructure can be converted to burn low levels of biomass fuels with relatively low capital investment. Co-firing is a lower risk option for the production of renewable energy compared to alternative uses of biomass such as biomass to biofuel production, and minimises waste (e.g. wood and agricultural waste) and the issues surrounding its disposal. The past few decades have seen a rise in the co-combustion of biomass fuels in existing coal-fired and gas-fired power plants[5].

The two main co-firing technologies utilised in coal-fired plants are direct co-firing and indirect co-firing. Figure 1-1 shows a schematic of these options, with direct co-firing (routes 2 and 3) showing the direct injection of pre-milled biomass into the pulverised coal pipework (route 2) or into the modified coal burners (route 3). The coal and biomass could be directly injected into dedicated burners. Secondly, indirect co-firing (routes 1, 4 and 5) shows the pre-mixing of the biomass with the coal and the milling and firing of the mixed fuel through the existing coal mills and firing system (routes 1 and 5). Finally, the gasification of the biomass followed by the combustion of the product gas in the boiler (route 4).

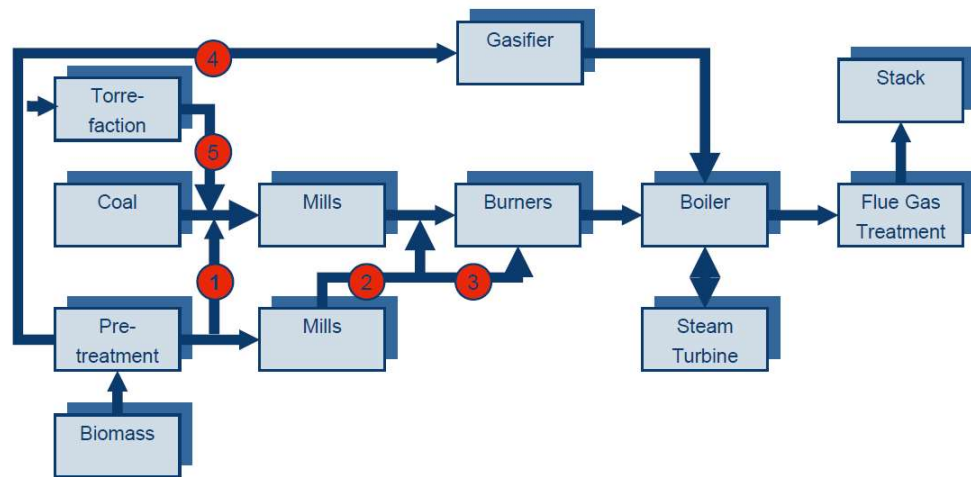


Figure 1-1: Co-firing biomass with coal options

The most widely used method is direct co-firing which has many associated challenges such as the tendency to produce ash deposits (e.g. slagging and fouling), the lack of flexibility to use different types of biomasses and the limited range of co-firing[6]. Furthermore, biomass tends to cause higher corrosion of boiler walls alongside the enhanced slagging and fouling propensity[7]. Further research into biomass co-firing and understanding the mineral transformations, ash deposits and slagging/fouling phenomena to offer mitigation strategies will improve the overall efficiency of power generation.

1.2 Pulverised Fuel Combustion and De-carbonisation

Coal is a highly versatile, energy-rich substance which has had many different uses throughout the ages, such as in cement and steel manufacturing, and liquid fuel production for the transport sector. The various combustion by-products such as fly ash, bottom ash and boiler slag have also proven useful additives in concrete manufacture, as well as a source of gypsum for plasterboard manufacture. As coal is one of the most abundant sources of fuel and historically the most affordable fuel for power generation in many developing and industrialised countries, there has been a continued effort to improve the environmental impact and efficiency of combustion processes to achieve near-zero carbon emissions.

One of the options available involves the deployment of high efficiency low emission (HELE) coal-fired power plants, utilising carbon capture, use and storage (CCUS). These technologies are commercially available and can reduce greenhouse gas emissions significantly from coal-fired power plants. The enhanced efficiencies mean that a higher amount of energy can be extracted from a single unit of coal. It has been estimated that increasing the average global efficiency rate of coal-fired power plants from 33% to 40% using this technology would cut the global CO₂ emissions by two gigatons, equivalent to the annual CO₂ emissions of India[8]. In addition to these reductions in greenhouse gas emissions, technology exists to significantly reduce other pollutants such as nitrogen oxides (NO_x), sulphur oxides (SO_x) and particulate matter (PM), which are important to address the growing air quality and health concerns.

Another option available to counteract the rise in CO₂ emissions involves using biomass feedstocks in replacement of coal to reduce the higher emissions associated with combusting pure coal. High calorific value biomasses such as woody herbaceous matter, agricultural residues, food waste and industrial wastes have been used. In comparison to coal, biomass has a relatively short geological time frame, spanning a few months to a few years, rather than thousands of years to form and mature. A major benefit for power generators is the ease of integration of biomass into pre-existing coal infrastructure with relatively few modifications. This significantly reduces the capital expenditure incurred to transition to lower carbon feedstocks.

Aside from the technological considerations, government subsidies such as the UK renewable obligations certificate (ROC), Feed in Tariffs (FIT) and Contracts for Difference (CfD) have sought to encourage renewable electricity generation through financial incentives, as well as various other tax reliefs such as enhanced capital allowances for businesses investing in qualifying low carbon energy technologies. Whilst these tax incentives can change power generators and consumers behaviour to reduce CO₂ emissions, the main driver is cost-effective technological advancement.

There are many current research challenges which require attention to optimise these biomass co-firing systems. Firstly, from an economic standpoint, although dependent on the boiler design, biomass has a lower thermal efficiency than coal due to the higher moisture contents, relatively smaller scales, lower calorific values and excessive ash deposition problems on boiler tubes. Additionally, the higher alkali and alkaline earth metal concentrations inherent

within the biomass fuel can increase the rate of corrosion effects on boiler and milling equipment compared to coal. The higher moisture content of biomass reduces the combustion efficiency, leading to power generators incurring additional handling, preparation and transportation costs, such as drying the biomass prior to combustion which can exceed the total fuel costs compared to fossil fuels. The ash fusion temperatures of biomass ashes are typically lower than coal due to the higher content of alkaline and alkali earth metals, at approximately 750°C compared to in excess of 1000°C for coal. This increases the probability of ash deposition and slag formation build up on the internal surfaces of the boilers, which can result in unscheduled shutdowns and plant maintenance.

1.2.1 Process Overview

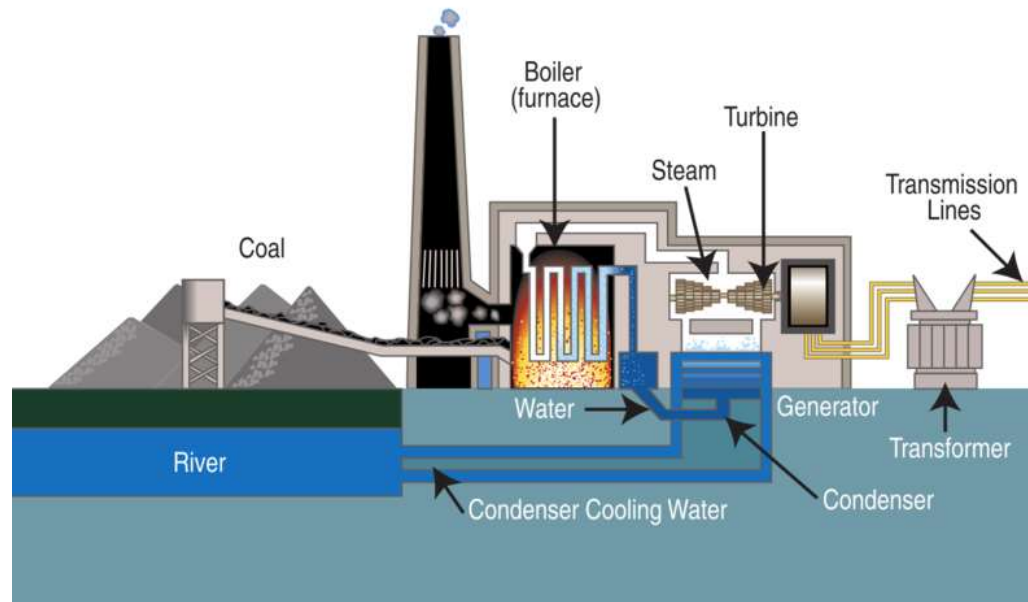


Figure 1-2: shows the process of pulverised fuel combustion for electricity generation

Coal is transported into the power plant via articulated lorries or unloaded from trains passing through the site. The coal is conveyed via belt and ramp conveyors to a feeder chute where the coal settles under gravity into hoppers, and at regular intervals is released to be pulverised using milling equipment. The fuel interacts with grinding media such as balls, rollers and hammers which causes the fuel particles to break and be ground into smaller particle sizes. This process generally involves the addition of a hot air stream through the milling equipment to reduce the moisture content of the fuel and entrain smaller particles into the classification section to be filtered according to size. The generally accepted particle size range is for 75% of the particles to be less than 75 μ m and less than 2% above 300 μ m in diameter. This particle size range

serves to produce a fine flowable powder to maximise the combustion efficiency in the boiler and minimise the unburned carbon content in the resultant ash.

The coal particles are then fed into the boiler section of the plant, where combustion occurs at high temperatures and the exothermic heat of reaction is transferred to the heat transfer surfaces or pipes containing high pressure water which boils to produce steam. This steam is used to spin a turbine, which is connected to an electrical generator. The gyrating motion of the turbine causes magnets to turn within copper wire coils inside a generator, this creates an electrical current to produce electricity which is usually transported along transmission and distribution power lines for consumption.

1.2.2 Combustion Systems

The solid fuel combustion systems available on the market can generally be categorised into the following types: fixed bed (grate) combustion, fluidised bed combustion and pulverised fuel combustion systems. These combustion systems are generally designed and constructed depending on the fuel type and quality to be fired, the extent of pre-combustion fuel processing, fuel-oxidiser ratio, gas flow conditions and the temperature range. These systems are integrated with fully automated process control to maintain safe operation to abide by the stringent environmental emission limits and have mechanical or pneumatic fuel-feeding capabilities. This section provides brief descriptions of these types of combustion technologies used on plant.

Fixed bed combustors

Fixed bed combustion is generally applicable to low-grade fuels with a high likelihood of ash deposition. These include fuels such as municipal solid wastes, straw and waste woods. The system operates by supplying primary air below the grate enabling the combustion process to occur on the grate pathway and secondary air above the grate to suppress NO_x formation. Grate furnace systems are particularly applicable to biomass fuels with high moisture content, varying particle sizes and high ash contents. The majority of the inorganic constituents are concentrated in the solid ash particles with the agglomerates formed, and are transported out of the system via the grate. However, a small fraction of the inorganics is entrained in the combustion flue gases as small fly ash particles and vapours. Therefore, the duct is usually cladded to minimise the effect of ash deposition and corrosion on the boiler wall. Additionally, the furnace temperature is restricted to values below 500°C to prevent chlorine-induced corrosion from raw fuels with high chlorine concentrations. Grate furnaces can be subdivided into fixed grates, travelling grates, vibrating grates, rotating grates and moving grates.

Fluidised bed combustors

Fluidisation bed combustion uses cylindrical vessels with a perforated bottom plate filled with an inert bed medium such as silica, sand or dolomite. The bed is fluidised by flowing air through the bottom plate. The bed medium is fluidised when the pressurised fluid (usually air) is passed through the medium and causes the solid particles to behave like a fluid. This creates a larger surface

area for heat transfer and effective mixing between the fuel, combustion air and bed material, resulting in a uniform temperature distribution for near complete combustion and higher efficiencies. The bed material is usually kept between 800-900°C to minimise pollutant formation, agglomeration due to low melting point ash phases, ash deposition and corrosion. A chemically inert material has the added benefit of inhibiting reactions between the fuel ash and bed material. In order to control SO₂ emissions for high sulphur-containing fuels, the addition of limestone is sometimes mixed with the bed material. These systems can either be as circulating fluidised beds (CFB), where the bed material is entrained within the upward jet flow, or where the bed material is stationary, termed the bubbling fluidised bed (BFB). CFBs are more operationally complex and require a cyclone unit to sequester the bed material. It is well recognised that using sand (quartz) as the bed medium results in high levels of erosion on heat transfer surfaces within the furnace, which can detach deposits. As such, slagging and fouling is usually not an issue with fluidised systems due to the low temperatures (reducing molten phases) and erosive behaviour of the particles.

Fluidised bed combustors are generally constructed to generate 30-350 MWe, utilising fuels with varying particle size distributions, moisture contents and ash contents such as waste wood, pelletised solid recovered fuels (SRF) and sewage sludges. The main operating consideration is bed agglomeration caused by chemical reactions between the bed material and the fuel derived inorganic vapours and molten salts and silicates. This can impede fluidisation and cause the unscheduled shutdown of the furnace.

Pulverised fuel combustors

Pulverised fuel (PF) combustors are the most prevalent type of coal combustion systems used worldwide. The pulverised fuel particles, with particle sizes typically below 300µm are usually transported into the burner using preheated air or recirculated flue gases before passing into the furnace. The particles are rapidly heated and release volatile combustible gases and upon reaction with oxygen produce a flue gas with entrained ash particles. Inside the combustion chamber the flue gas comes into contact with heat transfer surfaces such as boiler walls and tubes, whereby the heat is transferred to the water-steam cycle. These combustors are typically designed and constructed to achieve near complete combustion of the fuel particles before the flue gas approaches the tube banks. An important operational parameter is the furnace exit gas temperature as this should be carefully controlled to ensure that it remains below the ash softening and melting temperature of the fuel to reduce the likelihood of molten or sticky ash deposits forming and adhering to internal surfaces. However, this temperature should not be lowered so much as to reduce the extent of burnout achievable for particular fuels.

In PF combustion systems, ash deposition on heat transfer surfaces in the form of slagging and fouling is another concern. Slagging occurs when the ash particles are in the molten state and behave similarly to liquids, whilst fouling occurs when solidified particles accumulate and compact together outside of the flame radiation zone. As these particles accumulate with time, layers are formed which can be easily removed using a soot blower. Slagging or fouling

deposits are dependent on the inorganic composition and physical characteristics of the fuel as well as the operating conditions inside the boiler.

1.3 Motivation for the Research and Research Objectives

1.3.1 Motivation for the Project

The majority of governments have committed to strengthening their response to the threat of global warming and climate change through The Paris Agreement and the international community are becoming increasingly aware of the consequences of inaction in tackling rising carbon emissions. In the UK, the renewable obligation certificates (ROCs) scheme has promoted commercial scale electrical power generators to derive increasing proportions of feedstock from renewable sources and set penalties for non-compliance. Other initiatives such as Contracts for Difference (CfD) have additionally been implemented to account for volatile electricity prices for new and low-carbon initiatives. For European Union member states the Industrial Emissions Directive, a set of regulations requiring power stations to limit the emissions of certain gases and particulate matter during operation has been enforced resulting in numerous power station closures due to the cost of retrofitting.

Furthermore, the UK government has committed a plan to close power stations firing coal by 2025. The industrial response to this policy decision was to switch to biomass feedstocks to continue using existing power station infrastructure. Whilst some power stations have already undertaken full conversions to biomass, for the majority, further retrofitting is ongoing to extend the useful

economic life and provide electricity generation into the future. Whilst conversions to biomass or co-firing with coal seek to reduce CO₂ emissions using existing coal-fired infrastructure, this gradual transition from coal to biomass presents many operational challenges related to the boiler, particularly slagging and fouling, corrosion and erosion.

The conversion to biomass on existing coal-fired power station infrastructure has been fraught with challenges due to the high variations in biomass characteristics and feedstocks and is by no means the most efficient method of achieving carbon emission reductions, however, there are significant cost savings in retrofitting existing power stations. In order for power generators to reliably predict the outcome of biomass during combustion requires an in depth understanding of the individual unit operations. One such unit operation is the boiler or combustion furnace; initially designed and built to withstand coal combustion.

In a previous engineering doctorate funded by Doosan Power Systems Limited titled 'Sulphur Trioxide Behaviour and Absorption in CO₂ Rich Atmospheres'[9] the future research recommendations section highlighted the industrial need to develop a more comprehensive mineral library for biomass feedstocks and ashes to improve the understanding of co-firing, deposition behaviour and erosion rates. As a continuation from that project, this research has been devised to generate experimental data for ash formation and transformation models to aid in the prediction of slagging and fouling, corrosion and erosion. Through expanding the current literature on biomass combustion and seeking solutions to the common operational problems, world-wide generators will be

encouraged to invest in biomass generated power. Using a small-scale combustion rig that represents boiler conditions is a cost-efficient and flexible means of collecting experimental data without taking industrial boilers off-line. These experiments aim to reduce future CO₂ emissions and to extend the life of existing power plants to ease the transition to biomass for businesses.

Power generators aim to maximise the fuel combustion efficiency in their boiler systems, that is, to fully burn the fuel in a manner that will minimise the unburned carbon or char remaining in the ash. As such, the economic viability of the process is contingent on achieving as near to complete combustion as possible. To comply with more stringent environmental regulations on greenhouse gas emissions, predominately CO₂, co-firing biomass with coal has been employed across international power stations.

1.3.2 Aims of the Project

Fundamental understanding of the ash formation mechanism and the mineral transformations during pulverised combustion is an essential first step in predicting the ash deposition behaviour on the convective heat transfer surfaces of industrial-scale boilers. Ash-related issues can cause reduced boiler efficiency and unscheduled shutdowns from induced blockage, corrosion and erosion on utility boiler components.

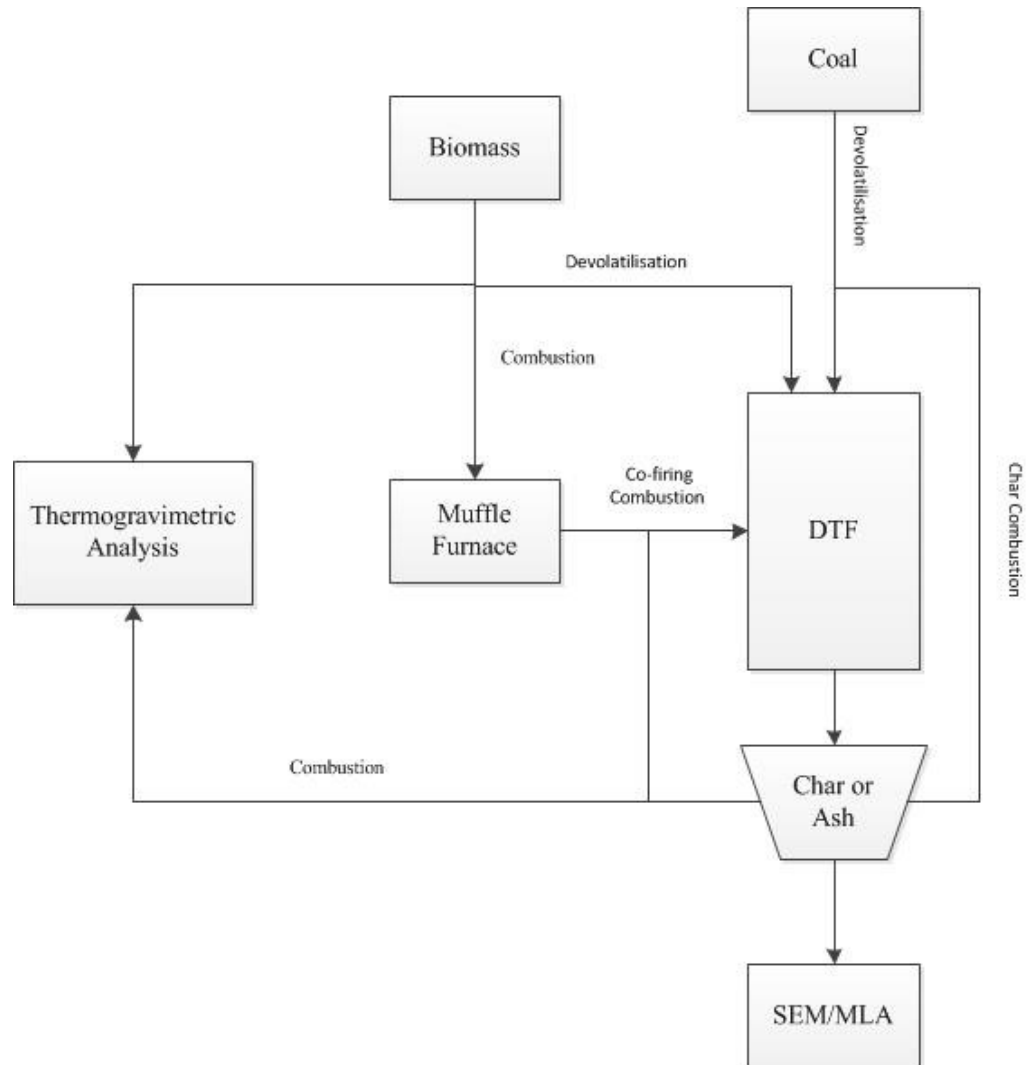
In the present study, firstly a selection of power station fly ashes were characterised from pulverised coal-fired boilers to investigate the erosion potential, morphology and chemistry typical of fly ash and aid the development of a sample preparation method for automated scanning electron microscopy.

The erosion data collected could be applied as a sub-routine to ash formation models.

Secondly, a series of experiments were conducted to characterise the chars and ashes obtained from a DTF from which the effect of residence time during pyrolysis and char burnout on the mineral transformations were investigated. The coals selected for these experiments were mainly from Europe, North America and South Africa, and were chosen based on their availability, their varying ash contents and due to their combustion characteristics typical of power plants worldwide. The coals were characterised using British standard methods, thermogravimetry for char reactivity, and most importantly, image analysis using computer-controlled SEM-EDX, otherwise known as Mineral Liberation Analysis (MLA).

Another study was undertaken using the DTF, which involved firing biomass ash with coal char to investigate the mineral occurrences, and the distribution and morphologies of alkali and alkaline earth metal aluminosilicate phases during the evolution of char burnout. For this purpose, South African coal char was blended with olive cake, sunflower and miscanthus ashes respectively and fired in the DTF over a range of residence times to provide a relative comparison of the extent of combustion and investigate the mineral interactions of each blend. The same mixed blends were prepared in a muffle furnace using a standard ashing procedure under proximate analysis conditions to simulate the behaviour of the co-fired ash at the bottom of the boiler. Correlations between the burnout characteristics with mineral composition, the mineral associations and the grain size distribution of the minerals were determined using MLA.

A schematic of the experimental procedure is detailed below:



Chapter 2: Literature Review

The following chapter provides a critical review of the current state of the art regarding the influence of mineral matter during pulverised fuel combustion, focusing on the mineral transformations and associations that occur during devolatilisation, char combustion and resultant ash formation. An extension to this section includes the fate of the biomass-derived mineral matter on the combustion process during co-firing biomass with coal. Finally, the current gaps in experimental data required for ash deposition related predictive modelling techniques is reviewed, with emphasis on the role of mineral matter on the particle impact erosion wear of boiler tubes. The conclusions of the literature review will form the basis of the research direction at the end of this chapter.

Firstly, the literature review provides a general overview of coal and biomass mineral properties and combustion environments that influence the formation of ash deposits and the relationship between the inherent mineral matter and intrinsic char reactivity. Secondly, a detailed examination into the current state of the art regarding the mineral transformations and associations that occur during pyrolysis and combustion, with particular attention on the formation of ash deposition-related minerals. Finally, the fundamentals and mechanisms of erosion and a review of automated mineral analysis, specifically the scanning electron microscope based mineral liberation analyser (MLA). This literature review will form a comprehensive background to the remaining chapters.

2.1 Fuels for Power Generation

2.1.1 Coal

Coal has been a major source of energy for centuries, fuelling the industrial revolution and providing electricity generation to economies worldwide. Historically, coal has been relatively inexpensive and is likely to remain the most affordable fuel for power generation in many developing and industrialised countries for decades to come and currently accounts for an estimated 41% of global electricity generated[1]. Furthermore, extensive improvements to existing power plant processes have increased efficiencies so that more electricity can be produced per unit mass of coal.

Coal is a biogenic derived, heterogeneous and complex structured sedimentary rock, formed from the lithification of biomass such as plant and animal organic matter. The coalification process involves the deposition, compaction and maturation of organic matter at high temperatures and pressures over a geological time scale of millions of years[10]. During coalification, the organic matter accumulates as peat and undergoes air oxidation, followed by decarboxylation and dehydration to form lignite. Further decarboxylation and hydrogen disproportioning produce bituminous coal and finally condensation of the aromatic rings to convert to semi-anthracite and carbonification to anthracite. During the coalification process, the carbon content increases and the oxygen, hydrogen and other volatile component contents decreases[11]. The lowest rank coal is lignite, which has a woody structure from decomposed vegetable matter, is brown to black in colour and has a high moisture content

and low calorific value compared to higher rank coals. Sub-bituminous and bituminous coals are black coloured with low moisture contents and higher calorific values. The highest rank coal is anthracite which has a low moisture content and high carbon content[12].

Coals are composed of discrete constituents called macerals and minerals, which are analogous to the organic and inorganic matter respectively[13]. The type and distribution of the macerals reflect the parent plant material and the deposition history of the coal. These two main groups influence the combustion behaviour. The macerals are divided into *vitrinite*, *liptinite* and *inertinite*. The most abundant maceral group is usually vitrinite, which originates from the lignin and cellulose of plant cell walls, and its reflectance varies more uniformly with rank than other maceral groups[14]. As such, the coal rank is assessed by means of the vitrinite reflectance values using microscopy. Liptinites are considered the most reactive of the macerals and are distinguished by a higher aliphatic fraction and a higher hydrogen content, arising from hydrogen-rich plant matter such as cuticles, resin, waxes and fats. Inertinite is derived from the same original plant matter as vitrinite and liptinite, however the material has already experienced primary transformations such as charring from forest fires, as such, inertinites have low hydrogen contents and relatively higher carbon contents, and more aromatisation. Inertinites can be sub-categorised into reactive and unreactive based on their reflectance values.

Most of the inorganic matter present in coals is in the form of minerals which are distributed as either included or excluded grains from the macerals. The occurrence of specific minerals within coal seams depends on the geographical

location of the deposit. The formation and arrangement of the minerals as dispersed or interlocked phases in the macerals are determined during the coalification process. The main mineral categories are *clays*, *oxides*, *carbonates*, *iron disulphides*, *hydroxides* and *sulphides*. The most common mineral group is generally the clay minerals, which account for between 60-80% of the total mineral matter[14]. The three main clay minerals are *kaolinite*, *illite* and *montmorillonite*, which can be sub-classified further. The most important oxide is *quartz*, which is either clastic or crystalline in nature. It is generally considered the most stable mineral within the coal, with an exceptionally high melting point in the region of 1600°C. Where the carbonates such as *siderite*, *ankerite*, *dolomite* and *calcite* are dominant in the coal matrix rather than clays and oxides, it is likely that lower ash fusion temperatures will result[14]. The presence of sulphur, either in organic form within the carbonaceous material or with the inorganic mineral matter as iron sulphides such as *pyrite* and *marcasite* is another important mineral present within coal.

Coal is the most abundant, safe and secure fossil fuel worldwide with an estimated one thousand billion tonnes of economically recoverable proven reserves amounting to 150 years of coal at current levels of production. Coal production and consumption are in decline in the majority of OECD countries due to more stringent environmental regulations making coal-fired power generation economically unfeasible. Despite this, in 2018, the total world coal production was 7,813 million tonnes, an increase of 250 million tonnes from 2017[1]. However, it is forecast that coal will remain an important global energy commodity until at least 2050 as developed and industrialised economies strive to transition to lower carbon energy technologies.

2.1.2 Biomass and Co-firing

Biomass co-firing, the combustion of biomass with coal, serves as an intermediate solution for developed and industrialised economies to reduce greenhouse gas (GHG) emissions whilst utilising existing coal-fired power plant assets to facilitate the transition to lower carbon energy technologies. Financial incentives have long been in existence, such as the UK renewable obligations certificate (ROC) to encourage power generators to shift away from coal, with the long-term objective of using more renewable feedstock sources.

Biomass refers to plant or animal derived organic material, generally categorised as virgin wood from forests, energy crops, agricultural residues, food waste and industrial waste and co-products. Biomass includes liquids and gases from the decomposition of non-fossilised and biodegradable material. In contrast to fossil fuels, biomass grows over a short period through photosynthesis by absorbing CO₂ from the atmosphere and upon burning releases the plants stored CO₂. The burning of biomass is generally considered not to add to the earth's CO₂ inventory and is considered 'carbon neutral'.

Table 2-1: Groups and subclassifications of feedstocks

Groups	Sub classifications	Description
Virgin	Terrestrial biomass	Forest biomass, grasses, energy crops, cultivated crops
	Aquatic biomass	Algae, water plants
Waste	Municipal solid waste	Municipal solid waste, biosolids, sewage, landfill gas
	Agricultural solid waste	Livestock and manures, agricultural crop residues
	Forestry residues	Bark, leaves, floor residues
	Industrial wastes	Demolition wood, sawdust, waste oil or fat

Biomass contains three main organic constituents, *cellulose*, *hemicellulose* and *lignin*. Cellulose is the primary structural component of cell walls in biomass and the most common compound on earth. It is hydrolysis-resistant, strong, linear and a crystalline long chain unbranched polysaccharide containing many glucose molecules.

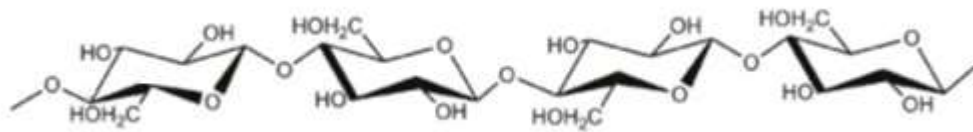


Figure 2-1: Structure of cellulose[15]

Hemicellulose is a polysaccharide with a random, branched amorphous structure with shorter and weaker chains than cellulose. Hemicellulose interacts with cellulose to strengthen plant cell walls. The main constituents include xyloglucans, xylans, mannans, glucomannans and betaglucans.

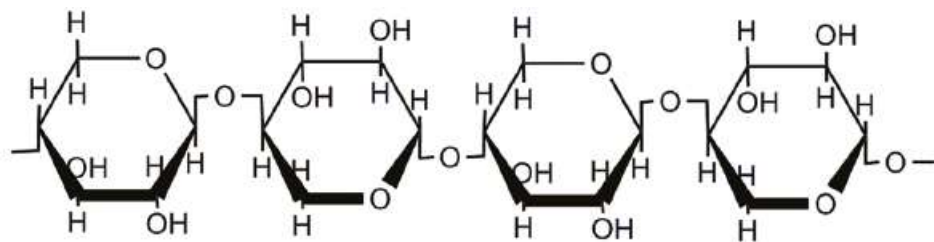


Figure 2-2: Structure of hemicellulose - xylan component[15]

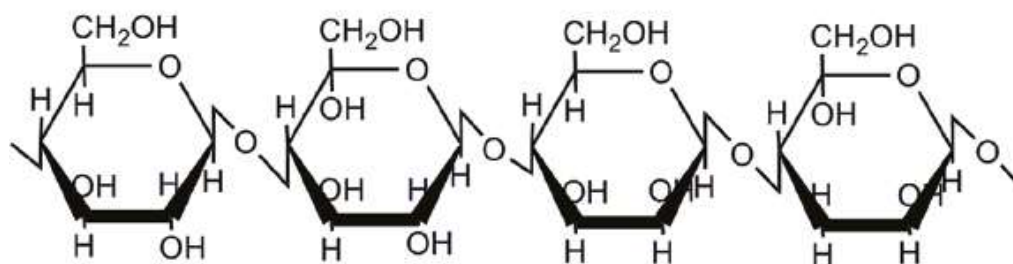


Figure 2-3: Structure of hemicellulose - glucomannan component[15]

Lignin is a cross-linked, phenolic macromolecular polymer containing a complex arrangement of aromatic alcohol groups called monolignols. It is hydrophobic and forms between the cell walls of plants, providing mechanical strength and rigidity. Lignin has the slowest rate of combustion of all the three constituents although a higher energy density than cellulose, it is the main component remaining as char and fixed carbon.

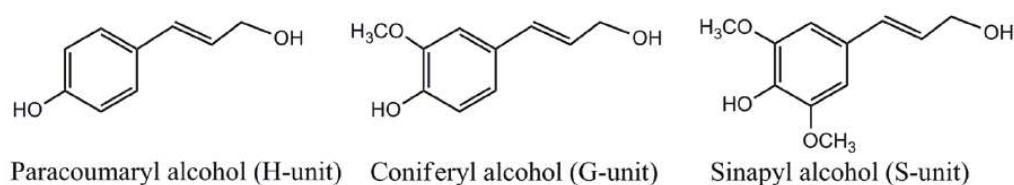


Figure 2-4: Structure of lignin[15]

2.1.3 Future Trends

Global coal demand continues to decline as lower gas prices, the uptake of alternative renewable energy and energy efficiency improvements are impacting coal consumption. In 2018, India and USA experienced a major

increase and decrease of coal consumption respectively. In the USA, coal has gradually been replaced with lower priced gas; in China, coal demand has fallen due to more stringent air quality requirements in the industrial and residential sectors; and in Europe, many countries are implementing a carbon price floor for coal use in power generation. It is expected that without carbon capture, utilisation and storage the long-term future of coal will be seriously constrained.

The share of coal in the global energy mix is forecast to decline from 27% in 2016 to 26% by 2022 due to lower demand growth relative to other fuels[16]. Despite this, coal still supplies a third of all energy used worldwide and contributes to around 40% of electricity generation, as well as playing a crucial role in the steel and iron industry. Although there are legitimate concerns surrounding air pollution and greenhouse gas emissions, coal will continue to be an important fuel in the global energy mix. However, governments and industry need to encourage less polluting and more efficient technologies to change the perception of coal to a cleaner source of energy for the decades to come.

Biomass addition into the energy mix will play a crucial role in reducing greenhouse gas emissions and achieving reduction targets by 2050. In 2019, biomass accounted for around 11% of the total electricity generation in the UK[17]. The range of biomass in power generation currently contributes 33 TWh of electricity, supported by long-term contracts under the RO, FIT and CfD schemes[17]. The incorporation of biomass to allow the decarbonisation of the current coal plants through co-firing and conversions, as well as using landfill gas, sewage gas and combined heat and power (CHP) from waste are the main

routes for delivery. Beyond 2020, the cost-effective deployment for biomass in power generation is likely to drop, and modelling work suggests this could be limited to wastes, CHP and biomethane in combined cycle gas turbine (CCGT) and open cycle gas turbine (OCGT) to provide peak electricity. Power generation systems that can combine biomass and carbon capture and storage (CCS) to allow for 'negative' carbon emissions are required to secure the role of biomass in power generation towards 2050.

In 2003, the UK hosted the world's largest biomass co-firing with coal project at Drax Power Station, Yorkshire. The plant started biomass co-firing at 10% heat input, amounting to 1.5Mt per year of biomass and abating 2 Mt per year of CO₂, generating 400 MWe of biomass-derived power. The proportion of biomass gradually increased until in 2019 the power station achieved a world first, installing a carbon capture system with the plant operating on 100% biomass. A similar co-firing project at Fiddlers Ferry, UK for two 500 MWe unit conversions to 20% thermal was undertaken in 2006 and has proven a dedicated co-firing system with multiple feedstocks such as wood pellets, palm kernels, olive stones and olive cake.

Projects such as these, although enabling a step change in biomass technological innovation, are heavily reliant on large capital investment and government subsidies to remain commercially viable. There is evidence to suggest that the future of biomass and waste thermal conversion is to produce smaller, modularised and compact power plants that can provide the necessary heat and power for communities at a local level. The current trends are that power generators are increasingly having to become more flexible, using highly

variable feedstocks such as low-grade biomass, municipal solid waste (MSW) and refuse-derived fuel (RDF) from many different suppliers. Additionally, as manufacturers and consumers are shifting away from single use plastics, and the scale of worldwide plastic pollution gains more attention, this may present an opportunity for the Energy from Waste sector to utilise plastics for power generation.

2.2 Factors Influencing Pulverised Fuel Combustion

Despite the short residence time, in the order of seconds, there are four distinct phases during the fuel combustion process to describe the conversion that fuel particles experience upon injection into a boiler at very high heating rates.

The first stage involves allowing the moisture to evaporate at temperatures less than 100°C leading to an exothermic energy release which lowers the combustion temperature and slows the rate of combustion. The inherent fuel moisture content is a primary variable for combustion, as higher moisture content fuels divert a greater proportion of the combustion heat to evaporate the water and can reduce the temperature below the minimum required to initiate combustion.

Secondly, pyrolysis or devolatilisation is the process of thermal decomposition of the fuel particles in the absence of an externally fed oxidising agent. The main products are tar and carbonaceous char combined with lower molecular weight gases. The pyrolytic devolatilisation process accounts for 70-80% of the weight loss encountered by the pulverised fuel particles during combustion[18] and lasts in the order of 30-100 ms resulting in porous char particles, which

depending on coal rank and type are enriched in carbon and depleted in oxygen and hydrogen.

The penultimate stage is char combustion or oxidation, which has the longest duration, lasting between several seconds and minutes[18]. This involves the burning of the char particles by diffusion of the reacting gas molecules, usually oxygen, from the surrounding atmosphere into the char structure. Subsequent adsorption and chemical reactions with the active sites of the internal and external char surfaces and pore walls occurs and desorption commences[19]. This process concludes that the burning or rate of reaction is dependent on the rate of mass transfer of oxygen to the particle surface and the chemical reactivity of the char. The influence of these two factors on char combustion varies with the surface area and porosity of the char, type and rank of the parent coal, the heating rate and combustion temperature[20]. The greater the surface area or smaller the size of the char particles, the more the total rate of reaction is controlled by the chemical reactivity relative to the diffusion of oxygen or reactant gases into the char.

The final stage is the relatively slow residual combustion of the remaining char fragments. The main char properties which influence the combustion efficiency to burn fuel particles to achieve as close to complete combustion as possible are size, morphology, active surface area and the catalytic effect of elements, such as iron and other reactive metals. Although the primary aim of biomass co-firing with coal is to reduce CO₂ emissions, there is the potential to increase the combustion efficiency, which is the amount of unburned combustible material remaining, through the biomass-derived volatile matter and reactive

metals enhancing the chemical reactivity and reducing the unburned carbon in the ash. However, despite many researchers claiming improved blend combustion efficiencies compared to coal-firing, as to whether the biomass organic volatiles or inherent minerals are the cause is still a matter for discussion.

Significant efforts have been made to understand the mineral transformations occurring during pulverised pyrolysis and combustion. One of the main objectives has been to strive to form relationships between the mineral matter composition and intrinsic char reactivity during combustion. Additionally, to produce an all-encompassing ash formation model that predicts the reaction kinetics, mineral species, particle size distributions and the tendency to form deposits, corrode and erode the boiler heat transfer surfaces depending on the physical and chemical parameters of the feed fuel. Despite this, more research is required to understand the mineral interactions during biomass co-firing.

2.2.1 Coal Type and Rank

Coal ranks can be broadly categorised into peat (a precursor to coal), lignite, sub-bituminous, bituminous and anthracite. As the rank increases, the inherent chemical properties such as fixed carbon increases, and the volatile matter decreases. As such, higher rank coals are harder to ignite and have higher ignition temperatures. Additionally, the higher rank coals such as anthracite and semi-anthracite exhibit longer ignition delays, in comparison to the lowest rank fuel, biomass, with the shortest ignition temperature and ignition delay. For coals the vitrinite reflectance is an accurate measure to differentiate between

the burnout performance with varying ranks[21]. The coal rank has also been linked to the reactivity during pulverised coal combustion, although other properties such as petrographic and mineral composition, particle size distribution and combustion conditions are important factors.

Recent studies have shown that the activation energy of higher rank bituminous coal is higher than lignite[22]. The faster the volatiles are released during the combustion process the shorter the ignition time and the higher the fixed carbon content and longer the burnout time. Additionally, the efficiency of the combustion process has been related to rank and the alkali and alkaline earth metals (AAEMs).

Previous workers highlighted that higher oxygen concentrations are needed for the higher rank coals to initiate combustion and that the combustion efficiency, decreased with increasing rank. Additionally, bituminous coals are the main type which swell during devolatilisation producing cenospheric chars which fragment. Sub-bituminous coals exhibit limited bulk fragmentation, whereas lignite particles produce extensive bulk fragmentation during devolatilisation.

2.2.2 Particle Size, Shape and Density

An examination of the experimental and theoretical studies conducted indicate that the particle size, shape and density are all important variables that have an effect on the behaviour of fuel particles during the combustion process. These particle properties particularly influence drying, the heating rate and the oxidation reaction rate. Usually the spherical particles devolatilise quicker compared to other shaped particles and the particle size has a limited influence

on the weight loss due to the heating rate being controlled by the heating rate of the carrier gas, so the larger particles are only heated at slightly lower rates than smaller particles. The mineral matter and maceral composition present within the char varies depending on particle size, which can influence the devolatilisation rate. Larger particles form more fragments than smaller particles due to larger internal temperature gradients. A decrease in particle size may lead to more complete combustion. In terms of erosion and ash transport within the boiler, the larger particles generally impact the internal boiler components by inertia, whereas smaller particles by thermophoresis or Brownian motion. It has been estimated that a particle twice the size of another will reach the deposit surface nearly three times faster mainly due to the inertial effect.

The influence of particle size during pulverised combustion can be described as follows; larger particles, typically $>100\mu\text{m}$ have smaller surface area to volume ratios leading to homogeneous ignition while smaller particles, $<100\mu\text{m}$ support heterogeneous ignition. These assumptions are derived from models of discrete burning particles rather than highly concentrated particles that occur during industrial pulverised combustion. As such, heterogeneous ignition is deemed most likely in dilute particle concentrations, whereas homogeneous ignition is considered to be prevalent where there is a greater release of volatile matter. In this respect, it can be difficult to ascertain the precise influence of particle size on combustion behaviour in real pulverised fuel boilers. However, smaller experimental studies, under constant heating rates and controlled carrier gas flow rates have shown that the devolatilisation and combustion processes can be evaluated.

Many studies have been conducted on the influence of particle size on coal and biomass conversion[23-26]. The extent of carbon burnout is an important operating characteristic for industrial scale boilers and the prediction of carbon loss at high conversions is required for a range of fuels, particle sizes and temperature histories. The particle size significantly impacts the combustion behaviour of solid fuels. The larger particle size fractions release limited amounts of volatiles due to mass transfer limitations compared to smaller particle sizes and the limited release of volatiles causes secondary reactions. Additionally, for the larger particles, there is a greater proportion of unburnt carbon in the fly ash after combustion.

2.2.3 Heating Rate

Heating rate has a significant influence on pulverised fuels during the combustion process. In general, higher heating rates such as those typically experienced in industrial-scale boilers or drop tube furnaces can increase the weight losses measured during devolatilisation and char combustion. Experimental studies have shown that higher heating rates produce greater volatile matter yields, particularly with bituminous and sub-bituminous coals[27]. Conversely, at lower temperatures the rate of devolatilisation and volatile yield is directly proportional to the heating rate or temperature. The heating rate used during the quantitative determination of thermogravimetric kinetic parameters is an important variable. It has been shown that non-isothermal TGA runs usually produce different char burnout times compared to isothermal runs. In order to overcome the heat and mass transfer limitations encountered during raw coal or biomass thermogravimetric kinetic studies, it is preferable to undertake the

devolatilisation step in a drop tube furnace to maximise the volatile matter yield and then perform char burnout studies on the TGA[28]. This reduces the influence of heating rate on the char burnout behaviour, by producing a char with a more porous structure and larger surface area for oxygen uptake for char burnout than is likely to be generated by initial thermogravimetric devolatilisation. However, the disadvantage of this approach is that the high heating rates of the DTF can induce thermal annealing, causing the volatilisation of some metals, removal of the char hydrogen and reduces the active sites available leading to a loss in char reactivity[28-33].

2.2.4 Macerals

Maceral composition has an important role in the combustion of pulverised coal. Indices, such as the maceral index (MI), have been developed to predict the combustion behaviour based on the nature of the coals using maceral compositions, mean vitrinite reflectance and the heating value[34]. These tools can be used to predict the extent of burnout, ignitability and flame stability. The burnout of the coal/blends depends on the initial volatile matter content, the physical structure of the char and the rate of diffusion of the burning char particles. This relationship fundamentally depends on the maceral compositions of the coal/blends. Macerals are divided into liptinite, vitrinite and inertinite. Liptinite has twice the volatile matter of vitrinite, and the highest hydrogen content of all the macerals. Liptinite has been connected to the ignitability and flame stability of various coals and shown to be of more significance during the pyrolysis stage than the combustion stage[35]. Additionally, it has been shown that the reactivity decreases as the maceral content increases in the order of

liptinite, vitrinite and inertinite. Conversely the ignition, flame stability and burnout improve. This follows the general observation that high volatile liptinite burns out quickly, vitrinite burns out according to its mean reflectance and due to its aromatic nature, inertinite is slow at achieving complete burnout.[35, 36]. The inherently unreactive nature of high inertinite coals has led to investigations into co-firing these coal types with biomass and other combustion-enhancing additives to improve the combustion efficiency.

Historically, optical microscopes have been used to perform maceral analysis with at least 500 macerals counted using a point counter system. This method is time consuming and subject to the expertise of the user to accurately identify the maceral grains[14]. Consequently, automated systems using fluorescence microscopy and image analysis were developed to improve the repeatability and reproducibility of maceral analysis across a wide variety of international coals[37-39].

More recent developments to further understand the maceral group composition and their interactions with the inherent mineral matter during coal combustion has utilised automated mineralogical techniques such as CCSEM, particularly QEMSCAN to distinguish between the different maceral groups based on their respective grey level intensities. This information is particularly valuable for CCSEM-based ash formation models to predict the size and chemistry of fly ash[40].

2.2.5 Char Burnout and Rate Kinetics

The burnout behaviour and reactivity are primarily a result of the structural properties of the char, which are derived from the devolatilisation conditions under which the parent coal is subjected. The dominant characteristics that influence the rate of char burnout under oxidising conditions are the pore size distribution, total surface area available for the gas-solid reactions and the intrinsic reactivity. The intrinsic reactivity of the char refers to the rate of reaction between the oxidising gas within the internal and external surface of the solid char structure, excluding mass and pore diffusion transfer limitations. Many workers report different parameters to provide an indication as to the intrinsic reactivity, such as peak temperature, burnout time and burnout temperature to compare different char samples produced under the same conditions.

The general trend is that the intrinsic char reactivity decreases with increasing rank of the coal, particle size, density and the relative inertinite content from the parent coal. The optical technique of vitrinite reflectance, as well as providing molecular characterisation and indicating the maturity parameters, can be related to the reactivity of the coal and the chars produced. This led to the variation of vitrinite reflectance of coals presented as a function of rank as a measure of reactivity[41]. The physical properties of the char vary with coal rank and coal origin, particle size distribution, and most importantly the pyrolysis operating conditions such as temperature, heating rate and residence time. The other properties that play a role in the conversion of char to ash include the mineral-mineral and mineral-organic associations, the swelling ratio which usually depends on the proportion of volatiles present in the parent coal, the

sphericity or how well rounded the particles are and the thickness of the char walls.

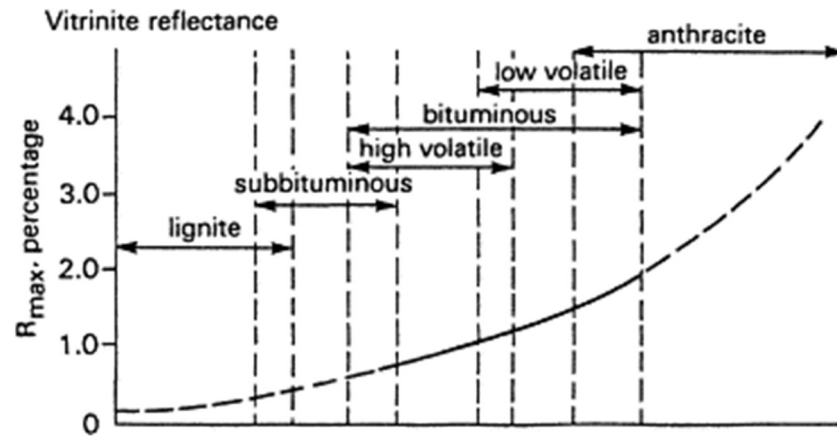


Figure 2-5: Variation of vitrinite reflectance with coal type[14]

The burning behaviour of coal and biomass during combustion are considerably different due to the physical and chemical properties. Biomass generally contains a higher proportion of volatile matter than coal, as well as lower bulk densities, lower calorific values, higher moisture contents and greater fire and explosion propensities. The majority of biomasses release volatiles at significantly lower temperatures than coal, and the proportion of volatiles is much higher. Therefore, the rate of release of volatiles for biomass in the pulverised fuel flame is a more significant parameter, compared to the rate of char oxidation for coal. The proportion of volatiles released from dry biomass varies with increasing temperature; typically, 10% between 200-300°C, 70% between 300-400°C and 20% between 400-900°C[42]. Biomass usually has lower activation energies and higher rates of volatile release compared to coal.

Generally, biomass has a lower fixed carbon content and more volatiles than coal, with a lower ash content, negligible sulphur contents and lower nitrogen contents. This contributes to more favourable combustion conditions[43]. The higher proportion of oxygen and hydrogen and lower carbon contents, reduces the heating values due to the amount of energy contained in the carbon-oxygen and carbon-hydrogen bonds being lower than in carbon-carbon bonds[44]. This higher oxygen content in coal suggests that there will be a higher thermal reactivity[45]. As a means of comparing various biomasses and coal, the volatile matter/fixed carbon (VM/FC) ratio is typically used, whereby biomasses have values >4.0 and coals <1.0[5].

2.3 Inorganic Constituents of Pulverised Fuels

The evolution of mineral matter during pyrolysis and combustion has been a topic of interest for decades due to the influence that the inorganic ash has on the effective operation of combustion systems. Boiler manufacturers have recognised the importance of understanding the mineral behaviour during thermal decomposition and have sought to generate models to predict ash deposition, corrosion and erosion under a variety of operating conditions.

The inorganic elements in solid fuels are present as discrete minerals, amorphous phases, organically associated cations, and cations dissolved in pore water. The minerals can either be included within the surrounding carbonaceous matter or excluded, acting as independent mineral particles. The generalised mineral occurrences are shown in Figure 2-6.

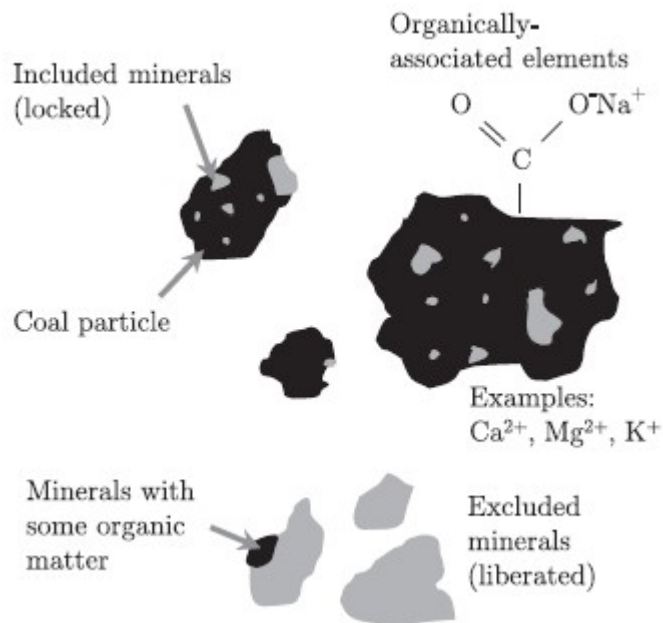


Figure 2-6: Inorganic constituents in coal and their occurrence[46]

For coal, the fraction of inorganic components that are organically associated varies with coal rank. Low-ranked sub-bituminous and lignite coals contain higher levels of oxygen, with approximately 25% of the oxygen in carboxylic acid groups[47, 48]. These carboxylic acid groups can act as bonding sites for cations such as sodium, magnesium, calcium, potassium, strontium, barium and other trace elements. Some elements may be present as chelate coordination complexes with pairs of adjacent organic oxygen functional groups. The cations originate from the biomass material from which the coal was formed. The ash-forming compounds occur in the fuel as included or excluded mineral particles, salts or organically bound into the fuel hydrocarbon matrix. The form of occurrence of the ash-forming elements in the fuel affects the transformations of these elements during combustion[49, 50].

The origin and occurrence of the mineral species within the carbonaceous coal or biomass matrix plays a role in metals catalysing the devolatilisation and char oxidation reactions. Studies have investigated the influence of individual mineral grains under reducing and oxidising conditions, at varying temperatures and pressures to inform on the transformation behaviour.

2.3.1 Minerals and Transformations

During combustion the inorganic constituents within coal undergo melting, fragmentation and chemical transformation and decomposition processes. Upon heating, a portion of the chemical species are expelled as gas, particularly mass loss from water molecules within the clay mineral matter, carbon dioxide from carbonates and sulphur from pyrite[51]. During the lower temperature devolatilisation stage the organically-bound inorganics are released and contribute to the mass loss in the proximate analysis of high ash coals[51], with attempts being made to calculate mineral correction factors for the kaolinite fraction[52]. Apart from the influence of temperature on the decomposition and mineral transformations, the oxidising or reducing gas atmosphere and composition play an important role in the resultant chemical transformations. Reducing environments with depleted oxygen affects the reaction pathway of the minerals, especially reducing zones within the internal pore network of burning char particles.

Figure 2-7 below shows the major coal mineral transformations as a function of temperature. Kaolinite or illite, are usually present in most coal seams and contribute to a high proportion of the overall mineral content. The transformation of kaolinite has been studied extensively, losing bound-water at 425-525°C to form metakaolinite, which then changes to mullite and amorphous quartz at approximately 900°C. The melting temperature of this amorphous phase is approximately 1700°C[53]. Illite contains the majority of iron, magnesium, potassium and/or sodium found within the clay minerals, and is often associated with pyrite. Similarly, to kaolinite, it decomposes at around 400°C forming an amorphous aluminosilicate. The melting point is highly dependent on the

composition, usually around 1400°C, although can be as low as 980°C for eutectic mixtures in the $K_2O-Al_2O_3-SiO_2$ ternary phase diagram[54, 55]. The illite included within the carbon matrix usually coalesces and forms low-temperature melting phases, whilst the excluded illite shows little signs of fragmentation or swelling.

Quartz is a very common mineral found within coal seams, and has a particularly high melting temperature and is deemed inert. Quartz can be liberated during the milling process as an excluded mineral, embedded in clay minerals or individually as an excluded pure mineral. Pure quartz does not melt below 1600°C and is generally present as angular, sharp and erosive particles. Quartz is reported to start volatilising at temperatures in excess of 1650°C[56]

Pyrite is reported to be an important contributor to deposit formation[53] and the chemical transformations are well understood[57-59]. Pure pyrite (Fe_2S) decomposes around 300°C, expelling sulphur and forming pyrrhotite ($Fe_{1-x}S$) under an oxygen atmosphere, oxidises to produce magnetite (Fe_3O_4) and finally, hematite (Fe_2O_3)[60]. The decomposition kinetics of pyrite are estimated to proceed as quickly as devolatilisation and the oxidation stage as quickly as char conversion[59]. Excluded pyrite has been observed to fragment with each parent grain yielding four child particles[61], whereas included pyrite produces lower melting temperature eutectic mixtures with aluminosilicates[57].

Carbonate minerals such as calcite ($CaCO_3$) start to decompose and release CO_2 at 800°C, whereas siderite ($FeCO_3$) and dolomite ($CaMg(CO_3)_2$) start to release CO_2 at 500°C and 750°C respectively[53, 54]. Sulphate minerals such

as gypsum ($\text{CaSO}_4 \cdot 2\text{H}_2\text{O}$) release water around 100°C forming the stable anhydrite (CaSO_4) mineral.

The chemical transformation pathways are governed by various boiler operating conditions such as temperature and oxygen concentration. The complexity of the associated minerals and inclusions within the coal matrix make predicting the ash melting temperatures and deposition rates challenging as the minerals are usually contaminated with other elements. Therefore, modelling the fate of pure minerals does not accurately represent real processes. The major coal mineral transformations during combustion have been studied, such as the oxidation of pyrite to iron oxide and the formation of crystalline and amorphous aluminosilicate phases[51], shown in Figure 2-8.

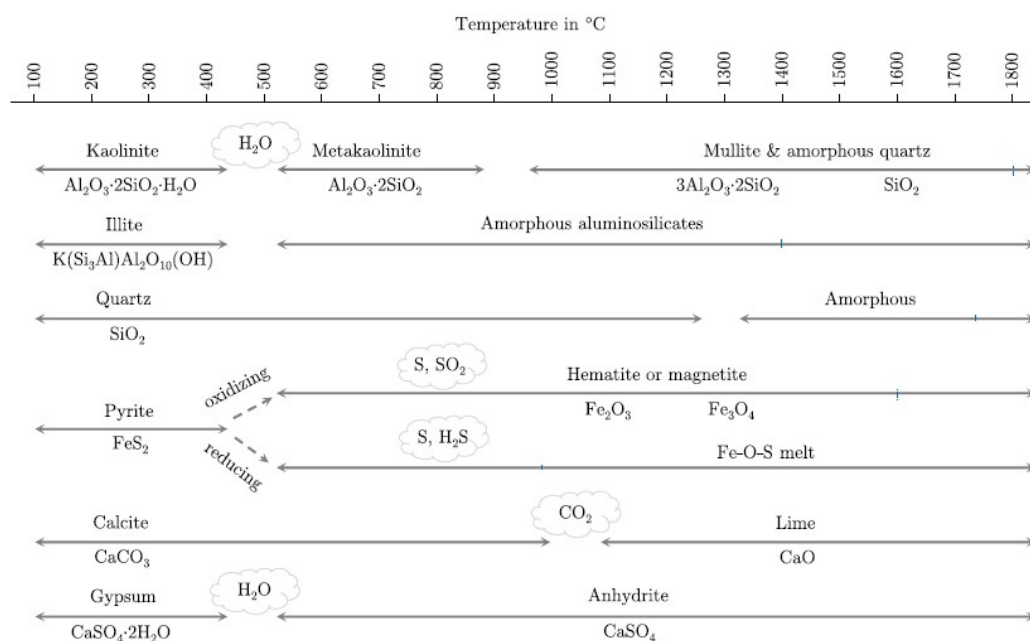


Figure 2-7: Mineral transformation of coal minerals as a function of temperature (modified from [54, 65, 66])

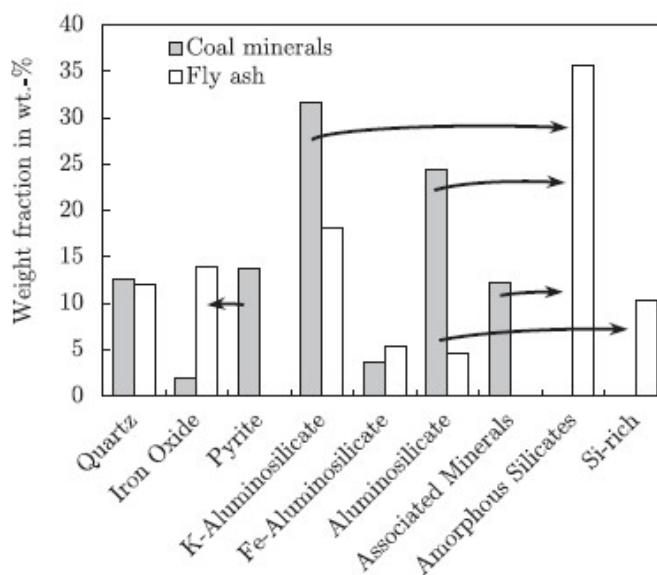


Figure 2-8: Bituminous coal mineralogy and fly ash composition before and after combustion

Simplified reactions for the phase mineral transformations of the inorganic matter are shown in Table 2-2, which includes the temperature ranges at which the decomposition occurs. However, further possible equations of the mineral phase reactions during devolatilisation and char combustion have been presented using CCSEM by Wen et al on a study of lignite, bituminous and anthracite coals and their derived chars and ashes from a laboratory-scale drop tube furnace[62].

Table 2-2 Chemical compositions and thermal decomposition reactions of
minerals (adapted from [52])

Mineral Species	Chemical Composition	Decomposition Reactions	T Range °C
Kaolinite	$\text{Al}_2\text{O}_3 \cdot 2\text{SiO}_2 \cdot 2\text{H}_2\text{O}$	$\text{Al}_2\text{O}_3 \cdot 2\text{SiO}_2 \cdot 2\text{H}_2\text{O} \rightarrow \text{Al}_2\text{O}_3 \cdot 2\text{SiO}_2 + 2\text{H}_2\text{O}$	400-600
Muscovite	$\text{K}_2\text{O}_3 \cdot 3\text{Al}_2\text{O}_3 \cdot 6\text{SiO}_2 \cdot 2\text{H}_2\text{O}$	$\text{K}_2\text{O}_3 \cdot 3\text{Al}_2\text{O}_3 \cdot 6\text{SiO}_2 \cdot 2\text{H}_2\text{O} \rightarrow \text{K}_2\text{O}_3 \cdot 3\text{Al}_2\text{O}_3 \cdot 6\text{SiO}_2 + 2\text{H}_2\text{O}$	450-700
Quartz	SiO_2	$\text{SiO}_2 \rightarrow \text{SiO}_2$	None
Hematite	Fe_2O_3	$\text{Fe}_2\text{O}_3 \rightarrow \text{Fe}_2\text{O}_3$	None
Rutile	TiO_2	$\text{TiO}_2 \rightarrow \text{TiO}_2$	None
Dolomite	$\text{CaCO}_3 \cdot \text{MgCO}_3$	$\text{CaCO}_3 \cdot \text{MgCO}_3 \rightarrow \text{CaO} + \text{MgO} + 2\text{CO}_2$	780-920
Ankerite	$2\text{CaCO}_3 \cdot \text{FeCO}_3$	$2\text{CaCO}_3 \cdot \text{FeCO}_3 + \frac{1}{2} \text{O}_2 \rightarrow 2\text{CaO} + \text{Fe}_2\text{O}_3 + 4\text{CO}_2$	700
Calcite	CaCO_3	$\text{CaCO}_3 \rightarrow \text{CaO} + \text{CO}_2$	920
Siderite	FeCO_3	$\text{FeCO}_3 + \frac{1}{2} \text{O}_2 \rightarrow \text{Fe}_2\text{O}_3 + 2\text{CO}_2$	580 + oxidation
Pyrite	FeS_2	$\text{FeS}_2 \rightarrow \text{pyrrhotite (Fe}_{1-x}\text{S, } x=0-0.2) + \text{other sulphides}$	Under N_2

	2FeS_2	$2\text{FeS}_2 + 7.5\text{O}_2 \rightarrow \text{Fe}_2\text{O}_3 + 4\text{SO}_3$	Oxidation
Albite	$\text{Na}_2\text{O} \cdot \text{Al}_2\text{O}_3 \cdot 6\text{SiO}_2$	$\text{Na}_2\text{O} \cdot \text{Al}_2\text{O}_3 \cdot 6\text{SiO}_2 \rightarrow \text{Na}_2\text{O} \cdot \text{Al}_2\text{O}_3 \cdot 6\text{SiO}_2$	None
Orthoclase	$\text{K}_2\text{O} \cdot \text{Al}_2\text{O}_3 \cdot 6\text{SiO}_2$	$\text{K}_2\text{O} \cdot \text{Al}_2\text{O}_3 \cdot 6\text{SiO}_2 \rightarrow \text{K}_2\text{O} \cdot \text{Al}_2\text{O}_3 \cdot 6\text{SiO}_2$	None
Gypsum	$\text{CaSO}_4 \cdot 2\text{H}_2\text{O}$	$\text{CaSO}_4 \cdot 2\text{H}_2\text{O} \rightarrow \text{CaSO}_4 \text{ (anhydrite)} + 2\text{H}_2\text{O}$	100-200

In contrast, fewer investigations into the chemical transformations of the inorganic species in biomass have been conducted. High-alkali biomasses such as straw and olive residues have shown the release of CO_2 from CaCO_3 , at temperatures between $850\text{--}1150^\circ\text{C}$, the evaporation of KCl and K_2CO_3 reacting with SiO_2 releasing CO_2 . Although even up to temperatures of 1450°C a proportion of the potassium remains as silicates[63, 64]. In terms of biomass ash formation, the majority of the attention has been related to the vaporisation and re-condensation phases, and few studies have investigated mineral inclusions with the organic matter and coarse fly ash formation[65].

The transformations of the included mineral grains are dependent on the combustion characteristics of the char particles. The majority of the non-volatile inorganic species remain with the char during combustion and a small amount of the ash is associated with the volatiles[66]. The inorganic constituents can exhibit two different types of behaviours during combustion[67]. The first scenario is that each mineral grain forms a single ash particle and the second

is that one ash particle is formed per coal particle. The differences in the fly ash particle size distribution between coals are due to the burning char characteristics. The main parameters are the composition, maceral distribution and combustion conditions which influences the extent of swelling, porosity and hollowness of the fuel particles. Highly vesicular char particles burn during combustion leading to disintegration into smaller particles. The majority of ash particles associated with the char have a high enough surface tension that the surface of the char particles does not wet.

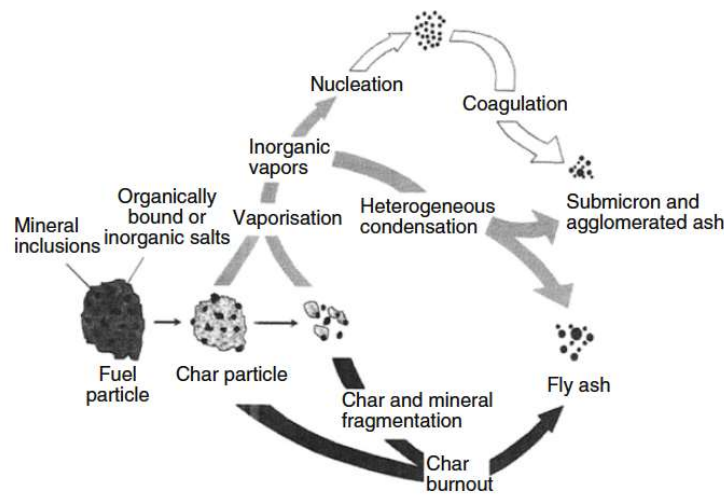


Figure 2-9: Physical transformations to form ash during coal/biomass combustion

The mineral matter associated with coal generally constitutes the most abundant forms, such as clay, quartz, carbonates, pyrite and various alkali and alkaline earth metal oxides. Some minerals are released during the milling process and are removed by beneficiation, mainly the free minerals that are not bound to organic structures, contrary to the included minerals entwined within

the organic carbon remain. Many workers have analysed and identified these mineral species using microscopy, chemical analysis techniques and diffraction methods to understand the role of the minerals during the combustion process. For example, it has been suggested that the thermal decomposition of the clays, carbonates and sulphides reduces the rate of temperature increase of the coal particles due to inbound water, which delays the ignition process. The higher reactivity of lower rank coals has been associated with the higher mineral content, particularly the alkali and alkaline earth minerals (AAEM) species, which can cause a catalytic effect during char burnout and combustion. The mineral composition and quantity also influence the resultant char particle size, and the low volatilisation temperature minerals such as potassium and sodium can be emitted with the volatile species during the initial stages of combustion. The mineral species inherent within coals, and more often biomass, that can act as catalysts are salts, such as NaCl, KCl and CaCl₂.

2.3.2 Catalytic Influence of Minerals

Previous investigators have highlighted two major factors that are important during coal and biomass char combustion and these are the formation of ash and catalyst effects[68]. Ash is formed during combustion and the evolution of this ash is determined by the furnace temperature and ash composition, i.e. whether the ash is molten or not. There are two modelling approaches which have been adopted. The first is that the ash forms a protective layer[69] surrounding the burning char particle and the char burning reactions are inhibited during combustion. The second is that the ash is expelled from the char particle leaving only ash within the surface layer[70] which blocks a fraction of the surface, leaving only a small fraction available for reaction.

Metal catalysts can have an effect on devolatilisation and char burnout, and are particularly important during biomass devolatilisation. It is understood that metals can catalyse the oxidation of carbon around 500°C, however there is less certainty as to the catalytic influence at industrial furnace conditions[68]. It has been shown that some metals such as iron do not reduce the activation energy of char oxidation but rather increase the pre-exponential factor, suggesting an acceleration of the reaction[71]. Mechanisms have been suggested based on the formation of a C – metal bond, whereby there is a weakening of the adjacent C-C bond and its use as an oxygen donor as shown in Figure 2-10 [72]

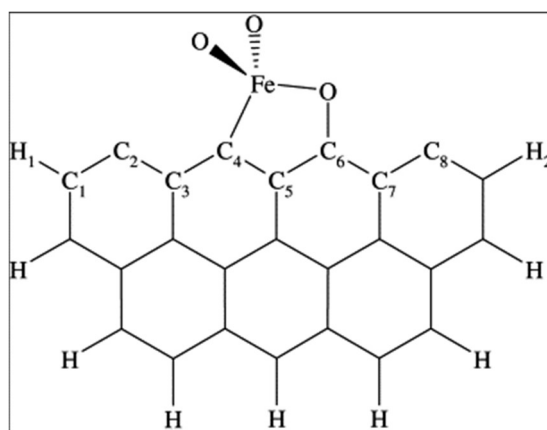


Figure 2-10: Catalytic mechanism for the reaction of iron atoms in the char structure[72]

However, for alkali metals an alternative mechanism is suggested, whereby a C-O-M bond is formed (where M can be Na, K or Ca) resulting in the weakening of the adjacent C-C bond and catalysing the reaction. This is likely to be the dominant mechanism for oxygenated biomass compounds as shown in Figure 2-11[73].

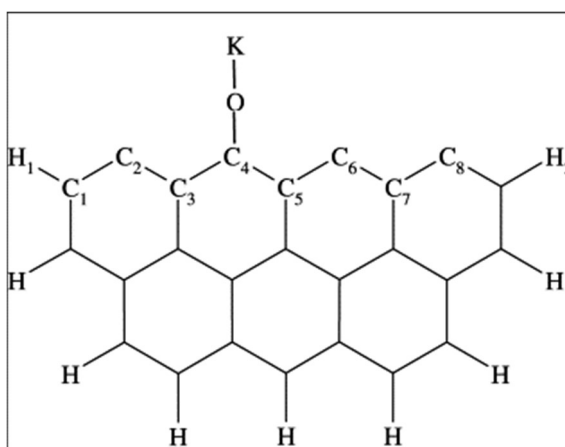


Figure 2-11: Catalytic mechanism for reaction of alkali metals[73]

Groups of metal atoms such as potassium and sodium can form during condensation, which are released into the gas phase during devolatilisation. These metals can be deposited as clusters or attach onto a C-O bond which acts as the nucleus for a cluster. It has been shown that cluster formation can result in reduced activation energies, and is the preferential mechanism at low reaction temperatures[74]. The influence of metals as combustion enhancing additives has been known for decades, and their effectiveness at reducing the activation energy has been attributed to the point of injection within the boiler flame and the amount of additive added relative to coal[75].

Experimental studies have shown that coals with high inertinite contents are less reactive and exhibit lower levels of burnout after combustion. This has led to further investigations into co-firing these unreactive coals with biomass to determine whether biomass derived AAEMs can catalyse the combustion reactions and reduce the residual unburned carbon in ash. However, a conclusive verdict on the influence of these minerals has not been presented in the literature.

2.3.3 Slagging and Fouling

The management of ash formed during pulverised fuel combustion is particularly important for biomass feedstocks due to the tendency to cause slagging and fouling phenomenon[76]. Slagging and fouling are common terms used to describe ash deposition on the heat transfer surfaces, where slagging refers to fly ash particles depositing and agglomerating on the surfaces exposed

to heat radiation, and fouling constitutes the deposition within the heat recovery section of the boiler[77].

Pulverised coal-fired boilers operate at high combustion temperatures between 1300-1700°C and residence times of around 2-5 seconds[78]. The initial trajectory (within the first 100s of milliseconds) of the coal or biomass particles is through the superheater and reheater tube banks. These sections suffer from the most severe corrosion and after prolonged operation result in deposit and molten slag formation, which usually results in tube failures during the lifetime of the boiler[79]. These first few hundred milliseconds of the particles journey can be simulated in a drop tube furnace at the high temperatures and heating rates encountered.

The diverse nature of biomass means that the composition varies considerably in terms of the organic and inorganic constituents[80-82]. The boiler design and operation are key factors dictating the composition of the resultant ashes and their tendency towards slagging and fouling. The low melting temperatures of sintered and molten ash deposits within the fireside section are caused by the inherently high oxide content of some biomasses[54, 81, 83, 84].

Power generators employ various techniques to predict the behaviours of slag and deposit formation when combusting biomass, especially during the maintenance, performance and cost-effectiveness assessments. The chemical and physical properties of the biomasses as well as the quantity fired are critically important. British and internationally recognised standards and indices

have been developed to minimise the slagging and fouling effects in combustion furnaces[85].

Slagging and fouling propensity cannot be predicted solely on the fuel properties[86], however relationships have been identified between the ash melting temperature and composition[87, 88]. The majority of the ash sintering predictive indices available have been developed for coal ash[54, 84, 89, 90], which has significantly different mineral types and compositions to biomass[81, 91-95]. These empirical formulas, originally developed for coal ash, when applied to biomass ashes produce large margin of errors to predict the biomass ash melting temperatures. However, correlations have been determined for biomasses based on phase diagrams[88].

There are a selection of mathematical indices which have been used extensively to assess the tendency of coals to undergo slagging and fouling, with some extended further to include biomass fuels[88, 96-100]. There are numerous mathematical indices applied to coals and biomasses, including the following:

Basic to acidic compounds ratio (B/A) is used to predict ash deposit behaviour. The basic compounds in ash ($\text{Fe}_2\text{O}_3 + \text{CaO} + \text{MgO} + \text{Na}_2\text{O} + \text{K}_2\text{O}$) lower the melting temperature[77], and are classed as the B group compounds. Whilst the compounds in the ash ($\text{SiO}_2 + \text{Al}_2\text{O}_3 + \text{TiO}_2$) increase the melting temperature, and are classed as the A group compounds. Since P_2O_5 has been shown to reduce the ash melting temperature it is added to the B group compounds[77, 101]. This produces the overall B/A ratio as:

$$\text{Base to acid ratio} = \frac{\text{Fe}_2\text{O}_3 + \text{CaO} + \text{MgO} + \text{Na}_2\text{O} + \text{K}_2\text{O} + \text{P}_2\text{O}_5}{\text{SiO}_2 + \text{Al}_2\text{O}_3 + \text{TiO}_2}$$

A simplified version of the B/A ratio was produced which omits ($\text{Na}_2\text{O} + \text{K}_2\text{O} + \text{P}_2\text{O}_5$) from the basic compound group B and (TiO_2) from the acid compounds group A. This is due to these elements, particularly potassium, are main constituents of slagging and fouling problems for biomass fuels[90].

$$\text{Simplified base to acid ratio} = \frac{\text{Fe}_2\text{O}_3 + \text{CaO} + \text{MgO}}{\text{SiO}_2 + \text{Al}_2\text{O}_3}$$

The *Babcock index* (R_s) is based on the B/A ratio, but includes the addition of the sulphur content to account for the sulphur-containing compounds such as sulphates which contribute to ash deposit formation under combustion temperatures[84, 86]. The sulphur can form alkali and alkaline earth (K, Ca, Na) sulphates but not when present as silicates[101]. Therefore the addition of SiO_2 can lead to K and Ca silicate formation which increases the biomass ash fusion temperatures[102]. It has been suggested that the addition of SiO_2 can be beneficial in preventing the formation of sulphur-containing deposits such as K_2SO_4 and CaSO_4 .

$$R_s = (B/A) \cdot S^d$$

Where S^d is the percentage of dry sulphur in the fuel and B/A is the ratio between basic and acidic compounds (overall equation).

Similarly, the *Fouling index* (F_u) is based on the B/A ratio but accounts for the alkali content ($\text{Na}_2\text{O} + \text{K}_2\text{O}$)[84]. As the alkali content is usually high in

biomass fuels (25-35%), a eutectic mixture is produced with silica[86, 101]. As such, higher fouling index values correlate to higher tendency to fouling. The equation is as follows:

$$Fu = (B/A).(Na_2O + K_2O)$$

Silica content (SiO_2) has been identified as the dominant element in slag samples from biomass fuels, suggesting that the formation of ‘sticky’ silicates is responsible for slagging[103, 104]. Experimental studies have shown that there is a strong correlation between the silica content in biomass ash and the fraction that builds up as slag in boilers[103], this led to the silica content of biomass to be used as a slagging indicator. Statistical analysis determined that the critical silicon content (given as SiO_2) was in the range of 20-25 wt% of the fuel ash[105], which was later validated and confirmed[106-108]. However, although pure silica melts at 1700°C, during combustion it combines with alkalis such as potassium and sodium to produce low-melting temperature eutectic mixtures[86, 109].

The *slag viscosity index* (Sr) calculates the percentage of silica in the basic compounds of the ash, excluding the alkali compounds. Higher Sr values correlate to a lower viscosity, and therefore a lower slagging tendency[84]. The following equation is applied:

$$Sr = (SiO_2.100)/(SiO_2 + Fe_2O_3 + CaO + MgO)$$

Ash fusion tests are used to determine the melting behaviour under controlled conditions. The ash samples are placed in a muffle furnace, pressed and

heated steadily and observed optically. The shape of the ash sample as a function of temperature is recorded and critical temperatures identified. There are numerous standards available in the literature for ash sample preparation and the testing procedure. The characteristic temperatures are defined as initial deformation temperature (IDT), softening (ST), hemispherical (HT) and fluid temperature (FT), respectively. Original equipment manufacturers that design power station boilers often use the ash fusion temperatures to select the maximum furnace exit temperature and for the estimation of slagging propensities using indices and bulk ash chemistry. For biomass, different critical temperatures are used for the ash fusion test. However, for biomass the initial deformation temperature (IDT) is replaced by the shrinkage starting temperature (SST). Also, the deformation temperature (DT) and the remaining critical temperatures are identical. The application of the ash fusion test by boiler designers is problematic because laboratory-derived ash is significantly different to boiler-derived ash due to the higher heating rates in industrial-scale boilers. At laboratory scale, the mineral transformation processes are slower. For example, laboratory ash absorbs SO_3 from sulphates and oxygen from ferric oxides which does not happen in a boiler. The heterogeneous nature of coal contributes to the ash melting temperatures.

Ash fusion studies have been conducted on coals to investigate ash deposition and mineral behaviour using ternary phase diagrams, with notably fewer studies performed on blending coal with biomass[110, 111]. CCSEM can provide useful information on the mineral compositions for each individual mineral grain and subsequently the transformation and melting behaviours. These mineral compositions can be displayed using ternary phase diagrams, although there

are limitations in using CCSEM for this analysis such as representative sample preparation, the maximum magnification and resolution of each particle and the number of particles analysed[65]. Additionally through tracing the individual occurrences and distribution of elements in minerals (Si, Al, Fe, S, Ca, Mg, Na, K, Ti and P) an indication of the likely melting temperatures of complex compounds and the mineral phases which contribute to slagging and fouling can be determined[112].

The softening temperature (ST) has been applied to slagging prediction models for biomass fuels, as there is a strong relationship between the fuel's ash melting point and ash composition. This has led to the proposal of detailed slagging prediction models[87] according to the ranges presented in Table 2-3. Finally, the initial deformation temperature (IDT) has been used to assess the slagging potential of biomasses. Biomass usually contains potassium in organic form, which thermally decomposes during combustion to produce low melting temperature phases[86]. Studies have shown a relationship between the IDT, where there is the initial onset of sintering, and the K_2O content of the biomass[83, 113]. This relationship was extended to provide different intervals for sintering tendencies as a function of the IDT[103], as shown in Table 2-3.

Furthermore, studies have shown that potassium-containing compounds such as K_2O and K_2CO_3 aside from contributing towards a catalytic effect, also increases the propensity for ash agglomeration with increasing concentration of K_2CO_3 [114]. This is due to potassium reacting with other minerals forming low melting point eutectics. This agglomeration mechanism has been investigated with potassium silicate ($K_2Si_4O_9$) and K_2CO_3 [115].

Table 2-3: Slagging and fouling indices[116]

Index	Range	Extent of slagging and fouling	Reference
SiO ₂ (%)	<20	Low	[105]
	20-25	Medium	
	>25	High	
B/A	<0.5	Low	[77]
	0.5-1	Medium	
	1-1.75	High	
	>1.75	Very High	
Rs	<0.6	Low	[54, 84, 101]
	0.6-2	Medium	
	2-2.6	High	
	>2.6	Very High	
Fu	<0.6	Low	[54, 84, 101]
	0.6 - 40	Medium	
	>40	High	
Sr	>72	Low	[84]
	65 - 72	Medium	
	<65	High	
ST (°C)	>1390	Low	[87]
	1250 - 1390	Medium	
	<1250	High	
IDT (°C)	>1100	Low	[103]
	900 - 1100	Medium	
	<900	High	

2.3.4 Ash Formation Modelling

A number of models and sub-models have been developed to predict the stepwise combustion process, from initial heating to remove moisture, the devolatilisation stages and ultimately char combustion to generate ash, under varying operating parameters applicable to typical boiler operation. The inorganic constituents undergo a multitude of physical and chemical transformations during combustion which are dependent on operating conditions and fuel characteristics. Consequently, it is extremely difficult to develop an all-encompassing mathematical model for all the different variable permutations, as the number of variables increases so does the complexity of the sub-models.

In an attempt to simplify the models, the different mechanisms such as char oxidation, devolatilisation, fragmentation and the various chemical reactions are decoupled and studied separately which results in multiple competing sub-models describing the same system. Additionally, the most important operating parameters such as temperature, pressure, heating rate and residence time with varying particle sizes, mineralogy and mineral matter compositions are simulated individually for simplification and can be connected to simulate real system behaviour. However, the most common approach for modelling ash formation during pulverised combustion involves separating the coarser ash from the aerosol particles. A generalisation is that the coarser ash usually contributes to slagging, fouling, corrosion and erosion, whilst the aerosols are more problematic to the environment and health hazards. The two most

important models for predicting the ash formation process are the coarse particle size distribution evolution model and aerosol ash formation model.

The coarse ash formation model includes the main physical transformations which are char fragmentation and/or coalescence which occur during combustion. This major model type has been investigated by many workers at varying operating conditions and has included the following sub-model types:

- Break up model;
- Fragmentation model based on thermally induced stress;
- Shrinking core model;
- Percolation model, and;
- Particle population balance model.

The break up model, formulated from laboratory and full-scale coal-fired boiler studies by Flagen and Friedlander[117] assumes that the char particles containing the mineral matter undergo fragmentation during combustion, with the first assumption that all the initial coal particles contain identical proportions of mineral matter irrespective of size and secondly that all the coal particles break up into exactly the same number of char particles during combustion. The output variable from this model, the breakup number, is influenced by the breakup of the char during char burnout, from the removal of material from the burning at the char surface and the fragmentation of discrete included and excluded mineral grains. This fundamental model has been exploited during engineering boiler design, and the vapourisation-condensation model for submicron particle formation was added as an extension to the model to validate the model with experiments.

The fragmentation model based on thermally induced stress developed by Dacombe[118] suggests that the fragmentation due to thermal stress is the main factor in particle breakup, due to the large temperature gradients encountered as larger particles heat up. This larger differential between inside and outside of large particles causes fragmentation, with a higher number of fragments formed compared to smaller particles. The model outcomes were that the smaller particle fragments are produced from the outer region of the char particle and a few large particles from the inner core of the char particles. Additionally, due to the smaller particles experiencing a lower temperature gradient resulting in less thermal stresses, the fragmentation can occur in the char burnout phase instead. The main conclusion of this model was that the degree of fragmentation was proposed to increase with particle size.

The shrinking core model, developed by Wilemski and Srinivasachar[119], as shown in Figure 2-12, concluded that ash particles are formed during combustion by transformations and interactions of the mineral inclusions within the coal particle. The growth of the ash particles on the char surface is modelled by redistribution and coalescence processes. Many redistribution sub-models have been investigated such as Monte Carlo methods to simulate the random distribution of minerals within the coal particles[120], analytical models which use Poisson statistics to determine the size and chemical composition distributions of the minerals based on CCSEM data and the random coalescence model to predict the particle size distribution with elemental composition[121, 122]. The major disadvantage of these sub-models is that the influence of the excluded minerals is not considered. This led to the use of an integrated method which combined Poisson statistics for distributing the

smallest minerals within the smallest coal particles and the Monte Carlo method for distributing the larger mineral within the larger coal particles.

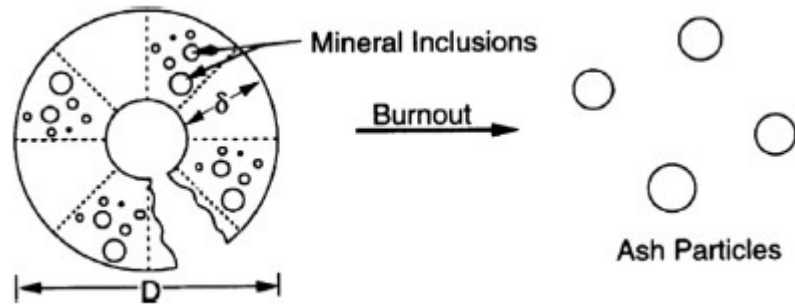


Figure 2-12: Ash formation model showing char fragmentation to ash during burnout from Wilemski and Srinivasachar[119]

The development of CCSEM has enabled studies on the mineral – mineral associations on cross-sections of commercial coals and their resultant ashes on a particle-by-particle basis[123-126], and this information has been used to predict ash formation and coal burnout behaviour[124, 127, 128]. Further CCSEM-based ash formation models were devised to predict ash deposition on large-scale combustors, slagging and fouling and tracing the minerals into the ash deposits[54, 129-131] These models were produced using proprietary software, and although presenting the output results and correlating well with experimental data; there is limited information on the mathematical codes used.

The most recent models have incorporated QEMSCAN into CCSEM-based models, which has the added benefit of assessing the mineral-organic associations as well as the mineral-mineral associations and utilises a species identification program (SIP) to analyse each pixel within a particle.

A further ash formation model was developed which included CCSEM data from high-rank coals whereby the included minerals were modelled using a Poisson distribution and the excluded minerals using a partial-coalescence model which bested suited the experimental data, as shown in Figure 2-13.

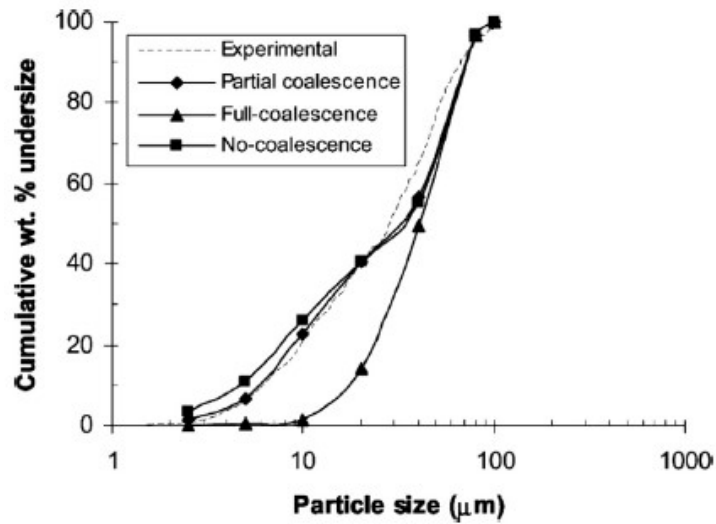


Figure 2-13: Cumulative particle size distribution comparison of experimental and model results at different levels of coalescence[128]

2.3.5 Impact of Biomass Firing and Co-firing with Coal on Ash Formation and Deposition

Ash deposition on the heat transfer surfaces of boilers has been researched extensively. The most recent studies have shown that biomass co-firing can increase the rate of ash deposition and sintering, with this rate increasing as the weight percentage of biomass increases[95]. The mineral species present within a particular coal or biomass significantly influences the transformation and formation of ash deposits, in terms of their resultant chemical and physical properties[126].

The characteristics of the deposits that form in combustion boilers are dependent on the chemical and physical characteristics of the intermediate ash species, geometry of the boiler, gas flow patterns, gas temperature, gas composition and gas velocity.

There are four main factors that contribute to the formation of ash deposits, which are as follows:

- Gas flow patterns that entrain impacting and sticky particles.
- Low excess-air conditions which cause localised reducing conditions (low oxygen concentration regions) which increases the amount of low melting point mineral phases.
- Molten deposit formation which collects impacting particles.
- Gas temperature increases due to less efficient heat transfer.

The types of deposits that form can be classified into four main groups:

- Metallic deposits usually from rich iron pyrite coals.
- Amorphous and homogeneous glassy deposits.
- Vesicular deposits (contain amorphous deposits and trapped bubbles).
- Partially fused, sintered deposits.

The main sintering mechanisms are dominated by aluminosilicate liquid phases and fuels that contain high proportions of iron pyrite, calcite and iron oxides. These minerals are important in deposit initiation and growth, with the initial deposition layers usually containing calcium oxide, magnesium oxide, iron oxides and glassy silicate phases.

Biomass combustion, and co-firing with coal introduces a range of ash-related problems such as deposition and corrosion. Potassium is the main chemical constituent which causes these ash-related issues. Potassium can be present as KOH, KCl, K_2SO_4 in the flue gas or as other forms depending on the fuel type, ash transformation chemistry and combustion conditions[132]. For certain biomasses such as straw, or those with high chlorine content, the chlorine can enhance the release of potassium resulting in KCl as the dominant potassium-containing species present in the high temperature flue gas[133, 134]. This KCl accelerates deposit formation and causes severe corrosion on heat transfer surfaces[135-139]. Furthermore, when fired with high sulphur-containing compounds, K_2SO_4 can form [140]. The low temperature eutectics between KCl and K_2SO_4 can result in melting temperatures as low as 690°C[141], producing sticky surfaces within the internals of the boiler and consequently accelerating slagging and fouling.

Studies have investigated numerous methods to overcome these ash-related issues in biomass boilers, including additives[142-145], co-firing[146], leaching[147-149] and anti-corrosion coatings. However, kaolin and coal fly ash have been used as effective additives to chemically capture the potassium species forming K-aluminosilicates with higher melting points. Coal fly ash specifically has been commercialised within full-scale biomass boilers[150, 151]. These studies showed that the formation of potassium-containing aerosols reduced and the aerosol composition altered from K-S-Cl rich to Ca-P-Si rich with the addition of coal fly ash.[150].

Further laboratory-scale experiments have been conducted studying the KCl capture behaviour of fly ash pellets by comparing with kaolin[152, 153]. It was shown that bituminous coal ash with high contents of Al and Si were as effective as kaolin at capturing KCl[154]. Although the lignite coal ash pellets, rich in Ca and Mg captured significantly less potassium[152]. Whilst coal fly ash usually contains a high proportion of unburned coal char, few studies have investigated the ash transformations of the coal char on capturing potassium within biomass ashes.

2.4 Erosion in Pulverised Combustion Boilers

The erosive wear of boiler components and ancillary equipment due to the impact of entrained ash particles on heat transfer surfaces in pulverised coal-fired boilers can have a significant influence on the operability and lifetime of the process equipment. The primary areas which are prone to erosive and abrasive wear are the feedstock mills, general pipework (particularly around elbows and bends), internally within burners, the gas-side section of heat exchanger tubes, convective section of the boiler and the internal surfaces within the pneumatic ash conveying equipment. The severity of the problem increases as the ash content of the coal being fired increases. For power plants firing these high ash content coals, it is of paramount importance that the operators have a functioning management and control strategy to mitigate the consequences of erosion and abrasion. It has been estimated that power plant operators pay billions of dollars per year on the maintenance and replacement of process equipment, electricity generation losses attributed to unscheduled shutdowns and other remedial measures caused by erosive and abrasive wear.

In the case of erosive and abrasive wear, the main culprit of the damage is attributed to the presence of inorganic mineral constituents within the coal and resultant ash, which typically have hardness values exceeding those of traditional stainless steels and other advanced materials used for boiler component manufacture. In contrast, the softer species commonly found within coals and ashes, such as carbonaceous matter and clay minerals have lower hardness values and less potential to cause erosion. However, with fly ashes the composition is more complicated, with molten and partially fused glassy

aluminosilicate phases formed during the coalescence, agglomeration and fusion of mineral matter present within the parent coal during the combustion process. These specific mineral species can have a significant impact on the erosive and abrasive wear of boiler components. In order to distinguish between erosion and abrasion the following definition should be applied. Abrasive wear refers to the sliding action of hard particles over the material surface or the pressing of particles over two sliding surfaces. In power plants this is mainly an issue which is prevalent within the coal handling, crushing and milling equipment, leading to increased maintenance costs. In contrast, erosive wear is associated with hard particles entrained with the gas flow that travel at high velocities and impact metallic component surfaces such as within the internal components of mills and burners, pipework and critically the convective section of boiler tubes.

One of the most important areas of the plant where impact erosive wear has historically been a major problem is the convective section of heat exchange boiler tubes. This is where the fly ash particles, generated within the furnace are impacting directly on the boiler tubes at significant velocities. This process can either be described as captive, whereby the fly ash particles can result in the formation or addition to ash deposits that have accumulated already on the boiler surfaces, or non-captive which leads to erosive wear. Practical experience has shown that erosive wear is usually associated with the superheater, reheater banks and economiser, occurring at flue gas temperatures below 1000°C, where the fly ash particles have a lower tendency to melt and adhere to tube surfaces. It is usually the case that after 5-15 years of continuous operation the pulverised coal-fired boilers start to experience

erosive wear. However, this time frame can be significantly reduced where high ash content coals are fired on a continual basis. Therefore, due to the inability to completely mitigate against the consequences of erosion outright, it is fundamental that the positioning of the convective tube banks and the maximum flue gas velocities expected during operation are optimised at the design stage to minimise the erosive wear rates. This requires the boiler equipment suppliers to take into account the variability in the intended feedstocks during the operational lifetime of the boiler.

2.4.1 Mechanism of Particle Impact Erosion

The mechanism of metal removal from the surface of a plant component is a relatively complicated phenomenon. The variables that influence the extent of erosive and abrasive wear can be attributed to the chemical nature of the erodent, the aerodynamics of the system, the angle of impact and the physical properties of the targeted surface. The main physical laws involved are the transfer of kinetic energy from the particle to the material during the impact and the rebound of the particle. The following equation describes the rate of erosive wear (ω), which includes the mass loss per unit mass of erodent, usually expressed in mg kg^{-1} . The erosive wear is a strong function on the velocity of the erodent particles (v)[155]:

$$\omega = kv^n$$

Where k is a constant and n is the velocity exponent, usually between 2 and 3. The general trend is that the wear rate increases significantly with increasing

particle impact velocity. The main properties that influence the erosivity of the ash particles can be summarised as follows:

- The hardness and mechanical strength of the particles.
- The particle size distribution, with the larger particles having a greater impact surface area relative to smaller particles of the same mass.
- The particle shape can have a significant influence, as particles with sharper, more protruding edges have a greater cutting action on ductile materials such as steel compared to rounded particles.

The erosion induced from fly ash particles within the boiler heat exchanger surfaces can cause metal degradation, either by direct removal of the tube material or through removal of the fireside corrosion oxide layers which increases the rate of corrosion (oxidation). In short, the higher the hardness of the boiler tube material, whether it be stainless steels or more advanced materials such as alloys, the lower the wear rate of the metallic materials. However, the influence of corrosion product formation and oxide removal can be the main contributor to metal wastage at surface temperatures above 427°C (800°F), whilst a combination of erosion with corrosion can lead to significant rates of metal loss. The main boiler operating parameters that influence erosive wear are well established, and can be summarised as[156]:

- Particle impact velocity, which is synonymous to the local gas velocity;
- Local particle concentration within a boundary volume in the gas stream;
- Angle of incidence of the particle collision with the component; and

- Relative concentration of erosive particles in the fly ash (such as quartz and iron oxides).

2.4.2 Measurement of Erosive Wear Rates

A review of the literature suggests that a significant amount of research has been conducted on erosion in combustion systems, which has generally investigated the following subject matters:

- The particle impact erosion wear of coal ash particles on boiler components;
- The assessment of erosivity of coals and ashes;
- The relative erosive wear of traditional and advanced boiler materials;
- The influence of boiler operating conditions such as gas and particle velocities, the impact angle of incidence and the temperature on the measure of erosive wear rate.

Boiler manufacturers have built custom erosion test rigs to further understand the erosion behaviour of coals and ashes on specific target materials under applicable test conditions. There are many different designs available and no consensus has been reached as to the best erosion test rig setup. The main technical approaches to the laboratory measurement of particle impact erosion include:

- Ambient temperature air jet impactors, whereby the erodent particles are accelerated towards the target material entrained within an air jet;
- High temperature erosion rigs, based on rotating arms or jet impactors;

- Pipe loop rigs, which simulate the erosion behaviour encountered during pneumatic conveying.

These erosion test configurations are employed to measure the erosion properties of solid fuel particles such as pulverised coal and fly ash under laboratory conditions and to measure the erosion resistance of specific materials such as stainless steels and alloys. The main data measurement recorded is the weight loss of the target material in milligrams per kilogram of erodent fired (mg kg^{-1}). An alternative measurement parameter is the width and depth of the erosion dent. These erosion studies are usually conducted as part of wider research and development projects, with the current technical knowledge the result of years of operational plant data.

2.4.3 Fundamentals of Erosion Wear on Boiler Tubes

In the late 1980s the technical literature on particle impact erosion, focusing particularly on coal fly ashes and ash deposits expanded considerably as detailed in a comprehensive monograph conducted by Erich Raask[155]. This included a review on the theoretical and practical aspects of erosion processes for coal-fired power plants. It is widely acknowledged that when utilising high ash content coals, the resultant fly ash leads to erosion which in part causes boiler tube failure, resulting in boiler tube replacement and a loss of availability, usually at great expense to the operator.

Erosive wear is a result of the progressive removal of material from a solid surface (i.e. usually steel) due to the mechanical interaction between solid particles, liquids or gases, or a combination of these and the surface material. The most important scenario involves the solid particles entrained within a stream of liquid or gas that interacts with the material surfaces. It is widely recognised that where solid particle impact erosion wear occurs, the main contributory variables are the mass, shape and hardness of the particles, as well as the particle velocity and the impingement angle upon impact with the material surface[157-164]. However, it has been acknowledged that further research is needed on the particle characteristics and their role in erosive wear[165].

There is an abundance of mineral species found within international coals, at varying concentrations depending on the coal's origin. However, the majority of coals contain oxides, sulphides, carbonates, phosphates and clay minerals,

with only the minerals which have hardness values greater than steel contributing to abrasive and erosive wear, as measured by the Mohs and Vickers hardness scales.

Previous workers have provided evidence to support that angular and large quartz particles cause more erosive wear to material surfaces than spherical and smaller particles containing significant amounts of elements such as calcium and sulphur[166-169]. However, the majority of this research examines the angularities and composition of a small number of particles through SEM images with limited statistical significance. An assessment on the angularities of larger number of fly ash particles, and their respective mineral compositions is required to support the assertion that angular quartz particles present a higher erosion risk than minerals of a similar hardness such as hematite.

Additionally, erosion studies at elevated temperatures suggested that the softening of glassy mineral phases reduces the erosivity of the ash and that individual angularities and microhardness values varied for SiO_2 and SiC particles[170]. Conversely, material properties such as the hardness and ratio of erodent particle hardness to material hardness on the erosive wear of materials is relatively well understood in the literature[162, 164, 171, 172].

Table 2-4 shows that the main mineral species within coal that are responsible for abrasive and erosive wear are quartz and pyrite. The other mineral species are softer than steel and therefore have little effect on the particle impact erosion wear of most boiler components. This has been demonstrated through collaborative experimental studies using an ambient air jet particle impactor and

detailed characterisation using a CCSEM[173]. This study conducted by Wells et al suggested the following:

- The erosion potential of pulverised coals is primarily caused by excluded mineral matter, defined as the minerals with less than 90% of their borders in contact with the carbonaceous coal matrix when viewed under an electron microscope.
- Only the mineral species with particle sizes above 25µm should be considered, as smaller particles have a negligible erosive wear effect.
- The quantities of quartz, pyrite, feldspar and garnet minerals within the pulverised coal are similar to those present within the raw coal.
- Although no supporting evidence was presented, for the coals studied, the angularity of the particles was deemed to have a negligible effect on the erosion process.
- The extent of erosive wear of the mineral species is a function of the quantity of each erosion inducing mineral present.

Table 2-4: Coal mineral species and hardness values[173]

Mineral Name	Chemical Formula	Mohs Hardness (Mohs scale)	Vickers Hardness (kg mm ⁻²)
Quartz	SiO ₂	7.0	1100-1550
Pyrite	FeS ₂	6.0-6.5	720-1840
Alkali feldspars	KNaSi ₃ O ₈	6.0	730
Mild steel	-	5.0-6.0	300
Siderite	FeCO ₃	4.0-4.5	200-250
Dolomite	CaMg(CO ₃) ₂	3.5-4.0	420-580
Ankerite	Ca(Mg,Fe)(CO ₃) ₂	3.5-4.0	350-490
Calcite	CaCO ₃	3.0	100-170
Muscovite	KAl ₃ Si ₃ O ₁₀ (OH) ₄	2.5-3.0	40-80
Kaolinite	Al ₂ Si ₂ O ₅ (OH) ₄	2.0-2.5	30-40
Illite	Fe and Mg substituting for K in muscovite	1.0-2.0	20-35
Solid glassy spheres with embedded mullite or quartz crystals	Pulverised coal fly ash particles	5.0	550-600
Non-spherical quartz particles		6.0-7.0	1100-1300
Spherical iron oxide particles		5.0-6.0	550-600

The results of the study conducted by Wells et al concluded using an ambient air jet impactor rig that the erosion wear rates for the coals tested were in the range of 0.5 to 5.5 mg of metal loss per kg of pulverised coal (the erodent) fired at a velocity of 40 m s^{-1} , and that the erosion rate was directly proportional to the excluded mineral particles with a diameter greater than $25\mu\text{m}$ and harder than steel, as shown below in Figure 2-14.

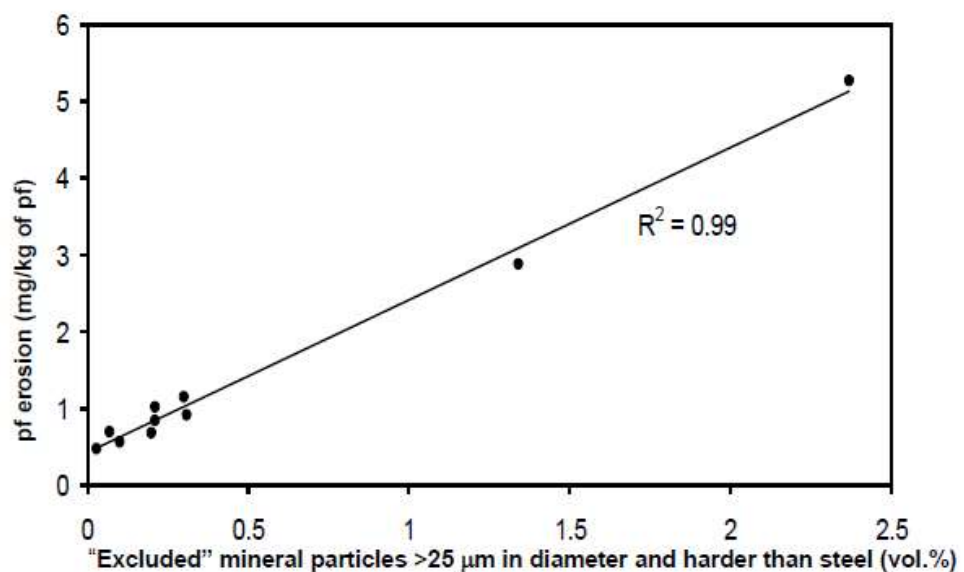


Figure 2-14: Measured pulverised coal erosion rate versus the hard mineral content of the coals with excluded mineral particles in excess of $25\mu\text{m}$ in diameter[173]

This study further presented a direct comparison between the relative erosion rates of two pulverised parent coals and the corresponding fly ashes collected from a 1 MWth combustion test rig. The results indicated that the measured erosion rates for these pulverised coals were 0.91 and 0.47 mg kg^{-1} respectively on a coal basis, and 8.49 and 5.44 mg kg^{-1} on an ash basis. It was suggested that there are two competing effects that influence the erosion potential, firstly

that the melting of the coal minerals usually produces more rounded particles, with less angularities which lowers the erosivity and secondly that the softer clay minerals are likely to transform into harder glassy spherical particles with varying internal porosities, which increases the erosivity. The relative erosion data is shown below:

Table 2-5: Relative erosion rate of two pulverised coals and corresponding fly ashes from a 1 MWth combustion rig after testing in an ambient air jet impactor at an impact velocity of 40 m s^{-1} [173]

Parameter	Coal A	Coal B
Moisture content of pulverised coal (%)	3.9	2.9
Ash content of pulverised coal, (% , dry basis)	11.2	8.8
Erosion rate for pulverised coal (mg kg^{-1} of coal)	0.91	0.47
Erosion rate for pulverised coal (mg kg^{-1} of ash)	8.49	5.44
Erosion rate for pulverised coal ash (mg kg^{-1})	9.65	7.60

These results show that the fly ash has the higher erosion rate compared to the parent coals when expressed in mg of metal loss per kg of pulverised coal ash.

This suggests that the formation of the fly ash and removal of the carbonaceous matter during combustion leads to an increase in the erosion potential compared to the mineral present in the parent coal. This suggests that the formation of harder glassy spherical particles has a more dominant effect than the angularity of the particles.

2.4.4 Modelling of Erosion Wear Rates on Boiler Tubes

Many researchers have investigated the particle impact erosion modelling at ambient and elevated temperatures in pulverised combustion boilers. This has involved detailed studies on single particle erosion models to describe the interaction between individual solid particles and the impacting surface, particularly for dilute concentrations of particles suspended in air such as experienced in pneumatic conveying, heat exchanger banks and through turbine blades. These individual particle erosion models exclude the particle-particle interactions and processes prevalent in high concentrations of solid particles within a gas flow which tend to have a cumulative effect at removing surface material. Additionally, as the erosion scar changes in depth and width as a function of time, the angle of impact between the erodent particles and the surface varies considerably. It should be noted that the irregular shape of the ash particles, particularly excluded quartz particles, can have relatively sharp features and their contact orientation upon impact is assumed to be random.

There are two erosive mechanisms which can occur on ductile materials resulting in a loss of material from the target specimen, for example:

- Cutting wear, from the impact of particles with sharp corners at low angles of incidence; and
- Extrusion to form ridges which result from rounded particles at high angles of impact.

The erosive wear of ductile materials is a combination of these two mechanisms, which are not mutually exclusive and are primarily dependent on the angle of impact, the properties of the particles and target material. The first single particle erosion model was developed by Finnie[157]. The main assumption of this model is that particles impacting the material surface at low angles of incidence will remove target material in a cutting action leading to plastic deformation. Additionally, the model assumes that the particles impact a smooth surface each time, when in real erosion systems multiple particles contact the same surface material which increases the surface roughness and not all particles colliding with the surface material cause material removal. The impacting particles have greater hardness values than the material and do not break up into smaller particle fragments upon contact.

$$W=c\frac{MV^2}{\phi_p K}\left[\sin(2\theta)-\frac{6}{K}\sin^2(\theta)\right]\tan\theta\leq\frac{K}{6}$$

Where

- W is the total volume of target material removed
- K is the ratio of vertical to horizontal (frictional) force
- ϕ is the ratio of the depth of contact to depth of the cut
- c is a constant to account for non-ideal particles compared to the erosion model
- M is the total mass of abrasive particles
- V is the abrasive fraction of the particles velocity
- p is the eroding surface flow stress
- θ is the angle of incidence

From the equation above the mass removed from the surface of the target material can be determined through multiplying by the target material density.

Single particle erosion models such as Finnie's erosion model, are highly idealised and cannot be used to calculate the absolute erosion rates. In the absence of accurate erosion models, power generators usually use experimental test rig results to investigate the influence of erosive particles on specific target materials. However, these models can be used with the hardness values of the erosive particles to calculate the particle constant, c to account for the non-ideal characteristics and provide estimates of the effects of other process parameters on the erosion rate.

There have been more recent erosion model developments reported in the literature such as Mbabazi et al. This model is a combined erosion wear mechanism intended for fly ash particle erosion on the plates of air heaters including the cutting action wear and plastic deformation wear. The yield stress of a metal can be related to the metals Vickers hardness number. The overall expression was obtained for predicting the erosion rate for a mild steel surface impacted by ash particles[174]:

$$E = \frac{0.47z^{4.95}\rho_m\rho_p^{1/2}V^3\sin^3\beta}{\sigma_y^{3/2}}$$

Where

z is the mass fraction of silica contained in the ash

ρ_m is the density of mild steel

ρ_p is the average density of ash particles

V is the impingement velocity

β is the impingement angle

σ_y is the yield stress of mild steel

This expression representing the erosion rate of the mild steel by fly ash samples from three power stations (South African coal fly ash) was examined based on comparing this model with the experimental values obtained in an erosion test rig investigation. When tested on three power station fly ashes (Matimba, Lethabo and Matla), the calibrated erosion model yielded erosion rates that were not more than 15% of the experimentally measured values. The Matla and Lethabo fly ashes have lower gradients which is attributed to the clusters of spherical ash particles which fragment and reduce the kinetic energy of the ash particles when impacting the mild steel.

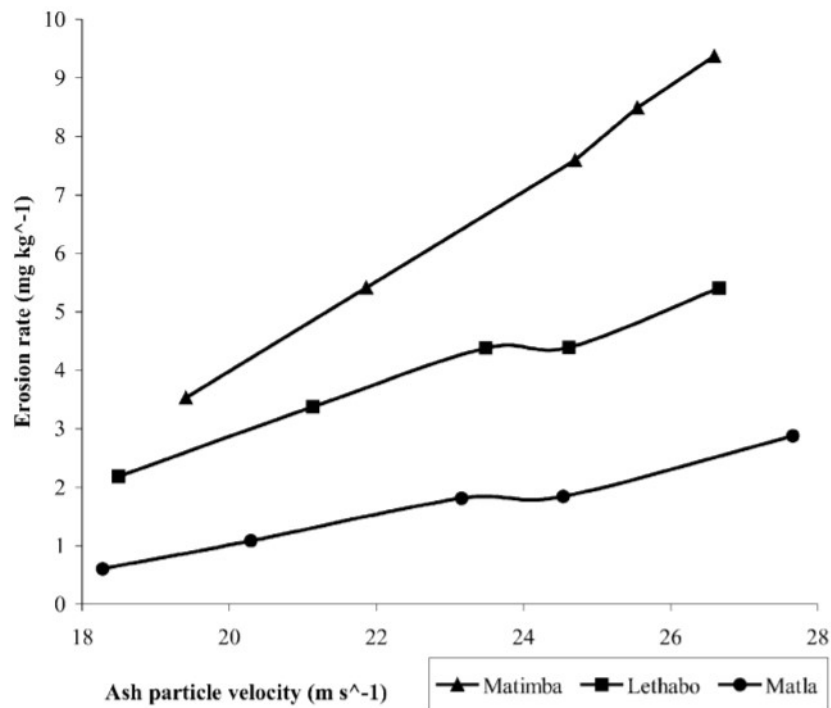


Figure 2-15: Experimental erosion rates on mild steel as a function of ash particle velocity at an impingement angle of 30°[174]

The experimental investigations conducted confirmed that the erosion rate on a mild steel target specimen with a stream of fly ash particles varies with the impingement angle, with the maximum reported erosion rate occurring at 30° and greater angles causing a decrease in the erosion rate. The Mbabazi erosion model equation exhibits a power law relationship with the ash particle impact velocity with the velocity exponent changing between 2-3 depending on the sphericity of the particles. Generally, a velocity exponent value of 3 is suitable to predict the erosion of mild steel. The silica content within the fly ash is another important parameter which significantly influences the erosion rate on mild steel, as confirmed by Raask[175]. Due to the similar Vickers hardness values of silica with pyrite, these types of erosion models could be further improved to include the influence of other hard minerals such as iron oxides on the erosion rates of mild steel.

It is evident that the development of erosion rate models to accurately describe the erosion rates of boiler tube surfaces when subjected to fly ash particles is a complex and difficult task. The erosion rate models described were performed under ambient conditions, when in reality boilers operate at very high temperatures. This introduces the influence of corrosion on the metal surfaces and a rate of metal loss which can be significantly higher than erosion models predict. This has led to researchers investigating erosion-corrosion models to predict the metal loss under high temperature boiler conditions.

2.5 Advanced Characterisation Techniques

Historically, in order to develop a better understanding of the mineral transformations there have been several main techniques used to characterise the mineral compositions and distributions within pulverised fuels, including optical microscopy, thermogravimetric analysis and low temperature x-ray diffraction, each with their own advantages and disadvantages. However, to characterise coal ash and char is challenging due to the fact that the mineral composition undergoes transformations as a result of the combustion process forming materials that are a complex mixture of mineral groups[176-179]. To overcome these challenges the SEM-based systems are used.

Computer controlled scanning electron microscopy (CCSEM), developed in the 1970-80s is an automated system which applied to combustion studies can classify the mineral size distribution and composition within pulverised coals, and more recently biomasses. The majority of this research uses scanning electron microscopy fitted with proprietary quantitative analytical software. The term CCSEM is synonymous with other automated mineralogical techniques such as quantitative evaluation of minerals by scanning electron microscopy (QEMSCAN) developed by CSIRO and the sister variant mineral liberation analysis (MLA) developed by FEI. These QEMSCAN and MLA techniques have also been referred to as SEM-based automated image analysis [173, 178, 180]. Previously workers initially used CCSEM to differentiate between coal minerals as included and excluded species. The sample preparation procedure involves mounting the coal, biomass, char or ash samples into an embedding material which is ground, polished and carbon coated, and placed into the scanning

electron microscope. In order to distinguish between the grey scales of the included and excluded minerals a discrete contrast between the embedding material and coal or biomass matrix is required. The literature suggests many methods which can be used to prepare the sample moulds, as follows:

Carnauba wax method which provides a good contrast for coal particles. This requires melting the solid wax at $95^{\circ}\text{C} \pm 5^{\circ}\text{C}$ in an oven before mixing in the particles. This method has a relatively short curing time of less than an hour, although the temperature must be gradually decreased to room temperature to prevent the wax from cracking upon cooling[181]. However, the higher density particles settle under gravity leaving a less representative portion of particles available for analysis.

Epoxy resin curing method increases the average atomic number by dissolving iodoform in epoxy resin and adding hardener with the particles. This method has a longer curing time of circa 3 hours, and similarly during the curing process the higher density particles settle via gravity. Further reported dynamic curing sample preparation techniques for QEMSCAN/MLA include using particle fractioned samples or bulk samples to optimise the representativeness of major to trace mineral phases[182]. These sample preparation techniques require further method development to produce a standardised dynamic curing method that can overcome the preferential gravity settling of higher density particles, artificial particle agglomeration during the curing process and mineral segregation. Ideally, the new procedure will minimise the air retained in the epoxy resin mould which produces bubble artefacts. After the sample is polished and carbon-coated, the cross section can be studied using SEM.

2.5.1 Application of CCSEM to Combustion Studies

Traditionally, the elemental composition present in raw coal is determined after standard ashing methods by XRF, and the metal oxide concentration calculated assuming the metals reside in the highest oxidation state. Whilst the advantages of this technique includes minimal and non-destructive sample preparation, there are significant limitations for accurate quantitative analysis such as low absorption emission intensity due to carbon matrix effects[183]. Similarly, the mineral constituents of the original coal are predicted from XRD ash analysis due to the high background continuum of amorphous macerals and amorphous aluminosilicate glassy phases that conceal the crystalline minerals[178].

In an attempt to preserve the original mineralogy in the coal for XRF or XRD analysis, low temperature plasma ashing procedures (below 150°C) can be employed to isolate the minerals from the organic fraction[184], however this is time consuming and likely that considerable unburned carbon will remain shrouding the minerals present. For the purposes of this research, a temperature of 500°C was utilised for low temperature ashing, this enabled the fixed carbon and volatile matter to be removed, albeit leading to the dehydration of some of the mineral species such as kaolinite and illite clay minerals. Due to the limitations with the current traditional analytical techniques, namely XRF and ICP-MS for metal oxide concentration, a more detailed examination of the mineral species present within the power station fly ashes was required, particularly the glassy aluminosilicate phases to elucidate the distribution of alkali and alkaline earth metals during the boiler combustion process. To this

end, MLA provides the requisite information to explore the elemental constituents of the mineral phases, particle size distribution data as a function of mineral species and graphical representation of the type of ash particles formed.

Combustion characterisation is an important aspect of environmental and operational quality control for pulverised fuel generating plants due to the fact that the breakdown of mineral species and transformation can be released into the surrounding atmosphere or produce undesirable by-products. From an operational and efficiency perspective, the mineral transformations can lead to ash deposition on the combustion furnace's heat transfer surfaces and superheaters. These deposits can cause unscheduled shutdowns for maintenance and cleaning, or even require the premature replacement of corroded pipes, reducing the operational efficiency.

CCSEM can be used to characterise coal and biomass, and their respective chars and ashes. Typical data collected includes the mineral composition, bulk particle size distribution, mineral-specific particle size distribution and the type (excluded or included). The main elements detected include Al, Ca, Cl, Fe, K, Mg, Na, P, Si, S and Ti. The elemental composition is scanned automatically by a computer and X-ray detectors are used to quantify the elements present within individual mineral grains. The composition of the mineral grain is then compared to a database of mineral compositions and subsequently classified and processed. A chi-squared statistical probability method is applied comparing the mineral reference spectra with the measured spectra from the sample. A match of 100% suggests that the measured mineral grain is identical

to the mineral reference spectra. For example, with a 70% probability match a mineral grain with a composition similar to quartz would be classified as pure quartz (SiO_2). Other minerals which can be logged onto the mineral database include kaolinite, illite, montmorillonite, gypsum, rutile and various aluminosilicates.

CCSEM analysis can provide important information on the chemical and physical properties of solid fuels which can be utilised in ash formation and mineral transformation models. Previous workers highlighted that the mineral grain composition can vary significantly within the same fuel sample, with each mineral grain exhibiting independent transformation and melting point behaviour[185]. In contrast to traditional ash oxide analysis by XRF or ICPMS, where only one average value is reported, the CCSEM data shows many points with variable composition. CCSEM has some limitations and challenges which must be considered during sample analysis. Firstly, particles in the sub-micron region cannot be detected unless very high magnifications are used, which significantly increases the analysis time per sample. Secondly, a high number of particles need to be analysed from a representative portion of the sample to obtain statistically meaningful and quantitative results. This is typically between 2000-4000 particles. This is particularly important when a broad particle size distribution must be determined. The chosen analysis magnification must be consistent between samples because different magnifications produce different results, and the grinding and polishing of the mould cross-sections must be standardised due to the fact that the probability of analysing a spherical particle at its pole is low. Additionally, the electron beam size must be kept constant because it restricts the lower limit of mineral inclusions and, if the particles have

not been sufficiently de-agglomerated and form clusters of two or more different mineral grains together then the mineral spectra cannot be distinguished, and incorrect compositions are reported. This leads to the cluster of individual particles being classified as one instead of multiple particles. There are other factors which influence the identification of mineral particles, such as the penetration depth of the electron beam on the lower detection limit and organically-bound inorganic species which cannot be identified or quantified.

Although more recent developments using QEMSCAN can provide information on mineral-mineral associations (two different mineral grains touching each other) and mineral-maceral associations, the commercially available CCSEM systems cannot provide data on the latter types of associations. This is primarily due to the difficulty in differentiating between the grey scale levels of the coal macerals and the epoxy resin. The main difference between CCSEM and QEMSCAN is that the particles within the cross section are analysed on a pixel-by-pixel rather than particle-by-particle basis respectively. The CCSEM provides an indication on the amount and type of included and excluded mineral grains, however the analyses do not include the organically-bound inorganics and limited information on the association of the carbonaceous coal material with the mineral grains.

Research conducted by Liu et al[186] used QEMSCAN to determine the mineral-maceral association for 14 different Australian coals revealed that the most abundant particle type contained no mineral grains. Of the coals analysed, only 10% of the particle cross-sections contained mineral inclusions. The study's findings defined three types of particles, as follows:

- Class 1: coal particles with 95% or more area containing organic material.
- Class 2: particles with included mineral grains containing 40-90% organic material.
- Class 3: excluded mineral grains containing less than 40% organic material.

In a further study[187], three coals were fed into a drop tube furnace at 1400°C under combustion conditions to produce simulated boiler ashes. After analysis of the coals and ashes it was concluded that illite, ankerite and siderite change their shape to spherical particles, while quartz, kaolinite and calcite do not change significantly. Additionally, mineral associations between quartz and kaolinite were discovered in contrast to particles of carbonates and silicates.

The mineral matter tends to distribute into the finer size fractions due to the fuel grinding process. Generally, the high mineral matter content and high particle densities tend to be ground to a finer size and liberate mineral grains. CCSEM models have been developed using the Poisson distribution law to describe the number of mineral inclusions per coal particle. For n mineral inclusions in m coal particles the probability P_j of finding j mineral particles in a coal particle can be calculated as follows:

$$P_j = \lambda^j \cdot \frac{e^{-\lambda}}{j!}$$

Where $\lambda = n/m$, the mean number of grains per coal particles and j is the number of mineral grains per coal particle which can be between 0 to n . The accuracy of this equation for coal particles reduces as the included mineral matter

increases. Furthermore, the number of mineral inclusions n per coal particle of a given size $d_{p,c}$ can be predicted as follows:

$$n = \frac{d_{p,c}^3 \cdot \rho_c}{M_{3,m} \cdot \rho_m} \cdot \omega_m$$

Where ρ_c and ρ_m are the densities of coal and the mineral inclusion respectively. $M_{3,m}$ the third moment of the mineral size distribution and ω_m the mass fraction of the mineral inclusion. The quantity of mineral inclusions present within particular coals is rarely reported in the literature. However, Monte Carlo simulations have been performed to distribute mineral matter with coal particles. Experimental studies have focused on mineral size and distribution however predictive tools have not been developed as these properties tend to be fuel specific. The low mineral content of biomass is particularly challenging, and power plant operators use the cheaper and quicker standardised ash fusion test to predict the slagging and fouling potential of fuels.

2.5.2 CCSEM Outputs

The raw data collected from automated scanning electron microscopes (CCSEM/MLA) can provide in-depth quantitative and qualitative information to determine the mineral categories, mineral grain size distributions, particle size distributions and mineral associations to develop a deeper understanding of the mineral behaviour during char devolatilisation and combustion. Additionally, in comparison to other chemical techniques, CCSEM/MLA technology can identify specific alkali and alkaline earth metal aluminosilicate phases which have low

melting temperatures and produce ternary phase diagrams to compare coals and biomasses regarding the distribution of silica, alumina and basic oxides to inform on the potential for slagging and fouling.

Ternary phase diagrams can be used to display the heterogenous nature of mineral matter in coal and biomasses. CCSEM data can be collected for individual mineral grains which are converted into compositions and presented as oxides. The mineral grains can then be shown on the ternary phase diagram (silicon dioxide – aluminium oxide – basic oxide) according to its composition. The included and excluded minerals can be presented on individual ternary phase diagrams to compare the variations in compositions of included and excluded mineral matter. For coals and biomasses with high variations in compositions of included mineral matter, this can be an indication of sticky particle formation. Usually a high amount of basic oxides (Fe_2O_3 , CaO , MgO , Na_2O , K_2O , P_2O_5) greater than 40% wt. in the excluded minerals means there is a greater tendency for fouling. Similarly, a high amount of basic oxides, exceeding 40% wt. in the included mineral matter fraction indicates a slagging tendency[126].

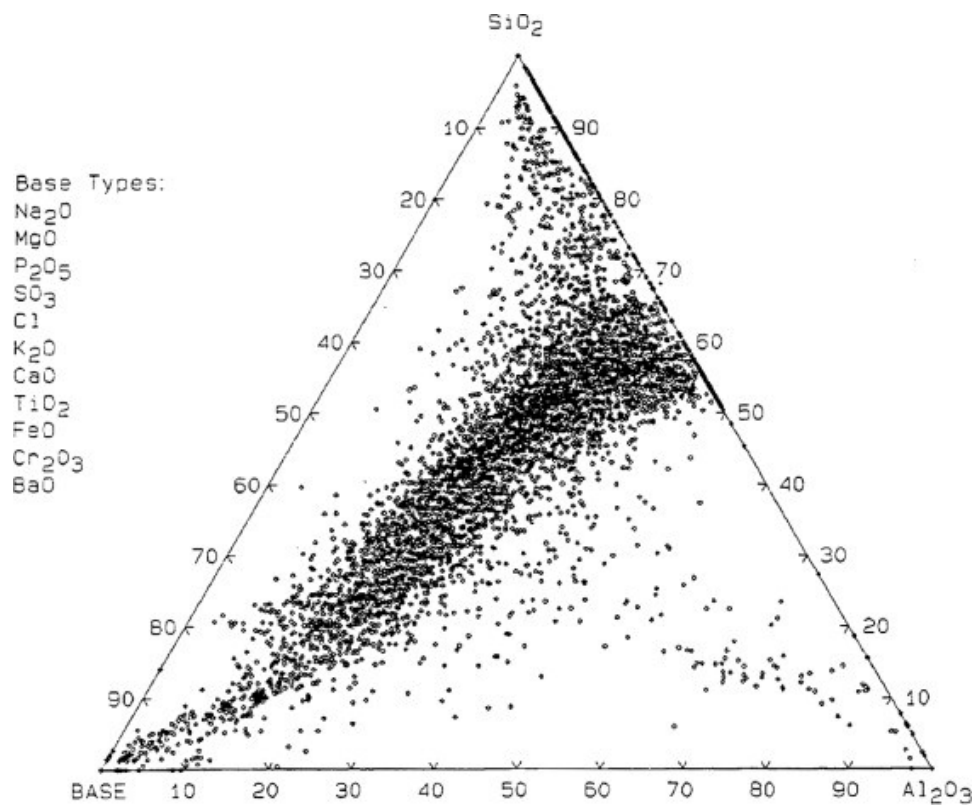


Figure 2-16: Ternary phase diagrams showing mineral phase composition distribution using CCSEM[120]

2.5.3 MLA vs CCSEM

There have been attempts in the literature to compare the various coal characterisation techniques with limited success. The main pitfall was the coal sample preparation procedure, particle detection and particle sizing methods which resulted in researchers calling for a standardised calibration procedure [188-190]. There has been a comparison between QEMSCAN systems and CCSEM conducted which led to the conclusion that the main difference is that QEMSCAN can measure on a pixel-by-pixel basis, providing very high resolution images in comparison to CCSEMs lower resolution particle-by-

particle images [40, 190]. However, there has not been a thorough comparison between MLA and CCSEM reported in the literature.

In terms of the setup of the MLA and CCSEM, there are three major components. This includes the SEM, the EDX system and the MLA/CCSEM data processing software [190]. The hardware comprises the electronics and lenses used to magnify the images and computer display. The software includes the adjustments to the contrast and brightness to focus the images and the backscatter electron detector settings. The EDX system includes the software to convert the EDX spectra to elemental composition. An additional feature is that this system can also be used for elemental mapping regions of interest to graphically show the bulk elemental compositions.

The MLA and CCSEM software enable the sample stage to automatically drive to collect information from the sample under pre-set conditions. The MLA has the added capability of offline data processing as well as the tools to export the data to other software packages. Prior to the advent of this automatic software, users had to manually drive to individual grains to study their composition, which was particularly time consuming and onerous. The latest technology allows for larger surface areas to be scanned at faster rates using state-of-the-art EDX detectors (a piece of hardware within the MLA).

Table 2-6: Measurement mode descriptions

Measurement Mode	Acronym	Description
Grain X-ray Mapping	GXMAP	Mineral grains are differentiated based on combining X-ray mapping and BSE image analysis. Highest spatial resolution and detail compared to all other measurement modes. Modal mineralogy and particle information collected.
X-ray Back-scattered Electron	XBSE	Mineral grains are differentiated based on grey scales (contrast and brightness) and X-ray trigger counts. Modal mineralogy and particle information collected.
Back Scattered Electron	BSE	Mineral grains are differentiated based on grey scale contrast and brightness. Image analysis only.
Sparse Phase Liberation	SPL	Searches for specific BSE grey scales and performs an XBSE on the particles of interest. Modal mineralogy and particle information collected.
X-ray Modal	XMOD	BSE differentiates between particles from the background and X-ray spectra are collected from the grid. Determines modal mineralogy only.

MLA measurements usually involve obtaining a BSE image and x-ray information from the sample surface. The mineral library of characteristic x-rays is developed at a similar accelerating voltage to that used during the measurements. A post processing mineral classification algorithm is used to match the x-rays to produce a colour coded classification image from which

elemental, mineralogical, textural and shape information of the particles within the image are determined[191].

Figure 2-17 outlines the decision-making process to determine which measurement mode is applicable to the sample. For the most complex mineral phases which have differing textural properties and mineral phases within each grain the more detailed and slower Grain X-ray Mapping (GXMAP) measurement mode is used as described in Table 2-6. Table 2-7 shows the institutions currently operating automated mineralogy systems worldwide.

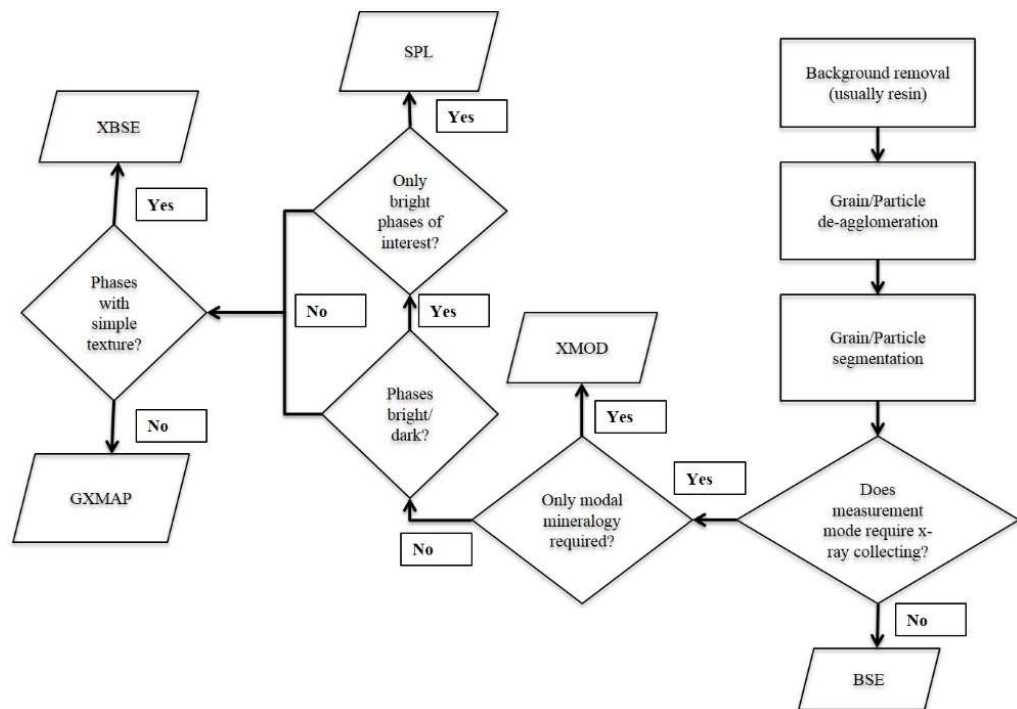


Figure 2-17: Measurement mode flow chart

Table 2-7: Institutions worldwide operating CCSEM systems

SEM/EDX Name and Specifications	Institution	Comments	Reference
Hitachi SN-3700, with Oxford Instruments INCA EDX Software	Energy Research Centre of the Netherlands	Tracor-Northern (TN) particle characterisation and recognition (PCR) CCSEM software	www.ecn.nl/home
Philips XL-40 SEM with 2 EDX detectors using Noran Thermofisher EDX Software	Geological Survey of Denmark and Greenland	CCSEM software not specified	[192]
LEO DSM 982 Gemini SEM, with Noran Voyager EDX detector	Graz University of Technology, Austria	CCSEM software not specified	[193]
SEM type unknown	University of North Dakota/EERC, USA	CCSEM software was the SEM Point Count (SEMPIC)	[194, 195]
Hitachi S-3200N SEM, with a NORAN EDX software	University of Kentucky, USA	Previous SEM was an ISI-100	[196, 197]
Stereoscan 240 (Cambridge Instruments Inc.) SEM has Link Analytical AN-10000 (Oxford Instruments) EDX	Middlesex University, UK	CCSEM is inactive. CCSEM software was MIDAS developed by John Watt (Middlesex University)	[198]
Jeol 733 superprobe SEM, with a 10mm ² active area EDX detector. SEM has Link Analytical DIGISCAN (now Oxford Instruments) EDX software	Imperial College, UK	CCSEM is inactive. Software not stated.	[199]
Jeol JSM 35U SEM with a TN 5500 EDX with ultrathin Be window.	Sandia National Laboratories	CCSEM is inactive. TN particle characterisation and recognition (PCR) CCSEM software used.	[200]
Jeol JSM 5600 SEM with EDAX CDU-LEAP detector	Chubu University, Japan	CCSEM software not specified.	[201, 202]

2.6 Impact of Literature Review on Research Direction

The focus of the literature review has been to provide an up-to-date assessment of the academic literature and guide the experimental research programme to generate statistically representative input data to ash formation and mineral transformation models. This is achieved through using a high temperature drop-tube furnace, smaller combustion-related research equipment and advanced characterisation to estimate the likely mineral transformations, extent of carbon burnout as a function of boiler residence time, and the influence of biomass addition to coal during firing a selection of commercially exploited coals and biomasses.

A comprehensive review of the literature shows that within combustion research, there are still a number of experimental questions which remain unresolved. Whilst extensive research has been undertaken on coal, there is a gap in knowledge related to the morphology, association and distribution of the inorganic mineral species present within biomass fuels which can be studied using advanced characterisation techniques. Particularly with regard to input data for ash formation models, such as the percolation models which have historically been effective in predicting coal ash formation.

The conclusions of the literature review and identified novel areas of research can be summarised as follows:

- Limited thermogravimetric studies and char burnout studies at varying residence times conducted using a drop tube furnace on international coals and biomasses. Char burnout profiles of DTF coal char and 500°C

biomass ash at 10, 30 and 50 wt% are to be investigated under air to determine the ignition temperatures and examine the synergistic effects.

- Limited understanding of the interactions between biomass-derived mineral species and coal-derived mineral species during char burnout and the types of alumina-silicate phases formed. Samples of biomass are to be ashed at 500°C to prevent alkali and alkaline oxides from volatilising and keep these minerals within the ash. The coal is to be volatilised at high temperature under a low residence time in the drop tube furnace to remove volatile carbon and to limit the extent of thermal annealing induced loss of reactivity. These samples are to be mixed at a high ratio and fed through the drop tube furnace at two residence times to compare the mineral transformations experienced.
- Development of an SEM-MLA sample mounting procedure to evenly distribute the particles within the cross section of the mounting material for viewing under the scanning electron microscope.
- Limited CCSEM ternary phase diagram data with high levels of biomass minerals and coal char using a drop tube furnace under realistic boiler operating conditions. Through analysing the ternary phase diagrams on more than 10,000 individual mineral grains can provide indications as to the types of aluminosilicates formed and the likely mineral transformations.

Additionally, in terms of erosion data from pulverised fly ashes there remains insufficient information on the following:

- Erosion rates of power station pulverised fly ashes from erosion test rigs.
- Detailed characterisation of power station fly ashes and their particle characteristics which contribute to erosion, such as angularity, mineral grain particle size distribution and composition. These samples are to be analysed in triplicate using an automated scanning electron microscopy mineral liberation analyser (SEM-MLA)

Chapter 3: Experimental and Theoretical Methods

3.1 Samples and Preparation

3.1.1 Samples

A total of fourteen samples have been used during this research – six coals, three biomasses and four power plant fly ashes. The coal and fly ash samples were supplied by Doosan Babcock Ltd and the biomasses by BF2RA – a consortium of leading energy, power and manufacturing companies.

Of the six coals, three are from the UK (Kellingley, Cumberworth and Roundwood), and the remaining three are from Poland (Stefanów region), North America (Illinois region) and South Africa (Koorfontein region). The Polish, North American and South African coals are internationally traded and currently utilised for power generation. The UK coals originate from mines that have ceased commercial operations, with the most recent closure of the deep coal mine, Kellingley. Nonetheless, these coals were selected to cover a wide range of ash contents and mineralogies from across the globe.

The three biomasses included Miscanthus (*Miscanthus × giganteus*) pellets, Spanish olive cake (*Olea europaea*) - a residual waste mixture from olive oil production, and Russian Sunflower husk (*Helianthus annus L.*) pellets.

The four fly ashes supplied are from power stations operating under coal-fired boiler conditions and were collected during plant shutdown. This includes Drax power station (Yorkshire, UK) which was firing a British deep-mined high volatile

bituminous coal; Longannet power station (Fife, Scotland) which was firing a world traded bituminous coal; Ratcliffe power station (Nottingham, UK) which was firing a high sulphur bituminous coal and Trimble County power station (Kentucky, USA) which was firing a US Eastern coal.

3.1.2 Dry Sieving

Coal fractions of 53-75 μm and 75-106 μm were produced from the bulk pulverised coal by dry sieving using a Retsch A200 Control (Hann, Germany) vibratory sieve shaker for 30 minutes at 1.5mm amplitude. Similarly, biomass fractions of 53-75 μm and 75-150 μm were prepared according to BS EN ISO 17827:2016[203]. The 53-75 μm size fractions were used for the initial DTF experiments. However, for the DTF re-firing tests the 53-75 μm and 75-106 μm coal fractions were used. A wider biomass size fraction of 53-150 μm was required for the muffle furnace ashing to provide sufficient sample for the DTF re-firing experiments.

3.1.3 Alpine Jet Sieving

An Alpine jet sieve was used to remove fine particles for each size fraction and ensure the fuel particles for DTF firing had a more uniform flow distribution. The jet sieve operated by providing vacuum suction underneath the sieve mesh with a rotating finger to evenly distribute the air flow across the sieve area and release trapped particles. The countdown timer was set to the maximum 15 minutes and vacuum pressure of 10 millibar to enable sufficient time and suction to remove the finest of particles.

3.1.4 Rotary Sample Divider

A rotary sample divider was used to divide the supplied gross fly ash into smaller quantities in a repeatable manner to provide representative samples containing a range of particle size fractions in accordance with BS ISO 1448:2007[204]. The supplied fly ash was reduced down to approximately 20g through passing a vibratory feeder, hopper and six containers to evenly distribute the sample material.



Figure 3-1: Rotary sample divider apparatus

3.1.5 Rotary Micro Riffler

A rotary micro riffler was used to divide the small rotary riffled fly ash into aliquots down to 0.1g in accordance with BS ISO 1448:2007[204]. The representative division was conducted on a Quantachrome rotary micro riffler through addition of the material to a vibrator bowl that feeds into 8 rotating test tubes. The feed vibration was kept constant at a $\frac{3}{4}$ turn and the test tube rotation speed at the slowest fixed rate. For representative division to the required sample size, a reduction ratio of 3 was selected.



Figure 3-2: Rotary micro riffler apparatus

3.2 Experimental and Theoretical Methods

The samples were characterised using a variety of standard and analytical techniques such as proximate and ultimate analysis, surface area and pore size distribution gas sorption analysis as well as automated image analysis and thermogravimetry. The characterisation procedures and methodologies are described in the following sub sections with the results for standard analysis presented.

3.2.1 Proximate Analysis and Ultimate Analysis

Thermogravimetric analysis measures the change in mass of a substance as a function of temperature or time as the sample is subjected to specific temperature and pressure conditions. This was employed for the proximate analysis of the coal and biomass samples[205] to measure the moisture content (M), volatile matter (VM), fixed carbon (FC) and ash contents (A). A 10-15 mg sample with placed into a platinum pan with a particle size range between 53-75 μ m and loaded into a TA Instruments Discovery thermogravimetric analyser. The sample was heated under a flow of nitrogen at a rate of 50°C/min to 110°C and held isothermally for 15 minutes to determine the moisture content. The temperature was then increased from 110°C at a rate of 50°C/min to 900°C and held for 15 minutes to determine the weight loss associated with the volatile matter. The gas was then switched to air and held isothermally at 900°C for 30 minutes to oxidise the char to determine the fixed carbon and ash content.

A summary of the sample methodology steps is shown below:

- 1) Select nitrogen gas
- 2) Turn data storage on
- 3) Ramp at 50°C/min to 110°C
- 4) Isothermal for 15 minutes
- 5) Ramp at 50°C/min to 900°C
- 6) Isothermal for 15 minutes
- 7) Select air gas
- 8) Isothermal for 30 minutes
- 9) Turn data storage off

The data collection system automatically saves relevant signals such as the weight loss, time and temperature for each sample; which is then transferred to an external computer for offline data processing using TRIOS software. Figure 3-3 shows an example TGA proximate analysis profile with the methodology outlined previously.

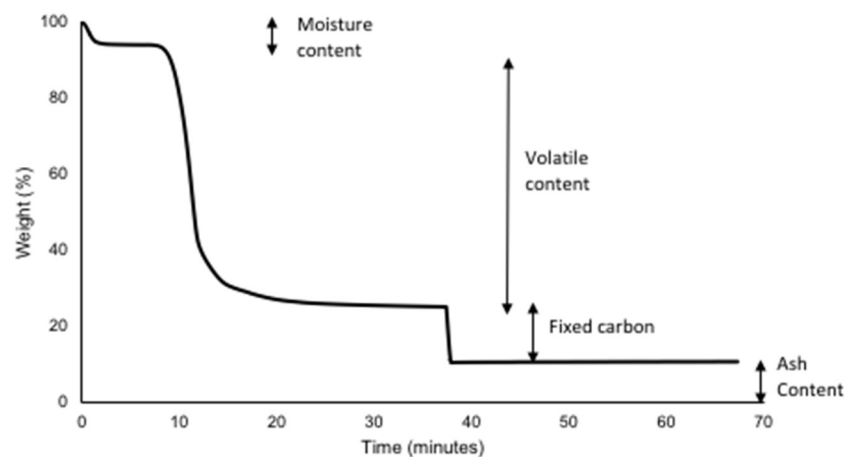


Figure 3-3: Typical proximate analysis graph

Ultimate analysis was required to determine the carbon, hydrogen, nitrogen and oxygen (by difference) contents of the fuel samples. The CHNS analyser was calibrated by running 10 blanks followed by 8 × 75 mg standard BBOTs (2,5-Bis(5-tert-butyl-2-benzo-oxazol-2-yl) thiophene), and a drift correction applied to ensure the measured carbon, hydrogen and nitrogen percentages were within the margin of error stated on the certified reference material. A 55 mg portion of the sample was added into the tin foil and loaded into the instrument.

The basic fuel analysis data for the coals and biomasses are listed in Table 3-1. The volatile matter contents (% dry, ash free) of the coals vary in the range from 29.53 – 42.11. Fuel ratios in the range of 1.37 - 2.39 and the carbon, nitrogen and sulphur contents (%dry, ash free) vary in the following ranges:

C	31-91 – 73.36
N	0.84 – 1.91
S	0.43 – 2.45

The volatile matter contents (% dry, ash free) of the biomasses vary in the range from 77.73 – 86.13. Fuel ratios in the range of 0.16 – 0.29 and the carbon, nitrogen and sulphur contents (% dry, ash free) vary in the following ranges:

C	43.91 – 45.92
N	0.56 – 2.47
S	0.10 – 0.24

Table 3-1: Proximate and ultimate analysis of samples

Sample	USA Illinois 13/0232	SA Koorfontein 15/0198	UK Kellingley 15/0196	UK Cumberworth 15/0051	POL Stefanów 15/0085	UK Roundwood 15/0052	UK Miscanthus	ESP Olive Cake	RUS Sunflower
Ash (%db)	9.06	14.39	19.83	26.80	30.61	57.77	1.98	8.16	10.42
VM (%daf)	38.37	29.53	37.49	35.36	41.00	42.11	86.13	77.73	82.21
FC (%daf)	61.63	70.47	62.51	64.64	59.00	57.89	13.87	22.27	17.79
FR FC/VM	1.61	2.39	1.67	1.83	1.44	1.37	0.16	0.29	0.22
C (%daf)	73.36	69.18	68.27	59.43	57.53	31.91	44.02	45.92	43.91
H (%daf)	5.15	4.27	4.85	4.31	4.27	2.57	5.87	6.15	6.08
N (%daf)	1.60	1.91	0.84	1.48	1.51	0.84	0.56	2.47	1.54
S (%daf)	2.45	0.58	2.38	0.43	0.80	0.67	0.10	0.19	0.24
O ^a (%daf)	17.44	24.06	23.66	34.35	35.89	64.01	49.46	45.26	48.24
Ash Class*	Low	Medium	Medium	Moderately High	High	Very High	Very Low	Very Low	Very Low

^aOxygen calculated by difference*; Ash yield classification according to BSI 11760: 2005; db = dry basis; daf = dry ash free basis.

3.2.2 TGA Loss on Ignition

Loss on ignition of the fly ash samples was measured according to a published methodology using a TGA Q600[206]. A 25 ± 5 mg sample of fly ash was placed into an alumina ceramic crucible and loaded into the TGA. Nitrogen was exposed to the apparatus at a flow rate of 30 mL/min for 30 minutes under isothermal atmospheric conditions to purge the lines of oxygen and stabilise the weighing balance. Once the readings stabilised, the sample was heated at $20^{\circ}\text{C}/\text{min}$ to 105°C and held isothermally for an hour to remove moisture from the samples. The sample was then heated at $20^{\circ}\text{C}/\text{min}$ to 750°C and held isothermally for an hour to remove volatile carbon. Immediately the gas was switched to air and held isothermally for a further 2 hours to measure the unburned carbon content. The analyses were repeated in triplicate.

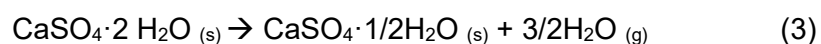
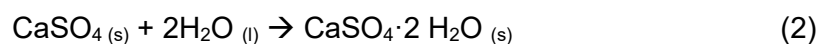
Table 3-2: Loss on ignition (LOI) of power station fly ashes

Fly Ash	As received basis (% weight)				LOI	Dry basis (% weight)		Relative error of LOI (%)
	Moisture	Volatile organic content	Ash	Unburned carbon		Ash	LOI	
Trimble	0.18	2.31	97.08	0.43	2.74	97.26	2.74	542.46
Drax	0.23	0.78	96.86	2.12	2.9	97.09	2.91	36.73
Ratcliffe	0.14	0.84	94.97	4.05	4.89	95.1	4.9	20.64
Longannet	0.25	0.76	91.69	7.3	8.06	91.92	8.08	10.37

Table 3-2 shows variations in the unburned carbon (char) and LOI (volatile organic content plus unburned carbon) remaining in the suite of power station fly ashes. The lowest to highest amounts of unburned carbon and LOI values follow the trend of Trimble > Drax > Ratcliffe > Longannet. This ranking provides an indication of the combustion efficiency, with the higher unburned carbon content from Longannet suggestive of a poorly operated boiler system.

The most recent standard ASTM C168-15 (2015), uses LOI values as an indicator for unburned carbon content and specifies 6% LOI for Class C (lignite or sub-bituminous derived) and F (bituminous and anthracite derived) as one of the chemical requirements for concrete applications[207]. Therefore, the Longannet fly ash LOI value which is greater than 6% means that this valuable by-product is unsuitable for building applications, and power generators would be subjected to a land fill gate fee for waste processing.

Conversely, Trimble has the lowest unburned carbon content (0.43 weight %), and the VOC (2.31 weight %) contributes significantly towards the LOI value (2.74 weight %). Therefore, the relative error between the LOI and unburned carbon values is particularly high for this fly ash (542.46 %), as calculated by Fan and Brown[208]. This large relative error can further be explained by the significant quantity of calcium present in the fly ash (8.42 %) as shown in Table 4-8. Furthermore, XRD analysis shown in Figure 4-2 confirmed this calcium to be associated with Gypsum ($\text{CaSO}_4 \cdot 2\text{H}_2\text{O}$), thought to be produced from interactions between anhydrite and water, which between 110 and 186°C form partially hydrated hemihydrate[209] as shown in equation (3). These calcium containing minerals will result in a loss of water, and hence weight reduction during LOI tests contributing to overestimates in the amount of unburned carbon reported[210].



Additional weight loss under the high temperature conditions of the LOI test can be attributed to other mineral phases such as carbonate decomposition, oxidation of sulphides, release of water from clay minerals and the dehydration of lime. These weight loss contributions can result in particular fly ashes being classified as unsuitable despite the actual carbon content being less than 6%[207]. However, Figure 3-4 of the elemental analysis of the fly ashes confirms that the carbon content (% dry ash free) increases directly correlate with TGA unburned carbon and LOI. The elemental analysis oxygen is calculated by difference and standard deviations are presented below the average values.

Fly ash	C (%daf)	H (%daf)	N (%daf)	O^a(%daf)
Trimble	0.60	0.13	0.16	98.96
	0.03	0.13	0.00	0.01
Drax	1.96	0.07	0.17	97.43
	0.30	0.07	0.17	0.01
Ratcliffe	3.88	0.09	0.17	95.73
	0.05	0.09	0.01	0.00
Longannet	7.39	0.10	0.25	92.09
	0.08	0.10	0.00	0.00

Figure 3-4: Elemental analysis of power station fly ashes

3.2.3 TGA Coal Burnout, Kinetics and Activation Energies

A char burnout study was required to determine the relative burnout times for the coal and biomass samples to provide an indicator of char reactivity. A 25 ± 5 mg fuel sample was heated under nitrogen at $50^{\circ}\text{C min}^{-1}$ to 110°C to remove moisture and held isothermally for 5 minutes, then rapid heating at $500^{\circ}\text{C min}^{-1}$ to 850°C , and held isothermally for 30 minutes to remove the volatile fraction. Once the mass had stabilised indicating the majority of the volatile fraction had been removed, the temperature was cooled and equilibrated to 475, 500, 525 and 550°C and the gas switched to air at a flow rate of 50 NmL min^{-1} and held isothermally to initiate char oxidation to the ash content. The sample was allowed to react until there was no appreciable mass loss.

The programme method is outlined below:

- 1) Select nitrogen gas
- 2) Turn data storage on
- 3) Ramp $50^{\circ}\text{C min}^{-1}$ to 110°C
- 4) Isothermal 10 minutes
- 5) Ramp $500^{\circ}\text{C min}^{-1}$ to equilibration temperature (475, 500, 525 or 550°C)
- 6) Select air gas
- 7) Equilibrate at the chosen temperature
- 8) Isothermal for 300 minutes (or other time to stabilise the weight)
- 9) Ramp $50^{\circ}\text{C min}^{-1}$ to 30°C
- 10) Turn data storage off

The Arrhenius equation was manipulated to determine the rate constants and activation energies. A thermogravimetric analyser was used to measure the time taken to achieve 90% conversion of the char to ash on a normalised basis through varying the isothermal temperature for combustion. The higher the

temperature the shorter the time period to achieve complete char burnout. The Arrhenius equation can then be rearranged to produce the plot as follows:

$$k = Ae^{\frac{E_A}{RT}}$$

$$\ln k = \ln A - \frac{E_A}{RT}$$

The equation can then be used to produce a linear Arrhenius plot of $\ln k$ (s^{-1}) vs $1/T$ (K^{-1}) with the gradient $-E_A/R$. Once the gradient of the line is determined the activation energy can be calculated. To calculate the 1st order rate constant k the following expression can be derived at 90% conversion of the char to ash, referred to as the t_{90} value:

$$\ln[A]_t - \ln[A]_o = -kt$$

$$[A]_t = [A]_o e^{-kt}$$

$$[A]_t = 0.9[A]_o$$

$$t = t_{90}$$

Substituting to solve for the k formula:

$$0.9[A]_o = [A]_o e^{-kt_{90}}$$

$$k = \frac{-\ln 0.9}{t_{90}}$$

The main input parameters are the 90% char burnout time determined from thermogravimetric analysis as described previously.

3.2.4 TGA Burnout of DTF Char

The DTF generated char burnout procedure is as follows. A 25 ± 5 mg DTF generated char sample was heated under nitrogen at $50^{\circ}\text{C min}^{-1}$ to 110°C to remove moisture followed by rapid heating at $50^{\circ}\text{C min}^{-1}$ and equilibration at 525°C before switching to an air atmosphere to initiate char oxidation to the ash content.

3.2.5 TGA Combustion Blends

A TGA combustion study was undertaken on the muffle furnace generated biomass ash and DTF coal char blends at 50:50 wt% to determine the influence the biomass minerals have on the thermal decomposition reactions during the combustion process. A 25 ± 5 mg pre-mixed blend was heated under a 100 Nml min^{-1} air atmosphere at $5^{\circ}\text{C min}^{-1}$ to 1000°C and held isothermally for 15 minutes. This identified the temperatures at which the greatest mass change occurred to determine whether there was an enhancement in the coal combustion with biomass ash addition at varying ratios.

3.2.6 Maceral and Vitrinite Reflectance Analysis

Maceral analysis was performed on two coal samples to determine the microscopic organic constituents such as vitrinite, liptinite and inertinite according to BSI ISO 7404-4 2017[211]. The samples were initially sieved for

the 53-75 μ m fraction to minimise the effects of particle size on the maceral composition for coal comparison. The particles were mounted, ground and polished in epoxy resin to produce a planar surface microsection using the same procedure described for SEM analysis, without the carbon coating applied. The analysis was conducted on a Leica optical microscope containing oil immersion lenses to produce reflected light images of the particles.

Vitrinite reflectance was also determined to provide an indication of the coal ranks, this is due to chemical and optical properties of vitrinite varying more uniformly during coalification than the maceral groups. The mean reflectance of the vitrinite maceral increases with the extent of aromatisation, and because the volatile matter component comprises the non-aromatic portion of the coal there is an inverse correlation of volatile matter and the mean reflectance.

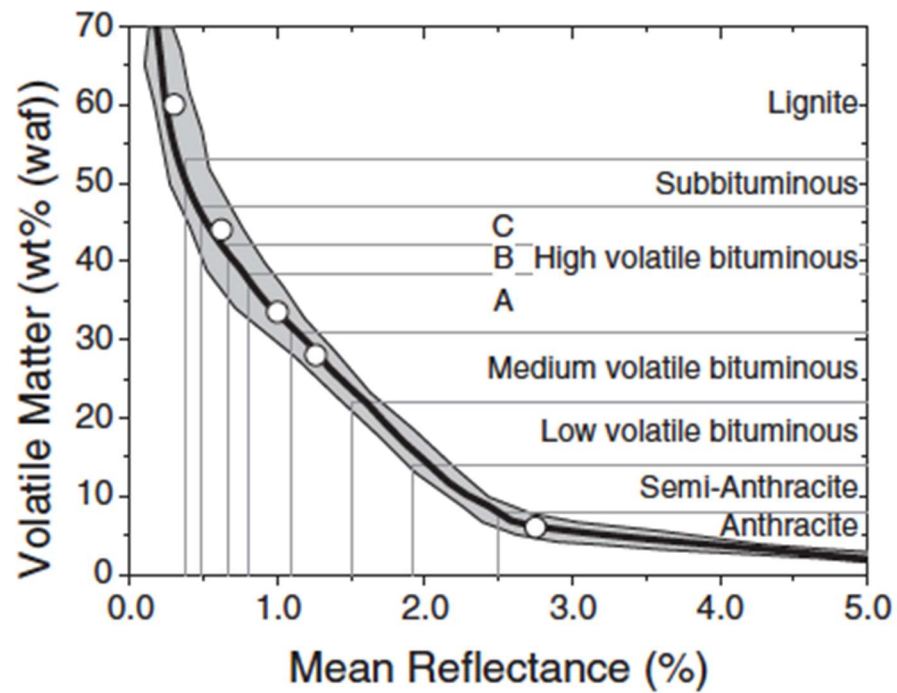


Figure 3-5: Coal rank definition diagram[14]

The measurement of reflectance (or reflectivity) can be defined by the following equation:

$$R = \frac{I_R}{I_0} \times 100\%$$

The determination of the reflectance values is made in an oil immersion using green light at 546nm, in accordance with the BSI ISO 7404-5:2009 method[212]. For the point analysis results to be statistically significant, 500 points per coal sample were measured and recorded. The reflectance's were divided into 0.05% point intervals and each reading attributed to each interval producing a histogram showing the frequency or volume fraction % of each random reflectance class. The three reflectance percentage parameters

determined are the minimum reflectance R_{\min} , arithmetic mean reflectance R_m and maximum reflectance R_{\max} . The maximum and minimum reflectance were determined through measurement of 500-point analyses with a reflectometer using polarised light. Figure 3-6 below shows the typical mean reflectance ranges expected to identify the coal ranks with other geochemical parameters.

Maturation rank		%Volatiles in coal (d.a.f.) *	Max. paleo Temp (°C)	Vitrinite reflectance (%)	Geochemical Parameters					Hydrocarbons		
Kerogen	Coal				CPI	Pyrolysis		C wt%	H wt%		H/C wt%	
						Tmax (°C)	P.I.					
Diagenesis	Peat	60		-0.2	5			67	8	1.5	Bacterial gas	
	Lignite			-0.3	3	400			70	8	1.4	Immature heavy oil
	Sub-bituminous		C		-0.4							
			B		-0.5	2	425			75	8	1.3
Catagenesis	High volatile bituminous	A	46	50	-0.6		0.1					
		B		-0.7	1.5	435						
		C		-0.8			0.2	80	7	1.1	Wet gas and oil	
		A	33	-0.9	1.2		0.3					
	Medium volatile bitumin.		-1.0	1.0	450							
	Low volatile bitumin		-1.3			0.4	85	6	0.85	Condensate		
			25	-1.5		475			87	5	0.7	
	Sem-anthrac.	13	170	-2.0		500						
Metagenesis	Anthracite		200	-2.5		550		90	4	0.5	Dry gas	
				-3.0								
	Meta-anthrac.	4	250	-4.0				94	3	0.38		
				-5.0				96	2	0.25		

Figure 3-6: Coal rank as a function of mean vitrinite reflectance[213]

From the histogram data the mean random reflectance value is calculated as an arithmetic mean and the corresponding standard deviation determined from the individual reflectance readings using the following equation:

$$s = \sqrt{\frac{\sum R_i^2 - \frac{\left(\sum R_i\right)^2}{n}}{n - 1}}$$

Table 3-3 shows the maceral analysis conducted on both coals which confirms the unreactive nature of the South African coal due to the high inertinite content. The higher volatile USA Illinois coal had a higher mineral content and vitrinite content indicative of higher reactivity. Figure 3-7 shows the vitrinite reflectance of the coals which confirms that both can be categorised as high-volatile bituminous coal in nature.

Table 3-3: Petrographic analysis of the maceral groups

Macerals	South African coal (%)	USA Illinois coal (%)
Vitrinite	45	68
Liptinite	4	7
Inertinite	51	20
Minerals	1	5

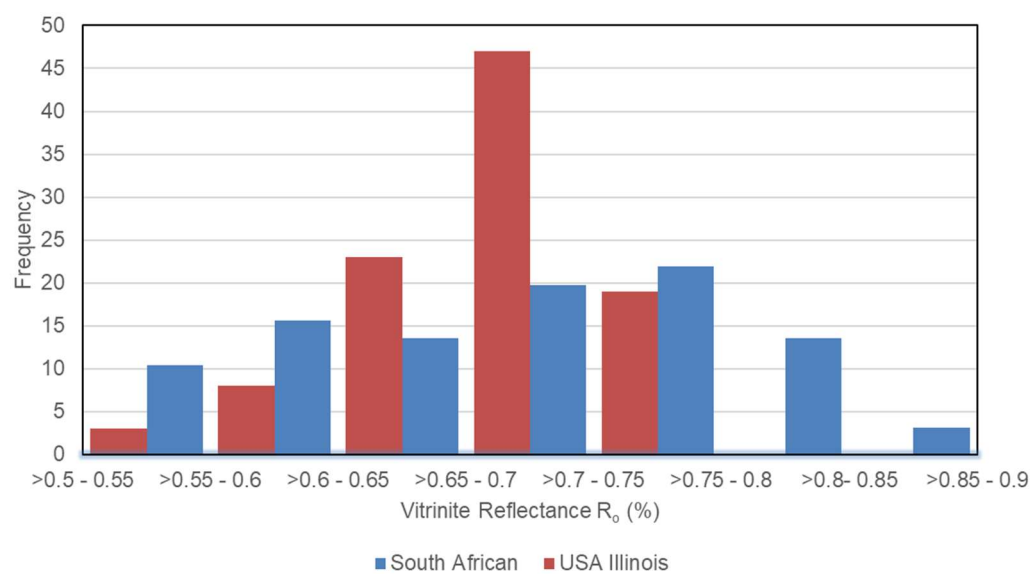


Figure 3-7: Mean random vitrinite reflectance R_o (%)

3.2.7 Adsorption Isotherms

Surface areas and pore size distributions were determined by gas sorption analysis using a Micrometrics ASAP® 2420 Accelerated Surface Area and Porosimetry system[214]. Langmuir, Brunauer-Emmett-Teller (BET) and Dubinin-Radushkevich (DR) adsorption isotherm models were used to investigate the morphological changes of the chars during pyrolysis and combustion. CO₂ accounted for the lower relative pressures and microporous nature of the chars due to the smaller molecule diameter compared to N₂. The adsorption gas is injected into the sample pores at various relative pressures and the respective volume at each pressure measured. As the relative pressure increases the thickness of the adsorbed film increases until the pores are saturated. Similarly, during the desorption process the relative pressure is reduced incrementally and the gas volume measured as the adsorbed molecules are liberated. These recorded measurements enable the construction of the adsorption and desorption isotherms.

The Dubinin-Radushkevich (DR) equation is widely used to assess the adsorption of gases and vapours into microporous materials such as coal[215]. CO₂ is used as the adsorbate for coal due to the smaller range of pore size diameters analysable by gas adsorption relative to nitrogen adsorption. The model has a semi-empirical approach based on the following assumptions:

- Applicable to adsorbents with a distribution of microporous pore sizes which are not extensively skewed.
- The adsorption surface of the carbonaceous material is heterogeneous.

The DR equation can be used to determine the total micropore volume of the carbonaceous material from the linear section of the adsorption isotherm plots which are produced using computer software. To calculate the volume of pores within the carbonaceous material structure that are filled as a function of pressure the following DR equation is applied:

$$\frac{V}{V_0} = \exp \left[-\frac{BT^2}{\beta^2} \ln^2 \left(\frac{P_0}{P} \right) \right]$$

The Brunauer-Emmett-Teller (BET) adsorption isotherm model was also used for a selection of coal chars. The main assumptions are as follows:

- The adsorption surface of the material is homogeneous and occurs across the entire surface equally without preferential sorption sites. Additionally, each adsorption site is classified as either occupied or unoccupied with a maximum of one adsorbate molecule per sorption site.
- Once a molecule has been adsorbed it can act as a single adsorption site for another gas molecule. No intermolecular interactions are considered including lateral adsorbate-adsorbate interactions, adsorbate-gas molecule interactions or non-sorption adsorbate-gas molecule interactions.
- At the top of the multi-layer adsorption site a local equilibrium exists between the surface-sorption site or the surface-adsorbate molecules with the gaseous phase molecules. Therefore, the rate of adsorption is equal to the rate of desorption and there is no change in the number of

adsorbed molecules at a constant vapour pressure (due to no pressure or concentration differential).

- The rate of reaction during the adsorption process is kinetically limited rather than by diffusion.

These assumptions can be used to produce the BET model for each adsorbed layer using the Arrhenius equation to determine the kinetic rates of adsorption and desorption based on the fraction of sorption sites at the surface. The BET equation for gas adsorption can then be defined as follows[216]:

$$v = \frac{v_m c p}{(p_0 - p) \left[1 + (c - 1) \left(\frac{p}{p_0} \right) \right]}$$

The equation can then be rearranged to form a linear function with the y-intercept and the slope used to solve for the constant c.

$$\frac{1}{v \left[\left(\frac{p}{p_0} \right) - 1 \right]} = \frac{c - 1}{v_m c} \left(\frac{p}{p_0} \right) + \frac{1}{v_m c}$$

The specific surface area can be determined according to the following equation:

$$S = \frac{v_m N_A}{22,400 \times m}$$

The specific surface area can be converted to a volume specific surface area by multiplying with the material density.

The Barret-Joyner-Halenda (BJH) method is a procedure for calculating the pore size distribution and pore volume from experimental isotherms using the modified Kelvin model of pore filling. This relates the amount of adsorbate removed from the pores in dimensionless units of relative pressure (P/P_0) as a function of the size of the pores. The model is usually applied to nitrogen desorption data measured at 77 K for mesoporous materials. This method only applies to the mesopore and smaller macropore size range, with pores that have mineral interconnections and regular shapes. The BJH model is accurate for pore sizes in the range of 2 nm to 150 nm.

3.2.8 X-ray Fluorescence Spectroscopy

Bulk chemical analyses of the major and minor elements was undertaken using an x-ray fluorescence (XRF) Bruker S8 Tiger. Approximately 1 gram of the sample was added into a sample holder with oil 2µm thick mylar film and analysed using a 7-minute full elemental analysis method. This provided a non-destructive means of analysing for the major elements (Si, Al, Fe, Ca, Mg, Na, K, Ti & P) in the char and ash samples. These elements can then be used to calculate the metal oxide concentrations assuming the highest oxidation states. The XRF data analysis software automatically converts the individual element compositions to the metal oxides and transfers the data to Microsoft Excel format.

3.2.9 X-ray Powder Diffraction

X-ray powder diffraction (XRD) was used for phase identification and semi-quantification of unknown crystalline minerals in the raw fuel samples and

muffle furnace and DTF generated chars and ashes to assess the changes in mineral constituents during combustion. An automated Bruker D8 Advance diffractometer with Cu-K α radiation and 0.6mm slit width was used. Samples were prepared onto the holders with a glass slide and readings were taken between 5° and 90° at 0.01° step size with 3 seconds per step, resulting in a total measurement time of 7 hours per scan. The X-ray tube generator was operated at 40 kV and 35 mA.

Although XRD is widely considered the most traditional method to determine the mineral and inorganic species, there are issues with analysing coal and biomass samples directly because the non-crystalline organic components produce an accentuated background which presents difficulties in distinguishing between peaks for selected minerals[217].

It is known that a significant proportion of fly ash contains amorphous phases which cannot be identified by XRD, this is due to the variations in mineral crystallinity, preferential alignment and the differential absorption of X-rays by selected minerals in a mixture and detection levels of 2-3 weight %.

XRD is a semi-quantitative method because the expected statistical errors of determination can be greater than 10%[218] based on low temperature ash (LTA) samples analysed during a Round Robin from 10 laboratories. In this study individual minerals were analysed with coefficients of variation ranging from 24% to 36%, which is significantly greater than the CCSEM coefficient of variation of 12%. Although the majority of fly ash contains amorphous mineral phases, XRD has proven a useful analytical technique to verify and validate the

results from CCSEM to aid the understanding of ash forming reactions [219, 220].

For the industrial fly ash samples, XRD was conducted at the University of Birmingham on a Panalytical Empyrean, scanning between 5° to 85° at 0.5° min⁻¹, which gave a total analysis time of 2.7 hours per sample.

3.2.10 Particle Analysis

Particle analysis on the pyrolysis and combustion products from the experiments and initial sample characterisation has been carried out using three methods. The first has been through mass-based sieve analysis to provide the mass fractions for particle size distributions. The second is through analysing the particle sizes using computer-controlled scanning electron microscopy and the third is through dynamic image analysis.

Dynamic image analysis is performed using a Retsch Technology Camsizer® P4 in accordance with the BS ISO 13322-2:2006 standard[221]. The technology uses two highspeed cameras, a zoom and basic camera to capture images at a rate of more than 30 frames per second at 1.3 megapixels each. The particles vibrate along the feeder under controllable operating conditions and drop between a planar light source and two cameras. The cameras capture images of the particles providing information on the size, shape, number, density and transparency for analysis. The particle range for measurement is between 30µm to 30mm. The cameras individually analyse the particles captured, with the zoom camera identifying the number of smaller particles uncaptured by the

basic camera. The camsizer reports particle sizes to the nearest μm with a ± 0.5 μm margin of error per reading.



Figure 3-8: Camsizer P4 setup

3.2.11 Drop Tube Furnace

The Drop Tube Furnace (DTF) at The University of Nottingham, developed by Elite Thermal Systems, was used to produce char and ash under similar conditions to those of industrial pulverised fuel boilers at a power station. The main components of the system include four vertically mounted and electrically heated silicon carbide elements encompassing a ceramic work tube, two trim heaters, water-cooled feeder and collector probes, a flow straightener, a cyclone product collector, an oxygen gas analyser and a custom-made screw feeder.

The DTF system has the ability to simulate industrial scale boiler conditions, specifically high heating rates of 10^4 to 10^5 K s⁻¹, maximum temperatures of 1600°C, short residence times of 200 to 600 ms and oxygen levels to simulate full-scale combustion. In order to estimate the residence time of the particles in the high temperature zone, the separation distance between the feeder and collector probes, and the temperature and gas flow rate were taken into account. The carrier gases, nitrogen and oxygen were available from external cylinders directly piped into the system. The cyclone separator below the collector probe enabled the products to be separated from the gaseous volatiles entrained in the carrier gas flow. A vacuum pump operated 1 L min⁻¹ above the carrier gas flow rate ensured that the volatiles were captured in the glass wool filter. For the initial experiments, the maximum operating temperature of 1450°C, a residence time of 200-600 ms and a carrier gas of pure nitrogen were used to replicate the initial devolatilisation step in the combustion process.



Figure 3-9: Control panel



Figure 3-10: Collection probe with cyclone and control system

A custom-made screw feeder system, designed and constructed in the Engineering workshop at the University of Nottingham, was used for each DTF experiment to provide a steady flow rate of fuel particles through the DTF system. The pulverised sample is placed in the hopper and passes through the rotating screw before falling under gravity into the feeder probe with a stream

of nitrogen at 1 L min^{-1} . A control panel with a dial gauge was connected to an electric motor to moderate the revolutions per minute of the screw thread. For all the experiments, the control panel was set to 3 which provided a feed flow rate of between 8 to 10 grams per hour.



Figure 3-11: Feeding system

3.2.11.1 Drop Tube Furnace Commissioning

Prior to commencing experimental runs on the DTF, it was necessary to set the residence time through adjusting the length of the metal rods to alter the separation distance between the feeder and collector probes. Previous researchers calculated the inlet gas flow rate required for a specific furnace temperature and residence time by assuming a laminar flow velocity profile and applying the ideal gas law to correct the gas flow rates for the high temperatures within the furnace. Additionally, a thermocouple wire was inserted down the feeder probe to record the actual temperature and the thermostat temperature

reading to account for the radial heat loss from the main heaters through the ceramic work tube.

With reference to Figure 3-12, the devolatilisation and combustion of the coal and biomass particles occurred in the centre of the system in the work tube. The system comprises of a pre-heater to raise the temperature of the particles and gas, the main heater and a trim heater. The work tube was ceramic with an internal diameter of 50mm, outside diameter of 55mm and 1.5m in length. The residence times employed in this research were 200ms and 600ms, corresponding to 22 and 65 cm respectively.

The residence time was calculated using an average laminar flow velocity profile, which assumed the following:

1. The fuel particles were entrained within the gas flow under a laminar flow regime.
2. The gas velocity was a function of the radial position across the work tube.

The laminar flow velocity profile can be written as follows:

$$\frac{V_r}{V} = 2 \left(1 - \frac{r^2}{R^2} \right)$$

Where V_r is the gas velocity at the centre of the work tube (r) and V is the average gas velocity across the entire radius of the tube (R). Therefore, in the centre of the tube, $r = 0$ and $V_r = V_0$, which simplifies to the expression:

$$V = \frac{1}{2} V_0$$

The velocity of the fuel particles, whether coal or biomass, down the centre of the work tube (V_0) can be derived from the particles residence time in the furnace (t) and the separation distance between the collector and feeder probes (L), resulting in the following:

$$V = \frac{1}{2} \frac{L}{t}$$

The velocity V can be determined from the volumetric flow rate (Q) of the gas passing through the DTF and cross-sectional area (A) of the work tube:

$$V = \frac{Q}{A} = \frac{Q}{\pi R^2}$$

The two previous equations can be re-arranged to calculate the residence time:

$$t = \frac{L\pi R^2}{2Q}$$

The nitrogen and oxygen gas were supplied to the DTF from external tanks at room temperature. The volumetric flow rates were measured indirectly using inlet rotameters located prior to the work tube inlet. These flow rate measurements were corrected to account for the high temperatures in the DTF by applying the ideal gas equation, where locations 1 and 2 are outside and inside the DTF respectively:

$$\frac{Q_1}{Q_2} = \frac{T_1}{T_2}$$

For the 200 ms residence time a 22 cm probe separation, work tube with an internal diameter of 50 mm, inlet gas flow rate of 11.2 L min⁻¹ and operating temperature of 1450°C were used. The volumetric flow rate can be calculated as follows:

$$Q_2 = \frac{11.2}{1000 \times 60} \times \frac{1450 + 273}{25 + 273} = 1.08 \times 10^{-3} \text{ m}^3\text{s}^{-1}$$

Therefore, the particle residence time can be calculated:

$$t = \frac{22}{100} \times \frac{\pi (0.025)^2}{2 \times 1.08 \times 10^{-3}} = 0.2 \text{ seconds} = 200 \text{ milliseconds}$$

Table 3-4 shows the thermostat settings and inlet gas flow rates required for the two residence times at 1450°C.

Table 3-4: DTF operation settings

Temperature (°C)	Residence time (ms)	Probe separation (cm)	Gas flow rate (L min ⁻¹)	Thermostat setting (°C)
1450	200	22	11.2	1530
	600	65	11.0	1480

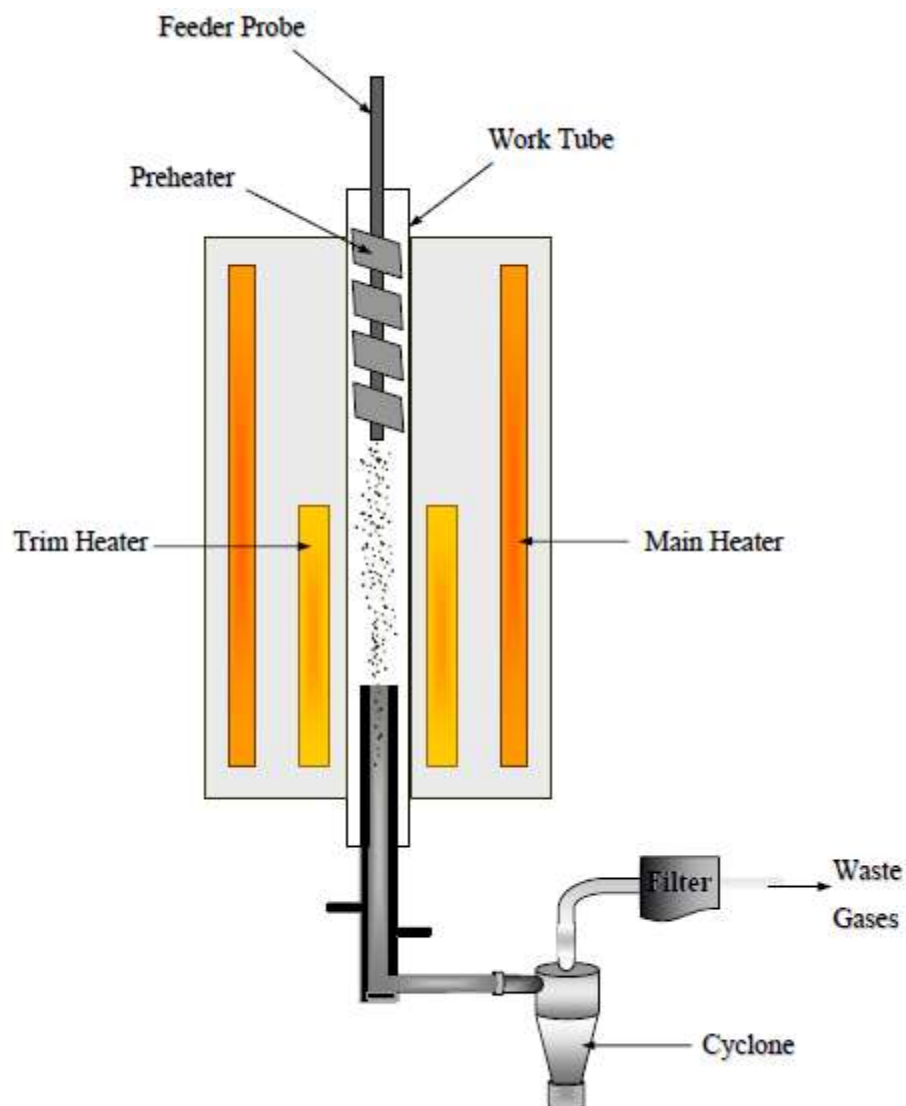


Figure 3-12 Schematic of the drop tube furnace

In order to accurately determine the oxygen concentration of the inert nitrogen carrier gas flowing through the drop tube furnace an ABB continuous gas analyser was setup to measure the volumetric percentages of oxygen and nitrogen. Prior to each test run the oxygen rotameter was adjusted to provide the correct oxygen and nitrogen concentrations. The gas analysis equipment was attached to the main gas feedline entering into the main combustion zone

of the drop tube furnace containing a swage lock valve to allow a small amount to be tapped off for gas analysis. In order to close the drop tube system to the atmosphere the screw feeding system had a plug to maintain a positive pressure for the particles to drop and fall into the system at the required flow rate.

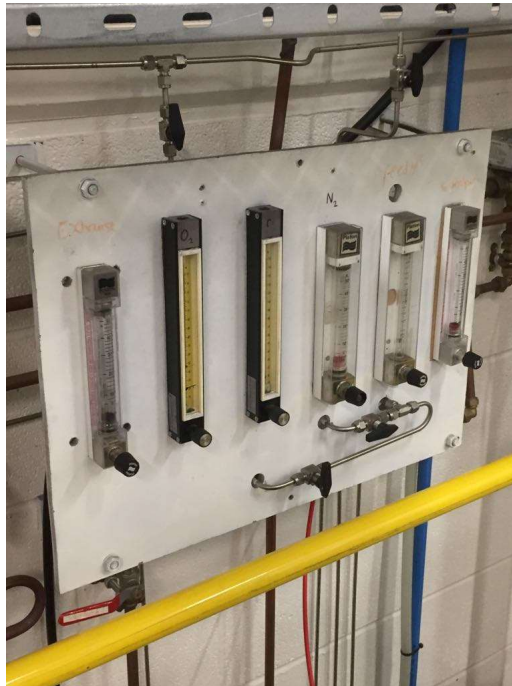


Figure 3-13: DTF volumetric gas flow analysers



Figure 3-14: ABB continuous oxygen gas analyser

3.2.11.2 Collection Efficiency

Historically, drop tube furnaces used for devolatilisation and combustion experiments have utilised an approach known as the 'ash tracer' method to measure the weight losses during char and ash production. This is to account for the release of tars, gases and soot which make a mass balance unreliable from feed and product weighing. This method can be used to determine the volatile yield for char pyrolysis under nitrogen and the loss on ignition or unburned carbon remaining after char combustion under a slightly oxidising atmosphere. By knowing the ash content of the coal or biomass and that of the char collected in the cyclone after passing through the drop tube furnace, the collection efficiency can be calculated. As a means of determining the repeatability of the DTF generated chars and ashes, a mass balance collection efficiency can be conducted for each set of runs. The collection efficiency for the DTF samples can be determined according to the following equation[222]:

$$\varphi (\%) = \frac{M_{\text{char}} \times A_{\text{char}}}{M_{\text{fuel}} \times A_{\text{fuel}}} \times 100\%$$

Where φ is the collection efficiency, M_{char} and M_{fuel} are the char and fuel masses collected and fed into the DTF respectively and A_{char} and A_{fuel} are the TGA ash contents (weight percentage) of the char and fuels respectively on a dry basis.

The TGA proximate analysis derived ash contents of the coal and biomass fractions and resultant chars at the two DTF residence times, 200 and 600 milliseconds at 1450°C are given in Table 3-5. From analysis of this data, it is evident that the average char ash content slightly increases with residence time

from 200 to 600 milliseconds, with the standards deviations showing limited statistical significance. However, the highest ash content coal, Roundwood, shows a clear trend that the char ash content increases with increasing residence time as the maximum 200 milliseconds and minimum 600 milliseconds collection efficiencies are 67.52% and 71.82% (4.30% difference) respectively. Similarly, this trend applies to the Illinois coal from 19.33% to 21.49%, albeit with a smaller difference of 1.28% and in spite of the lower ash content. For the biomasses the ash content increases with residence time, with generally larger standard deviations owing to the greater amount of volatile matter.

Table 3-5: Ash contents of coals and biomass chars (53-75µm fractions)

Type	Coal/Biomass Fraction	Fraction Ash Content (wt% dry basis)	Char Ash Content (wt% dry basis)	Char Ash Content (wt% dry basis)
			200 ms	600 ms
Coal	Cumberworth	26.8	35.64	39.21
		0.07	4.69	1.18
	Roundwood	57.77	67.16	73.84
		0.01	0.36	2.02
	Kellingley	19.83	32.38	32.46
		0.09	0.19	1.09
	Stefanów	30.61	51.76	53.46
		0.26	2.32	0.33
	Illinois	9.06	19.33	21.49
		0.08	0.45	0.43
	Koorfontein	14.39	22.94	22.99
		0.03	0.63	0.62

Biomass	Miscanthus	13.87	26.79	29.72
		0.32	2.49	0.07
	Sunflower	10.42	31.99	33.24
		0.34	1.70	7.19
	Olive Cake	8.16	28.69	32.65
		0.06	2.29	1.00

The char yield and collection efficiencies during pyrolysis are shown in Table 3-6. This table shows that the ash tracer method determined collection efficiencies for the coal and biomass samples show inaccuracies and poor reproducibility. The general trend is that the collection efficiency decreases as the residence time increases, with the largest standard deviation for the 600 millisecond residence time. This shows there is significant variability in the percentage difference between the amount of fuel fed and that collected on consecutive runs using the DTF system. The causes of these discrepancies arise due to several factors which will be considered below.

Firstly, coals and biomasses which have low ash contents can exhibit large variations in determined ash contents resulting from experimental error in the DTF and thermogravimetric analysis. This can occur when there is a negligible change in weight during the combustion or pyrolysis decomposition in the DTF at two different residence times which cannot be detected by thermogravimetric analysis.

Additionally, the high temperature operating conditions of the DTF during these pyrolysis tests may give rise to ash volatilisation, whereby there is a loss of alkali and alkaline earth metals such as K, Mg, Na and Ca. This behaviour may be particularly prevalent at the higher 600 millisecond residence time due to the

extended time the particles experience the high temperatures. Nonetheless, the residence time exposure of the fuel particles during these tests is very low compared to the standard coal ashing technique.

During the thermal conversion process in the reactor work tube section of the DTF, the fuel particles undergoing pyrolysis may experience divergent flow trajectories when the volatile components are expelled from the fuels surface. As such, low temperature melting phases may become sticky and adhere to the work tube, probes and the cyclone system leading to an underestimation in the collected weight measurements. There are also further particle losses as less dense particles entrained in the carrier gas flow pass into the cyclone filter system.

Another source of error encountered in the measured particle collection efficiency results from the thermal quenching of the particles from the main heater zone in the work tube into the lower temperature, trim-heater zone passing through the water-cooled collector probe. This temperature gradient could result in the re-condensation of volatile components onto the particles surface or onto the walls of the collector probe. Consequently, due to the build-up of residues between each test run, the vacuum pump suction flow rate was increased and air was passed down the feeder probe to dislodge any particle remnants from the feeder and collector probes into the cyclone and glass wool filter. Also, the collector probe was cleaned after approximately 12 grams had been fed, and between samples the DTF was shutdown to allow for the feeder probe to be thoroughly cleaned to avoid cross-contamination.

As discussed, there are numerous experimental errors arising from the ash tracer method, however the procedure is simple and has been used by coal workers for decades. More recently, alternative approaches involving doping with known quantities of minerals have been investigated, however these methods also incur errors [223, 224].

Table 3-6: Char yield and collection efficiency for the pyrolysed chars

Type	Coal/Biomass Fraction	Char Yield (g/g of feed)		Collection Efficiency (%)	
		200ms	600ms	200ms	600ms
Coal	Cumberworth	0.46	0.28	66.83	37.21
		0.05	0.16	6.83	20.89
	Roundwood	0.64	0.32	82.20	37.59
		0.01	0.12	0.75	13.44
	Kellingley	0.29	0.19	47.06	31.58
		0.05	0.04	8.56	6.95
	Stefanów	0.46	0.44	78.23	76.72
		0.02	0.33	3.74	56.87
	Illinois	0.18	0.14	38.35	28.98
		0.04	0.05	10.88	9.73
	Koorfontein	0.52	0.51	83.23	81.26
		0.01	0.06	1.77	9.69
Biomass	Miscanthus	0.08	0.08	14.94	8.39
		0.02	0.01	4.00	1.61
	Sunflower	0.03	0.11	35.82	8.17
		0.01	0.04	11.67	0.61
	Olive Cake	0.12	0.07	27.47	8.17
		0.04	0.05	21.35	1.88

3.2.12 Erosion Test Rig

An erosion test rig was used to measure the erosion rates of various fly ash samples through firing the particles at metal target specimens. The main components of the test rig include the following:

- Feed hopper with a vibratory feeder;
- Vertical accelerating tube;
- Target specimen chamber and holder;
- Cyclone and particulate filters;
- Air pump with a control valve and mass flow meter.

The test rig operates by pumping air at a controlled velocity through a vertical accelerating tube towards a metal target specimen. The fly ash particles are fed into the air flow from a vibrating chute feeder and entrained in the air stream. The mass flow rate of the entrained fly ash particles can be controlled by adjusting the feed vibration speed. The erosion tests require approximately 2 kg of fly ash. The particles are fired towards the metal target specimen, usually carbon steel (30 x 30 x 1 mm dimensions) which is attached to a clamp at the required impact angle. It should be noted that the impact angle is set using a metallic protractor (set between 0 – 90°) attached to the specimen chamber, usually at an impact angle of 45°. The impact angle is calculated as 90° minus the coupon specimen angle.

Once the target specimen has been contacted, the erodent particles pass through the cyclone, 10 µm and 1 µm filters respectively, and the remaining air passes through a mass and volumetric flow meters before being exhausted into the atmosphere. The air flow rate can be controlled to set a maximum air

velocity of 120 m s^{-1} , but is usually set between $30\text{-}60 \text{ m s}^{-1}$ for the test runs. These erosion experiments usually involve firing a controlled mass of erodent particles at a target specimen under specific impact angles and velocities. The post-examination of the weight loss from the erosive wear of the target specimen is determined. The erosion rate is usually expressed in units of mg kg^{-1} , which translates to the weight loss of material from the target specimen per unit mass of erodent material fired. For more detailed analysis, an examination of the structural defects on the surface of the eroded target specimen can be explored using microscopic techniques to inform on the erosion wear mechanism.

The procedure for the operation of the erosion test rig is as follows:

1. Clean the target specimen with a cloth to remove any visible surface deposits such as rust. If necessary, use a small amount of acetone to clean properly and allow to dry.
2. Assign and record the target specimen's unique identification name and project number into the log book. For runs at impact angles of 45° and below use a $30 \times 20\text{mm}$ specimen and for runs above 45° use a $60 \times 30\text{mm}$ specimen.
3. Weigh the target specimen on an analytical balance to 3 decimal places and record the weight in the log book.
4. Weigh approximately 2 kg of the erodent material (fly ash) and record the weight in the log book.
5. Weigh the $10 \text{ }\mu\text{m}$ and $1 \text{ }\mu\text{m}$ filters on the analytical balance to 3 decimal places and record the weights in the log book.

6. Attach the target specimen to the specimen chamber holder with the clamp and grub screws.
7. Align the target specimen at the required angle using the metal protractor on the specimen chamber and record the angle in the log book. Close the specimen chamber lid using the wing nuts.
8. Position the accelerating tube exit above the target specimen and fix in place with the locking nut on the specimen chamber.
9. Load the erodent material (fly ash) into the feed hopper.
10. Check that the air flow control valve is fully open and the bypass valve is closed.
11. Turn on the air pump.
12. Adjust the control valve to the volumetric flow rate required for the target air velocity at the tube exit. The CGR rotary gas meter will be used to set the target volumetric flow rate. Isothermal runs are conducted at 5 minute intervals with the volume readings (in nm^3) calculated. The control valve is adjusted and the process repeated until the target flow rate is reached.
13. When the correct airflow has been reached, start the stop watch and the vibratory feeder.
14. Calculate the volumetric air flow rate at regular intervals using the CGR meter and stop watch. Adjust the control valve when required to keep the air flow rate at the target level. Record the mass flow rate and CGR rotary volumetric flow rate in the test log book.
15. When all the fly ash has passed through to the spent collector, stop the vibratory feeder and air pump.
16. Disconnect the accelerating tube and the top of the specimen chamber.

17. Open the control valve fully and switch on the air pump to brush away any remaining fly ash from the chamber. Switch off the air pump.
18. Disconnect the erodent collector from the cyclone and weigh. Record the reading in the log book.
19. Remove the 10 μm and 1 μm filters and weigh. Record the readings in the log book.
20. Remove, clean and re-weigh the target specimen. Record the reading in the log book.
21. Determine the weight loss of the target specimen and the erosion rate using the following expression:

$$\text{Metal loss per kg of erodent} = \frac{SW_I - SW_F}{CW_I - CW_F} \left(\frac{\text{mg}}{\text{kg}} \right)$$

SW_I = initial test specimen weight (mg)

SW_F = final test specimen weight (mg)

CW_I = initial spent erodent collector weight (kg)

CW_F = final spent erodent collector weight (kg)

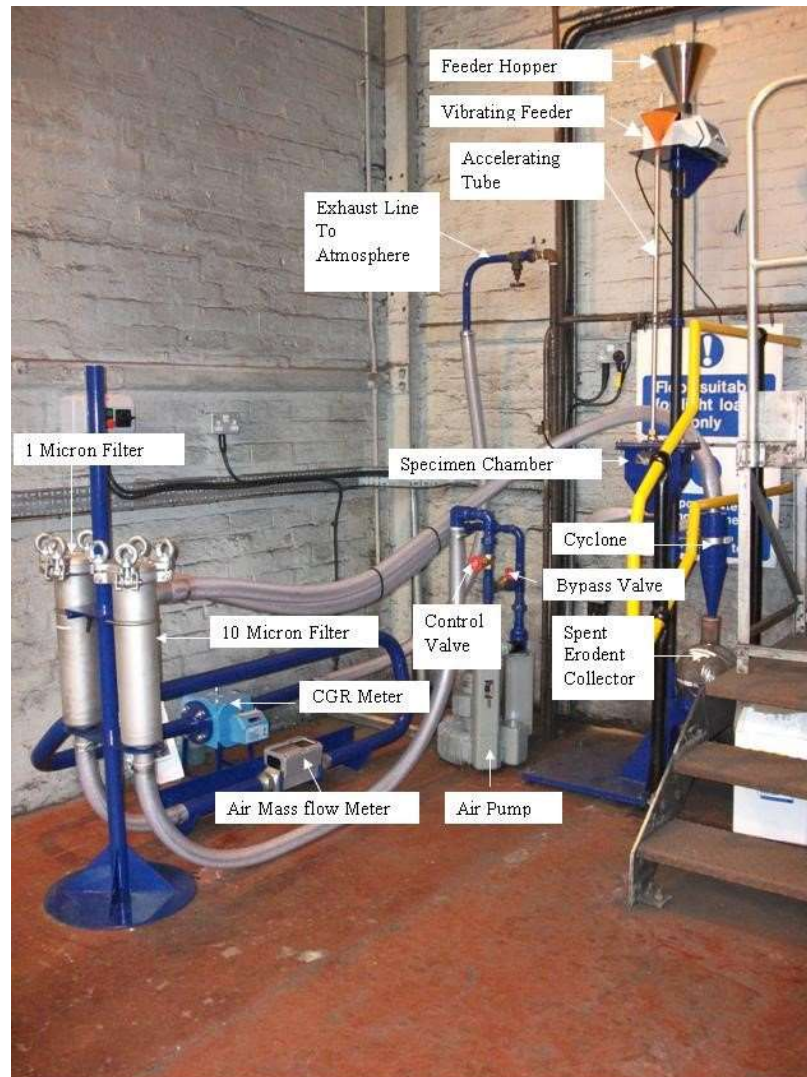


Figure 3-15: Schematic of the erodent test rig apparatus

3.3 Mineral Liberation Analysis – Scanning Electron Microscopy

In conjunction with XRD mineral phase identification, a FEI mineral liberation analyser (MLA) – a Quanta 600 scanning electron microscope equipped with energy dispersive spectroscopy (SEM-EDS) and a computer-controlled stage was utilised to provide further quantitative information on the composition and associations of the mineral species and morphological changes during combustion. Using this MLA system, the distribution of alkali and alkaline earth metals in the aluminosilicate phases could be more accurately determined provided that a comprehensive mineral database could be developed.

3.3.1 Coal and Biomass Sample Preparation

Sample blocks for MLA-SEM were produced by mounting in carnauba wax for the coal, biomass and char samples, and epoxy resin for ashes. These mounting mediums provided sufficient contrast and brightness to distinguish between the carbonaceous matrix and mineral species. Carnauba wax blocks were prepared by melting the wax at 90-100°C in an oven, and adding approximately 1 gram of sample to a mounting pot. The mounting pot containing sample and a glass rod were pre-heated in the oven at 90-100°C before the melted wax was added up to the two-thirds mark. The oven was switched off to allow the carnauba wax to cool slowly and prevent thermal cracking. Epoxy resin blocks were prepared by adding Struers epofix resin, hardener and sample in the mounting pots in an 8:1:1 weight ratio respectively. The pots were placed into a vacuum oven to release bubbles in the mixture for curing overnight. For samples which contained biomass, a non-aqueous method was

devised using a solution of 10% volume glycerol / 90% industrial methylated spirit instead of using water during the grinding and polishing steps to reduce the dissociation of metal halide salts such as potassium chloride (KCl).



Figure 3-16: Epoxy resin, hardener, stirring pot and weighing apparatus

3.3.2 Fly Ash Sample Preparation

Sample preparation is the most important step for microscopic image analysis to produce repeatable and accurate results for mineralogical assessment. It was necessary to devise a dynamic epoxy curing method to take into account the varying fly ash particle size fractions in the riffled samples to minimise particle segregation; due to the differential settlement of particles based on mineral density during sample mounting. Additionally, to de-agglomerate the particles during sample preparation, rather than during the image processing step using the commercial MLA software.

The method involved the addition of a mixture of epoxy resin and hardener to the fly ash in a 12 ml glass vial with an 8:1:1 weight ratio of epoxy resin to hardener to fly ash respectively, which resulted in a curing time of approximately

3 hours. The epoxy resin, hardener and fly ash were mixed thoroughly in the glass vial with a metal rod in a figure of eight motion for 5 minutes until homogeneous and a sealed cap secured. The glass vial, containing the mixture, was then placed onto a rotating shaker whereby slow rotational, reciprocal and vibrational motions were applied for the duration of the curing process.

Figure 3-17 shows the rotating shaker settings and apparatus to disperse the fly ash particles during curing process respectively. Table 3-7 shows the curing settings used for the samples.

Table 3-7: Dynamic epoxy curing settings

Motion type	Turning angle (°)	Speed (rpm)	Time (min)
Rotational	360	5	20
Reciprocal	1	-	20
Vibrational	5	-	5



Figure 3-17: Grant PTR-35 rotator apparatus

Afterwards, vertical cross sections of the glass vials were cut using a diamond saw and re-mounted using epoxy resin and hardener in 30 mm diameter moulds. A standard grinding and polishing procedures detailed in section 3.3.3 was used on the sample mounts to provide a smooth and void-free surface for MLA.

3.3.3 Grinding, Polishing and Coating

For grinding and polishing the surface of the sample blocks a Struers Pedemat Rotopol polisher was used to remove scratches and voids. Firstly, the surface of the block was ground to expose the particles using silicon carbide paper at 600 and 1200 grit sizes under a 30N force at 300 rpm disc speed for one minute respectively. Then, polishing was undertaken using 9, 3 and 1 μm plates using their respective diamond suspensions (or only 10% volume glycerol / 90% industrial methylated spirit for coal and biomass samples) under a 30N force at

300 rpm disc speed for one minute respectively. A maximum of 6 blocks could be polished at once.



Figure 3-18: Struers rotapol-1 grinder and polisher

3.3.4 MLA Setup and Operating Parameters

The MLA setup and operating parameters are crucial to ensure the samples are analysed in a repeatable and reproducible manner. As such, the operating parameters were kept constant for all the coal, biomass and char sample mounts, with an accelerating voltage of 15 kV, magnification of 300x and electron beam spot size of 7. For ash samples, identical conditions were used except a magnification of 1000x to account for the smaller particles. For each sample mount, at least 20,000 particles were analysed for statistically representative data collection, according to BS ISO 13322-1:2014[225].

The following procedure was followed to setup the SEM with sample mounts for each MLA run:

SEM setup

1) Introducing sample mounts to SEM and exchange

- The beam was turned off and the chamber vented.
- The sample block holder removed, new sample mounts added to the holder and sprayed with a compressed air can to remove dust particles on the surface of the samples.
- The sample holder was placed back into the SEM and pumped down until a suitable vacuum level was reached and the SEM icon turns green.
- The high voltage beam was set to the appropriate kV for the sample run (i.e. 15, 20 or 25).

- Once the beam has been turned on, drive to the Faraday Cup and allow the beam to stabilise for approximately half an hour or more.

2) *Setting up the SEM*

- Once the beam has stabilised, drive to position 7 on the MLA sample holder (centre block in the holder).
- Focus the SEM on the block.
- Link the z-axis and type in the working distance (13mm) and press Enter. Lock the z-axis to ensure the detector does not move during MLA runs. This sets the working distance for the holder (varies between MLAs and depends on the detector set-up).

3) *Check and optimise the beam*

- Drive to the quartz or copper standard on the SEM.
- Turn on videoscope and line scan and change the gun tilt to optimise the beam. The videoscope line will move up and down depending on changes to the beam tilt. This sets the lowest and highest greyscale levels for the run.
- Check the crossover, which is usually left of centre of the spot. Note that if the kV changes or the filament is replaced this needs to be re-checked.

4) *Checking the specimen current*

- Drive the stage to the Faraday Cup on the SEM and magnify 100,000x with a full frame and no spot.
- Confirm the specimen current on the Keithley Sourcemeeter (press the ZCHK button to show the nA reading). For quartz running at 15 kV normally runs at ~10 nA. To increase or decrease the specimen current, change the spot size.
- There are trade-offs between the specimen current, spot size and counts. A higher specimen current may require a larger spot size and subsequent reduction in beam resolution, but will achieve a higher number of counts per second (kcps). A lower specimen current will need a smaller spot size, and will give slower counts, but will have a higher beam resolution (suitable for fine-grained coal minerals and fly ashes).

5) *Energy calibration*

- Open the Esprit software.
- Drive to the quartz standard using the SEM controls.
- Magnify to 100,000x and turn the spot on.
- In the Esprit software, go to system and spectrometer.
- Choose the medium calibration and first detector, collect spectra and save.
- Choose second detector, collect spectra and save.
- Return to the spectra and select both detectors.

- Collect a quartz spectrum on a specimen to check the counts per second (kcps) and deadtime (%) are correct. There should be approximately 100-150 kcps and a 30% deadtime. If not then change the spot size and press acquire to adjust.

The SEM is now ready to setup the MLA measurement run.

- **MLA measurement project setup**

- Start new project
 - Name the project
 - Right-click on project and add sample names to the project using the + button to add new samples.
 - Add measurement types to the samples (e.g. XBSE, GXMAP, XMOD, SPL_Lt etc). GXMAP settings provide the highest accuracy and data collection.

- **Set measurement parameters – basic setup**

- Finish measurements
 - To scan the entire surface of the sample specimen, add a few 0s to the default values on the number of frames, particles and minutes boxes.
 - Otherwise, the user can set limits on the number of frames, particles or time.
- Image
 - Scan speed is normally set to 16.
 - Start at frame 0.
 - Frame resolution GXMAP 1000.
- Feature
 - Minimum particle size 1.
 - Maximum particle size 10.
 - Adjust the auto background removal to identify only the particles and not the mounting medium.

- Separation
 - Turn on/off using the checkbox.
 - Turn on/off the automatic de-agglomeration of images.
 - Under the drop down menu and select image calibration to collect a BSE image to view the BSE grey levels across a frame.
- **X-ray collection**
 - Acquisition time
 - This is the time taken for collecting each x-ray spectra during a run.
 - This is dependent on the number of counts required for each spectra. The more counts the higher the accuracy, however the less counts the faster the run.
 - Use the acquisition time calculator in the drop-down menu. Put a spot on a dark phase (i.e. quartz).
 - In Esprit software, collect a spectra and whilst it is collecting record the counts per second (kcps) and deadtime (DT) reading for each detector.
 - Go back to the acquisition time calculator. Add kcps for both detectors and enter into calculator the cps (kcps x 1000)
 - Average the DT% for both detectors and enter this value – this should be <30% for Bruker detectors.
 - Enter the number of counts required for each spectra. A minimum of 2000 on quartz will give more counts on brighter phases. Need to balance accuracy with speed.
 - This will give an acquisition time value to enter into the x-ray collection parameters.

- **Mineral search (SPL)**
 - BSE search range.
 - Enter the range of BSE values to trigger x-ray collection.
 - A second BSE search range can also be set.
 - Frame guide size determines the area around the bright phase to be included in the frame.
 - Minimum grain size is the smallest grain size that will trigger x-ray collection.

- **High voltage kV selection**
 - When to select 15kV, 20kV or 25kV for an MLA run.
 - The voltage of the beam is important as it needs to be high enough to excite L-lines in minerals that may be in the sample if required.

- **XBSE_Std measurements**
 - This measurement mode can be used to create new entries in the mineral list for x-ray spectra that do not fit within any of the current entries in the list (i.e. unknown spectra are listed as new entries).

- **GXMAP measurements**
 - This measurement mode can be used to select BSE grey level range triggers or specific x-ray spectrum triggers to identify grains or phases for detailed x-ray mapping.
 - GXMAP provides a full range of results in the dataview software for extraction and analysis.

- **Measurement magnification settings**
 - XBSE_Std and GXMAP measurements ~300x minimum (any less may result in shadows on the image from the detectors).

- As a rule of thumb, the largest particle should take up about 10% of the frame for the coal/fly ash.
- **Create sample block holder**
 - Create a new sample block holder and select the appropriate holder type.
 - Samples are automatically put into the holder – remove if necessary.
 - Click and drag samples to desired locations in the sample block holder.
 - Save holder with a recognisable name and date.
- **Online setup**
 - Select measurements you want to run by checking the box.
 - Set BSE level for the run.
 - Drive to a sample block and find a large/clean grain of the dominant bright phase/quartz or copper containing mineral depending on the standard used.
 - Put a spot in the middle of this grain.
 - This grain becomes the standard for monitoring the BSE level throughout the run. The SEM will drive back to this grain and take a BSE reading which is recorded in the log file to allow you to track changes to the beam variation in the BSE over the course of the run.
 - In drop down menu next to sample – select standard (STD).
 - Turn on videoscope/line scan on SEM. Change the brightness and contrast to get the correct BSE grey level. BSE grey level is 0-255.
 - Brightness moves the bottom line and contrast moves the top line. The aim is to align the bottom line of the videoscope along the bottom of the frame, and the top line about 2/3 of the way up.

- Zoom to 100,000x magnification and get SEM data. Check the grey level value and if required, adjust the brightness and contrast until the desired grey level is achieved.
 - Select the Faraday Cup in the sample drop down menu.
 - Drive to the Faraday Cup on the SEM.
 - Record the position.
 - Go to 100,000x magnification.
 - Get SEM data.
 - Save the block holder to save these changes.
 - Set the conditions for each sample.
 - Click on each measurement in turn and go to the sample block.
 - Focus on the sample block at 1000x magnification and do not link because the z-axis should be locked.
 - Go to the measurement magnification.
 - Get SEM data.
 - This must be done for each measurement on each sample. Note that re-focusing is not required for multiple measurements on the same sample.
 - Once complete – go through each sample and check the total frames and magnification for each measurement.
- **Check parameters**
 - Click the check parameters icon and if there are no warnings – click start.
 - Watch for a few frames to ensure the measurement is collecting the mineral data correctly.
 - Check measurement log file (C: drive – FEI folder)



Figure 3-19: FEI Quanta 600 Mineral Liberation Analyser (MLA)

Chapter 4: Automated Mineralogy and Erosion Rate Experimental Results of UK Power Station Fly Ashes from Different PF Combustions

4.1 General Introduction

This chapter presents the mineralogies from different pulverised combustions and the experimental results of an erosion test programme on three UK power station fly ashes obtained from the convective sections of pulverised coal-fired boilers after shutdown. The objective of this chapter is to compare the fly ashes measured erosion rates and assess the influence of the mineral matter and particle size distribution on the erosion potential using computer-controlled scanning electron microscopy, otherwise known as mineral liberation analysis (MLA). This chapter extends the body of research conducted at the sponsor company as outlined in the following publication[173].

A unique mineral categories database has been developed using specific elemental composition criteria in order to define the pure minerals and alkali/alkaline earth metal aluminosilicate phases present within the fly ashes. This required the collection of x-ray spectra and pure mineral reference materials to generate the mineral library. A comparison of the major elements determined by MLA and traditional chemical analysis was undertaken and appreciation of the errors and statistical variation were considered to verify and validate the mineral database.

This mineral database enabled the chemical characterisation of electron micrographs and coloured mosaics of the four fly ash samples to visually show

the variations in mineral species within the complex ash structures formed during the combustion process.

The investigation involved thermogravimetric analysis (TGA) to conduct loss-on-ignition (LOI) tests to estimate the combustible or unburned carbon contents of the supplied fly ashes. Additionally, traditional chemical analysis was performed such as x-ray fluorescence (XRF) and x-ray diffraction (XRD) to inform on the mineral species and metal oxides present within the samples. The MLA mineral composition data showed good agreement with XRD and XRF analysis.

Mineral grain size distributions of the quartz and hematite for the fly ashes showed that the quartz particle size is a dominant factor in the erosion rate of ashes, and may be more significant than the overall quartz composition present within the sample. A quantitative assessment of the angularity was conducted, which was deemed to have a negligible effect on the erosion rate.

Furthermore, this chapter provided a baseline mineral species database that can be used for the other chapters investigating coal and biomass co-firing combustion.

4.2 Development of a Mineral Database

Mineral identification and quantification through automated MLA/SEM-EDX analysis requires the generation of a mineral reference library of standards. For the power station fly ashes presented, this library required the collection of high-quality x-ray spectra for mineral reference standards and minerals from the samples. For accurate and repeatable results, the x-ray spectra were collected under identical measurement conditions used during the automated runs, such as electron beam energy (15 kV), spot size (7) and magnification (1000x).

During the automated run the measured x-ray spectra for each individual particle in the sample was compared to the mineral spectra in the standard reference library. A user-defined pattern matching probability based on a modified chi-squared probability density function provides an indication of the difference between the measured x-ray spectra and the mineral reference spectra[226]. For example, a pattern matching probability of 95% means provided the measured spectra is at least 95% similar to the mineral reference spectra the measured particle area will be assigned to this mineral. A measured spectrum that is not at least within the 95% matching probability will be assigned to the unknown category, and the user will have to individually collect the spectra for this particle area after the run to assign to a new mineral.

$$\text{Chi Squared test } (X^2) = \sum \frac{(\sigma_i - e_i)^2}{E_i}$$

Whereby σ_i is the observed frequency and E_i is the expected frequency.

Table 4-1 shows the respective probability values corresponding to the percentage values displayed for each EDX spectra collected.

Table 4-1: Pattern match probability values to assess reliability and classification results

Percentage Value (%)	Probability value
100	1
94	2.51E-10
88	6.31E-20
81	3.98E-30
75	1.00E-40
69	2.51E-50
63	6.31E-60
56	3.98E-70
50	1.00E-80
44	2.51E-90
38	6.31E-100
32	1.58E-110
25	1.00E-120
19	2.51E-130
13	6.31E-140
6	3.98E-150
1	4.13E-160

A collection of standard mineral samples was required to collect x-ray spectra from pure minerals for the mineral reference library. This involved purchasing select minerals associated with coal combustion from the Clay Minerals Society[227] and Sigma Aldrich. These minerals have been displayed in Table 4-2.

Table 4-2: Standard Reference Minerals

Mineral name	Supplier
Illite-smectite	Clay Minerals Society
Illite	Clay Minerals Society
Montmorillonite	Clay Minerals Society
Kaolinite	Clay Minerals Society
Mullite	Sigma Aldrich

In conjunction with pure mineral standards, x-ray spectra derived from individual samples were required to generate a comprehensive mineral reference library. The development of the mineral reference list was an iterative process, continually increasing as more samples were analysed in order to reduce the percentage area of unknown particle spectra. As such, an arbitrary unknown area percentage of 10% was selected for each sample. Table 4-3 and Table 4-4 show the mineral database and elemental compositions of the standard minerals and the EDX spectra collected using this iterative process.

The selection of operating parameters during the sample setup on the MLA software are important to yield representative results and account for associated errors during measurement. A high number of x-ray counts was required to effectively differentiate between the grey levels of the various aluminosilicate phases, at least 100,000 counts per second. Additionally, at least 20,000 particles were analysed to provide mineral composition data within the 95% confidence interval. The Grain X-ray Mapping (GXMAP) measurement mode was selected on the MLA measurement software due to the complexity of the ash composition with regards to the alkali and alkaline aluminosilicate phases.

Table 4-3: Elemental compositions of MLA minerals

Group	Mineral	Density (kg m ⁻³)	Molecular Weight Z	Elemental Compositions (weight %)																			Empirical Formula
				C	H	O	Si	Al	Fe	Ca	Mg	Ti	Na	K	S	Mn	P	Cl	Ba	Zn	F	Cr	
Oxides	Quartz	2.63	10.80	-	-	53.26	46.74	-	-	-	-	-	-	-	-	-	-	-	-	-	-	-	SiO ₂
	Hematite	5.30	20.59	-	-	30.05	-	-	69.95	-	-	-	-	-	-	-	-	-	-	-	-	-	Fe ₂ O ₃
	Rutile	4.25	16.39	-	-	40.05	-	-	59.95	-	-	-	-	-	-	-	-	-	-	-	-	-	TiO ₂
Carbonates	Calcite	2.71	12.57	12.00	-	47.95	-	-	-	40.04	-	-	-	-	-	-	-	-	-	-	-	-	CaCO ₃
	Dolomite	2.85	10.87	13.02	-	52.06	-	-	-	21.73	13.18	-	-	-	-	-	-	-	-	-	-	-	CaMg(CO ₃) ₂
	Ankerite	3.05	13.61	11.63	-	46.52	-	-	16.23	19.52	3.53	-	-	-	-	2.66	-	-	-	-	-	-	CaFe _{0.6} Mg _{0.3} Mn _{0.1} (CO ₃) ₂
	Fairchildite	1.17	14.25	-	-	44.22	0.18	-	-	24.93	0.90	-	0.34	27.99	0.44	-	0.24	0.76	-	-	-	-	K ₂ Ca(CO ₃) ₂
Halides	Sylvite	1.16	17.79	-	-	3.19	0.04	0.06	-	-	-	-	-	54.22	-	-	-	42.49	-	-	-	-	KCl
Clays	Kaolinite (Al-silicate)	2.60	10.24	-	156	55.78	21.75	20.90	-	-	-	-	-	-	-	-	-	-	-	-	-	-	Al ₂ Si ₂ O ₅ (OH) ₄
	Montmorillonite (Na/Ca/Mg Al-silicate)	2.35	10.08	-	2.29	58.23	25.55	9.21	-	0.91	2.76	-	1.05	-	-	-	-	-	-	-	-	-	Na _{0.2} Ca _{0.1} Al _{1.5} Mg _{0.5} Si ₄ O ₁₀ (OH) ₂ ·4H ₂ O
	Illite (Mixed Al-silicate)	2.75	10.87	-	1.34	55.08	25.25	9.00	1.43	-	1.87	-	-	6.02	-	-	-	-	-	-	-	-	K _{0.6} (H ₃ O) _{0.4} Al _{1.3} Mg _{0.3} Fe _{0.1} Si _{3.5} O ₁₀ (OH) ₂ ·(H ₂ O)
Micas	Muscovite (K Al-silicate)	2.83	11.34	-	0.45	47.36	21.13	20.30	-	-	-	-	-	9.80	-	-	-	-	-	-	0.95	-	KAl ₃ Si ₃ O ₁₀ (OH) _{1.9} F _{0.1}
	Biotite (Mg/K/Fe Al-silicate)	3.10	12.17	-	0.40	43.38	19.44	6.22	6.44	-	14.02	-	-	9.01	-	-	-	-	-	-	1.09	-	KMg _{2.5} Fe _{0.5} AlSi ₃ O ₁₀ (OH) _{1.75} F _{0.25}
Garnets	Almandine (Fe Al-silicate)	4.20	15.62	-	-	38.58	16.32	10.84	33.66	-	-	-	-	-	-	-	-	-	-	-	-	-	Fe ₃ Al ₂ Si ₃ O ₁₂
	Pyrope (Mg Al-silicate)	3.75	10.65	-	-	47.63	20.90	13.38	-	-	18.08	-	-	-	-	-	-	-	-	-	-	-	Mg ₃ Al ₂ Si ₃ O ₁₂
	(Fe/Ca Al-silicate)	2.92	14.95	-	-	38.47	13.32	9.12	20.87	15.06	3.16	-	-	-	-	-	-	-	-	-	-	-	Fe ₂ MgCa ₂ Al ₂ Si ₃ O ₁₅
	Grossular (Ca Al-silicate)	1.71	13.10	-	-	40.71	18.03	13.73	-	26.33	-	1.20	-	-	-	-	-	-	-	-	-	-	Ca ₃ Al ₃ Si ₃ O ₁₂
Feldspars	Plagioclase (Ca/Na Al-silicate)	2.69	11.38	-	-	47.28	31.12	9.96	-	7.40	-	-	4.24	-	-	-	-	-	-	-	-	-	Na _{0.5} Ca _{0.5} Si ₃ AlO ₈
	Orthoclase (K Al-silicate)	2.75	11.85	-	-	45.99	30.28	9.69	-	-	-	-	14.04	-	-	-	-	-	-	-	-	-	KAlSi ₃ O ₈
	Sanidine (K/Na Al-silicate)	2.58	11.30	-	-	48.18	31.71	10.16	-	-	-	-	2.60	7.36	-	-	-	-	-	-	-	-	(K,Na)AlSi ₃ O ₈
	Albite (Na Al-silicate)	2.62	10.77	-	-	48.66	31.50	10.77	-	0.76	-	-	8.30	-	-	-	-	-	-	-	-	-	NaAlSi ₃ O ₈
Phosphates	Apatite	3.19	14.22	-	0.06	38.76	-	-	-	39.37	-	-	-	-	-	-	18.25	2.32	-	-	1.24	-	Ca ₅ (PO ₄)(F,Cl,OH)

Table 4-4: Elemental compositions of MLA minerals (continued)

Sulphides	Pyrite	5.01	20.65	-	-	-	-	-	46.54	-	-	-	-	53.46	-	-	-	-	-	-	-	FeS ₂
	Pyrrhotite	4.62	22.23	-	-	-	-	-	62.33	-	-	-	-	37.67	-	-	-	-	-	-	-	Fe(1-x)S
	Sphalerite	4.00	25.39	-	-	-	-	-	-	-	-	-	-	32.91	-	-	-	-	67.09	-	-	ZnS
Sulphates	Barite	4.48	37.34	-	-	27.42	-	-	-	-	-	-	-	13.73	-	-	-	58.85	-	-	-	BaSO ₄
	Anhydrite	2.97	13.42	-	-	47.01	-	-	-	29.44	-	-	-	23.55	-	-	-	-	-	-	-	CaSO ₄
	Gypsum	2.30	12.12	-	2.34	55.76	-	-	-	23.27	-	-	-	18.62	-	-	-	-	-	-	-	CaSO ₄ ·2H ₂ O
	Polhalite	1.75	14.08	-	-	39.04	5.20	2.15	5.92	11.52	8.33	-	-	20.96	5.47	-	0.96	-	-	-	0.45	K ₂ Ca ₂ Mg(SO ₄) ₆ ·2H ₂ O
Mixed sulphates	Ca sulphate	1.50	14.06	-	-	41.43	0.64	-	-	34.72	-	-	-	23.21	-	-	-	-	-	-	-	N/A
	Ca/Mg sulphate	1.68	13.51	-	-	41.90	0.59	0.36	3.26	27.75	13.59	-	-	11.87	-	0.68	-	-	-	-	-	N/A
Mixed oxides	K oxide	1.05	15.40	-	-	32.81	0.35	-	1.25	-	-	-	0.41	64.58	-	-	0.60	-	-	-	-	N/A
	Fe/K oxide	5.11	19.56	-	-	31.82	0.19	0.15	59.07	1.27	0.48	-	0.25	6.52	0.15	-	-	-	-	-	-	N/A
	K/P/Mg/Ca oxide	1.19	14.78	-	-	28.20	1.34	-	-	4.84	9.09	-	-	43.95	1.81	-	9.72	1.05	-	-	-	N/A
	Ca oxide	1.39	14.67	-	-	43.14	0.31	-	-	53.28	-	-	-	3.27	-	-	-	-	-	-	-	N/A
	Ca/K/Si/P oxide	1.31	13.57	-	-	46.46	0.46	0.17	0.20	23.63	1.85	-	0.26	15.80	6.15	-	5.02	-	-	-	-	N/A
	Cr oxide	5.23	19.16	-	-	34.03	0.14	0.45	2.29	-	-	3.37	-	-	-	-	-	-	-	-	59.72	N/A
	Al oxide	2.11	11.19	-	-	38.80	-	59.30	-	-	-	1.33	-	-	-	0.57	-	-	-	-	-	N/A
	Mg/Ca/K/Fe oxide	1.58	13.28	-	-	41.35	1.82	0.39	7.07	14.02	21.98	-	0.80	10.29	0.10	-	2.10	0.08	-	-	-	N/A
Mixed aluminosilicates	Fe/Ca Al-silicate	2.92	14.95	-	-	38.47	13.32	9.12	20.87	15.06	3.16	-	-	-	-	-	-	-	-	-	-	N/A
	Ca Al-silicate	1.71	13.10	-	-	40.71	18.03	13.73	-	26.33	-	1.20	-	-	-	-	-	-	-	-	-	N/A
	Ca/Mg/Na Al-silicate	1.65	13.78	-	-	34.79	13.38	12.59	0.22	33.81	1.84	-	2.19	0.76	-	-	0.42	-	-	-	-	N/A
	Ca/Mg Al-silicate	1.74	12.19	-	-	40.59	20.69	13.64	0.31	15.11	9.50	-	-	-	0.16	-	-	-	-	-	-	N/A
	Ca/P Al-silicate	1.53	13.83	-	-	40.39	4.90	6.44	0.14	36.38	-	-	-	-	-	11.75	-	-	-	-	-	N/A
	Ca/K/Mg/Fe Al-silicate	1.69	12.03	-	-	47.91	21.53	5.45	2.25	7.91	5.29	-	0.59	6.13	-	-	2.94	-	-	-	-	N/A
	Ca/K/P/Mg Al-silicate	1.46	13.30	-	-	43.59	5.90	1.59	1.31	19.91	4.56	-	1.09	12.05	-	-	10.00	-	-	-	-	N/A
	Ca/Na Al-silicate	1.58	11.96	-	-	46.56	23.67	1.83	1.13	10.22	2.65	0.21	6.40	4.33	-	-	3.00	-	-	-	-	N/A
	Ca/Na/K Al-silicate	1.74	11.61	-	-	43.37	30.88	14.38	-	6.13	-	-	3.31	1.70	-	-	0.23	-	-	-	-	N/A
	Ca/P/Mg Al-silicate	1.82	14.93	-	-	20.62	25.97	1.92	1.60	34.02	7.58	-	-	0.41	-	-	7.84	0.04	-	-	-	N/A
	K/Na Al-silicate	1.60	11.26	-	-	51.16	27.81	10.14	-	-	-	-	1.36	9.53	-	-	-	-	-	-	-	N/A
	K/Fe/Ca/Na Al-silicate	2.01	13.55	-	-	35.07	20.21	11.10	7.13	5.67	0.58	-	4.97	14.29	-	-	0.74	0.24	-	-	-	N/A

4.3 Erosion Rig Experimental Results of Power Station Fly Ashes and Mineralogical Analysis

As previously described in section 3.2.12, an erosion test rig was used to assess the relative erosion rates of the power station fly ashes generated under different combustion conditions. The purpose of the rig was to simulate the particle impact velocities experienced within the internal convective section of industrial boilers. Through firing the fly ash particles at high velocities towards steel target specimens using this test rig, combined with detailed chemical and physical characterisation, trends can be determined to facilitate improvements to erosion models.

Table 4-5 shows the raw erosion data collected during the erosion test runs at the sponsor company, with Figure 4-1 showing the corresponding erosion rate graph of the power station fly ashes. The results of the erosion tests with the Drax, Longannet and Ratcliffe fly ash samples were carried out at a standard impact angle of 45° using a steel target specimen at air velocities at the end of the accelerating tube between 10-60 m s⁻¹. These conditions were previously used by Wells[173]. All the results show that the erosion rate increases with increasing air velocity, and that for the Longannet and Ratcliffe fly ashes the data showed reasonable fits to power law trends with r^2 values of 0.97 and 0.99 and exponent values of 2.2 and 2.5 respectively. For the Drax fly ash, more experimental measurements are required at the lower air velocities. The Trimble County fly ash could not be tested due to insufficient sample quantity available.

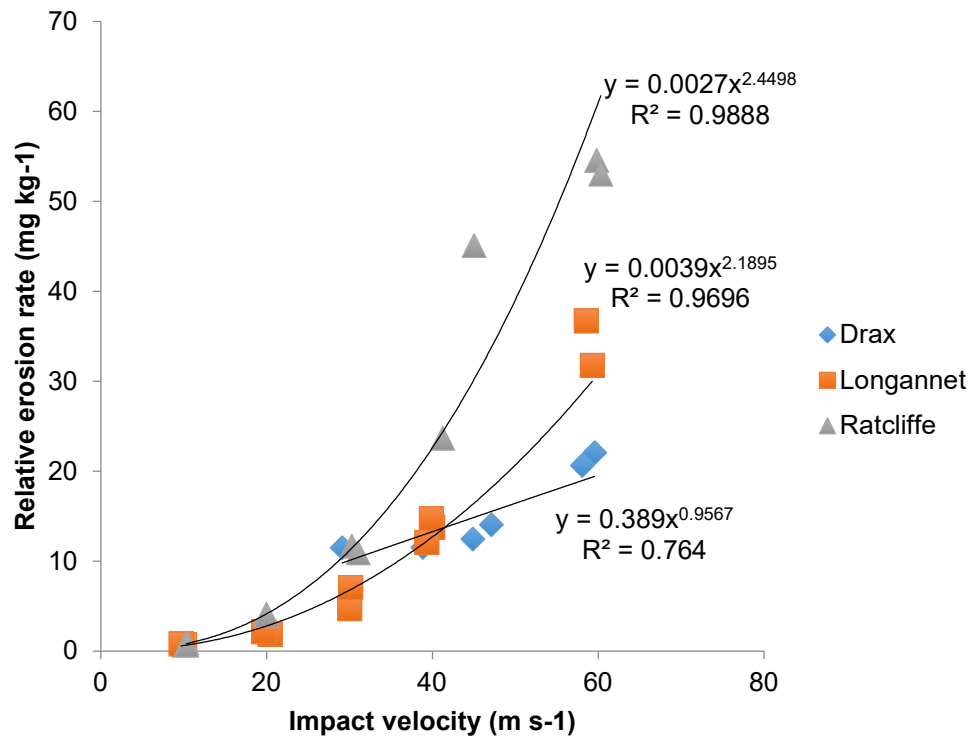


Figure 4-1: Relative erosion rate as a function of the particle impact velocity
for the power station fly ashes

The measured erosion rates for the three fly ashes at an impact angle of 45° and air velocity of 40 m s⁻¹ are as follows:

Drax	11.5 mg kg ⁻¹
Longannet	13.7 mg kg ⁻¹
Ratcliffe	22.9 mg kg ⁻¹

The significantly higher erosion rate for the Ratcliffe fly ash can be attributed to the higher average particle size compared to the other fly ashes.

Table 4-5: Erosion test results for power station fly ashes

Erodent	Angle	Velocity (m s⁻¹)	Ash weight (g)	Weight loss (mg)	Erosion rate (mg kg⁻¹)
Drax fly ash	45	47.08	1669	23.5	14.08
		44.82	1557	19.4	12.46
		59.53	1594	35.2	22.08
		58.06	1593	32.9	20.65
		29.09	1052	12.1	11.5
		38.82	2001	23.1	11.55
Longannet fly ash	45	40	2000	27.6	13.8
		39.86	2000	29.3	14.7
		58.54	2000	73.5	36.7
		30	2000	9.4	4.7
		59.26	2000	63.5	31.75
		30.11	2000	14.1	7.05
		39.32	2003	24.2	12.08
		20.39	1957	3.7	1.89
		19.65	2002	4.3	2.15
		10.1	2000	1.4	0.7
		9.68	2000	1.6	0.8
Ratcliffe fly ash	45	39.64	2000	45.1	22.5
		59.78	2000	109.2	54.6
		60.3	2001	106.1	53.04
		41.2	2001	47.4	23.69
		30.23	2001	23.4	11.69
		31.01	2000	21.9	10.95
		19.92	2000	8.2	4.1
		20.01	2001	7.9	3.95
		10.32	2001	1.9	0.95
		10.32	1999	1.4	0.7

Table 4-6: Fly ash particle size analysis data by dry sieving

Sample % < mm	Fly ash Drax (14/0028)	Fly ash Trimble (14/0027)	Fly ash Longannet (14/0029)	Fly ash Ratcliffe (14/0198)
0.300	99.19	99.95	99.91	89.2
0.150	96.02	99.54	98.93	80.5
0.106	91.23	98.17	96.63	69.1
0.075	84.07	94.25	91.99	54.9

Table 4-7: Fly ash particle size distribution by laser light scattering (Malvern)

Sample % < mm	Fly ash Drax (14/0028)	Fly ash Trimble (14/0027)	Fly ash Longannet (14/0029)	Fly ash Ratcliffe (14/0198)
1.26	100	100	100	95.26
0.724	100	100	100	82.34
0.550	99.99	99.98	99.97	75.29
0.240	97.41	99.49	98.01	60.57
0.158	92.78	98.19	93.39	51.54
0.120	88.02	96.34	88.04	43.65
0.091	82.19	93.15	81.01	35.62
0.079	79.02	90.90	77.03	32.00
0.060	72.35	85.02	68.57	26.04
0.046	65.07	77.61	59.87	21.80
0.030	51.71	65.06	46.97	17.44
0.020	35.20	52.64	34.76	10.50
0.010	12.20	34.20	18.02	5.32
0.0050	4.57	18.41	7.75	2.90
0.0025	2.79	8.54	3.44	1.64
0.0011	1.62	3.96	1.60	0.63

The fly ash particle size analysis data by dry sieving and fly ash particle size distribution by laser light scattering shown in Table 4-6 and Table 4-7 show that

the Ratcliffe fly ash has 10.8% of retained particles greater than 300 μm and 4.7% of retained particles greater than 1.26 mm respectively. As previous studies have concluded, the erosion rate increases with particle size[228]. This is likely to be the main cause for the higher erosion rate, although the Ratcliffe fly ash has the highest percentage of hematite (Fe_2O_3) and lowest percentage of quartz (SiO_2) of the fly ashes, as shown in Table 4-8. Furthermore, the Ratcliffe fly ash has the highest base-to-acid ratio at 0.46 due to the very high concentration of hematite relative to the other fly ashes. This hematite is likely to derive from pyrite in the parent coal, which has similar hardness values to that of quartz expressing significantly higher Vickers hardness values than steel, as shown in Table 2-4.

Table 4-8: X-ray fluorescence data of power station fly ashes (conducted by Doosan Babcock)

Oxides	Trimble	Drax	Ratcliffe	Longannet
SiO ₂	51.10	53.17	47.12	54.24
Al ₂ O ₃	19.77	25.23	17.36	22.84
Fe ₂ O ₃	10.35	9.91	17.51	6.25
CaO	8.42	1.99	7.19	2.73
MgO	1.60	1.49	2.13	1.68
TiO ₂	0.93	0.90	0.74	1.01
Na ₂ O	0.93	0.83	0.67	0.57
K ₂ O	1.80	3.01	1.86	1.71
P ₂ O ₅	0.32	0.16	0.21	0.41
SO ₃	3.98	0.72	0.88	0.52
BaO	0.16	0.11	0.12	0.14
SrO	0.09	0.06	0.06	0.11
C	0.54	2.43	4.16	7.78
SiO ₂ : Al ₂ O ₃	2.59	2.11	2.71	2.37
SiO ₂ : Fe ₂ O ₃	4.94	5.36	2.69	8.68
SiO ₂ - 1.5 Al ₂ O ₃	21.00	15.40	21.30	19.90
B/A ratio	0.33	0.22	0.46	0.17

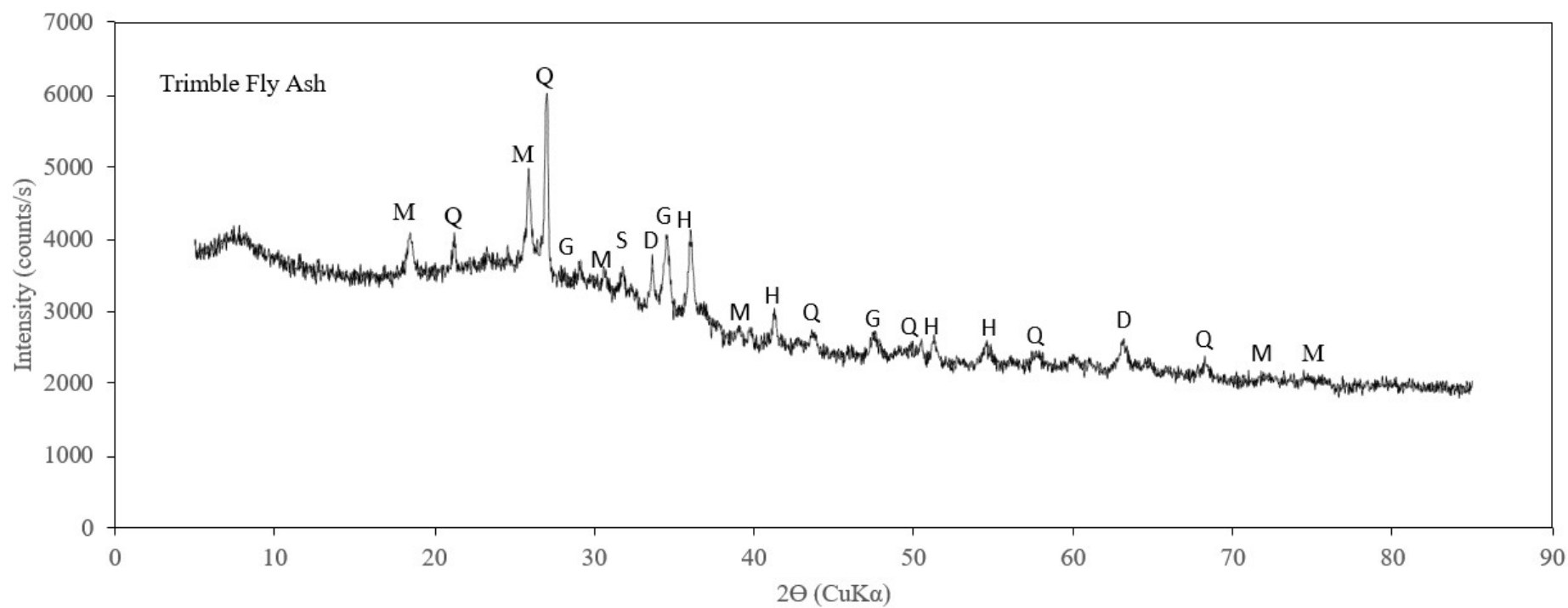


Figure 4-2: X-ray diffraction of Trimble County fly ash

Q: Quartz (SiO_2), M: Mullite ($3\text{Al}_2\text{O}_3\cdot 2\text{SiO}_2$), H: Hematite (Fe_2O_3) I: Illite ($(\text{K},\text{H}_3\text{O})(\text{Al},\text{Mg},\text{Fe})_2(\text{Si},\text{Al})_4\text{O}_{10}[(\text{OH})_2,(\text{H}_2\text{O})]$)

G: Gypsum ($\text{CaSO}_4\cdot 2\text{H}_2\text{O}$), S: Spinel (MgAl_2O_4), D: Dolomite ($\text{CaMg}(\text{CO}_3)$)

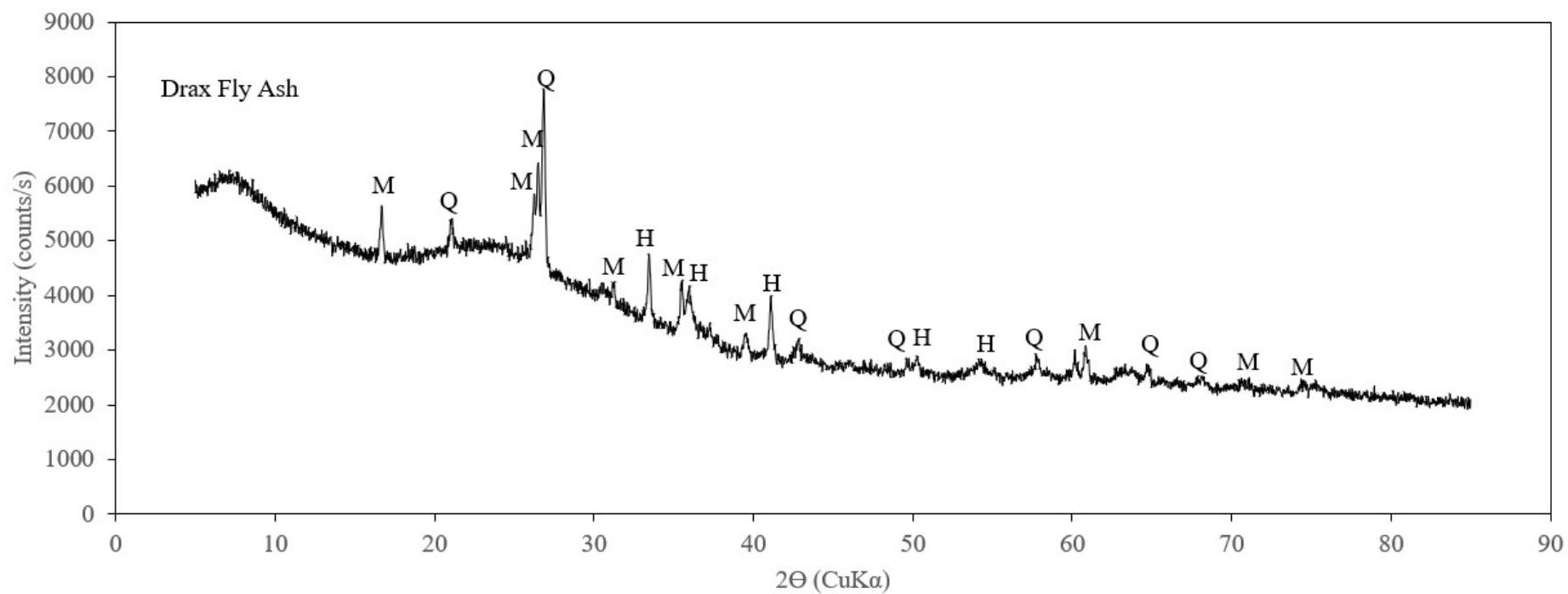


Figure 4-3: X-ray diffraction of Drax fly ash

Q: Quartz (SiO_2), M: Mullite ($3\text{Al}_2\text{O}_3 \cdot 2\text{SiO}_2$), H: Hematite (Fe_2O_3) I: Illite ($(\text{K}, \text{H}_3\text{O})(\text{Al}, \text{Mg}, \text{Fe})_2(\text{Si}, \text{Al})_4\text{O}_{10}[(\text{OH})_2, (\text{H}_2\text{O})]$)

G: Gypsum ($\text{CaSO}_4 \cdot 2\text{H}_2\text{O}$), S: Spinel (MgAl_2O_4), D: Dolomite ($\text{CaMg}(\text{CO}_3)_2$)

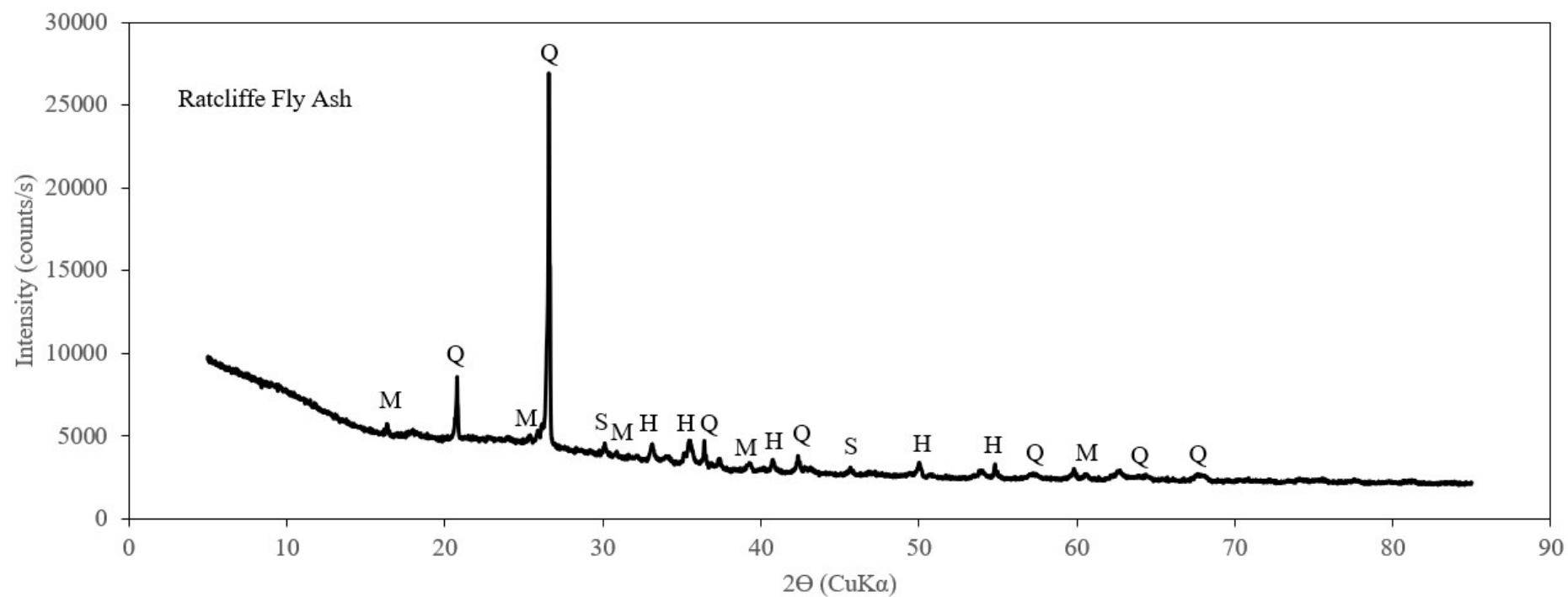


Figure 4-4: X-ray diffraction of Ratcliffe fly ash

Q: Quartz (SiO_2), M: Mullite ($3\text{Al}_2\text{O}_3 \cdot 2\text{SiO}_2$), H: Hematite (Fe_2O_3) I: Illite ($(\text{K}, \text{H}_3\text{O})(\text{Al}, \text{Mg}, \text{Fe})_2(\text{Si}, \text{Al})_4\text{O}_{10}[(\text{OH})_2, (\text{H}_2\text{O})]$)

G: Gypsum ($\text{CaSO}_4 \cdot 2\text{H}_2\text{O}$), S: Spinel (MgAl_2O_4), D: Dolomite ($\text{CaMg}(\text{CO}_3)$)

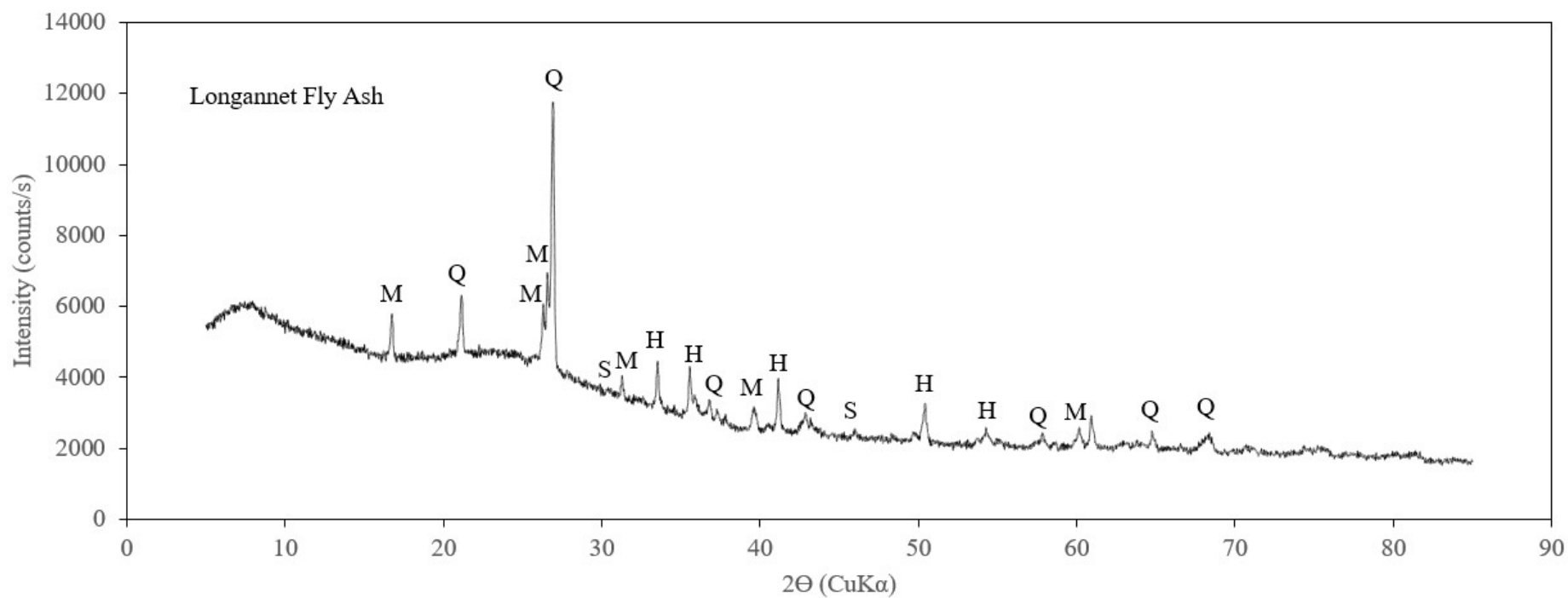


Figure 4-5: X-ray diffraction of Longannet fly ash

Q: Quartz (SiO_2), M: Mullite ($3\text{Al}_2\text{O}_3 \cdot 2\text{SiO}_2$), H: Hematite (Fe_2O_3) I: Illite ($(\text{K}, \text{H}_3\text{O})(\text{Al}, \text{Mg}, \text{Fe})_2(\text{Si}, \text{Al})_4\text{O}_{10}[(\text{OH})_2, (\text{H}_2\text{O})]$)

G: Gypsum ($\text{CaSO}_4 \cdot 2\text{H}_2\text{O}$), S: Spinel (MgAl_2O_4), D: Dolomite ($\text{CaMg}(\text{CO}_3)_2$)

4.3.1 MLA Mineral Compositions of the Power Station Fly Ashes

SEM-MLA was used to characterise the mineral compositions of the fly ashes. A representative bulk sample of each fly ash was taken using a rotary sample divider and rotary micro riffler to extract a sample for block preparation, grinding and polishing and SEM-MLA analysis. The dominant minerals present within all the fly ash samples were kaolinite, illite, quartz and hematite, with various smaller weight percentages of mixed aluminosilicates and mixed oxides. These mineral compositions were confirmed by XRD and XRF analysis. The XRF analysis has considerably higher amounts of pure quartz than the MLA mineral compositions because the majority of the silicon is present within the clay minerals such as kaolinite and illite.

The mineral composition data shows that quartz, kaolinite and illite which would have been present in the initial coals have not changed appreciably. Whereas the carbonates such as calcite, dolomite and ankerite have decomposed to form many different mixed aluminosilicate products such as Ca/Na/K Al-silicates, Fe/Ca Al-silicates and Ca/Mg/Na Al-silicates. The coloured mosaics suggest complex melting between quartz, kaolinite, illite and mixed aluminosilicates such as Fe/Ca Al-silicates (see Ratcliffe particle below with Figure 4-6).

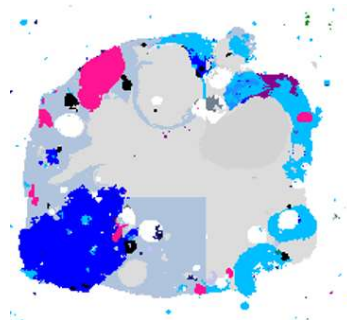


Table 4-9: Mineral compositions of power station fly ashes

Mineral Groups	Mineral Species	Trimble County	Drax	Ratcliffe	Longannet
Fixed/volatile carbon	C/H/O/S	0.08%	0.15%	0.19%	0.36%
Oxides	Quartz	12.80%	10.03%	12.83%	13.92%
	Hematite	6.49%	3.96%	4.86%	0.94%
	Rutile	0.01%	0.02%	0.02%	0.05%
Carbonates	Calcite	0.00%	0.00%	0.00%	0.00%
	Dolomite	0.01%	0.01%	0.02%	0.03%
	Ankerite	0.10%	0.61%	1.15%	0.20%
	Fairchildite	0.00%	0.00%	0.00%	0.00%
Halide	Sylvite	0.00%	0.00%	0.00%	0.00%
Clays	Kaolinite	4.15%	7.07%	6.38%	24.03%
	Montmorillonite	1.79%	1.47%	1.71%	4.89%
	Illite	42.95%	59.29%	50.75%	44.65%
Micas	Muscovite	0.54%	1.08%	0.63%	0.78%
	Biotite	0.01%	0.06%	0.01%	0.01%
Garnets	Almandine	7.05%	4.57%	6.07%	1.82%
	Pyrope	0.03%	0.03%	0.05%	0.10%
Feldspars	Plagioclase	0.00%	0.00%	0.00%	0.00%
	Sanidine	0.68%	0.54%	0.56%	0.63%
	Orthoclase	0.23%	0.23%	0.26%	0.15%
	Albite	0.07%	0.09%	0.05%	0.23%
Phosphates	Apatite	0.07%	0.02%	0.09%	0.07%
Sulphides	Pyrite	0.00%	0.00%	0.00%	0.00%
	Pyrrhotite	0.00%	0.02%	0.02%	0.01%
	Sphalerite	0.00%	0.00%	0.00%	0.00%
Sulphates	Barite	0.01%	0.00%	0.01%	0.00%
	Anhydrite	0.00%	0.00%	0.00%	0.00%
	Gypsum	0.01%	0.00%	0.00%	0.00%
	Polyhalite	0.00%	0.00%	0.00%	0.01%
	Ca sulphate	1.38%	0.07%	0.07%	0.02%

Mixed Sulphates	Ca/Mg sulphate	0.08%	0.06%	0.08%	0.11%
Mixed Oxides	K oxide	0.00%	0.00%	0.00%	0.00%
	Fe/K Oxide	2.11%	0.73%	1.92%	1.33%
	K/P/Mg/Ca oxide	0.00%	0.00%	0.00%	0.00%
	Ca oxide	4.79%	0.44%	0.78%	0.16%
	Ca/K/S/P oxide	0.01%	0.00%	0.00%	0.00%
	Cr oxide	0.00%	0.00%	0.00%	0.00%
	Al oxide	0.00%	0.00%	0.00%	0.00%
	Mg/Ca/K/Fe oxide	0.02%	0.02%	0.09%	0.08%
Mixed Aluminosilicates	Fe/Ca Al-silicate	3.49%	4.56%	5.91%	0.76%
	Ca Al-silicate	1.11%	0.49%	0.64%	0.26%
	Ca/Mg/Na Al-silicate	3.04%	0.33%	0.50%	0.23%
	Ca/Mg Al-silicate	1.05%	0.45%	0.91%	0.79%
	Ca/P Al-silicate	0.12%	0.07%	0.05%	0.13%
	Ca/K/Mg/Fe Al-silicate	0.06%	0.05%	0.07%	0.03%
	Ca/K/P/Mg Al-silicate	0.00%	0.00%	0.01%	0.02%
	Ca/Na Al-silicate	0.03%	0.01%	0.03%	0.01%
	Ca/Na/K Al-silicate	4.43%	2.54%	2.29%	2.68%
	Ca/P/Mg Al-silicate	0.16%	0.07%	0.11%	0.06%
	K/Na Al-silicate	0.89%	0.54%	0.56%	0.33%
	K/Fe/Ca/Na Al-silicate	0.15%	0.30%	0.29%	0.13%

4.3.2 MLA Coloured Image Analysis of Power Station Fly Ashes

 C/H/O/S	 Quartz	 Hematite
 Rutile	 Calcite	 Dolomite
 Ankerite	 Fairchildite	 Sylvite
 Kaolinite	 Montmorillonite	 Illite
 Muscovite	 Biotite	 Almandine
 Pyrope	 Plagioclase	 Sanidine
 Orthoclase	 Albite	 Apatite
 Pyrite	 Pyrrhotite	 Sphalerite
 Barite	 Anhydrite	 Gypsum
 Polyhalite	 Ca sulphate	 Ca/Mg sulphate
 K oxide	 Fe/K Oxide	 K/P/Mg/Ca oxide
 Ca oxide	 Ca/K/S/P oxide	 Cr oxide
 Al oxide	 Mg/Ca/K/Fe oxide	 Fe/Ca Al-silicate
 Ca Al-silicate	 Ca/Mg/Na Al-silicate	 Ca/Mg Al-silicate
 Ca/P Al-silicate	 Ca/K/Mg/Fe Al-silicate	 Ca/K/P/Mg Al-silicate
 Ca/Na Al-silicate	 Ca/Na/K Al-silicate	 Ca/P/Mg Al-silicate
 K/Na Al-silicate	 K/Fe/Ca/Na Al-silicate	

Figure 4-6: MLA mineral species legend

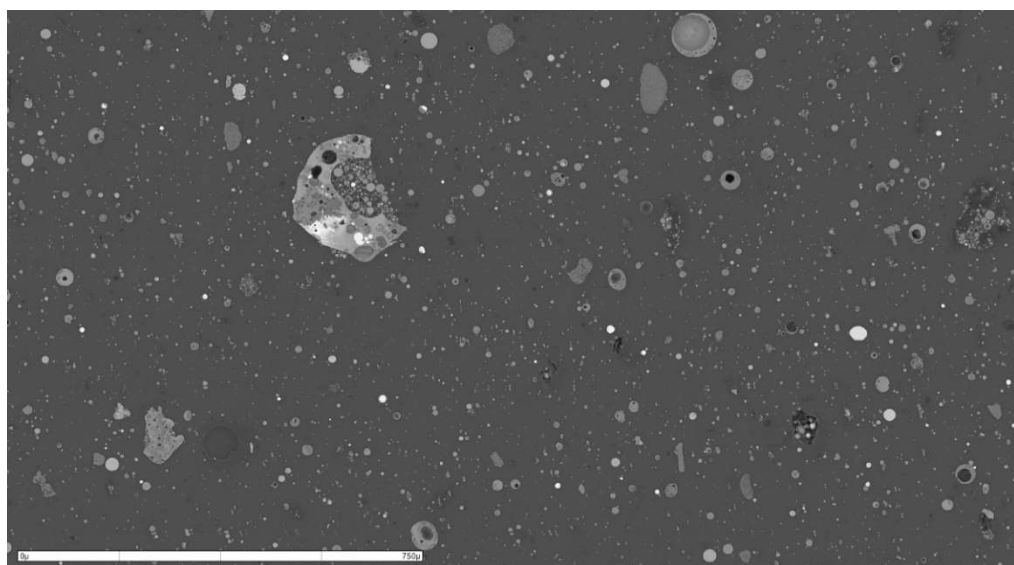


Figure 4-7: Electron micrograph of Trimble County fly ash (USA, Kentucky)

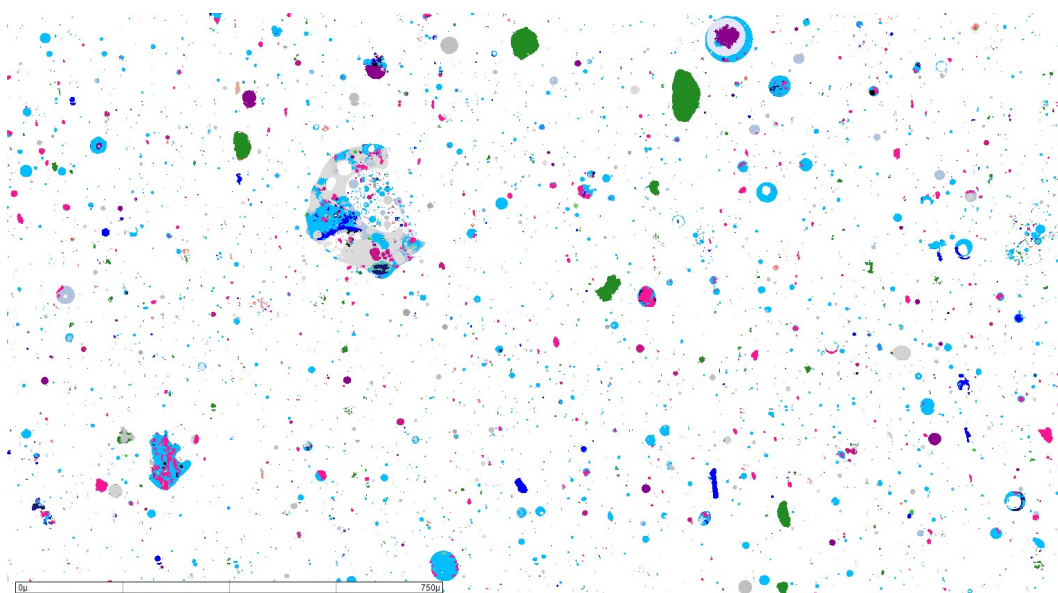


Figure 4-8: MLA coloured mosaic of Trimble County fly ash (USA, Kentucky)

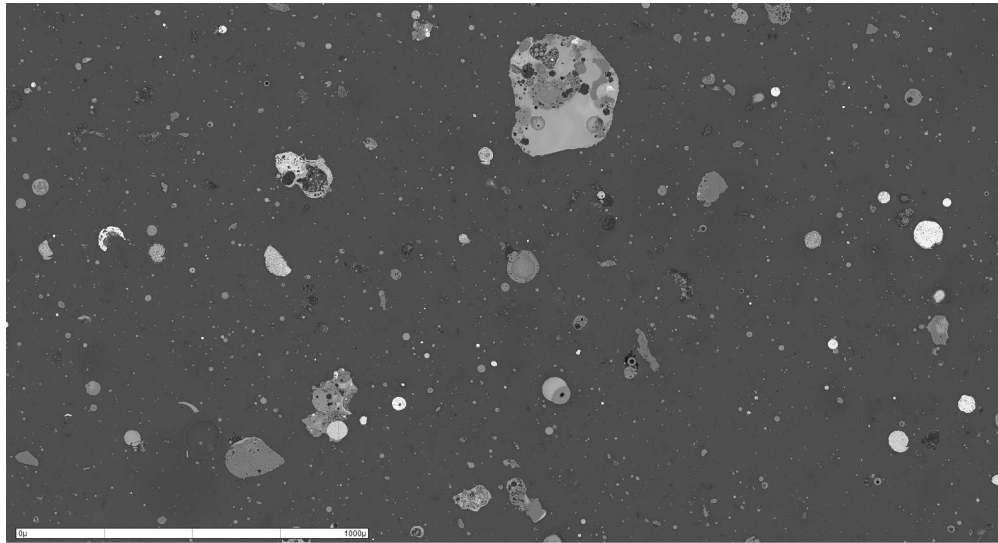


Figure 4-9: Electron micrograph of Drax fly ash (UK, Yorkshire)

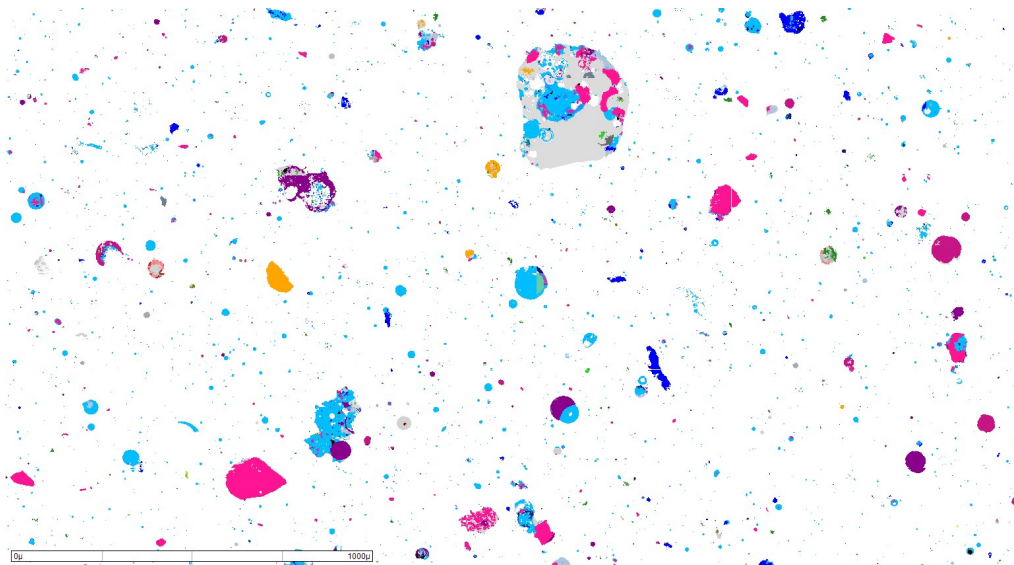


Figure 4-10: MLA coloured mosaic of Drax fly ash (UK, Yorkshire)

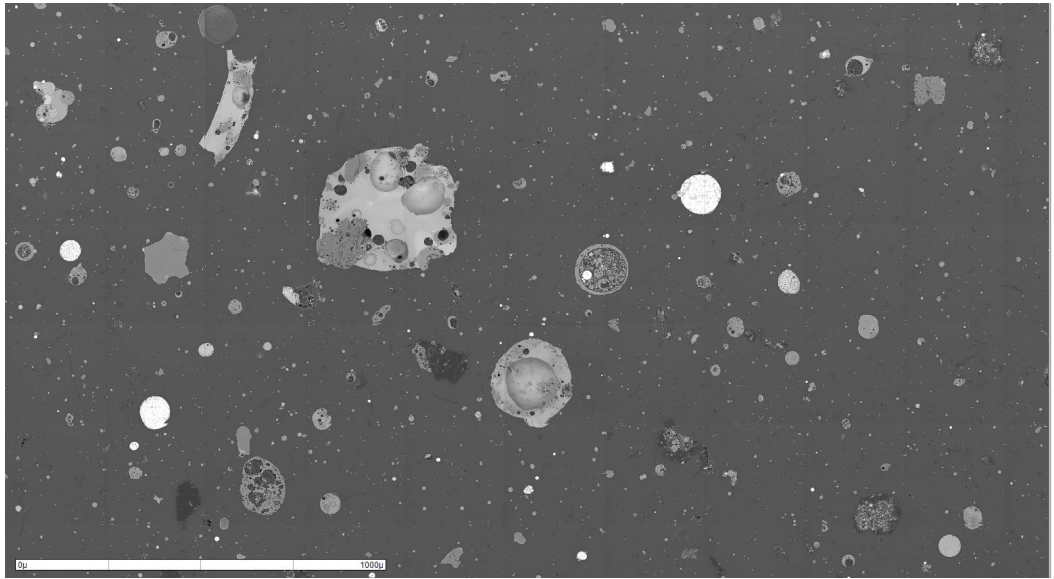


Figure 4-11: Electron micrograph of Ratcliffe fly ash (UK, Nottinghamshire)

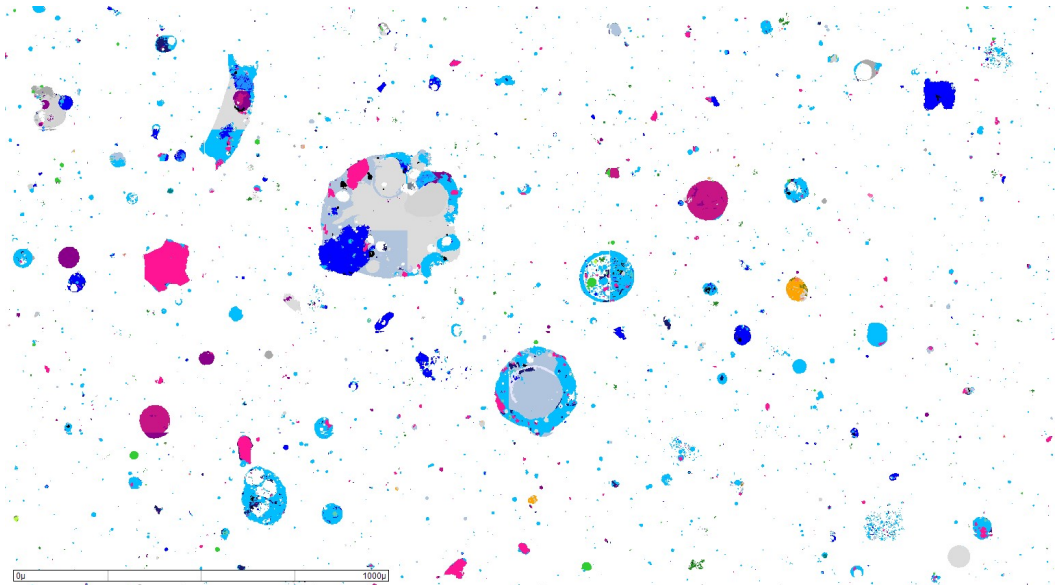


Figure 4-12: MLA coloured mosaic of Ratcliffe fly ash (UK, Nottinghamshire)

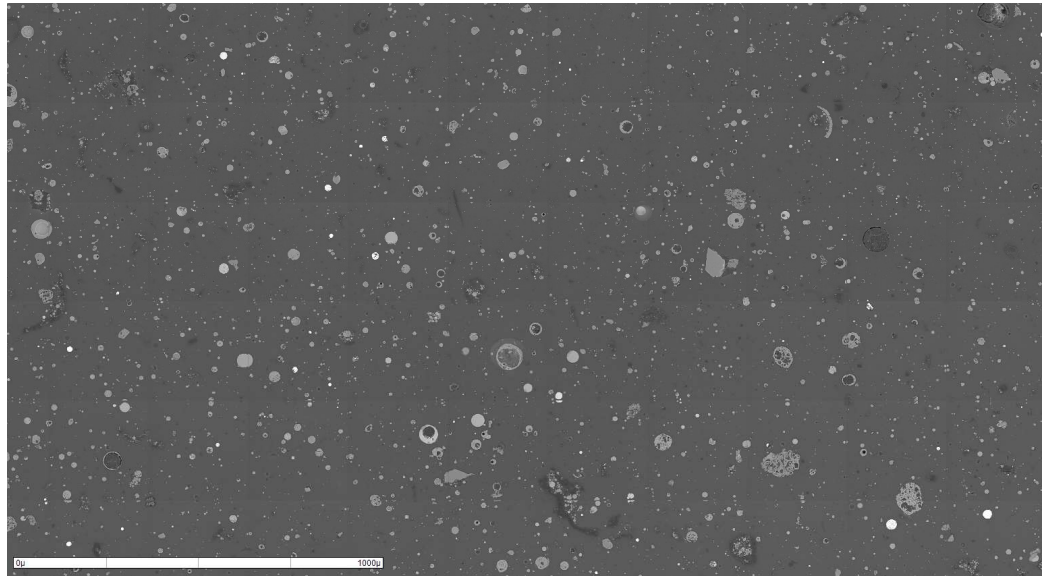


Figure 4-13: Electron micrograph of Longannet fly ash (UK, Fife)

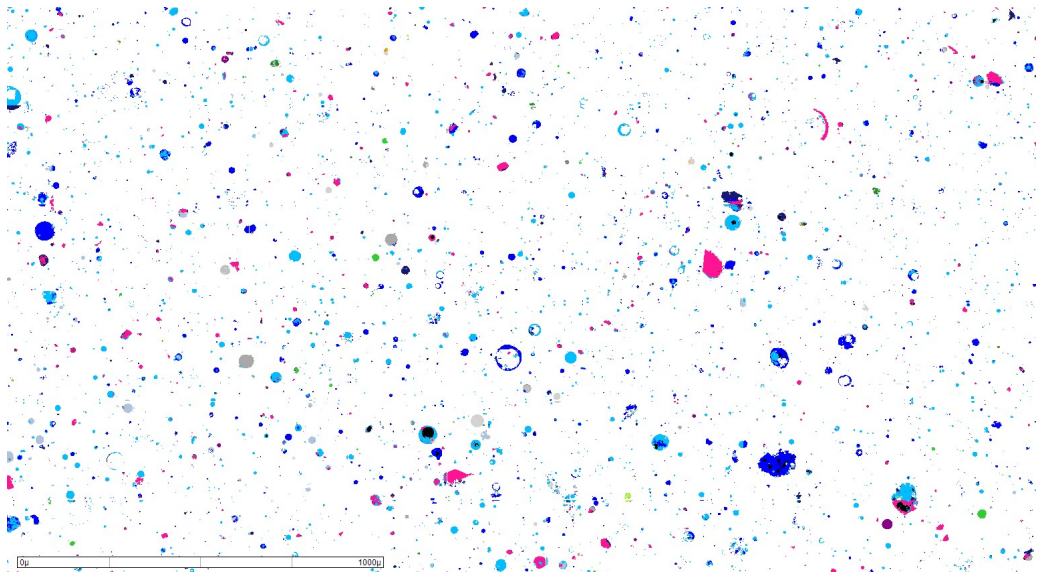


Figure 4-14: MLA coloured mosaic of Longannet fly ash (UK, Fife)

4.3.3 MLA Assessment of the Tendency for Slagging and Fouling

The MLA data presented in Table 4-9 can be converted to the elemental compositions and displayed graphically using ternary phase diagrams for the main chemical components of the fly ash samples, SiO_2 - Al_2O_3 - CaO or SiO_2 - Al_2O_3 - Fe_2O_3 . The respective fly ash ternary phase diagrams can then be compared to Figure 4-18 and Figure 4-19 to identify the likely minerals formed.

Figure 4-15 shows that the majority of the analysed compositions are equidistant from the SiO_2 - Al_2O_3 axis and are derived from the decomposition of clay minerals. Some of the points lie close to the SiO_2 apex and would be high melting point quartz particles and these particles which are close to the SiO_2 - Al_2O_3 apexes have high melting temperatures, very high viscosities and would contribute to minimal ash deposition issues[229]. However, the majority of the particle points are crystalline mullite as confirmed by XRD in Figure 4-4. In Figure 4-16 the points which lie close to Fe_2O_3 apex are a result of the decomposition and oxidation of pyrite (FeS_2).

There are a significant number of particles spreading away from SiO_2 - Al_2O_3 towards CaO or Fe_2O_3 . These compositions indicate the occurrence of chemical reactions between the aluminosilicates and decomposition products of calcite (CaCO_3), dolomite ($\text{CaMg}(\text{CO}_3)_2$), siderite (FeCO_3), other carbonates or pyrite (FeS_2). The Ca and Fe are fluxing species and bond to the aluminosilicates, lowering the melting temperature and viscosity of the ash.

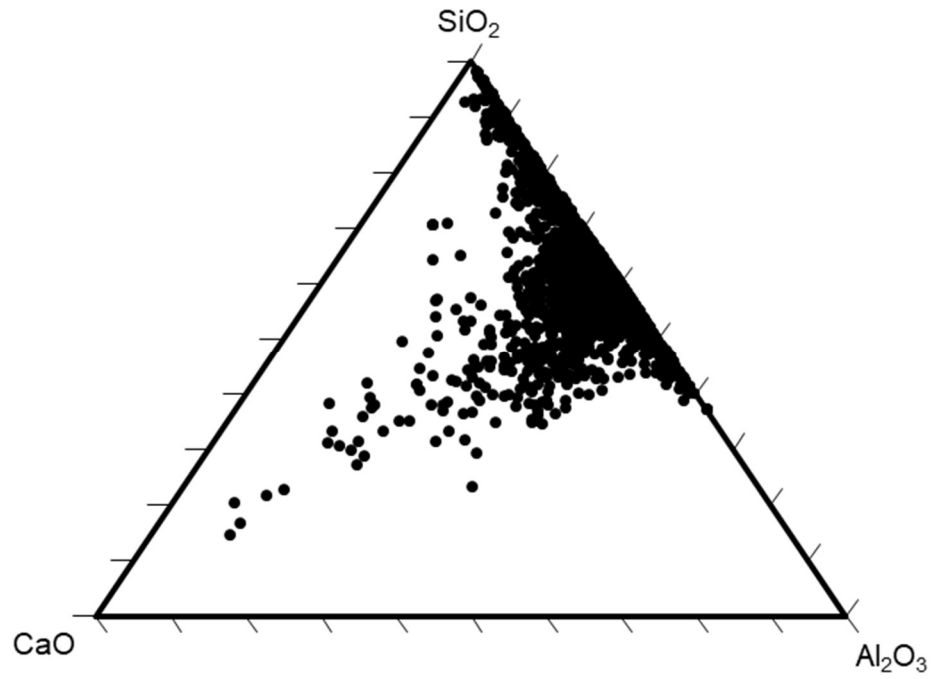


Figure 4-15: SiO_2 - Al_2O_3 - CaO ternary phase diagram for Ratcliffe fly ash

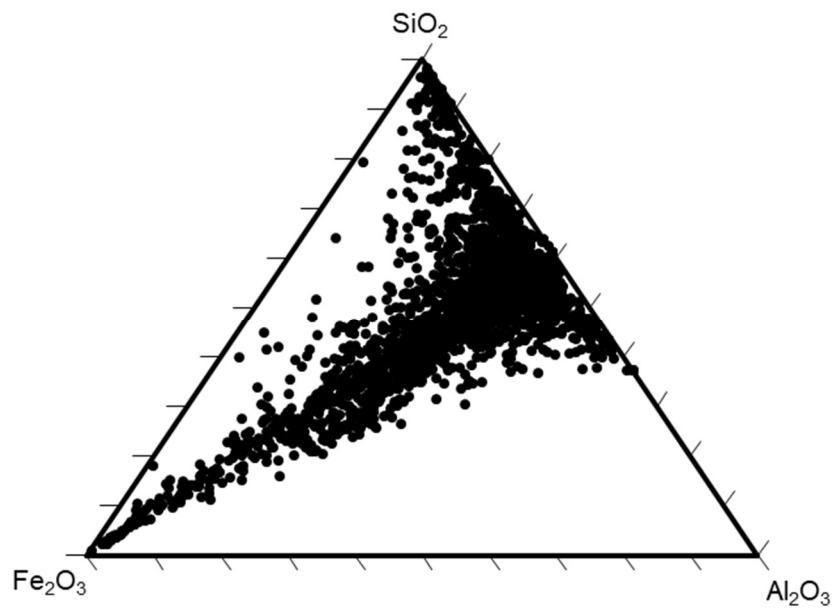


Figure 4-16: SiO_2 - Al_2O_3 - Fe_2O_3 ternary phase diagram for Ratcliffe fly ash

The MLA mineral composition data and ternary phase diagrams show that there are limitations with bulk ash analyses for understanding the nature and minerals formed in fly ashes.

Figure 4-17 shows relatively good agreement between the pure metal oxide compositions determined by XRF spectroscopy and calculated from the elemental compositions using the MLA. Figure 4-16 shows that the high Fe_2O_3 content includes the distribution of Fe with glassy aluminosilicate phases producing Fe/Ca aluminosilicates mineral phases with similar Fe:Ca ratios as Almandine ($\text{Fe}_3\text{Al}_2(\text{SiO}_4)_3$) and some Fe/K aluminosilicates. The presence of these iron-containing aluminosilicates is usually present within fly ashes prone to slagging phenomenon. In terms of erosion, it would be expected that the partially melted or glassy aluminosilicates would reduce the erosion rate, however as shown in Figure 4-16, there are a significant number of individual mineral grains within the iron-containing Spinel group.

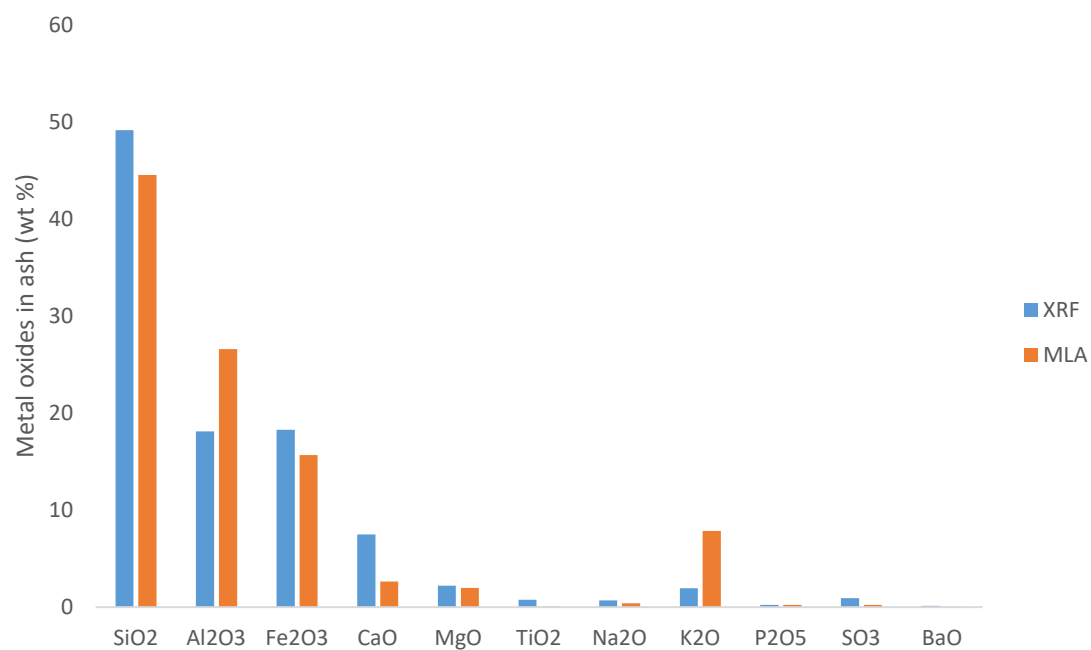


Figure 4-17: Comparison of metal oxide compositions from XRF and MLA of the Ratcliffe fly ash

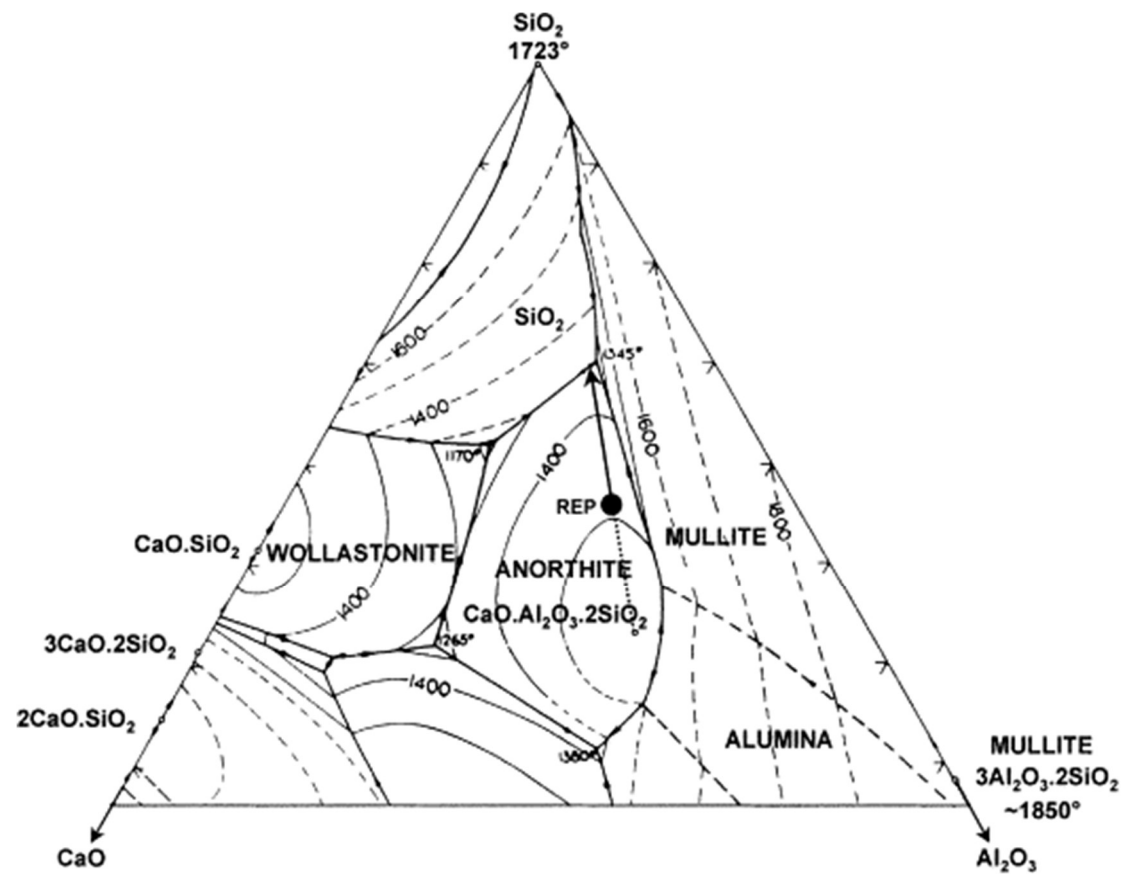
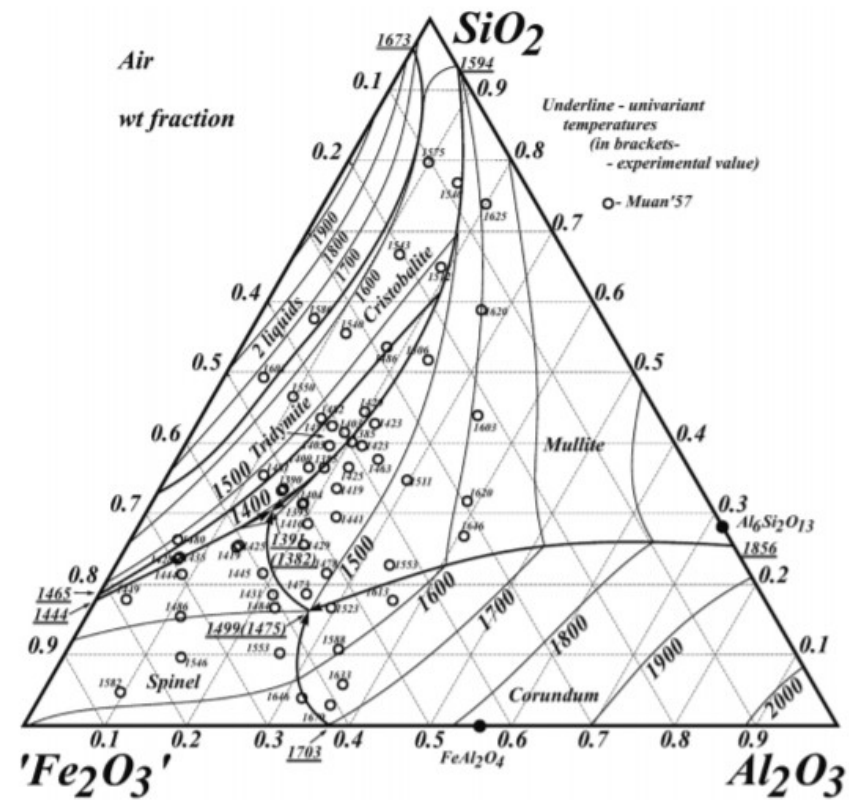


Figure 4-18: CaO - Al₂O₃ - SiO₂ ternary phase diagram[230]



4.3.4 Influence of the Mineral Grain Particle Size Distributions and Associations and the Relationship with Erosive Wear

The MLA particle size distribution data in Figure 4-20 supports that conducted by sieve analysis and laser light scattering, as shown in Table 4-6 and Table 4-7 respectively. The Ratcliffe fly ash contained the largest particles, with some in the region of 300 μm . However, whilst it is widely accepted that particle size is a critical parameter in assessing the erosion rate of fly ashes, there has been little research into the influence of specific mineral particle sizes and their relation with erosive wear.

Analysis of the quartz grain size distribution suggests that the quartz particle size is an important contributor to the higher erosion rate of the Ratcliffe fly ash. As shown in Figure 4-1, the erosion rate of Ratcliffe is 1.7 times greater than the Longannet fly ash. Additionally, the maximum quartz particle size of the Ratcliffe fly ash (180 μm) is 2.4 times greater than Longannet (75 μm). Previous studies have suggested that for UK coals the quartz is usually found as large 'free' or excluded particles, in comparison to pyrite which is often 'included' in the soft clays and coal matrix[232]. Figure 4-21 confirms that the largest excluded particles are quartz with some exceeding 180 μm , whilst the hematite particles are less than 100 μm .

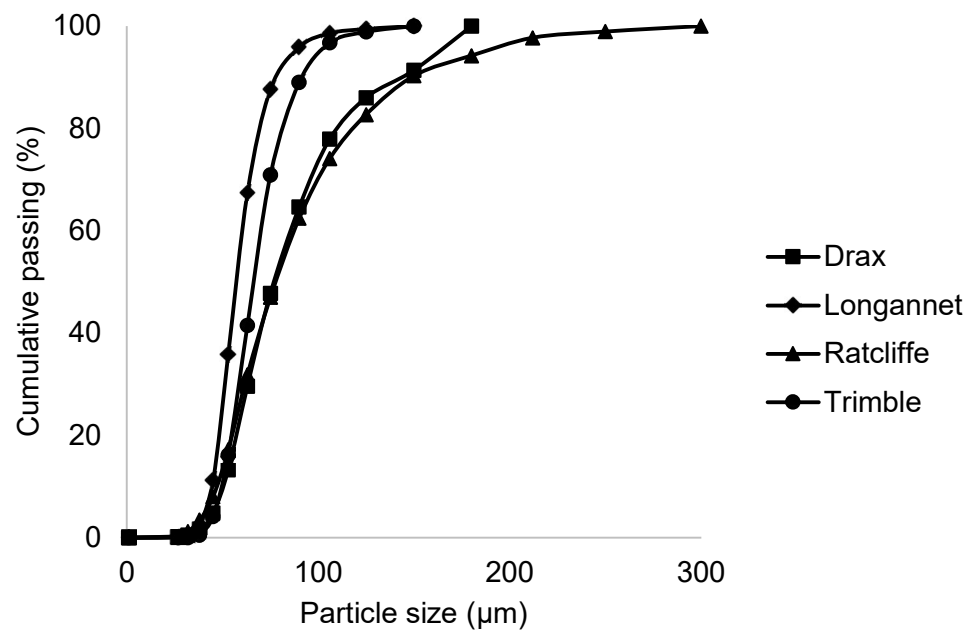


Figure 4-20: Particle size distributions of the power station fly ashes

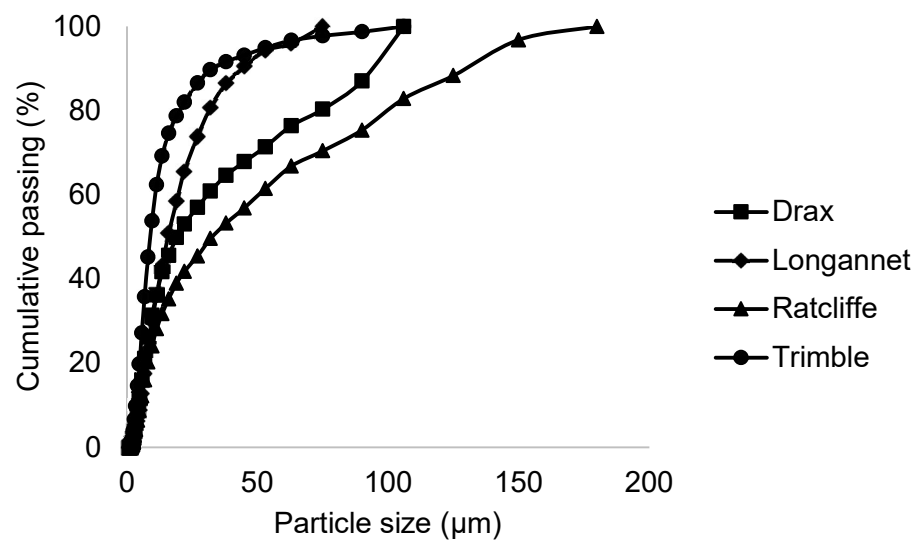


Figure 4-21: Quartz grain size distributions of the power station fly ashes

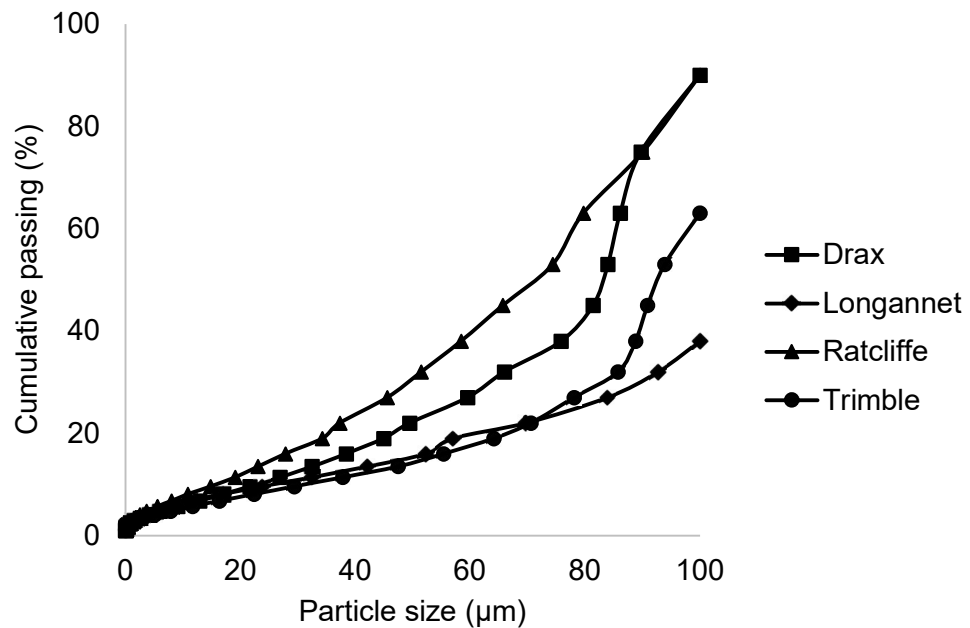


Figure 4-22: Hematite grain size distributions of the power station fly ashes

Observations of the coloured mosaics in Figure 4-10 (Drax fly ash) and Figure 4-11 (Ratcliffe fly ash) show that whilst the majority of the quartz displayed still remains excluded after combustion, the hematite (formed from the oxidation of pyrite) is present as spherical excluded particles as the pyrite has likely been released from the clay and carbonaceous matter during combustion.

The figures below show the mineral associations of the power station fly ashes, that is, the extent to which the minerals are included or excluded from the carbon matrix or other surrounding minerals. For example, a mineral may have a mineral distribution that is 70% volume excluded, whereby the particle has a 70% free surface and the remaining 30% volume is associated (or in contact) with other mineral species. In the literature, the mineral associations usually present only the total included and excluded percentages, without indicating the

specific minerals which are associated with one another. The plots presented below provide an indication as to which mineral groups are interacting and likely exhibiting coalescence and melting behaviour. The figures show that the majority of the minerals contain included unburned fixed/volatile carbon.

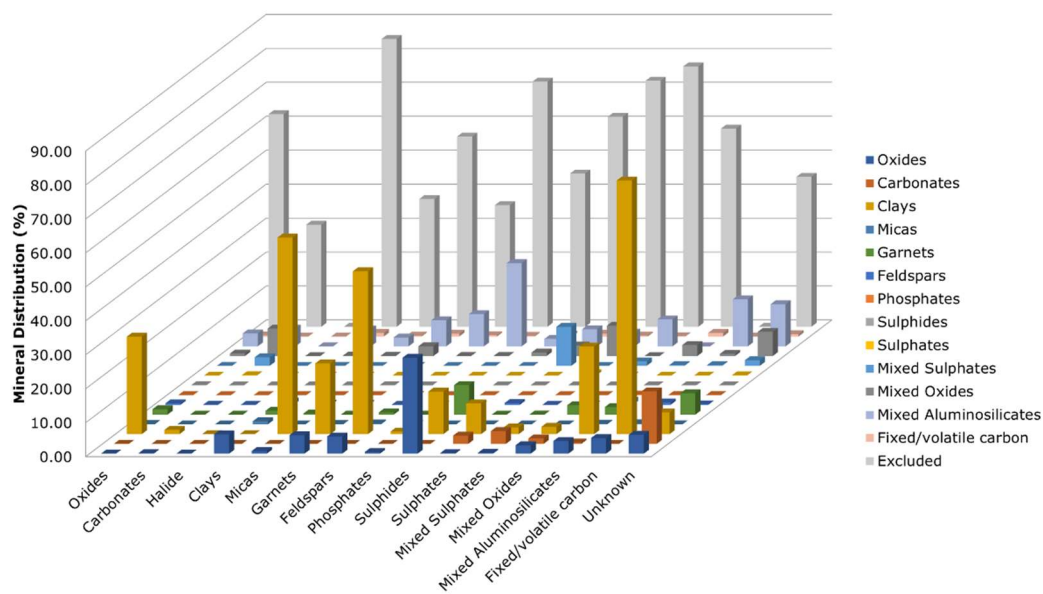


Figure 4-23: Mineral matter distribution and associations in Ratcliffe fly ash

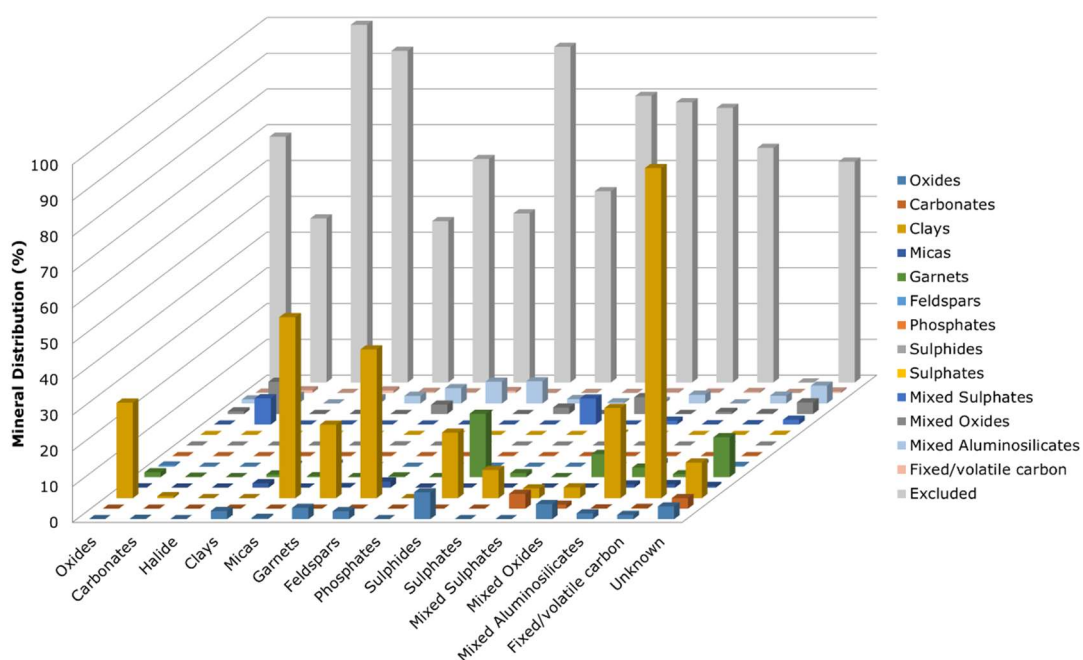


Figure 4-24: Mineral matter distribution and associations in Drax fly ash

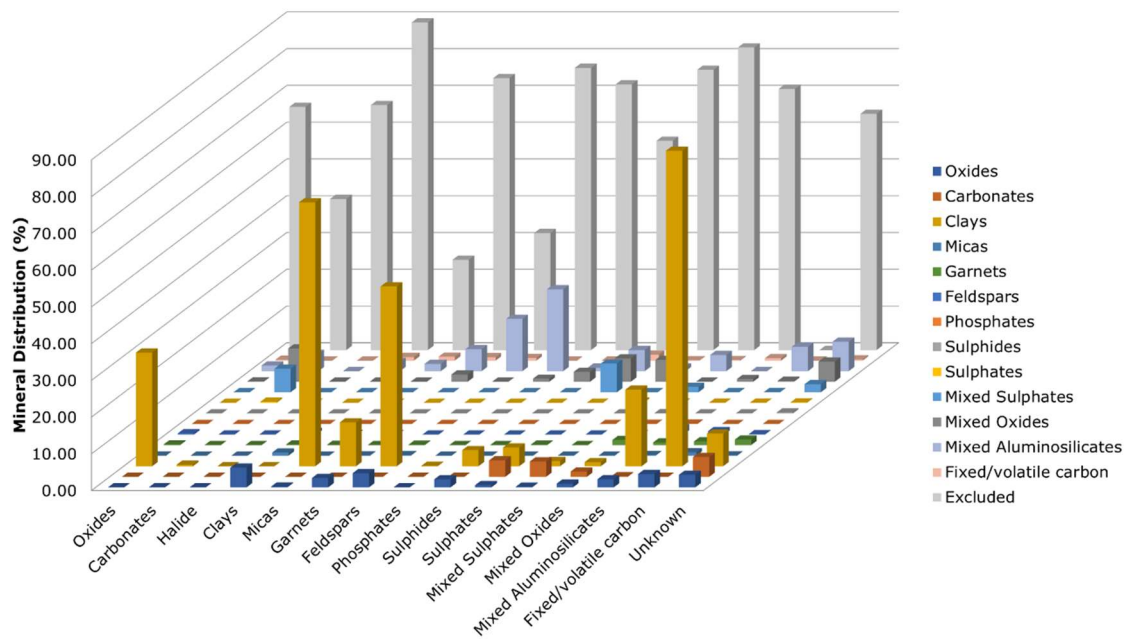


Figure 4-25: Mineral matter distribution and associations in Longannet fly ash

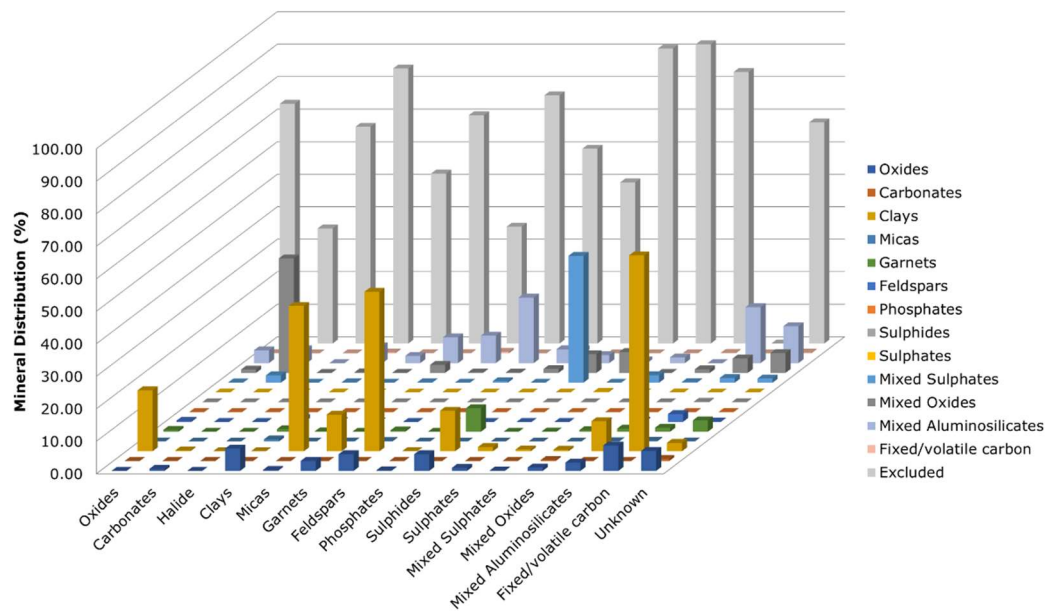


Figure 4-26: Mineral matter distribution and associations in Trimble fly ash

4.3.5 Influence of Mineral Angularities on Erosive Wear

The angularity of the bulk minerals present within the fly ashes and the individual minerals is reported to have a negligible effect on the erosion rate[233]. However, in order to test this theory, the angularities were computed for each fly ash from the MLA software using the following formula:

$$\text{Angularity} = \frac{\sum ([\text{radius}] - [\text{radius equivalent ellipse}])}{[\text{radius equivalent ellipse}] \text{ in } 1^\circ \text{ increments}}$$

Table 4-10 shows the angularities of the individual mineral species and the bulk minerals for each fly ash. It is evident that there is a positive correlation between the angularity of the quartz grains and the erosion rate, as both these parameters follow the order Ratcliffe>Longannet>Drax, however, the quartz angularity still remains an unlikely primary cause of the increased erosion rate.

Table 4-11 shows the actual number of individual grains identified for each mineral analysed for the angularity and the normalised number of individual mineral grains in order to compare the four fly ashes. The normalised number of quartz grains shows that despite the Longannet fly ash containing more quartz mineral grains (38,383) than the Ratcliffe fly ash (32,291) and similar bulk angularities (59.00 and 58.25 respectively) the Ratcliffe fly ash still had 1.7 times the erosion rate.

Table 4-10: Mineral angularities and relative standard deviations (%) of the power station fly ashes

Minerals	Ratcliffe		Longannet		Drax		Trimble	
	Mean Angularity	Relative Standard Deviation	Mean Angularity	Relative Standard Deviation	Mean Angularity	Relative Standard Deviation	Mean Angularity	Relative Standard Deviation
Hematite	38.13	2.54	31.80	2.01	32.82	2.05	30.67	1.97
Illite	43.94	1.51	46.89	1.53	43.31	1.44	38.75	1.60
Kaolinite	60.46	1.42	55.30	1.48	59.07	1.40	53.68	1.48
Quartz	45.34	1.51	44.92	1.42	42.04	1.38	38.16	1.45
Bulk	58.25	1.51	59.00	1.53	57.65	1.50	49.05	1.46

Table 4-11: Individual mineral grains and total grains in power station fly ashes

Minerals	Number of grains							
	Ratcliffe (actual)	Ratcliffe (normalised)	Drax (actual)	Drax (normalised)	Longannet (actual)	Longannet (normalised)	Trimble (actual)	Trimble (normalised)
Hematite	2,392	3,811	2,943	3,843	721	900	5,484	5,111
Illite	182,336	290,530	251,882	328,914	193,217	241,169	153,618	143,180
Kaolinite	19,471	31,025	23,920	31,235	75,219	93,886	14,894	13,882
Quartz	20,266	32,291	21,708	28,347	30,751	38,383	49,695	46,318
Other	89,334	142,343	82,446	107,660	100,677	125,662	312,761	291,509
Total grains	313,799	500,000	382,899	500,000	400,585	500,000	536,452	500,000

4.4 Chapter Conclusions

The erosion rates of three pulverised coal fly ashes have been determined using an erosion test rig through firing the particles at various velocities up to 60 m s^{-1} at a 45° steel target specimen. The Ratcliffe fly ash had the highest erosion rate due to the high quartz and iron oxide contents, and largest average particle diameter.

SEM-MLA characterisation was performed on all the power station fly ashes using a unique mineral database tailored to characterise the alkali and alkaline earth mineral aluminosilicate phases (mixed aluminosilicates) and mixed oxides. The dominant MLA mineral species identified and semi-quantified within all fly ashes included quartz, kaolinite, illite and hematite minerals. This was confirmed by XRD and XRF analysis. Coloured mosaics of all the fly ashes show the heterogeneous nature of all the fly ash samples and verify the dispersed particles produced during the MLA sample preparation procedure.

Mineral grain size distribution graphs were generated using MLA for the fly ashes, and suggested that the particle size of quartz is a more dominant factor in the erosion rate than hematite.

Ternary phase diagrams confirmed that more detailed MLA characterisation is preferred over XRD and XRF data to identify and semi-quantify the mineral species in the fly ashes. Comparisons of the phase diagrams to the reference literature and the MLA mineral database have identified the presence of Fe/Ca aluminosilicates, which are low melting point phases and contributors towards slagging behaviour.

There is limited data available related to the influence of particle angularity on erosion rates. This study suggested that particle angularity has negligible impact compared to chemical composition and particle size because the average mean angularity of Longannet fly ash was similar to that of Ratcliffe fly ash, despite the large difference in erosion rates.

Chapter 5: Mineral Transformations and Associations during Coal Devolatilisation and Char Burnout in a Drop Tube Furnace

5.1 General Introduction

This chapter presents the results of the experiments performed on the drop tube furnace for the individual coal and biomass pyrolysis study. Prior to starting the test runs the dimensions of the DTF were measured, specifically the feeder and collector probe separation distance to calculate the volumetric flow rate and residence times the fuel particles experience at a given temperature. For the initial investigation, six coals and three biomasses at one particle size fraction were selected. The experiments aimed to investigate the changes that the fuel particles experience under a high heating rate and inert atmosphere during the 200 and 600 millisecond residence times, whilst providing an assessment on the repeatability of the DTF system.

In the second section, chemical characterisation of the DTF generated coal and biomass char samples are presented, such as thermogravimetric tests to compare the char burnouts at the two drop tube residence times, and analysing changes in particle characteristics such as particle size during the pyrolysis process using dynamic image analysis. Finally, the DTF generated chars were ashed at 500°C under an air atmosphere to remove the unburned carbon for x-ray diffraction and automated mineral analysis using scanning electron microscopy.

5.2 Experimental Matrix

This section provides an overview of the experimental test runs conducted on the drop tube furnace and the operating conditions used. For the test runs performed the residence time was varied to change the extent of volatile removal from the solid coal particles.

Table 5-1: Coal devolatilisation runs and experimental operating conditions
conducted on the drop tube furnace

Sample	Carrier gas	Temperature (°C)	Residence time (milliseconds)	Particle size (µm)
SAC	N ₂	1450	200	53-75
SAC	N ₂	1450	600	53-75
KC	N ₂	1450	200	53-75
KC	N ₂	1450	600	53-75
ST	N ₂	1450	200	53-75
ST	N ₂	1450	600	53-75
RW	N ₂	1450	200	53-75
RW	N ₂	1450	600	53-75
CW	N ₂	1450	200	53-75
CW	N ₂	1450	600	53-75
CO	N ₂	1450	200	53-75
CO	N ₂	1450	600	53-75

The DTF chars were combusted under air in a muffle furnace at 500°C to preserve the minerals and remove the volatile and fixed carbon for XRD analysis. A muffle furnace was used for these char burn-out experiments to produce larger quantities of ash for XRD, MLA and XRF analysis and to ensure that the carbon had been completely burnt off leaving the minerals intact. The DTF only operates at higher temperatures where low melting temperature elements such as K and Na would be lost from the char structure.

Table 5-2: Muffle furnace experiments on DTF coal chars (produced at 1450°C, 200ms)

Sample	Carrier gas	Temperature (°C)	Residence time (hours)	Particle size (µm)
SAC (200ms)	Air	500	12	53-75
KC ((200ms)	Air	500	12	53-75
ST (200ms)	Air	500	12	53-75
RW (200ms)	Air	500	12	53-75
CW (200ms)	Air	500	12	53-75
CO (200ms)	Air	500	12	53-75

Table 5-3: Coal burnout runs and experimental operating conditions conducted on the drop tube furnace

Sample	Carrier gas	Temperature (°C)	Residence time (milliseconds)
SAC (200ms)	5% O ₂	1450	200
SAC (200ms)	5% O ₂	1450	600
SAC (200ms)	10% O ₂	1450	200
SAC (200ms)	Air	1450	200

5.3 DTF and TGA Experimental Study

Six coals and three biomasses were selected for the study, on the basis that the coals represent different global regions and ash contents typically encountered during pulverised combustion on plant. Similarly the biomasses are representative of those used for co-firing with coal in UK and other European coal-fired power plants[234].

5.3.1 Coal and Biomass Characterisation

Proximate and ultimate analysis for the coal and biomass samples are presented in Table 3-1 . The dry ash contents of the coals show significant variation, the USA Illinois (9.06%) can be classified as low ash, South African Koorfontein export (14.39%) and UK Kellingley (19.83%) are medium ash, UK Cumberworth (26.80%) is moderately high ash and Polish Stefanów (30.61%) and UK Roundwood (57.77%) are high ash content coals[235]. These coals were selected with a wide range of ash contents because it was envisaged there would be different char burnout rates due to the catalytic effect of metal elements on fixed carbon combustion[236]. Additionally, from a practical standpoint the higher ash coals provide a larger quantity of ash for further analysis after DTF pyrolysis and combustion.

The biomass samples include miscanthus (*Miscanthus × giganteus*) pellets, a rapid growing energy crop with a low mineral content; Russian sunflower husk (*Helianthus annuus* L.) pellets, a by-product of sunflower oil extraction; and Spanish olive cake (*Olea europaea*), a waste mixture from olive oil production. These biomasses have been used for dedicated biomass and co-firing with coal applications for power generation across Europe. Miscanthus has been used

for 100% firing at the recently closed Ironbridge power plant in Shropshire, UK; sunflower husk (between 10-20% by heat input) co-firing with coal at the Drax power plant in Yorkshire, UK[237] and olive cake (up to 10% by weight) co-firing with coal at the Cottam power plant in Lincolnshire, UK[238].

As an energy crop, Miscanthus has the highest volatile matter (VM) and relative to the coals, the biomass samples are classified as containing very low ash contents. The inclusion of these biomasses in the study are primarily due to the relatively high concentrations of alkali and alkaline earth metals. Information on the source of the biomass samples are detailed in the following reference[239].

5.3.2 Drop Tube Furnace Conditions

The chars were prepared at 200 and 600 millisecond residence times at a temperature of 1450°C under atmospheric pressure and a nitrogen atmosphere. Previous studies at the University of Nottingham on DTF systems used similar residence times to observe variations in volatile release for char production [240, 241]. The devolatilisation process was undertaken at 1 atm and under a nearly pure nitrogen atmosphere (0.01% oxygen in nitrogen) from external cylinders. Previous investigators opted to use a 1% oxygen in nitrogen atmosphere for char production to prevent contamination of condensed tars onto the char structures, however, this was deemed unnecessary considering the DTF is an open system and to mitigate partial oxidation of the generated chars.

The char combustion process was performed at 1 atm and under a slightly oxidising atmosphere of 5%vol and 10%vol oxygen in nitrogen. For all the

experiments, a screw feeder system operating at approximately 6 g hr⁻¹ was used to consistently disperse a small stream of particles into the furnace and prevent blockages in the feeder probe. The carrier gas flow rate was operated at 11.2 and 11.0 L min⁻¹ for the 200 and 600 millisecond residence times respectively. The vacuum pump was 1 L min⁻¹ above the carrier gas flow rate to provide enough suction to draw particles into the cyclone system. To ascertain the repeatability of the DTF, each test run was performed in at least duplicate.

5.3.3 DTF Devolatilisation and Surface Area

Drop tube furnaces are used to simulate the high temperatures, the high heating rates and the short residence times typical of industrial-scale boiler systems. For decades it has been widely accepted that the amount of volatiles released during pyrolysis and combustion in these furnaces can exceed the volatile matter measured in standard proximate analysis[242]. The particles are entrained in the gas stream and flow evenly through the system upon heating. However, as previously discussed, there are significant losses incurred during operation for mass balance purposes. Therefore, the ash tracer technique can be used to calculate volatile yield (V_{DTF}) using the ash content weight percent of the fed coal (A_{fuel}) and the corresponding char (A_{char}) on a dry basis.

$$V_{DTF}(\% \text{ dry}) = 100 \times \frac{(A_{char} - A_{fuel})}{A_{char}}$$

$$V_{DTF}(\% \text{ dry ash free}) = 10^4 \times \frac{(A_{\text{char}} - A_{\text{fuel}})}{(A_{\text{char}} \times (100 - A_{\text{fuel}}))}$$

Considering the errors associated with applying the ash tracer technique, it is common-place to determine a fraction known as the R factor to compare the DTF volatile weight loss with the fuel's proximate volatile matter. This value provides an indication of the extent of volatile release, calculated as follows[243]:

$$\text{R Factor (\% dry ash free)} = \frac{\text{Fuel weight loss}}{\text{Proximate volatile matter of fuel}}$$

The weight loss from the direct mass balance of the fuel and collected char, coupled with the proximate volatile matter by thermogravimetry were used to produce estimates of the R factor.

Table 5-4: Proximate and DTF volatiles and R factors for coal and biomass
chars

Coal/Biomass Fraction	Particle Size	Proximate Volatiles	DTF Volatiles (wt% daf)		R factor	
	µm	(wt% daf)	200ms	600ms	200ms	600ms
Cumberworth	53-75	35.4	33.9	43.2	0.96	1.22
Roundwood	53-75	42.1	33.1	51.5	0.79	1.22
Kellingley	53-75	37.5	48.3	48.5	1.29	1.29
Stefanów	53-75	41.0	61.6	58.9	1.50	1.44
Illinois	53-75	38.4	58.2	63.6	1.52	1.66
Koornfontein	53-75	29.5	43.5	43.7	1.47	1.48
Miscanthus	53-75	86.1	95.2	94.5	1.11	1.10
Olive Cake	53-75	77.7	81.7	76.6	1.05	0.99
Sunflower	53-75	82.2	78.8	75.3	0.96	0.92

Table 5-4 shows the mean values for the DTF volatile release and R factors for the coal and biomass fractions as a function of residence time. The data shows that generally the volatile release from the DTF is greater than proximate methods and increases as a function of residence time[27, 244, 245]. This indicates there is enhanced devolatilisation at the higher temperatures and heating rate used in the drop tube furnace[246]. However, an outlier is the Roundwood coal, whereby there was greater retention of volatiles at 200 milliseconds than the proximate volatiles. Additionally, the South African Koorfontein coal, with the lowest proximate volatile matter content, exhibited negligible difference in DTF volatiles between the 200 and 600 millisecond runs inferring that complete volatile expulsion had already occurred.

For the biomass samples, Table 5-4 shows that only the DTF volatiles for olive cake exceed the proximate volatile matter. It is likely that a proportion of the potassium and other ash mineral species have volatilised at the high DTF temperature (1450°C) during pyrolysis causing an underestimation of low-ash biomasses in the drop tube furnace[223]. However, the results indicate that the sunflower husk required a longer residence time in order to release the same mass percentage of volatiles determined by standard proximate analysis.

Table 5-5: Surface area analysis of DTF chars from coal and biomass samples

Sample (residence time)	BET surface area (m² g⁻¹)	D-R equivalent surface area (m² g⁻¹)	D-R limiting micropore capacity (cm³ g⁻¹ STP)
South African (200 ms)	43.0 ± 1.2	47.0	9.2
South African (600 ms)	22.8 ± 1.3	29.5	6.5
USA Illinois (200 ms)	47.9 ± 0.4	68.6	15.0
USA Illinois (600 ms)	49.7 ± 4.5	57.4	12.6
Miscanthus (200 ms)	136.8 ± 1.3	177.0	39.0
Miscanthus (600 ms)	315.7 ± 5.0	411.7	90.1
Sunflower (200 ms)	199.4 ± 3.3	259.5	56.8
Sunflower (600 ms)	449.9 ± 31.0	602.7	132.0
Olive cake (200 ms)	122.4 ± 1.4	156.9	34.3
Olive cake (600 ms)	121.8 ± 1.2	159.2	34.8

Table 5-5 shows the surface area analysis of the coal and biomass chars generated at 200 and 600 milliseconds at 1450°C in the DTF. This data shows that of the coals, the USA Illinois char has a higher surface area and micropore capacity than the South African Koorfontein char using the Dubinin-Radushkevich (D-R) model. The higher D-R surface area of the USA Illinois char may be due to lower ash content of the coal, resulting in less mineral inclusions blocking the internal char structure during devolatilisation[247]. This theory is further supported in Figure 5-1, where the USA Illinois char is shown to have a higher cumulative pore volume at 200 ms and 600 ms compared to the South African coal chars at the same residence times.

From the D-R model of the coal chars, which accounts for the micro porosity of type I isotherms, the equivalent surface areas decreased with increasing residence time. South African coals typically contain higher proportions of calcium carbonates[248], therefore an explanation could be that the decomposition of CaCO_3 forming CaO crystallites has reduced the surface area of the char through blocking the char pores, which because of sintering, have average pore diameters within the mesopore and micropore ranges[247].

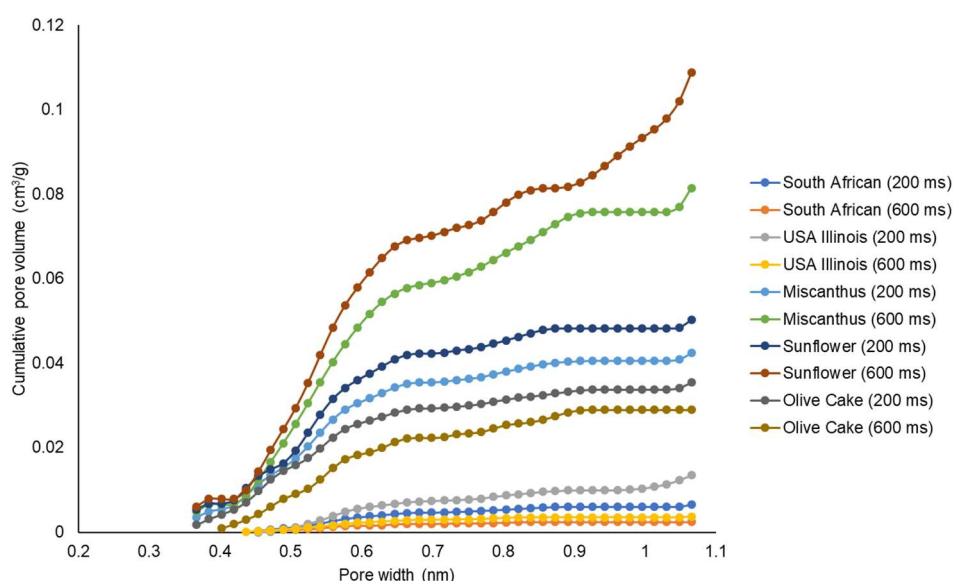


Figure 5-1: CO₂ adsorption data showing cumulative pore volume and pore width for the DTF coal and biomass chars

There have been limited studies conducted on the influence of the internal surface area of biomass during devolatilisation under a nitrogen atmosphere using a drop tube furnace. The CO₂ sorption results presented in Table 5-5 suggest that the biomasses exhibit higher surface areas than the coals, and that for each biomass there is an increase in the specific surface area and micropore capacity as the residence time increases. The sunflower char has the highest surface area, closely followed by miscanthus and olive cake chars. In Figure 5-1, it is evident that whilst the cumulative pore volumes increase for sunflower and miscanthus as the residence time increases, the olive cake has an inverse relationship. This suggests that whilst the sunflower and miscanthus pores are widening and enlarging, in contrast, olive cake has already fully expelled the volatiles at the 200 ms residence time and the pores are collapsing

and coalescing causing a reduction in the micro porosity, forming mesopores or macropores[246].

5.3.4 TGA Coal Burnout & Reactivity

Table 5-6 shows the TGA coal combustion kinetic parameters derived from isothermal runs at 475, 500, 525 and 550°C for the 53-75 µm coal fractions. In order to assess the combustion reactivity's of the coal fractions, the activation energies and pre-exponential factors were calculated. The experimental Arrhenius rate kinetics methods are outlined in 3.2.3.

Table 5-6: TGA isothermal coal combustion kinetic parameters

Sample (53-75 µm)	Apparent activation energy (kJ mol⁻¹)	Pre-exponential factor (s⁻¹)	R² value
UK Roundwood	91.0	10.9	0.99
USA Illinois	112.7	5.7	0.99
UK Kellingley	116.8	15.0	0.99
UK Cumberworth	119.0	11.6	0.99
POL Stefanów	125.3	16.4	0.99
South African	131.7	16.9	0.99

The South African Koornfontein coal had the highest apparent activation energy, with the value corroborating with other studies[249-251]. Generally, the higher the apparent activation energy to initiate char combustion the lower the reactivity and the higher the pre-exponential factor the higher the collision frequency between reacting particles. Figure 5-2 shows that this coal had the highest char burnout time which exceeded 200 minutes at a char burnout temperature of 475°C. The inherent unreactive nature of the South African coal is likely due to the higher relative inertinite content, as presented in 3.2.6.

It is widely recognised that the high temperature and heating rate conditions of industrial scale boilers can result in thermal annealing, that is, char deactivation or reactivity losses of the fuel particles resulting in a loss of surface area, loss of active sites and loss of active site reactivity[252]. Thermal annealing has been defined as the complex transformations of the carbonaceous material during heat treatment categorised by the loss of hydrogen and oxygen, and elimination of edge carbon sites due to coalescence of aromatic rings, and defect elimination[253]. As such, it is important that subsequent DTF char particles generated for mineral transformation studies are produced at the lowest residence time in order to limit the extent of deactivation and reduce the influence of this variable during the char combustion and ash formation stages.

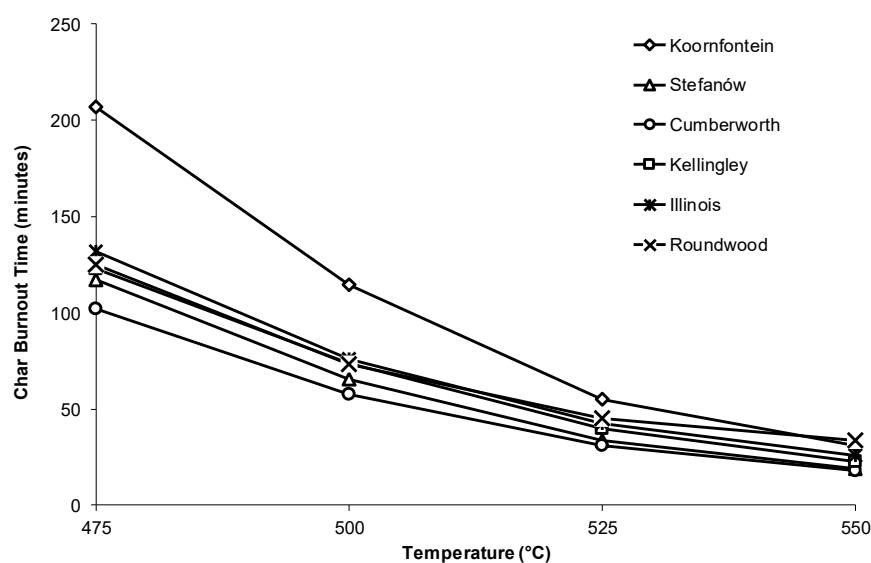


Figure 5-2: Char burnout times from TGA isothermal char combustion at different temperatures

Figure 5-2 shows the char burnout times at the isothermal temperatures used to determine the activation energies and pre-exponential factors for each coal. Aside from the char burnout time decreasing with increased isothermal temperature, it is evident that the time difference to reach the ash content is greater at the lower temperatures for each coal.

These chars were formed using a pure nitrogen stream for DTF devolatilisation, contrary to previous researchers who opted to produce char with 1% oxygen to burn off tar compounds, which may have also contributed to artificially activating the chars and improving oxygen uptake into the char active sites[254-257].

Table 5-7: Char burnout kinetic parameters for South African Koornfontein coal

Char production	Residence time	Temperature (°C)	1 st order rate constant (min ⁻¹)	95% char burnout time (min)
DTF	600 ms	1450	0.012	239.7 ± 4.9
	200 ms	1450	0.013	225.0 ± 1.0
TGA	15 min	900	0.053	55.2 ± 0.7

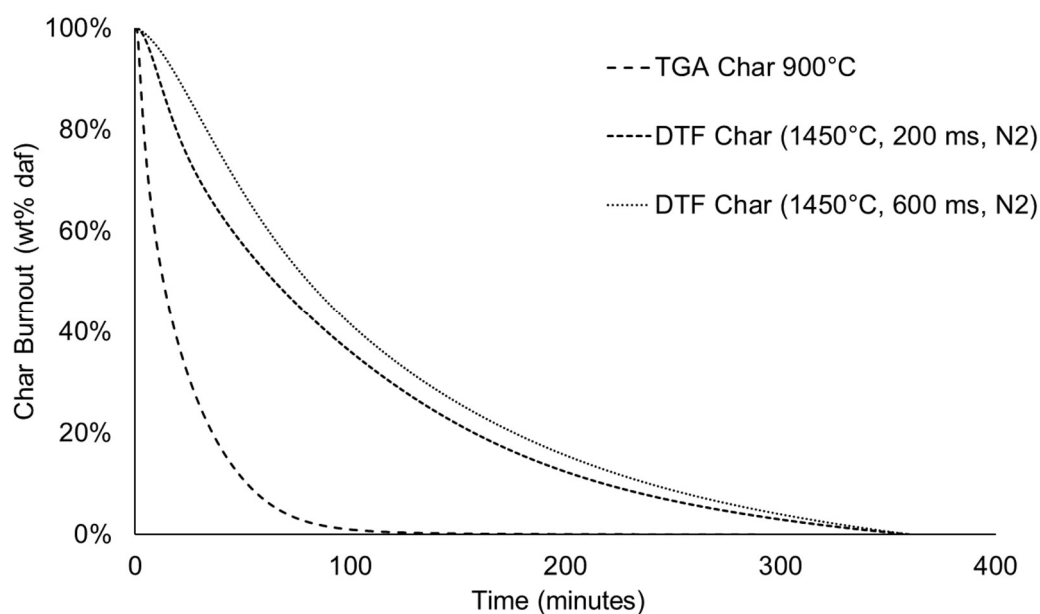


Figure 5-3: Char burnout profiles of TGA char and DTF char at different residence times for South African Koornfontein coal

Figure 5-3 shows that the TGA chars generated under nitrogen at a devolatilisation temperature of 900°C following char combustion under air at 525°C exhibited faster burnout times than the DTF generated chars at 200 and 600 milliseconds respectively. The TGA method procedures are detailed in section 3.2.3 and 3.2.4. The higher temperature (1450°C) and heating rate (10^5 °C s⁻¹) of the DTF, have a significant influence on the char burnout behaviour compared to the conditions using the TGA (500°C min⁻¹, 900°C). This higher temperature in the DTF means a greater quantity of volatiles released per gram of coal compared to the TGA. Additionally, the rate of volatile release during the evolution from coal to char in the TGA may have been inhibited due to mass and pore diffusion limitations resulting from the packing arrangement of coal particles in the TGA pan[258] Also, the more reactive nature of the TGA char

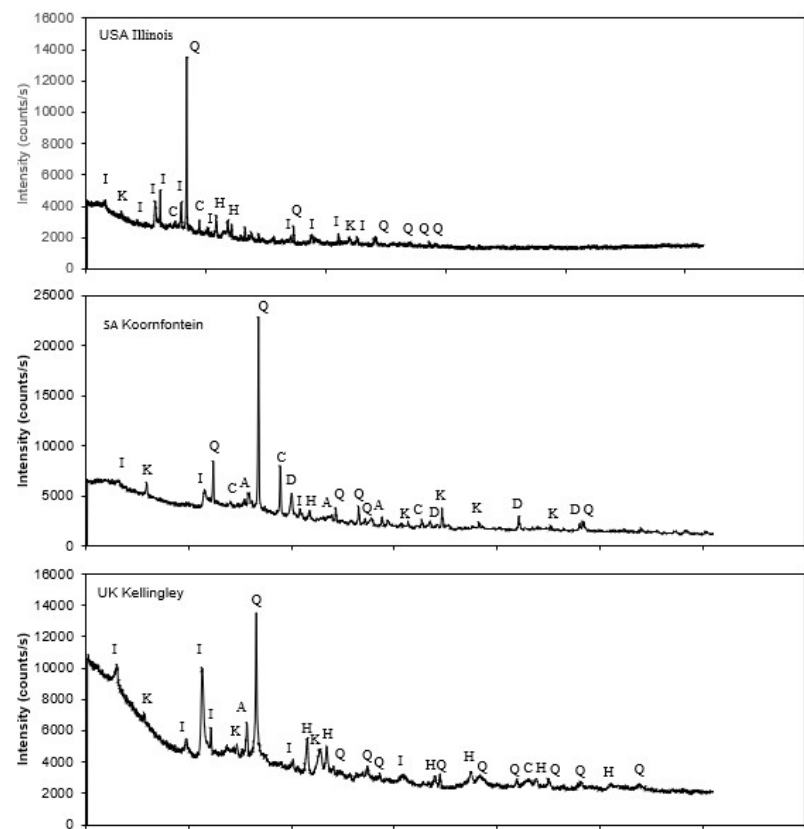
may be due to residual hydrogen retained in the chars[259]. As such, Table 5-8 shows there is less hydrogen in the 600 ms char compared to 200 ms char.

Table 5-8: Elemental analysis of DTF chars at 200 and 600 milliseconds

Char	RT (ms)	T (°C)	Elemental analysis (wt % dry ash free)			
			C	H	N	O
DTF	600	1450	74.85 ±0.12	0.14 ±0.01	1.35 ±0.00	23.65 ±0.11
	200	1450	73.99 ±0.11	0.33 ±0.01	1.59 ±0.01	24.04 ±0.12

These results indicate the presence of a char deactivation or thermal annealing effect, whereby the DTF coal chars experience a loss in reactivity due to the higher temperature and heating rates. A combination of the reactivity data and elemental analysis provides evidence to use the 200 ms residence time for subsequent char generation in the upcoming sections and chapters. The remaining DTF generated char burnout profiles are displayed in Appendix 1.

Figure 5-4 and Figure 5-5 show the coal mineral species present after 500°C muffle furnace ashing under air. All the coals include quartz, illite, kaolinite and hematite minerals intact, with the exception that the South African and USA Illinois coals contain calcite which decomposes at temperatures exceeding 750°C[260]. The XRD of the coals indicates that the coals contain stable oxides at 500°C, it is likely that the formation of these stable minerals hinder the thermal annealing process and it has been postulated that at temperatures exceeding 1200°C, char oxidation becomes ineffective at preventing thermal annealing due to more mineral transformations occurring[261].



Q: Quartz (SiO_2)

K: Kaolinite ($\text{Al}_2\text{Si}_2\text{O}_5(\text{OH})_4$)

H: Hematite (Fe_2O_3)

I: Illite ($(\text{K},\text{H}_3\text{O})(\text{Al},\text{Mg},\text{Fe})_2(\text{Si},\text{Al})_4\text{O}_{10}[(\text{OH})_2,(\text{H}_2\text{O})]$)

C: Calcite (CaCO_3)

H: Hematite (Fe_2O_3)

D: Dolomite ($\text{CaMg}(\text{CO}_3)_2$)

A: Anhydrite (CaSO_4)

Figure 5-4: XRD of muffle furnace coal ashes (500°C, air)

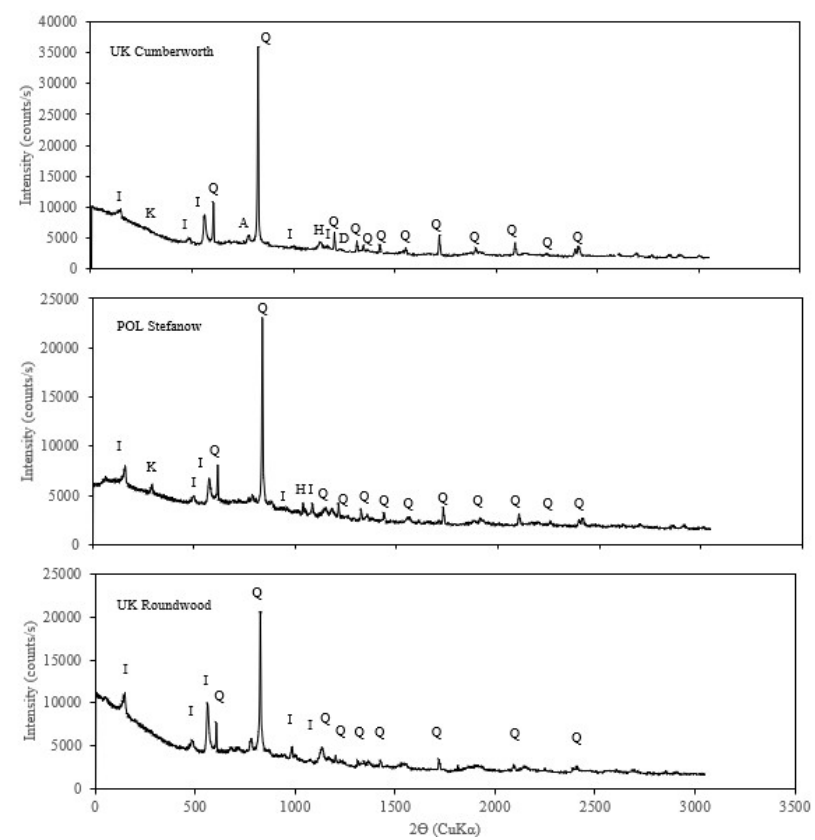


Figure 5-5: XRD of muffle furnace coal ashes (500°C, air) (continued)

5.3.5 DTF Char Firing

The pulverised coal fractions (53-75 μ m) were initially pyrolysed in the DTF operating at 1450°C and 1 atmosphere under a pure nitrogen stream at the 200 and 600 ms residence time. Three grams of each coal, performed in triplicate were run to assess repeatability, and fed into the system to produce char. A small amount of sample was fed to prevent the feeder and collector probes from blocking. The coals and collected chars were carefully weighed for the ash tracer technique. The least reactive South African Koorfontein (1450°C, 200ms, N₂) chars were re-fired in the DTF at 1450°C at the 200 and 600 ms residence times, in an atmosphere containing 5% and 10% oxygen in nitrogen respectively, to determine the most appropriate oxygen concentration to measure changes in fixed carbon content with the addition of biomass ash in the next chapter. As a means to produce enough DTF ash for analysis, between one to three grams of pyrolysed char sample was required, depending on coal type, residence time and oxygen concentration. The fed chars and collected ashes were carefully weighed to calculate the collection efficiencies. Finally, considering the significant sample losses incurred during DTF operation and in order to maximise the amount of ash for further characterisation, low temperature ashing at 500°C \pm 10°C was performed on each of the six coal chars to generate ash for mineralogical studies.

Ash yields and collection efficiencies of the DTF South African Koorfontein 200 ms generated char re-fired under 5% O₂, 10% O₂ and air atmospheres are shown in Table 5-9. In a similar manner to the DTF devolatilisation test runs, it is evident that the ash yields and collection efficiencies decrease as a function of increased residence time, which is in agreement with previous studies[28].

Table 5-9: Re-fired char ash yields and collection efficiencies for South African
Koornfontein 200ms char

Char Fraction	Atmosphere	Ash Yield (g/g of char fed)		Collection Efficiency	
		200ms	600ms	200ms	600ms
South African (Koornfontein)	5% O ₂	0.53	0.24	64.47	22.99
		0.03	0.06	3.67	1.59
	10% O ₂	0.24	0.13	60.31	55.40
		0.07	0.03	18.60	14.95
	Air	0.33	0.13	13.77	8.95
		0.39	0.19	2.43	1.45

However, the ash content of the DTF char ashes measured by TGA analysis shown in Table 5-10 suggests that there is a clear trend that the ash content increases with residence time and oxygen concentration respectively. These results indicate that re-firing the 200 ms char with a gas stream containing above 5% oxygen in nitrogen leads to nearly complete combustion at the 600 ms residence time, with virtually no unburned carbon or char remaining in the residue. This validates the 5% oxygen concentration to investigate the mineral transformation behaviour for the biomass ash doped DTF coal chars in the next chapter.

Table 5-10: TGA ash contents of the DTF ashes for the South African
Koornfontein 200ms char

Char Fraction	Atmosphere (% vol)	TGA ash content of 200ms char (wt% dry)	TGA ash contents of DTF ash (wt% dry)	
			200ms	600ms
South African (Koornfontein)	5% O ₂	22.93 0.63	26.56 0.07	70.61 0.18
	10% O ₂		58.24 4.48	98.74 0.71
	Air		68.63 0.78	99.03 0.54

5.4 Mineral Characterisation of Coals, Chars and Ashes

In order to evaluate the transformation of the mineral species within the coal samples during the devolatilisation and combustion processes in the DTF, a computer-controlled scanning electron microscope (CCSEM), otherwise known as a mineral liberation analyser (MLA) provided a means to quantify the changes in mineral compositions, their associations and physical characteristics. A mineral library was created which included standard mineral EDX spectra composed of pure mineral species, and more complex miscellaneous mineral mixtures that contain varying proportions of trace elements, particularly the mixed aluminosilicates formed during char and ash formation. This section investigates the chemical and physical changes that occur during devolatilisation and char combustion of the coal samples when fired in the DTF. A muffle furnace was used to mimic the longer residence time conditions of the bottom ash which accumulates during boiler operation.

5.4.1 DTF and Muffle Furnace Samples

Table 5-11 shows the samples analysed by MLA with the respective number of particles and x-ray counts measured. The mounting procedure, outlined in 3.3.1 using carnauba wax, was used for each sample. The MLA operating conditions were kept constant with an accelerating voltage of 15 kV, magnification of 300x, spot size 7 and a minimum measured particle size of 10 μm . In order to determine the repeatability of the MLA technique, three repeats for each raw coal fraction were required to calculate standard deviations and confirm that at least 20,000 particles provided sufficient confidence in the measured mineral compositions and physical characteristics. In terms of x-ray counts, an average of approximately 260,000 were measured. Each sample required approximately

3 hours for x-ray collection, and additional time for mineral collection and analysing the results. The higher the number of particles analysed and x-ray counts collected the more computational time was required.

Table 5-11: CCSEM/MLA samples with the respective number of particles and
x-ray counts

Sample name	Coal type	Particles analysed	X-ray counts
Raw coals (53-75µm)	South African	19,977	474,122
	UK Cumberworth	18,996	421,216
	UK Kellingley	20,271	346,306
	USA Illinois	20,178	447,172
	UK Roundwood	19,929	307,932
DTF chars (1450°C, 200 ms)	South African	31,203	61,014
	UK Cumberworth	20,766	187,056
	UK Kellingley	15,840	216,082
	USA Illinois	22,613	147,078
	UK Roundwood	20,184	747,694
500°C muffle furnace ash of DTF chars	South African	142,961	408,076
	UK Cumberworth	22,924	86,484
	UK Kellingley	23,653	151,932
	USA Illinois	23,212	114,866
	UK Roundwood	20,692	172,380
Ashes of DTF chars (1450°C, 200ms, 5% O ₂)	South African	20,783	70,542
Ashes of DTF chars (1450°C, 600ms, 5% O ₂)	South African	20,314	89,652
Ashes of DTF chars (1450°C, 600ms, 10% O ₂)	South African	20,602	264,710

5.4.2 Repeatability of the MLA Mineral Characterisation

In order to validate the repeatability of the SEM-MLA system, three sample moulds were prepared for each coal. This serves to confirm that the sample mounting, grinding and polishing procedures produce samples that have a well dispersed and segregated distribution of particles with negligible statistical variation in the mineral composition for each mineral species identified. Table 5-12 shows the averages and standard deviations (as weight percentages %) based on three sample moulds for each 0-75 μm coal fraction. The standard deviations reported show how much the weight percentages for each mineral differ across the three sample moulds for each 0-75 μm coal sample. This data shows that the C/H/OS, which is the carbonaceous matter as either the volatile or fixed carbon component constitutes the highest mean proportion and standard deviations for each coal. As expected, the C/H/O/S mineral species corresponds to the elemental carbon and, volatile and fixed carbon contents presented in the Table 3-1, showing the proximate and ultimate analysis. This provides further confidence in the identification and semi-quantification ability of the SEM-MLA system. Additionally, Table 5-12 shows that the major mineral groups identified in all the coals are the oxides (mainly quartz and hematite), clays (mainly kaolinite and illite) and sulphides (mainly pyrite).

The figures below show the back scattered electron (BSE) micrographs and coloured mosaics for each coal, highlighting the mineral distribution and evidence of the particle dispersion. The mineral species legend in Figure 5-6 shows all those minerals represented in Table 5-12.

Table 5-12: SEM-MLA Mineral compositions of raw 0-75 µm coal fractions showing mean and standard deviations for three representative samples (weight percentage % basis)

Mineral Groups	Mineral Species	South African Koornfontein		UK Cumberworth		UK Kellingley		USA Illinois		UK Roundwood	
		Mean	Std.dev	Mean	Std.dev	Mean	Std.dev	Mean	Std.dev	Mean	Std.dev
Fixed/volatile carbon	C/H/O/S	67.54	3.41	50.49	1.18	56.43	6.15	77.32	1.57	15.78	2.89
Oxides	Quartz	3.85	0.61	10.71	0.43	1.57	0.62	4.19	0.89	5.39	0.21
	Hematite	0.23	0.08	0.10	0.06	0.01	0.01	0.19	0.13	0.63	0.19
	Rutile	0.06	0.01	0.04	0.01	0.01	0.01	0.04	0.02	0.03	0.02
Carbonates	Calcite	0.00	0.00	0.00	0.00	0.00	0.00	0.00	0.00	0.00	0.00
	Dolomite	1.23	0.28	0.00	0.00	0.00	0.00	0.18	0.10	0.00	0.00
	Ankerite	0.12	0.02	0.00	0.01	0.00	0.00	0.01	0.02	2.74	0.15
	Fairchildite	0.00	0.00	0.00	0.00	0.00	0.00	0.00	0.00	0.00	0.00
Halide	Sylvite	0.00	0.00	0.00	0.00	0.00	0.00	0.00	0.00	0.00	0.00
Clays	Kaolinite	13.33	1.12	4.21	0.15	5.04	1.65	4.83	0.25	2.54	0.08
	Montmorillonite	0.74	0.13	0.94	0.04	1.34	0.42	0.55	0.26	0.83	0.07
	Illite	4.88	0.54	24.99	0.57	26.78	4.29	3.37	0.24	61.05	1.87

Micas	Muscovite	0.02	0.01	0.08	0.06	0.01	0.01	0.04	0.02	0.31	0.05
	Biotite	0.00	0.00	0.00	0.00	0.00	0.01	0.05	0.06	0.02	0.03
Garnets	Almandine	0.04	0.02	1.58	0.18	0.03	0.03	0.08	0.06	0.70	0.03
	Pyrope	0.00	0.01	0.03	0.03	0.03	0.02	0.03	0.03	0.06	0.01
Feldspars	Plagioclase	0.00	0.00	0.00	0.00	0.00	0.00	0.00	0.00	0.00	0.00
	Sanidine	0.07	0.06	0.02	0.01	0.02	0.01	0.07	0.04	0.15	0.07
	Orthoclase	0.00	0.01	0.02	0.02	0.01	0.01	0.01	0.00	0.04	0.04
	Albite	0.03	0.04	0.13	0.05	0.05	0.03	0.04	0.03	0.17	0.03
Phosphates	Apatite	0.53	0.11	0.02	0.02	0.03	0.02	0.04	0.01	0.09	0.02
Sulphides	Pyrite	0.55	0.19	0.03	0.00	4.53	2.31	4.71	0.21	0.83	0.32
	Pyrrhotite	0.25	0.04	0.01	0.00	2.38	0.66	1.26	0.29	0.38	0.08
	Sphalerite	0.00	0.00	0.00	0.00	0.00	0.00	0.00	0.00	0.00	0.01
Sulphates	Barite	0.01	0.01	0.00	0.01	0.03	0.05	0.01	0.01	0.43	0.15
	Anhydrite	0.00	0.00	0.00	0.00	0.00	0.00	0.00	0.00	0.00	0.00
	Gypsum	0.01	0.02	0.00	0.00	0.01	0.01	0.03	0.04	0.04	0.04
	Polyhalite	0.15	0.02	2.41	0.33	0.03	0.02	0.56	0.25	1.24	0.04
Mixed Sulphates	Ca sulphate	0.01	0.02	0.00	0.00	0.03	0.03	0.07	0.05	0.05	0.04
	Ca/Mg sulphate	0.11	0.05	0.00	0.01	0.00	0.00	0.03	0.03	0.05	0.05

Mixed Oxides	K oxide	0.01	0.01	0.00	0.00	0.00	0.00	0.00	0.00	0.00	0.00
	Fe/K Oxide	0.60	0.26	2.26	0.24	0.10	0.03	0.26	0.16	2.63	0.47
	K/P/Mg/Ca oxide	0.00	0.00	0.00	0.00	0.00	0.00	0.00	0.00	0.00	0.00
	Ca oxide	1.18	0.11	0.01	0.00	0.05	0.05	0.54	0.04	0.24	0.07
	Ca/K/S/P oxide	0.03	0.02	0.13	0.05	0.00	0.01	0.01	0.01	0.59	0.17
	Cr oxide	0.00	0.00	0.00	0.00	0.00	0.00	0.00	0.00	0.00	0.00
	Al oxide	0.02	0.01	0.00	0.00	0.00	0.00	0.03	0.05	0.01	0.01
	Mg/Ca/K/Fe oxide	0.00	0.00	0.00	0.00	0.00	0.00	0.00	0.00	0.00	0.00
Mixed Aluminosilicates	Fe/Ca Al-silicate	0.02	0.01	0.16	0.02	0.01	0.00	0.06	0.05	1.41	1.82
	Ca Al-silicate	0.02	0.02	0.01	0.01	0.00	0.00	0.00	0.01	0.11	0.04
	Ca/Mg/Na Al-silicate	0.06	0.01	0.01	0.01	0.00	0.01	0.06	0.04	0.05	0.03
	Ca/Mg Al-silicate	0.06	0.03	0.01	0.01	0.00	0.01	0.01	0.01	0.04	0.01
	Ca/P Al-silicate	0.53	0.11	0.01	0.01	0.02	0.01	0.04	0.01	0.02	0.01
	Ca/K/Mg/Fe Al-silicate	0.37	0.03	0.23	0.06	0.10	0.05	0.08	0.04	0.11	0.05
	Ca/K/P/Mg Al-silicate	0.01	0.01	0.00	0.00	0.01	0.01	0.00	0.00	0.00	0.00
	Ca/Na Al-silicate	0.17	0.06	0.12	0.03	0.10	0.09	0.24	0.23	0.14	0.11
	Ca/Na/K Al-silicate	0.29	0.03	0.12	0.02	0.27	0.31	0.37	0.04	0.31	0.08
	Ca/P/Mg Al-silicate	0.05	0.02	0.01	0.01	0.00	0.01	0.02	0.03	0.01	0.01
	K/Na Al-silicate	0.02	0.01	0.03	0.02	0.37	0.37	0.04	0.04	0.06	0.03
	K/Fe/Ca/Na Al-silicate	2.82	0.51	1.06	0.10	0.60	0.61	0.50	0.03	0.67	0.15

	C/H/O/S		Quartz		Hematite
	Rutile		Calcite		Dolomite
	Ankerite		Fairchildite		Sylvite
	Kaolinite		Montmorillonite		Illite
	Muscovite		Biotite		Almandine
	Pyrope		Plagioclase		Sanidine
	Orthoclase		Albite		Apatite
	Pyrite		Pyrrhotite		Sphalerite
	Barite		Anhydrite		Gypsum
	Polyhalite		Ca sulphate		Ca/Mg sulphate
	K oxide		Fe/K Oxide		K/P/Mg/Ca oxide
	Ca oxide		Ca/K/S/P oxide		Cr oxide
	Al oxide		Mg/Ca/K/Fe oxide		Fe/Ca Al-silicate
	Ca Al-silicate		Ca/Mg/Na Al-silicate		Ca/Mg Al-silicate
	Ca/P Al-silicate		Ca/K/Mg/Fe Al-silicate		Ca/K/P/Mg Al-silicate
	Ca/Na Al-silicate		Ca/Na/K Al-silicate		Ca/P/Mg Al-silicate
	K/Na Al-silicate		K/Fe/Ca/Na Al-silicate		

Figure 5-6: MLA mineral species legend

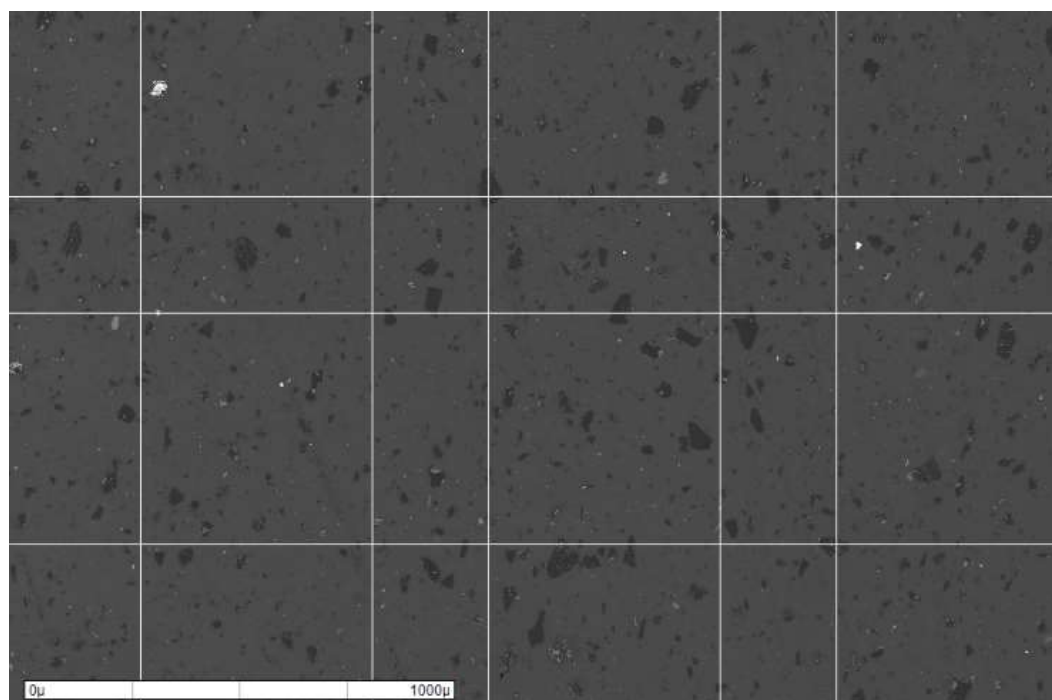


Figure 5-7: Electron micrograph of SA (Koorfontein) coal 0-75 µm fraction

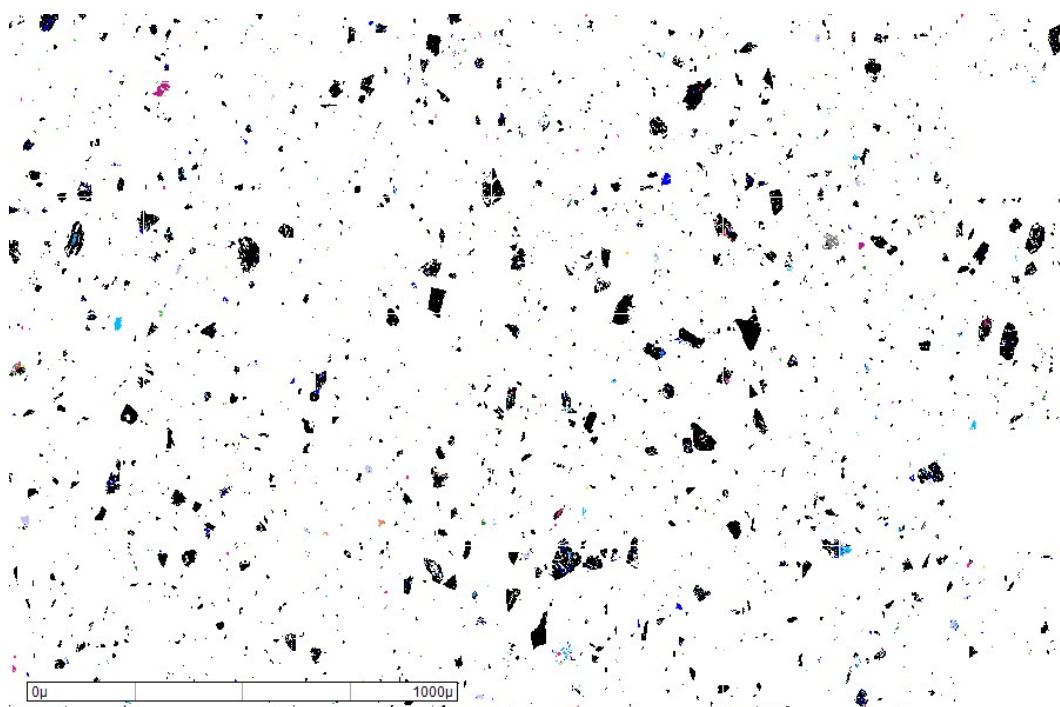


Figure 5-8: MLA coloured mosaic of SA (Koorfontein) 0-75 fraction

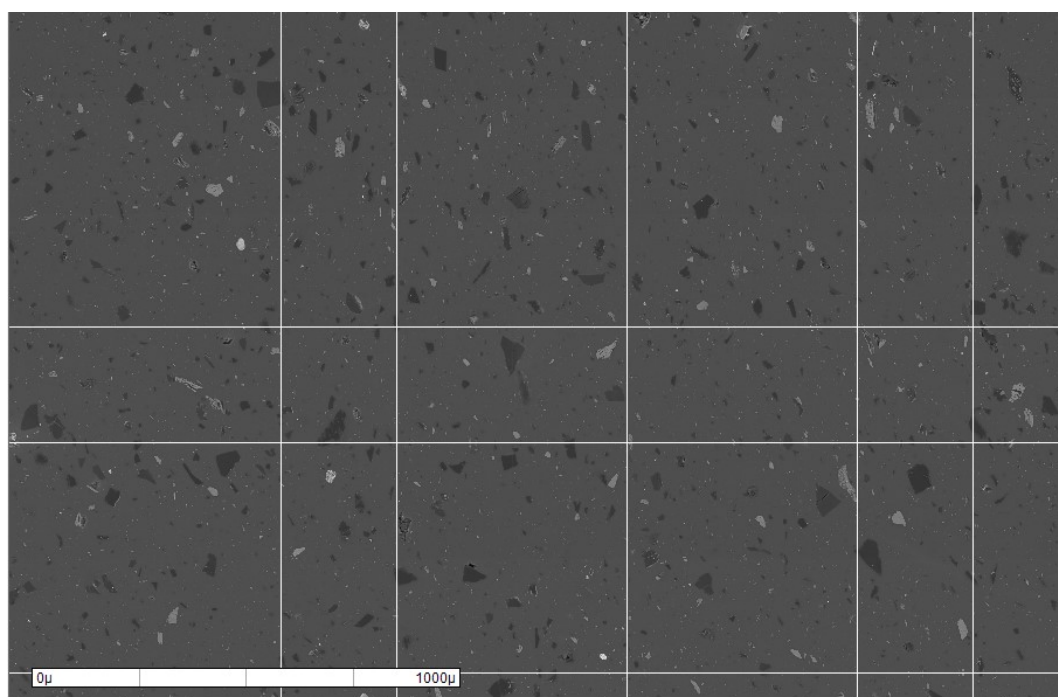


Figure 5-9: Electron micrograph of UK (Cumberworth) coal 0-75 μm fraction

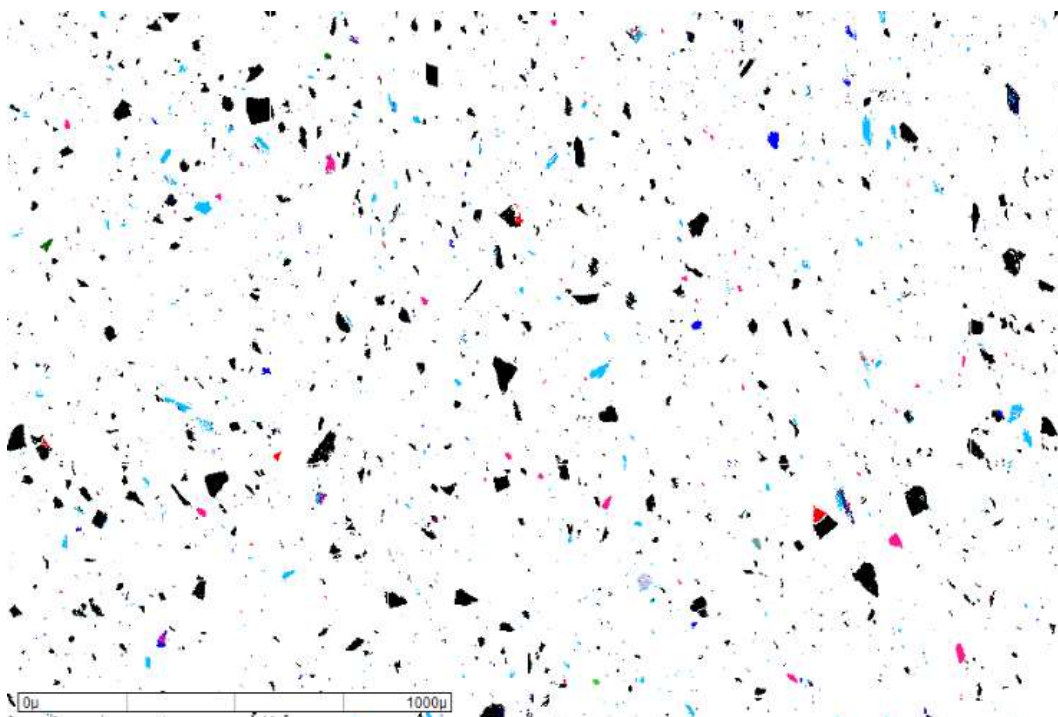


Figure 5-10: MLA coloured mosaic of UK (Cumberworth) 0-75 fraction

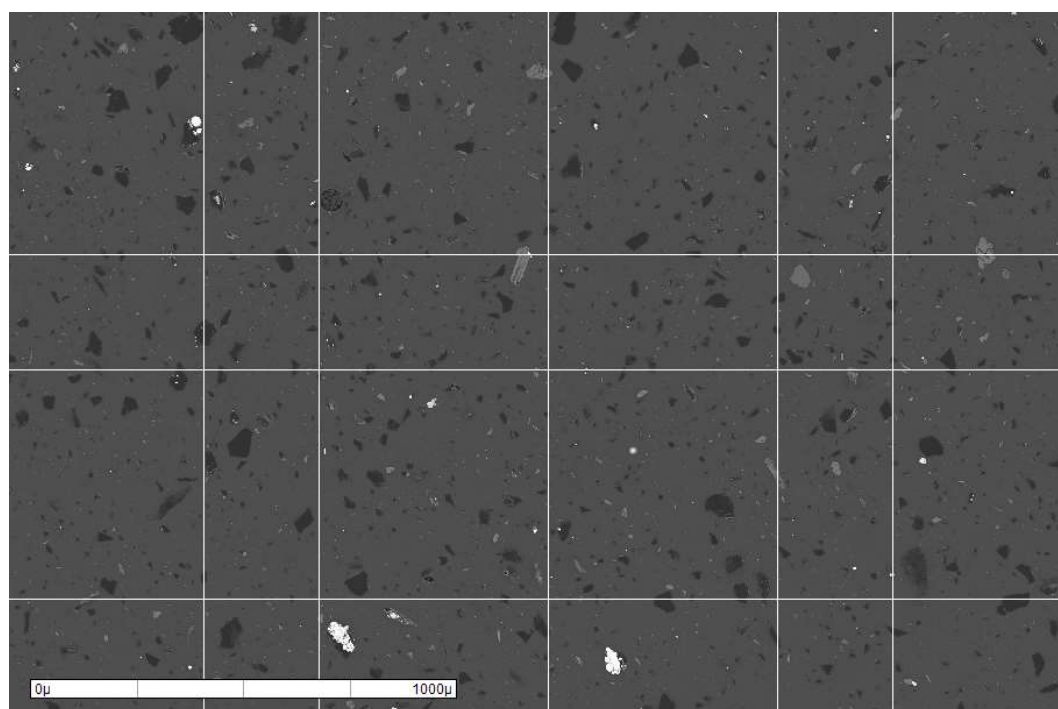


Figure 5-11: Electron micrograph of UK (Kellingley) coal 0-75 µm fraction

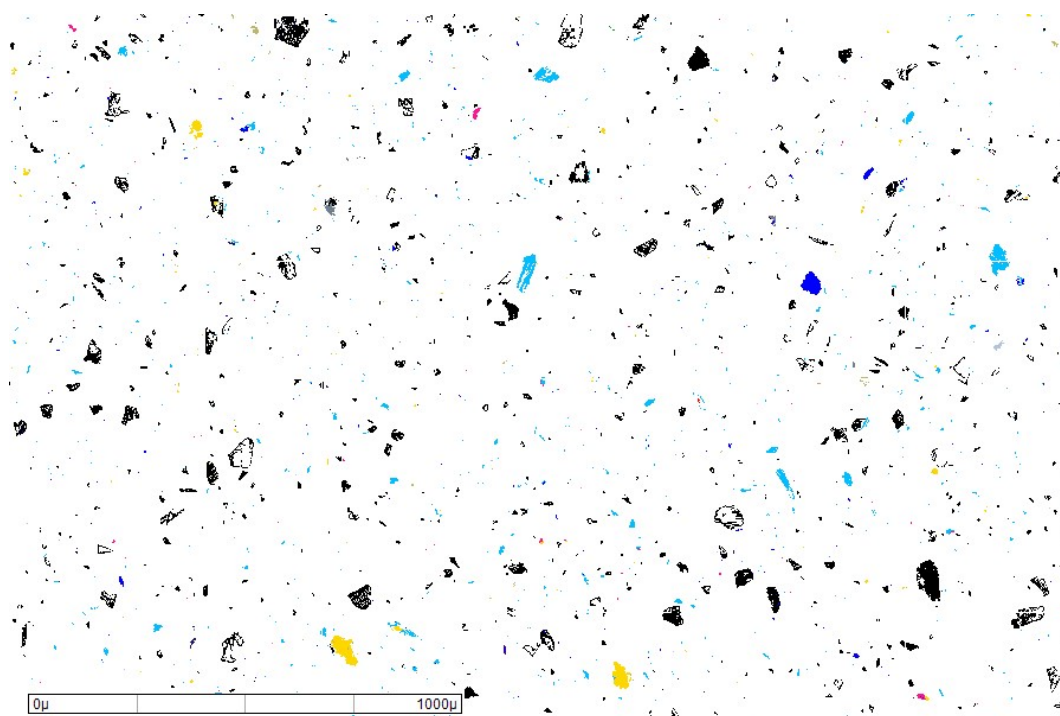


Figure 5-12: MLA coloured mosaic of UK (Kellingley) 0-75 fraction

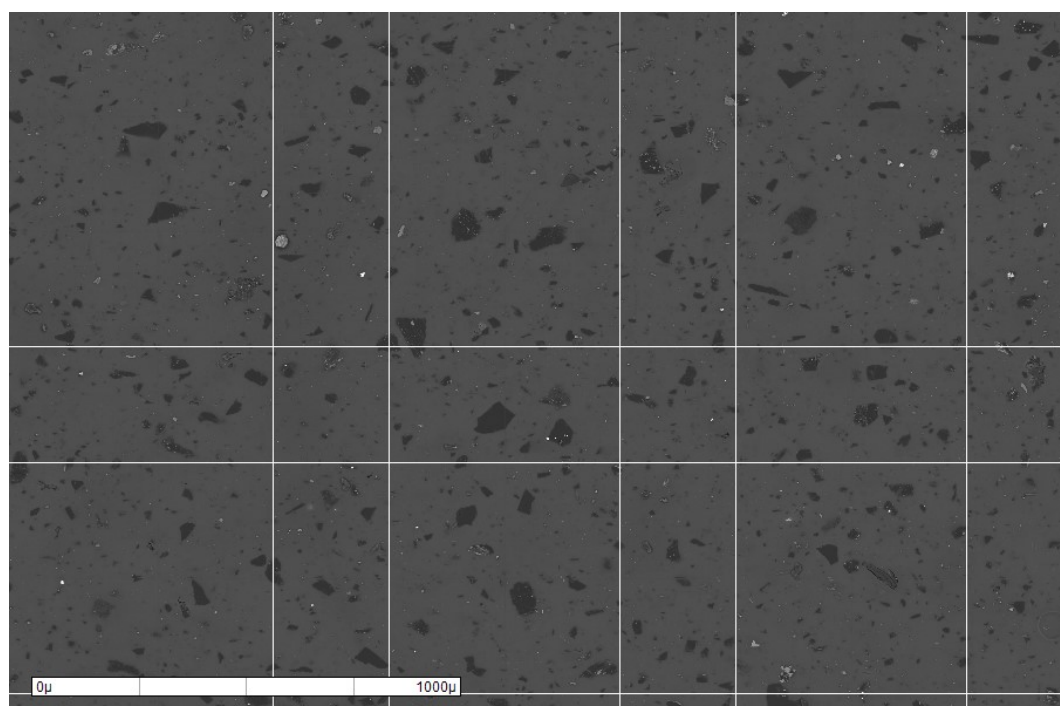


Figure 5-13: Electron micrograph of USA (Illinois) coal 0-75 μm fraction

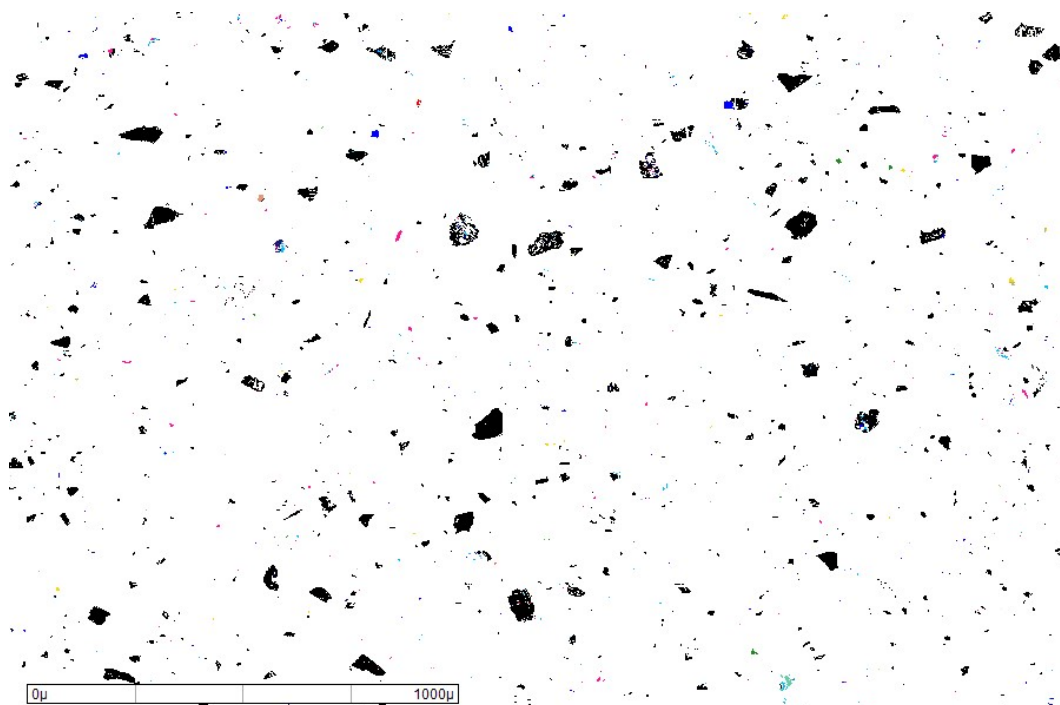


Figure 5-14: MLA coloured mosaic of USA (Illinois) 0-75 fraction

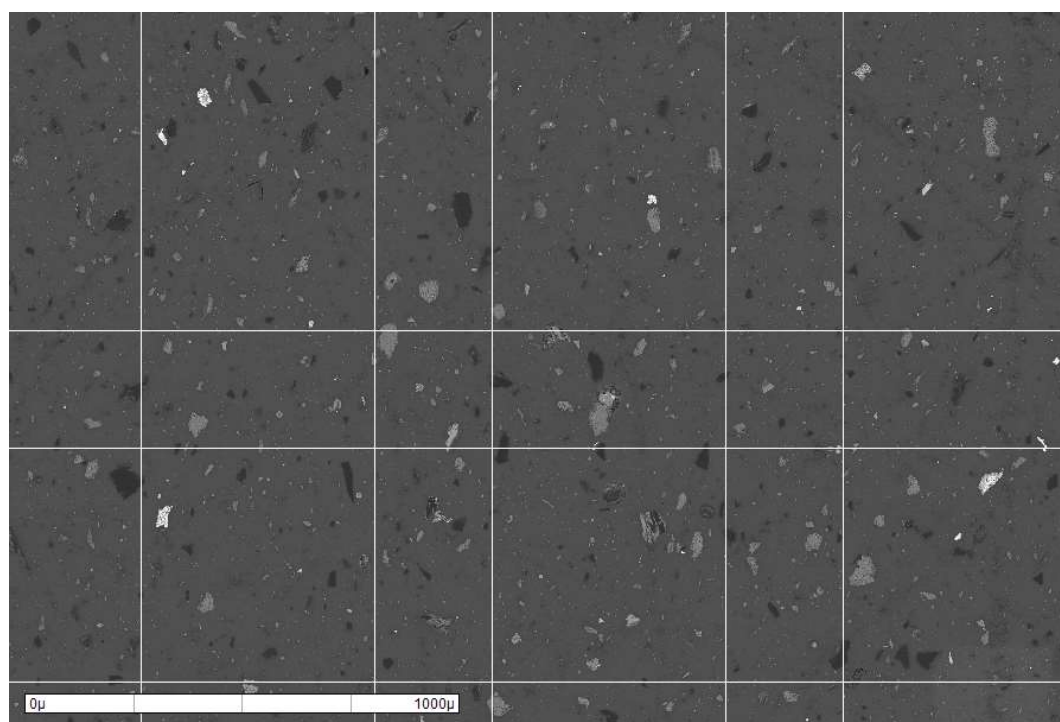


Figure 5-15: Electron micrograph of UK (Roundwood) coal 0-75 µm fraction

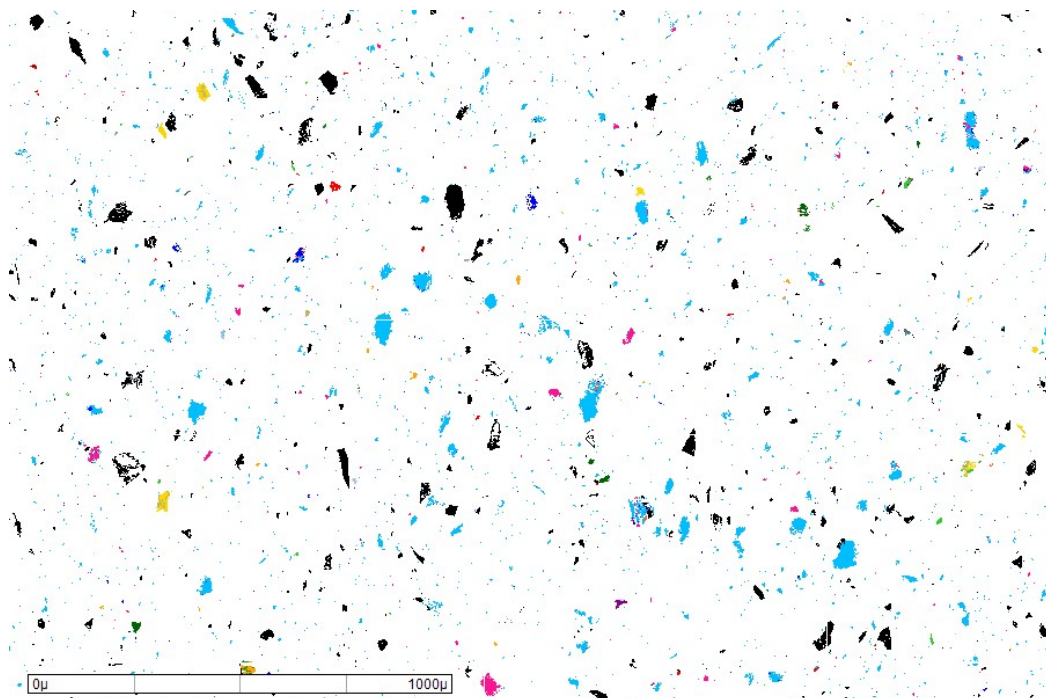


Figure 5-16: MLA coloured mosaic of UK (Roundwood) 0-75 fraction

5.4.3 Mineral Transformations and Associations during Devolatilisation and Char Combustion

The MLA mineral compositions of the 0-75 μm coal fractions presented in 5.4.2 confirmed that there was little statistical variation between consecutive MLA sample runs, however such a broad particle size range was not operationally feasible to fire into the DTF and so narrower 53-75 μm coal fractions were used. This section shows the mineral compositions of the 53-75 μm coal fractions, and the respective chars and ashes generated in the drop tube furnace under devolatilisation and char combustion conditions. The purpose is to determine the likely mineral transformations and the interactions of the minerals by investigating the extent of included and excluded mineral grains. Ternary phase diagrams have been produced to compare the initial coal, DTF char and DTF ashes produced. This information is important data to predict the likely deposition behaviour for specific fuels, in terms of the coalescence of minerals to form ash deposits in pulverised coal combustion boilers. This data can also be utilised as input parameters for ash formation models to predict the likely particle size distribution, minerals formed and the types of mineral phases which contribute to ash deposition phenomena. The following data has been presented in this section for each coal under study:

- Electron micrographs, coloured mosaics and mineral compositions of baseline 53-75 μm coal ash produced in a muffle furnace at 500°C.
- Electron micrographs and coloured mosaics of the 53-75 μm coal fraction, DTF char formed at 200 ms residence time and the resultant ash formed under the 5% O_2 at 200 ms and 600 ms respectively.

- Mineral category changes and likely transformations during devolatilisation and char combustion.

Table 5-13: Mineral compositions of 53-75 µm raw coal fractions (weight %)

Mineral Groups	Mineral Phase	South African Koornfontein	UK Cumberworth	UK Kellingley	USA Illinois	UK Roundwood
Fixed/volatile carbon	C/H/O/S	59.99%	67.89%	66.94%	82.52%	30.95%
Oxides	Quartz	4.61%	4.38%	4.75%	1.83%	4.49%
	Hematite	0.00%	0.08%	0.00%	0.17%	0.55%
	Rutile	0.11%	0.04%	0.02%	0.02%	0.03%
Carbonates	Calcite	0.05%	0.00%	0.00%	0.00%	0.00%
	Dolomite	0.43%	0.00%	0.00%	0.07%	0.04%
	Ankerite	0.02%	0.03%	0.01%	0.00%	3.90%
	Fairchildite	0.00%	0.01%	0.00%	0.00%	0.00%
	Sylvite	0.00%	0.00%	0.00%	0.02%	0.01%
Clays	Kaolinite	14.76%	2.72%	2.44%	3.54%	2.02%
	Montmorillonite	2.54%	1.70%	0.55%	1.04%	0.94%
	Illite	10.60%	19.50%	13.25%	3.40%	49.93%
Micas	Muscovite	0.60%	0.14%	0.46%	0.29%	0.60%
	Biotite	0.01%	0.06%	0.01%	0.00%	0.01%

Garnets	Almandine	0.02%	1.18%	0.02%	0.07%	0.76%
	Pyrope	0.03%	0.01%	0.00%	0.01%	0.02%
Feldspars	Plagioclase	0.00%	0.00%	0.00%	0.00%	0.00%
	Sanidine	0.15%	0.03%	0.01%	0.03%	0.19%
	Orthoclase	0.03%	0.01%	0.01%	0.01%	0.06%
	Albite	0.20%	0.14%	0.01%	0.07%	0.19%
Phosphates	Apatite	0.50%	0.00%	0.03%	0.02%	0.03%
Sulphides	Pyrite	0.65%	0.01%	7.87%	3.76%	0.93%
	Pyrrhotite	0.48%	0.05%	3.31%	1.74%	0.44%
	Sphalerite	0.00%	0.00%	0.00%	0.00%	0.00%
Sulphates	Barite	0.06%	0.00%	0.00%	0.05%	0.22%
	Anhydrite	0.00%	0.00%	0.00%	0.00%	0.00%
	Gypsum	0.00%	0.00%	0.00%	0.01%	0.02%
	Polyhalite	0.03%	0.00%	0.00%	0.00%	0.01%
Mixed Sulphates	Ca sulphate	0.00%	0.00%	0.01%	0.05%	0.12%
	Ca/Mg sulphate	0.70%	0.00%	0.00%	0.07%	0.10%
Mixed Oxides	K oxide	0.00%	0.00%	0.00%	0.00%	0.00%
	Fe/K Oxide	0.20%	1.56%	0.03%	0.11%	1.90%

	K/P/Mg/Ca oxide	0.00%	0.00%	0.00%	0.00%	0.00%
	Ca oxide	0.61%	0.03%	0.19%	0.42%	0.16%
	Ca/K/S/P oxide	0.04%	0.00%	0.00%	0.02%	0.19%
	Cr oxide	0.00%	0.00%	0.00%	0.00%	0.00%
	Al oxide	0.00%	0.00%	0.01%	0.01%	0.04%
	Mg/Ca/K/Fe oxide	0.00%	0.00%	0.00%	0.00%	0.00%
Mixed Aluminosilicates	Fe/Ca Al-silicate	0.01%	0.01%	0.00%	0.08%	0.18%
	Ca Al-silicate	0.00%	0.00%	0.00%	0.00%	0.13%
	Ca/Mg/Na Al-silicate	0.07%	0.01%	0.01%	0.02%	0.08%
	Ca/Mg Al-silicate	0.03%	0.00%	0.00%	0.01%	0.03%
	Ca/P Al-silicate	2.00%	0.01%	0.03%	0.12%	0.07%
	Ca/K/Mg/Fe Al-silicate	0.01%	0.01%	0.00%	0.00%	0.02%
	Ca/K/P/Mg Al-silicate	0.02%	0.00%	0.00%	0.02%	0.01%
	Ca/Na Al-silicate	0.14%	0.27%	0.01%	0.17%	0.07%
	Ca/Na/K Al-silicate	0.18%	0.04%	0.04%	0.20%	0.36%
	Ca/P/Mg Al-silicate	0.08%	0.00%	0.00%	0.00%	0.06%
	K/Na Al-silicate	0.01%	0.05%	0.01%	0.01%	0.08%
	K/Fe/Ca/Na Al-silicate	0.00%	0.03%	0.00%	0.01%	0.08%

Table 5-14: Mineral compositions of DTF coal chars produced at 1450 °C and 200 ms (weight %)

Mineral Groups	Mineral Phase	South African Koorfontein	UK Cumberworth	UK Kellingley	USA Illinois	UK Roundwood
Fixed/volatile carbon	C/H/O/S	24.34%	34.03%	25.61%	27.23%	30.41%
Oxides	Quartz	9.80%	7.05%	7.21%	8.85%	2.58%
	Hematite	0.00%	0.03%	0.00%	0.00%	0.64%
	Rutile	0.19%	0.01%	0.00%	0.01%	0.04%
Carbonates	Calcite	0.00%	0.00%	0.00%	0.01%	0.00%
	Dolomite	0.18%	0.00%	0.00%	0.01%	0.01%
	Ankerite	0.01%	0.00%	0.00%	0.00%	0.87%
	Fairchildite	0.01%	0.03%	0.00%	0.00%	0.00%
	Sylvite	0.00%	0.00%	0.00%	0.00%	0.00%
Clays	Kaolinite	49.70%	11.46%	15.11%	27.21%	1.32%
	Montmorillonite	2.65%	3.01%	1.84%	2.89%	2.26%
	Illite	5.11%	38.25%	20.70%	8.69%	55.65%
Micas	Muscovite	0.10%	0.20%	0.11%	0.28%	0.58%
	Biotite	0.00%	0.00%	0.00%	0.00%	0.01%
Garnets	Almandine	0.08%	0.76%	0.00%	0.06%	0.97%
	Pyrope	0.00%	0.01%	0.02%	0.00%	0.00%

Feldspars	Plagioclase	0.00%	0.00%	0.00%	0.00%	0.00%
	Sanidine	0.00%	0.05%	0.05%	0.02%	0.58%
	Orthoclase	0.00%	0.02%	0.00%	0.00%	0.33%
	Albite	0.07%	0.10%	0.01%	0.12%	0.17%
Phosphates	Apatite	0.17%	0.03%	0.00%	0.01%	0.04%
Sulphides	Pyrite	0.00%	0.00%	14.81%	0.00%	0.00%
	Pyrrhotite	0.76%	0.08%	13.53%	17.39%	0.64%
	Sphalerite	0.00%	0.00%	0.00%	0.00%	0.00%
Sulphates	Barite	0.00%	0.00%	0.00%	0.00%	0.17%
	Anhydrite	0.00%	0.00%	0.00%	0.00%	0.00%
	Gypsum	0.00%	0.00%	0.00%	0.00%	0.00%
	Polyhalite	0.09%	0.02%	0.00%	0.01%	0.00%
Mixed Sulphates	Ca sulphate	0.00%	0.00%	0.02%	0.20%	0.01%
	Ca/Mg sulphate	0.60%	0.00%	0.02%	0.24%	0.10%
Mixed Oxides	K oxide	0.00%	0.00%	0.00%	0.00%	0.00%
	Fe/K Oxide	0.83%	3.32%	0.06%	1.97%	0.31%
	K/P/Mg/Ca oxide	0.00%	0.00%	0.00%	0.00%	0.00%
	Ca oxide	0.64%	0.08%	0.08%	0.92%	0.23%

	Ca/K/S/P oxide	0.00%	0.00%	0.00%	0.15%	0.12%
	Cr oxide	0.00%	0.00%	0.00%	0.00%	0.00%
	Al oxide	0.01%	0.07%	0.01%	0.10%	0.01%
	Mg/Ca/K/Fe oxide	0.24%	0.01%	0.02%	0.19%	0.02%
Mixed Aluminosilicates	Fe/Ca Al-silicate	0.01%	0.02%	0.00%	0.01%	0.37%
	Ca Al-silicate	0.03%	0.00%	0.00%	0.07%	0.09%
	Ca/Mg/Na Al-silicate	0.16%	0.00%	0.02%	0.23%	0.18%
	Ca/Mg Al-silicate	0.29%	0.01%	0.00%	0.17%	0.14%
	Ca/P Al-silicate	2.20%	0.07%	0.10%	0.70%	0.05%
	Ca/K/Mg/Fe Al-silicate	0.01%	0.04%	0.00%	0.02%	0.02%
	Ca/K/P/Mg Al-silicate	0.03%	0.00%	0.00%	0.01%	0.00%
	Ca/Na Al-silicate	0.14%	0.10%	0.11%	0.12%	0.10%
	Ca/Na/K Al-silicate	1.16%	0.64%	0.11%	1.90%	0.32%
	Ca/P/Mg Al-silicate	0.34%	0.00%	0.00%	0.01%	0.02%
	K/Na Al-silicate	0.00%	0.37%	0.41%	0.20%	0.12%
	K/Fe/Ca/Na Al-silicate	0.02%	0.07%	0.00%	0.00%	0.49%

Table 5-15: Mineral compositions of muffle furnace coal ashes produced at 500°C under air (weight %)

Mineral Groups	Mineral Phase	South African Koorfontein	UK Cumberworth	UK Kellingley	USA Illinois	UK Roundwood
Fixed/volatile carbon	C/H/O/S	1.77%	9.35%	4.72%	4.10%	0.87%
Oxides	Quartz	11.75%	21.13%	5.43%	11.98%	22.06%
	Hematite	0.09%	0.03%	0.02%	0.21%	0.08%
	Rutile	0.10%	0.00%	0.00%	0.02%	0.00%
Carbonates	Calcite	0.00%	0.00%	0.00%	0.00%	0.00%
	Dolomite	0.13%	0.00%	0.00%	0.00%	0.03%
	Ankerite	0.04%	0.00%	0.00%	0.00%	0.99%
	Fairchildite	0.01%	0.00%	0.00%	0.00%	0.00%
	Sylvite	0.00%	0.00%	0.00%	0.00%	0.00%
Clays	Kaolinite	63.20%	14.32%	23.44%	20.97%	15.96%
	Montmorillonite	3.88%	6.37%	4.41%	5.50%	3.74%
	Illite	2.53%	41.93%	51.81%	8.64%	39.19%
Micas	Muscovite	0.33%	0.32%	0.64%	0.14%	0.85%
	Biotite	0.00%	0.00%	0.00%	0.00%	0.00%
Garnets	Almandine	0.13%	0.79%	0.40%	1.28%	1.26%
	Pyrope	0.00%	0.00%	0.00%	0.06%	0.23%
Feldspars	Plagioclase	0.00%	0.00%	0.00%	0.00%	0.00%
	Sanidine	0.19%	0.20%	0.21%	0.08%	0.19%
	Orthoclase	0.07%	0.20%	0.05%	0.00%	0.02%
	Albite	0.07%	0.03%	0.15%	0.19%	0.14%
Phosphates	Apatite	0.26%	0.00%	0.02%	0.01%	0.00%
Sulphides	Pyrite	0.00%	0.00%	0.00%	0.00%	0.00%
	Pyrrhotite	0.01%	0.00%	0.01%	0.35%	0.00%
	Sphalerite	0.00%	0.00%	0.00%	0.00%	0.00%

Sulphates	Barite	0.10%	0.00%	0.00%	0.00%	0.12%
	Anhydrite	0.00%	0.00%	0.00%	0.00%	0.00%
	Gypsum	0.00%	0.00%	0.00%	0.02%	0.00%
	Polyhalite	0.17%	0.00%	0.00%	0.00%	0.03%
Mixed Sulphates	Ca sulphate	0.71%	0.13%	0.25%	3.72%	0.49%
	Ca/Mg sulphate	2.81%	0.00%	0.01%	0.44%	0.94%
Mixed Oxides	K oxide	0.00%	0.00%	0.00%	0.00%	0.00%
	Fe/K Oxide	1.18%	0.59%	4.11%	36.90%	4.04%
	K/P/Mg/Ca oxide	0.00%	0.00%	0.00%	0.00%	0.00%
	Ca oxide	4.79%	0.00%	0.03%	0.25%	0.11%
	Ca/K/S/P oxide	0.04%	0.00%	0.00%	0.00%	0.01%
	Cr oxide	0.01%	0.00%	0.00%	1.03%	0.00%
	Al oxide	0.14%	0.11%	0.07%	0.02%	0.01%
	Mg/Ca/K/Fe oxide	0.36%	0.00%	0.00%	0.03%	0.90%
	Fe/Ca Al-silicate	0.10%	0.02%	0.09%	0.15%	0.54%
Mixed Aluminosilicates	Ca Al-silicate	0.08%	0.00%	0.01%	0.06%	0.08%
	Ca/Mg/Na Al-silicate	0.36%	0.06%	0.03%	0.10%	0.33%
	Ca/Mg Al-silicate	0.48%	0.23%	0.03%	0.21%	0.52%
	Ca/P Al-silicate	1.87%	0.01%	0.05%	0.25%	0.18%
	Ca/K/Mg/Fe Al-silicate	0.06%	0.02%	0.01%	0.06%	0.03%
	Ca/K/P/Mg Al-silicate	0.01%	0.00%	0.00%	0.00%	0.00%
	Ca/Na Al-silicate	0.09%	0.03%	0.03%	0.14%	0.04%
	Ca/Na/K Al-silicate	1.68%	1.73%	2.70%	2.47%	1.86%
	Ca/P/Mg Al-silicate	0.24%	0.00%	0.00%	0.02%	0.04%
	K/Na Al-silicate	0.17%	2.30%	1.13%	0.61%	4.03%
	K/Fe/Ca/Na Al-silicate	0.03%	0.07%	0.14%	0.00%	0.09%

Table 5-16: Mineral compositions of the DTF ashes produced from DTF South

African Char (1450°C, 200ms, N₂) (weight %)

Mineral Groups	Mineral Phase	SAC DTF (1450°C, 200ms, 5% O ₂)	SAC DTF (1450°C, 600ms, 5% O ₂)	SAC DTF (1450°C, 600ms, 10% O ₂)
		Ash	Ash	Ash
Fixed/volatile carbon	C/H/O/S	7.89%	1.44%	2.50%
Oxides	Quartz	14.64%	13.12%	15.60%
	Hematite	0.07%	0.30%	1.40%
	Rutile	0.00%	0.03%	0.08%
Carbonates	Calcite	0.00%	0.01%	0.03%
	Dolomite	0.33%	0.18%	0.66%
	Ankerite	0.12%	0.00%	0.17%
	Fairchildite	0.00%	0.04%	0.00%
Halide	Sylvite	0.00%	0.00%	0.00%
Clays	Kaolinite	58.68%	66.29%	51.67%
	Montmorillonite	5.81%	4.92%	6.33%
	Illite	3.40%	1.67%	7.74%
Micas	Muscovite	0.31%	0.71%	0.18%
	Biotite	0.00%	0.04%	0.00%
Garnets	Almandine	0.08%	0.16%	0.45%
	Pyrope	0.00%	0.00%	0.00%
Feldspars	Plagioclase	0.00%	0.00%	0.00%
	Sanidine	0.04%	0.15%	0.34%
	Orthoclase	0.07%	0.14%	0.08%
	Albite	0.06%	0.03%	0.05%
Phosphates	Apatite	0.03%	0.01%	0.58%
Sulphides	Pyrite	0.00%	0.00%	0.00%
	Pyrrhotite	0.01%	0.00%	0.01%
	Sphalerite	0.00%	0.00%	0.00%
Sulphates	Barite	0.00%	0.00%	0.00%
	Anhydrite	0.00%	0.00%	0.00%
	Gypsum	0.00%	0.00%	0.00%
	Polyhalite	0.03%	0.00%	0.01%
Mixed Sulphates	Ca sulphate	0.02%	0.02%	0.00%
	Ca/Mg sulphate	0.17%	0.17%	0.44%
Mixed Oxides	K oxide	0.00%	0.00%	0.00%

	Fe/K Oxide	1.08%	1.16%	0.65%
Mixed Oxides Mixed Aluminosilicates	K/P/Mg/Ca oxide	0.00%	0.00%	0.00%
	Ca oxide	1.04%	2.85%	1.56%
	Ca/K/S/P oxide	0.02%	0.02%	0.00%
	Cr oxide	0.00%	0.00%	0.60%
	Al oxide	0.01%	0.01%	0.02%
	Mg/Ca/K/Fe oxide	0.51%	0.30%	0.20%
	Fe/Ca Al-silicate	0.05%	0.05%	0.27%
	Ca Al-silicate	0.09%	0.17%	0.92%
Mixed Aluminosilicates	Ca/Mg/Na Al-silicate	0.40%	0.64%	0.97%
	Ca/Mg Al-silicate	0.48%	0.75%	0.92%
	Ca/P Al-silicate	1.65%	1.28%	1.71%
	Ca/K/Mg/Fe Al-silicate	0.05%	0.03%	0.08%
	Ca/K/P/Mg Al-silicate	0.01%	0.00%	0.00%
	Ca/Na Al-silicate	0.21%	0.04%	0.11%
	Ca/Na/K Al-silicate	2.26%	2.59%	3.03%
	Ca/P/Mg Al-silicate	0.24%	0.16%	0.54%
	K/Na Al-silicate	0.14%	0.48%	0.03%
	K/Fe/Ca/Na Al-silicate	0.02%	0.02%	0.06%

Table 5-17: XRF data of raw coal samples

Oxides	UK Cumberworth	UK Roundwood	Poland Stefanów	UK Kellingley	South African	USA Illinois
SiO ₂	58.00	51.50	53.14	47.40	46.19	45.71
Al ₂ O ₃	24.58	27.15	30.60	29.34	29.42	26.86
Fe ₂ O ₃	7.73	7.59	6.67	12.70	3.12	13.28
CaO	2.09	2.75	2.16	1.23	8.20	4.52
MgO	1.30	2.09	1.16	1.38	1.88	1.00
TiO ₂	0.77	0.94	1.40	1.20	1.72	1.28
Na ₂ O	0.37	0.45	0.41	1.45	0.21	0.00
K ₂ O	3.31	4.56	2.20	4.00	0.62	1.33
P ₂ O ₅	0.27	0.19	1.47	0.20	1.89	0.85
SO ₃	1.34	2.36	0.48	0.75	6.14	4.87
BaO	0.09	0.32	0.15	0.11	0.27	0.00
SrO	0.04	0.04	0.08	0.05	0.26	0.12
C	0.11	0.07	0.09	0.19	0.07	0.18
SiO ₂ : Al ₂ O ₃	2.36	1.90	1.74	1.62	1.57	1.70
SiO ₂ : Fe ₂ O ₃	7.50	6.78	7.97	3.73	14.80	3.44
SiO ₂ - 1.5 Al ₂ O ₃	21.13	10.78	7.24	3.38	2.05	5.42
B:A ratio	0.18	0.22	0.17	0.27	0.21	0.28

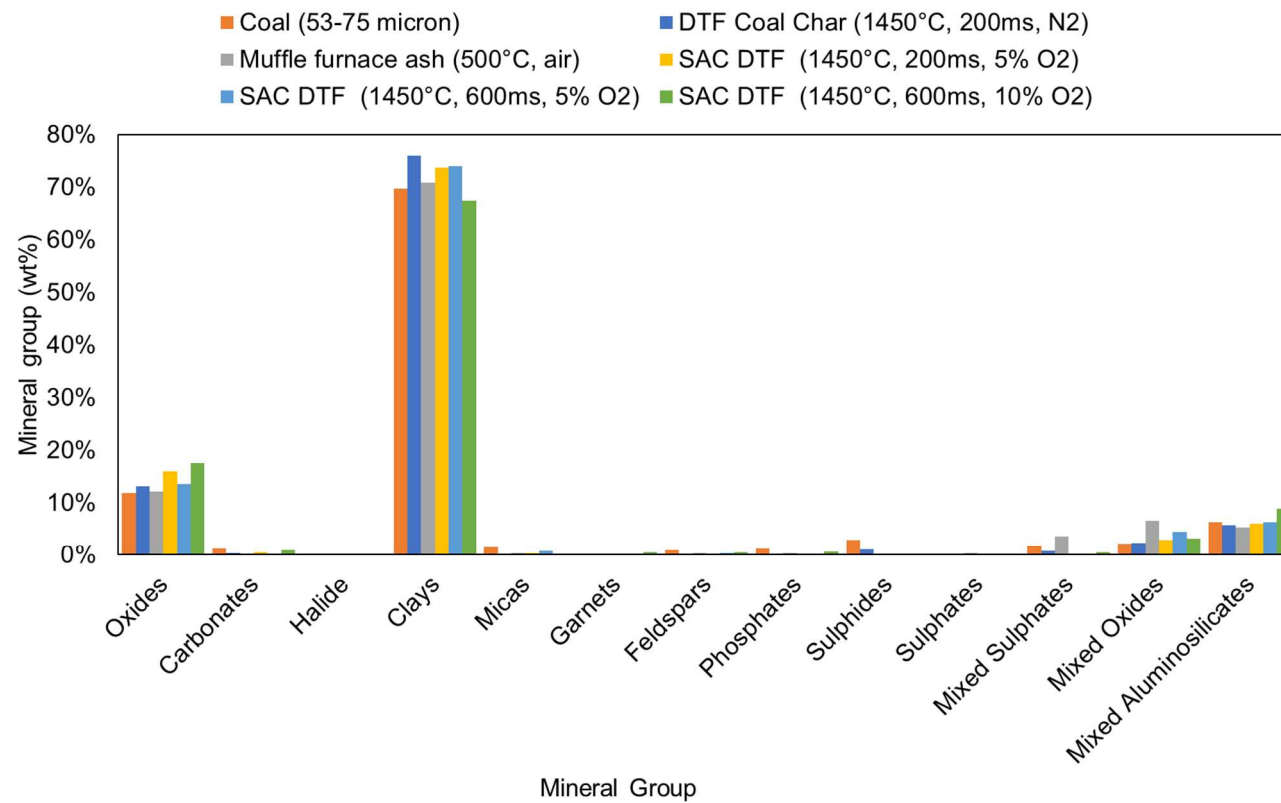


Figure 5-17: Mineral group changes of South African (Koorfontein) Coal during devolatilisation and char combustion

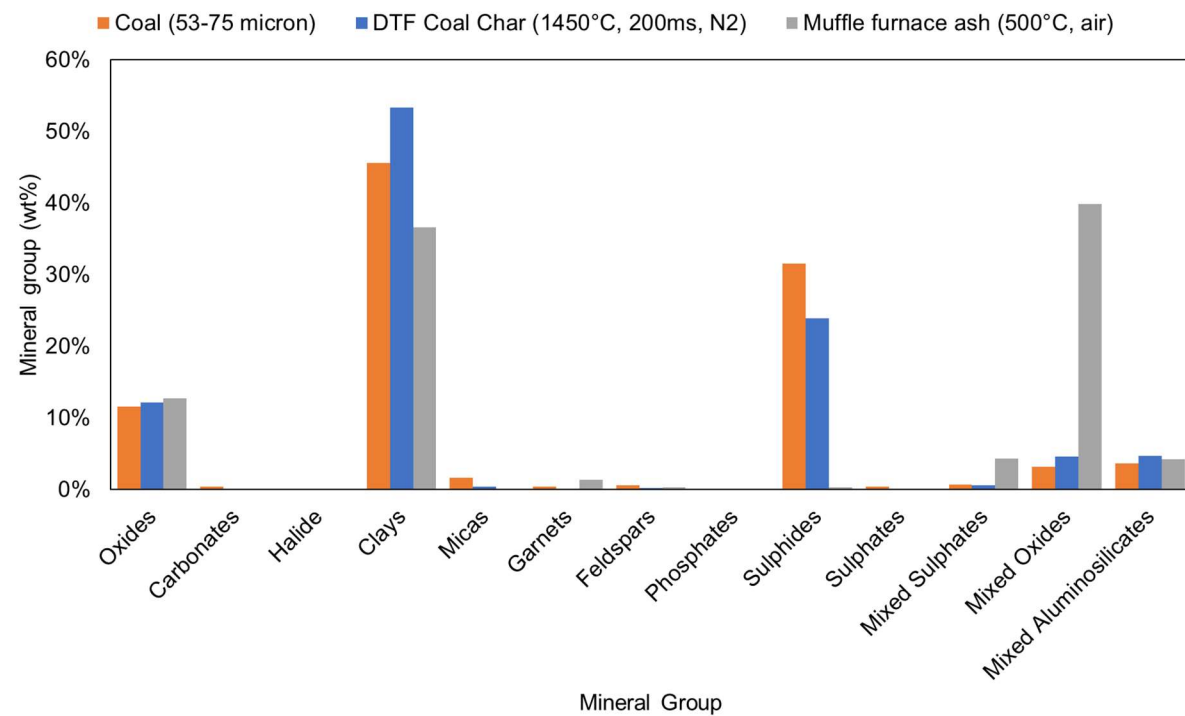


Figure 5-18: Mineral group changes of USA Illinois Coal during devolatilisation and char combustion

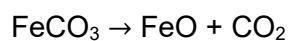
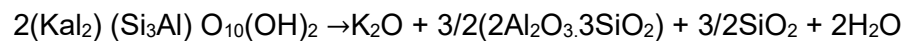
Table 5-13, Table 5-14 and Table 5-15 show the MLA data of the mineral species present within the five coals. It is evident that quartz, kaolinite, pyrite and illite are the major minerals found in the five coals, whilst minor minerals such as montmorillonite and muscovite account for smaller fractions, depending on coal origin. It should be noted that the elemental compositions of these minerals have been previously outlined in Table 4-3 and Table 4-4. These minerals have been identified by XRD in Figure 5-4 and Figure 5-5. The mineral association data shows the mineral volume distribution percentage between the mineral groups and the fixed/volatile carbon, and the physical association on the MLA coloured mosaics. Previous studies have used 2D graphs showing the partitioning of elements within the included and excluded minerals[62], whilst these 3D graphs show the specific minerals which are associating with one another.

Figure 5-17 shows that during coal devolatilisation and char combustion there were few prominent mineral transformations which occurred except the minor decomposition of pyrite and pyrrhotite to hematite. The clay (aluminosilicate) and oxide minerals remained stable and a small amount of the fluxing elements (K, Na and Ca) transformed into the mixed aluminosilicate group. These minor mineral transformations are characteristic of unreactive coals[262].

Figure 5-19 shows the included minerals enclosed within the fixed/volatile carbon which are less susceptible to mineral transformations than the excluded minerals, whereas after devolatilisation and the loss of volatile carbon the majority of these minerals are excluded at the high temperatures and heating rates, as shown in Figure 5-20. It would be expected that a considerable fraction of minerals remain within the char structure surrounded by fixed carbon. The

muffle furnace ash at 500°C, shown in Figure 5-21, shows that all the fixed/volatile carbon has been removed leaving only the excluded minerals with few mineral associations suggesting a negligible amount of melting behaviour. However, at higher temperatures more significant mineral transformations will occur. Figure 5-22 shows char combustion at 1450°C, 5% O₂ and 200 ms where the originally excluded minerals start to coalesce, particularly the mixed oxides and mixed aluminosilicate groups. As the residence time increases further to 600 ms, as shown in Figure 5-23, the excluded mineral associations with mixed aluminosilicates increases further, possibly due to the laminar, entrained flow mixing between the carrier gas and solid particles in the DTF. At this stage the fixed carbon has been fully combusted leaving the minerals within the ash.

In contrast, Figure 5-18 shows the USA Illinois coal mineral transformations during devolatilisation and muffle furnace ashing at 500°C. The common mineral transformations are clearly shown, particularly the reduction of pyrite to pyrrhotite and subsequent oxidation to iron oxide. However, rather than pure hematite formation, an Fe/K oxide phase is formed containing trace potassium. The fluxing of potassium is likely to originate from the clay minerals, such as illite. The formation of Fe/K oxide could result from the following mineral phase reaction producing a mixture of FeO and K₂O[62]:



The remaining coal mineral transformation are displayed in Appendix 2.

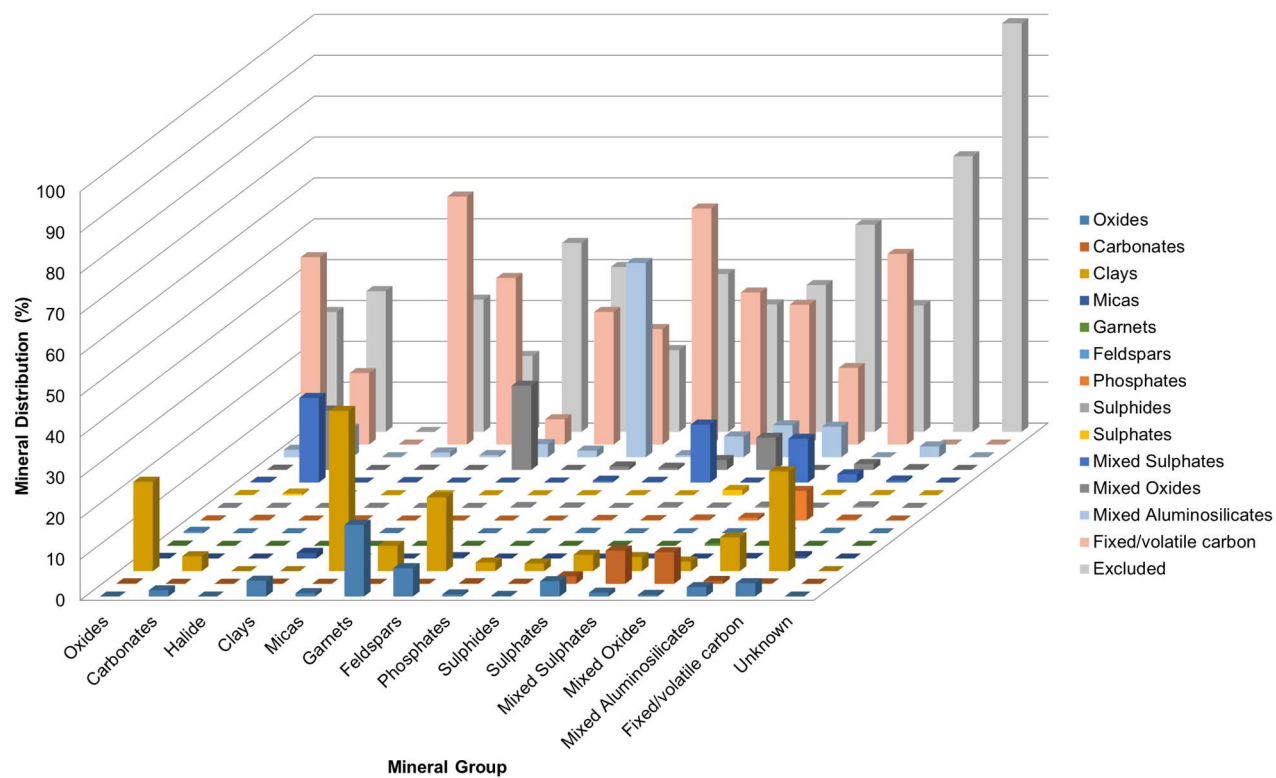


Figure 5-19: Mineral associations of South African (Koorfontein) 53-75 µm coal fraction

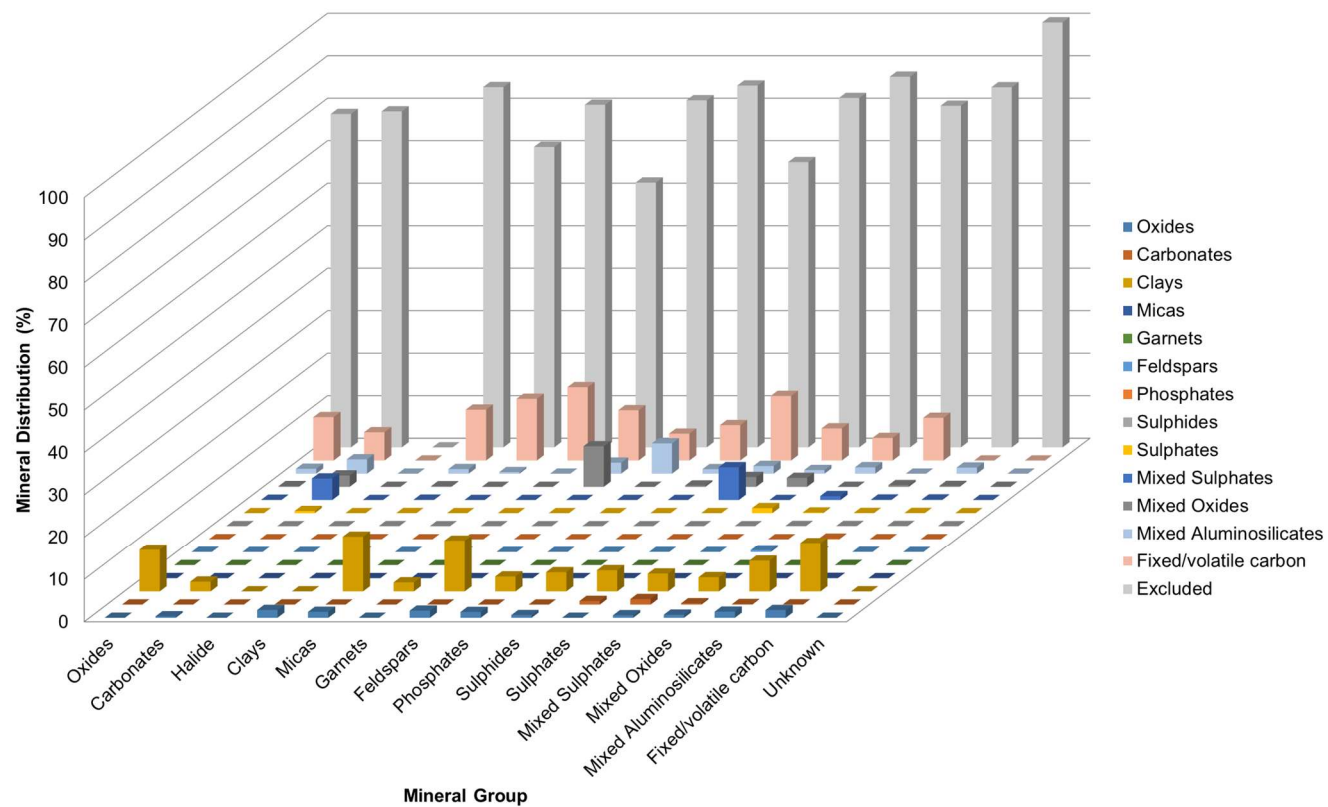


Figure 5-20: Mineral associations of DTF South African (Koornfontein) Char (1450°C, 200 ms)

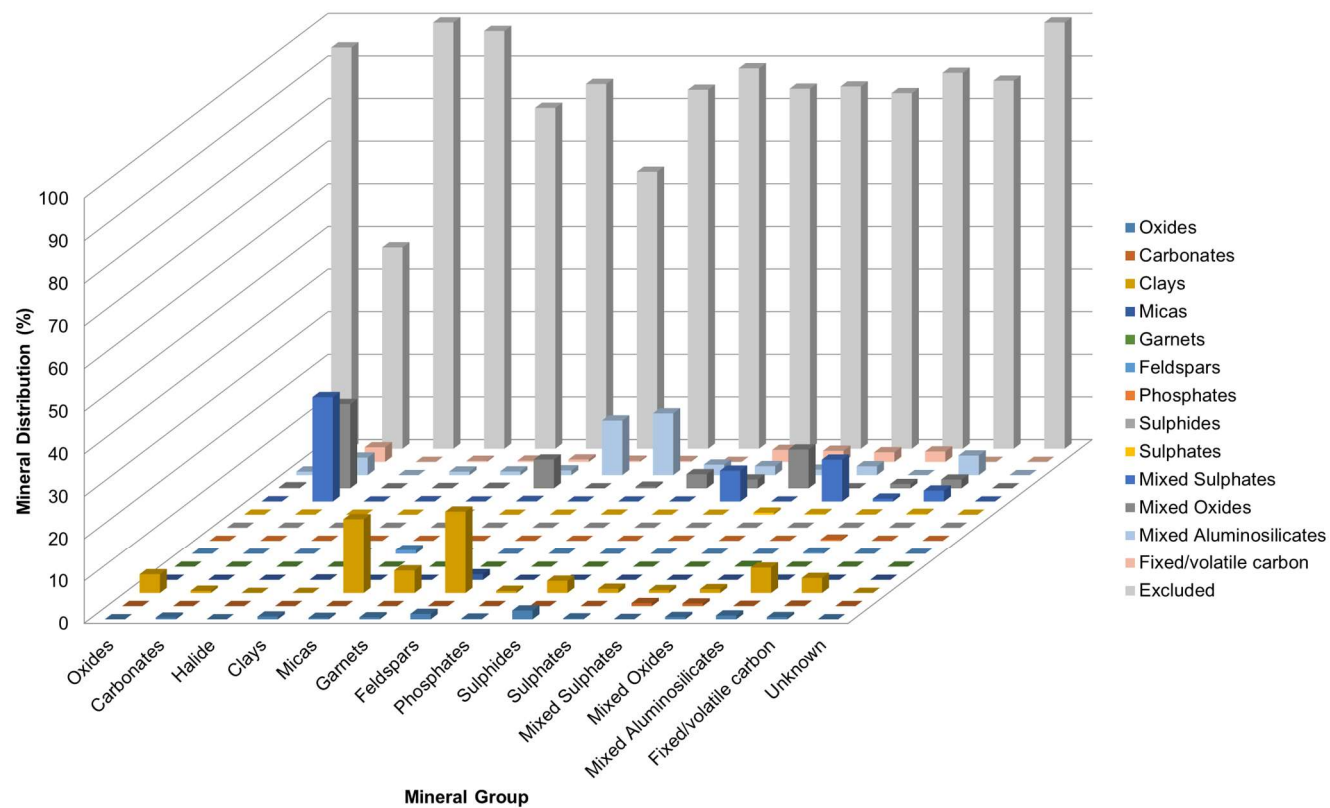


Figure 5-21: Mineral associations of South African (Koorfontein) muffle furnace ash at 500°C

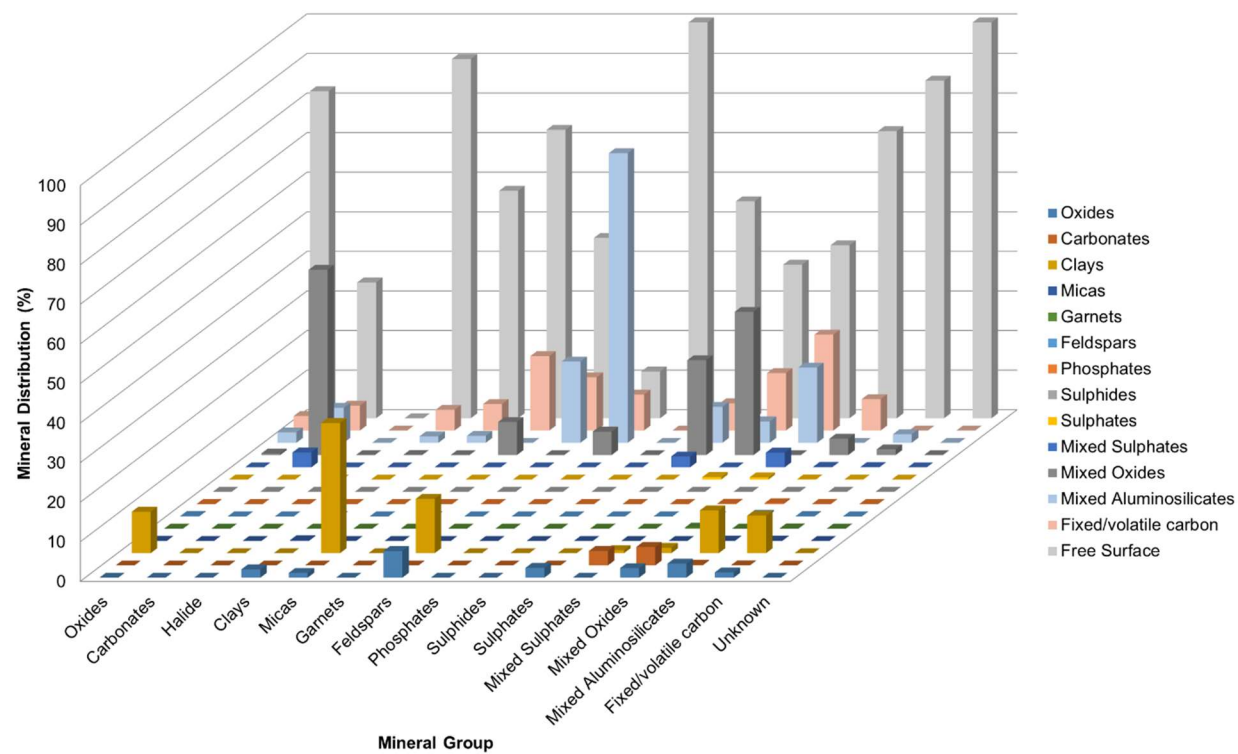


Figure 5-22: Mineral associations of DTF South African (Koorfontein) ash (5% O₂, 1450°C, 200 ms)

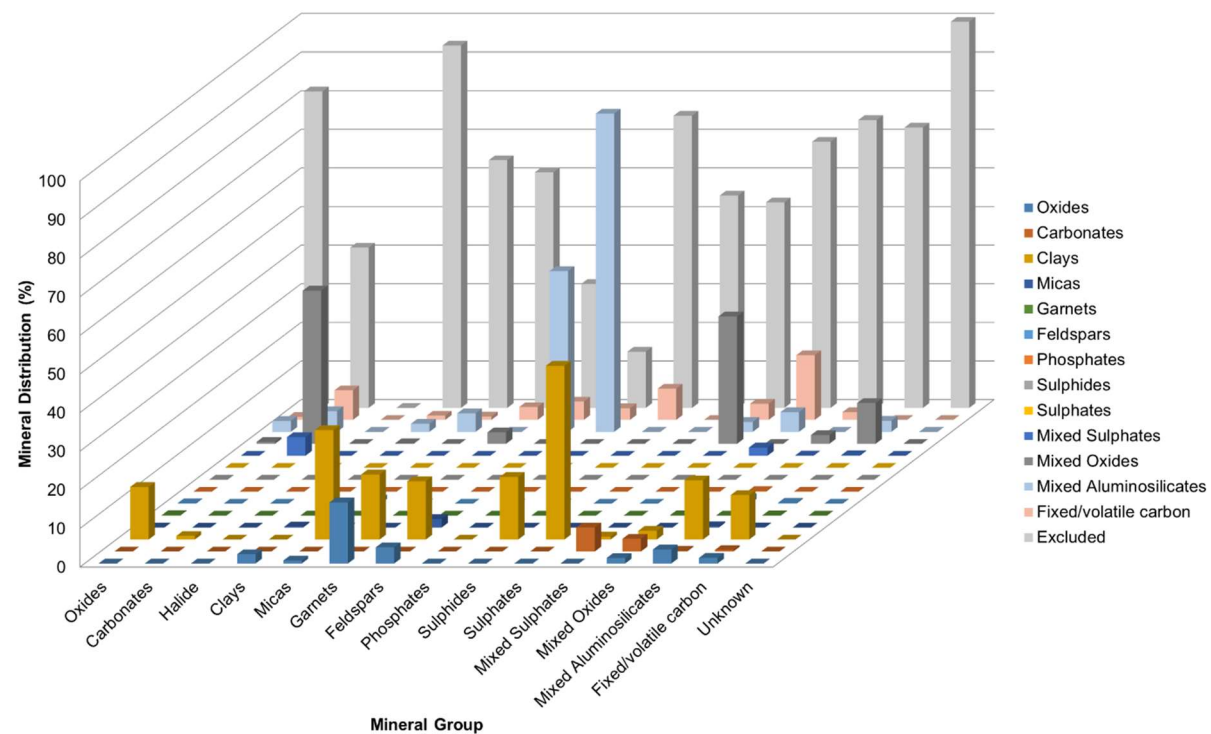


Figure 5-23: Mineral associations of DTF South African (Koorfontein) ash (5% O₂, 1450°C, 600 ms)

5.4.4 MLA Coloured Mosaics of Coal Fractions, DTF Chars, DTF Ashes and Muffle Furnace Ashes

The BSE images and coloured mosaics presented below show the evolution of the individual coal particles during devolatilisation and char combustion in the drop tube furnace. Figure 5-26 shows that the SAC particles contain predominately carbonaceous matter with kaolinite and some quartz interspersed amongst the grains. The particles are slightly elongated with angular edges, typical of coal. Figure 5-28 shows the DTF SAC char particles with the common char morphologies such as tenuisphere, crassisphere, tenuinetwork, crassinetwork, inertoid and fusinoid[263]. Finally, Figure 5-30 shows the muffle furnace ash particles, which are evidently smaller in size due to fragmentation and contain a larger quantity with rounded features.

Previous studies have investigated the morphological changes of pure coal-firing and co-firing of coal with woody biomasses to ascertain the melting behaviour, and hence propensity to cause slagging[264]. CCSEM analysis was used to quantify the number of spherical particles in the BSE images based on the circularity shape index. This CCSEM/MLA data can be used as a tool to predict slagging and fouling during coal and co-firing combustion. The circularity index (f_{circi}) can be described as follows, which is a function of the cross-sectional area (A) and perimeter (P) of the particle[265]:

$$f_{\text{circ}} = \frac{4\pi A}{P^2}$$

Particles with circularities ranging between 0.6 and 1 were compared, where a circularity of 1 is a perfectly spherical particle. A cumulative number distribution graph, shown in Figure 5-24, was plotted to show the percentage of particles within each sample which fell within this range. This graph indicates that for the South African coal sample, the number of particles within the 0.6 to 1.0 circularity range started with the coal containing 12% and then progressively increased during devolatilisation (22%) and char combustion (32% and 34% for 200 and 600 ms respectively) in the DTF. In the muffle furnace the SAC ash produced a slightly lower value of 28%, likely due to the lower melting temperature of 500°C. This shows that the number of spherical particles in the DTF ash are nearly three times the number present within the original coal sample. This suggests that the particles are exhibiting melting behaviour during the devolatilisation and combustion process.

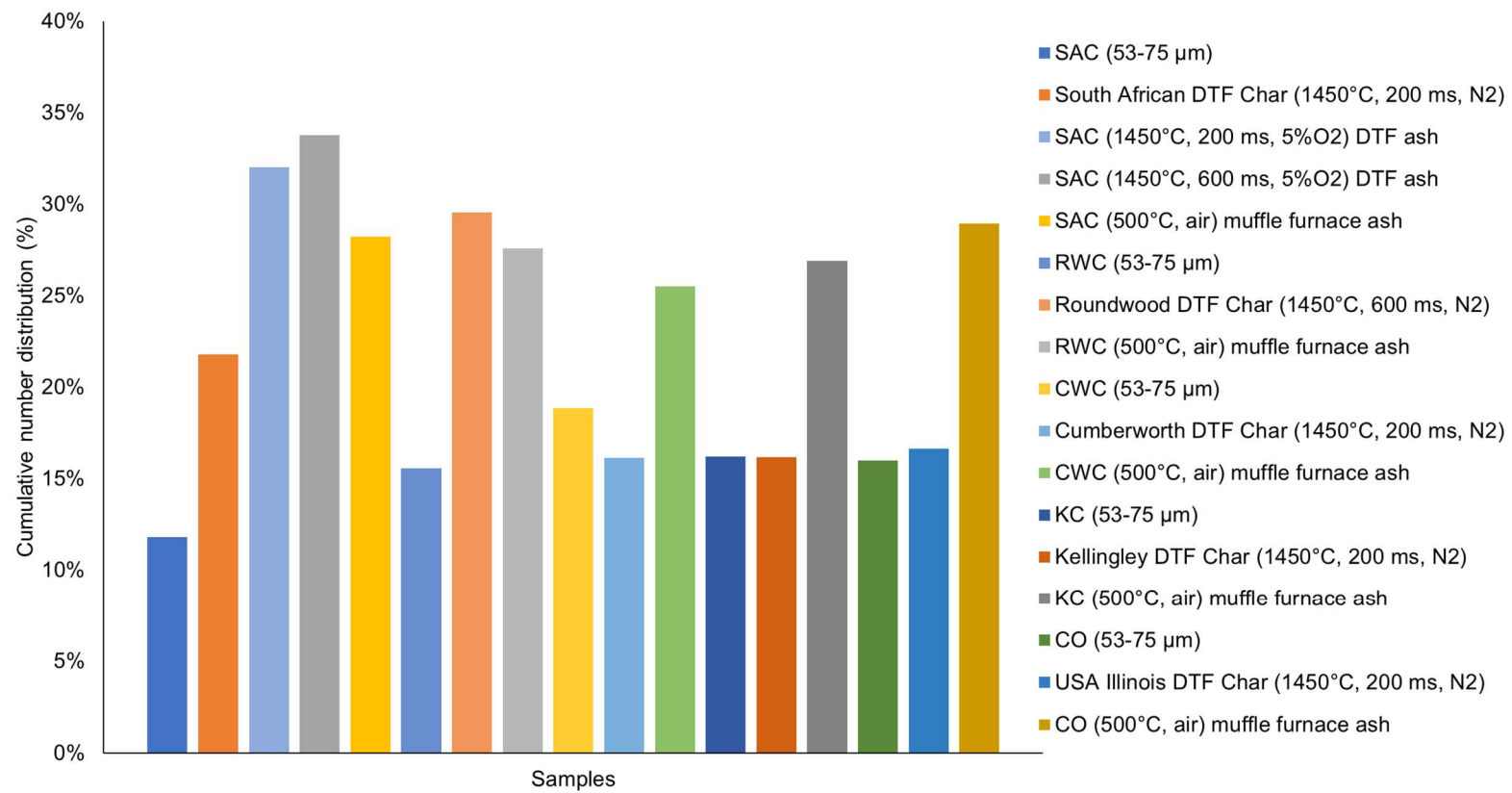


Figure 5-24: Cumulative number distribution (%) of the percentage of particles with a circularity between 0.6 - 1.0 within each sample.

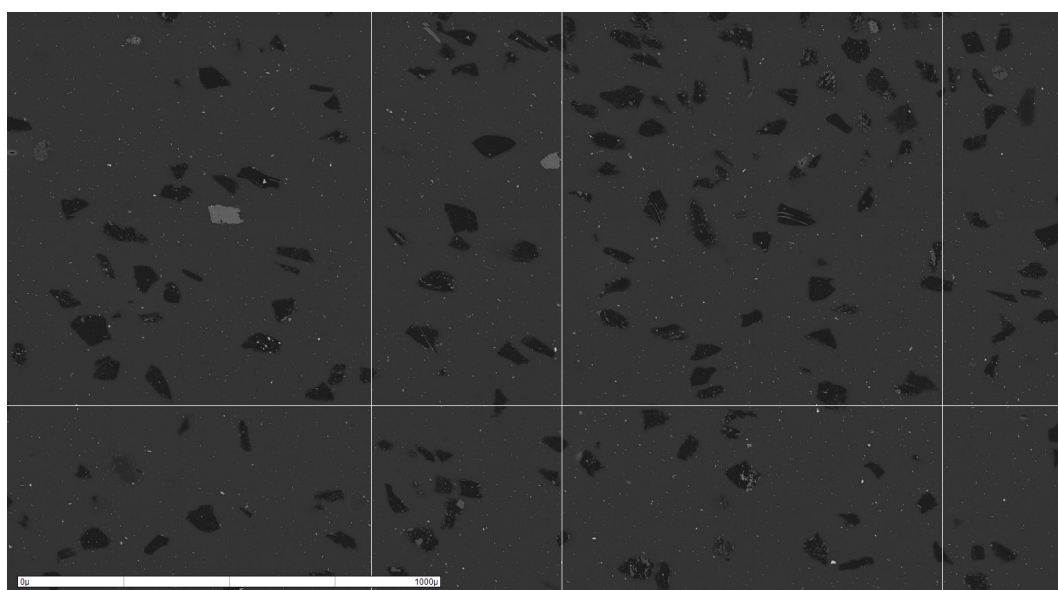


Figure 5-25: Electron micrograph of South African (Koorfontein) 53-75 µm
fraction

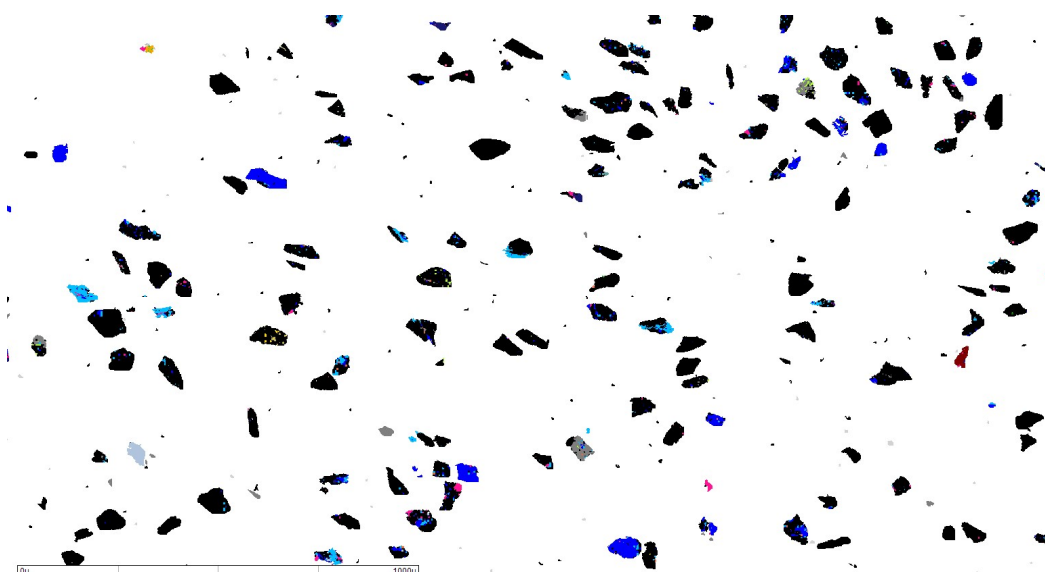


Figure 5-26: MLA coloured mosaic of South African (Koorfontein) 53-75 µm
fraction

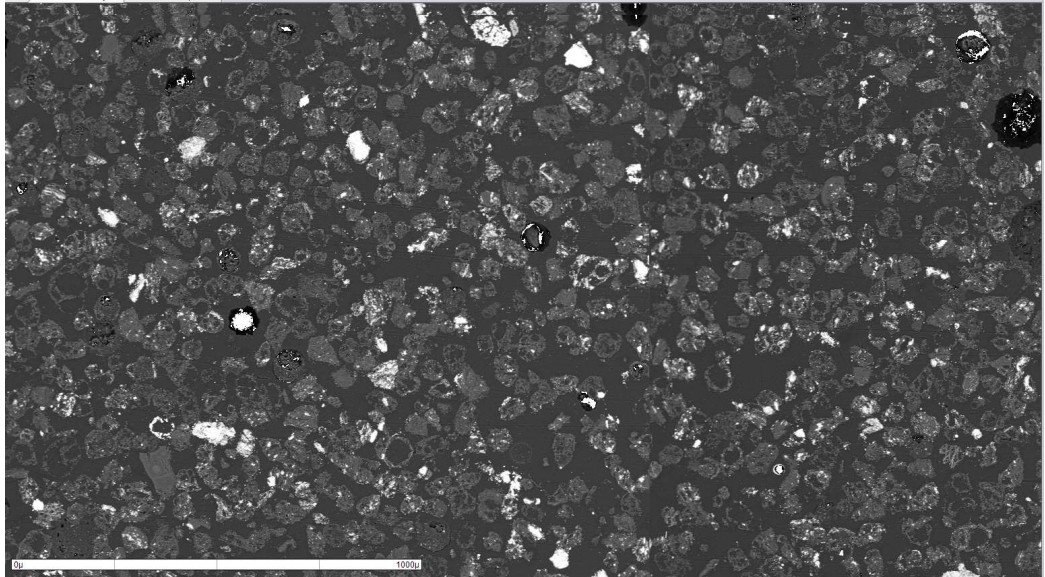


Figure 5-27: Electron micrograph of DTF South African (Koornfontein) Char
(1450°C, 200 ms)

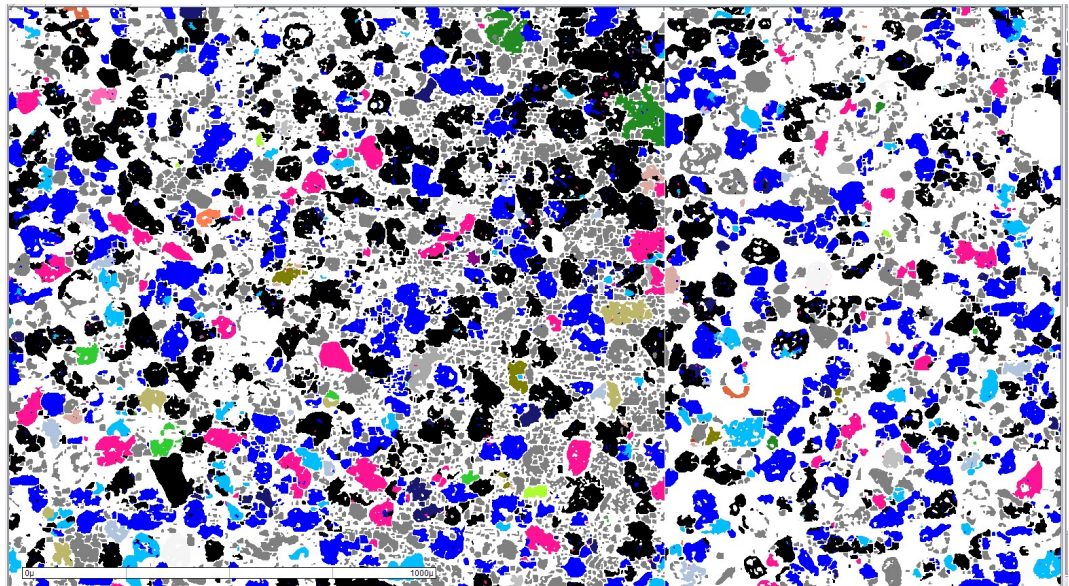


Figure 5-28: MLA coloured mosaic of DTF South African (Koornfontein) Char
(1450°C, 200 ms)

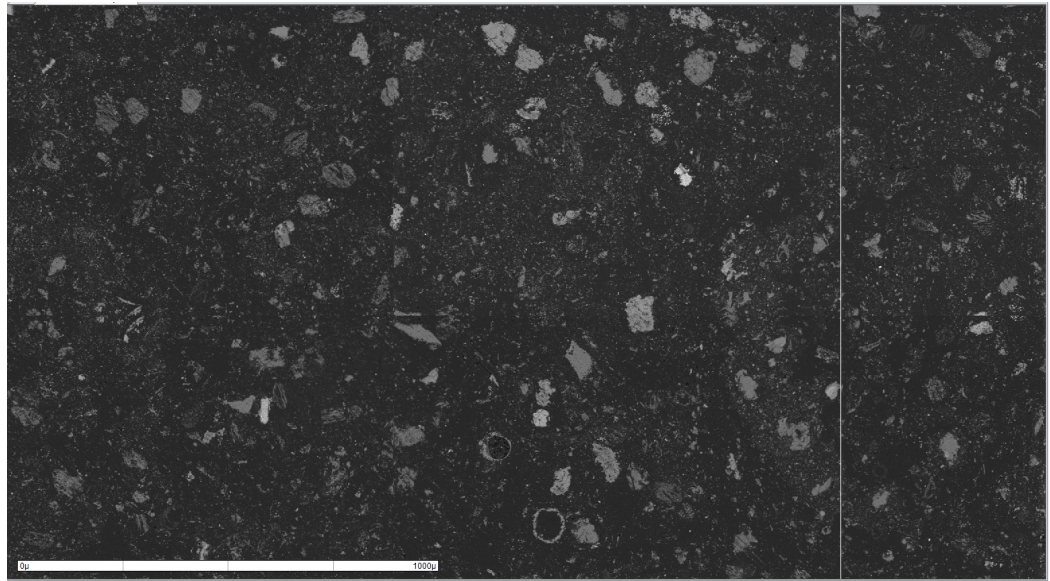


Figure 5-29: Electron micrograph of South African (Koorfontein) Ash (500°C muffle furnace)

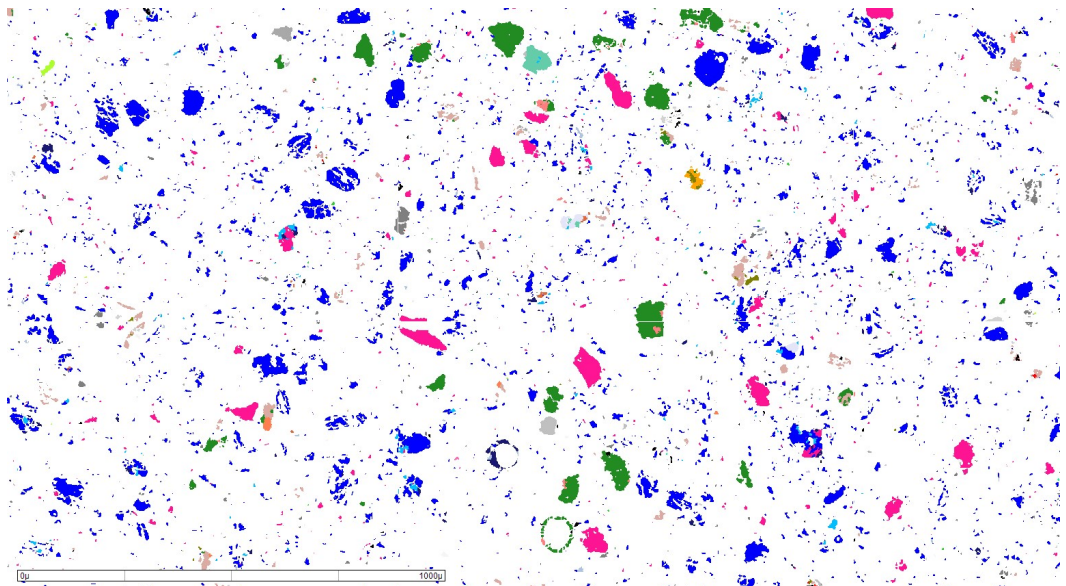


Figure 5-30: MLA coloured mosaic of South African (Koorfontein) Ash (500°C muffle furnace)

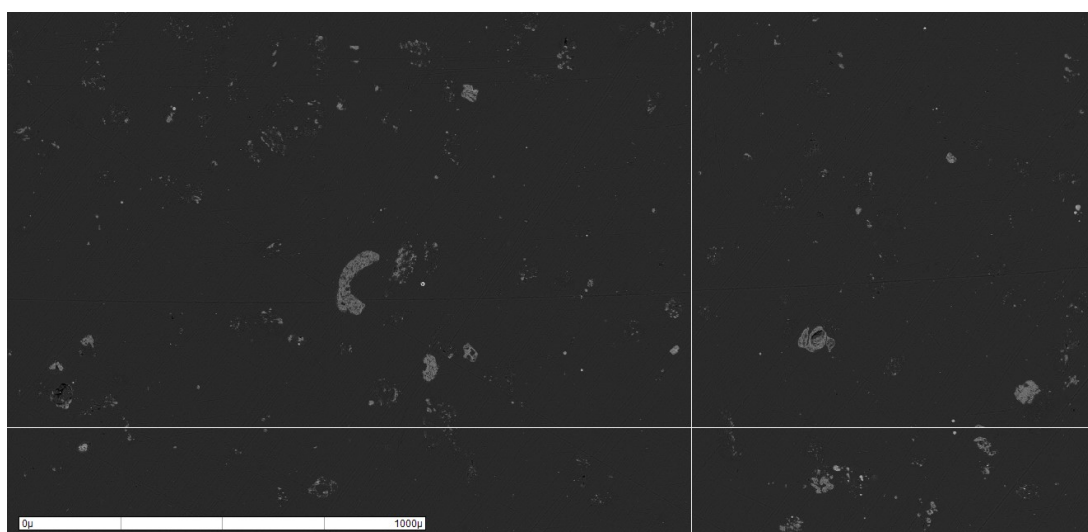


Figure 5-31: Electron micrograph of DTF South African (Koorfontein) Ash
(1450°C, 5%O₂, 200 ms)

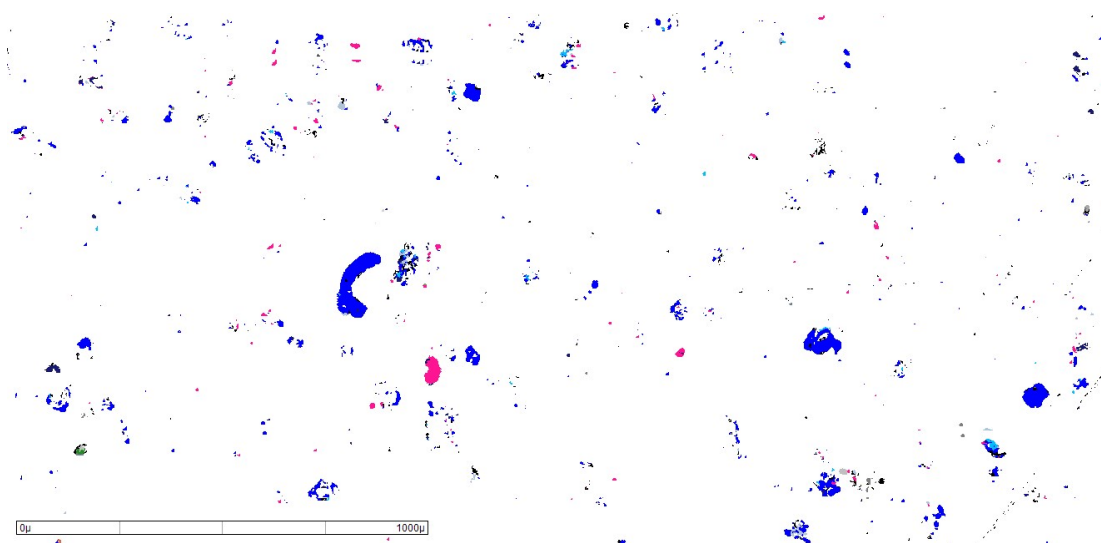


Figure 5-32: MLA coloured mosaic of DTF South African (Koorfontein) Ash
(1450°C, 5%O₂, 200 ms)

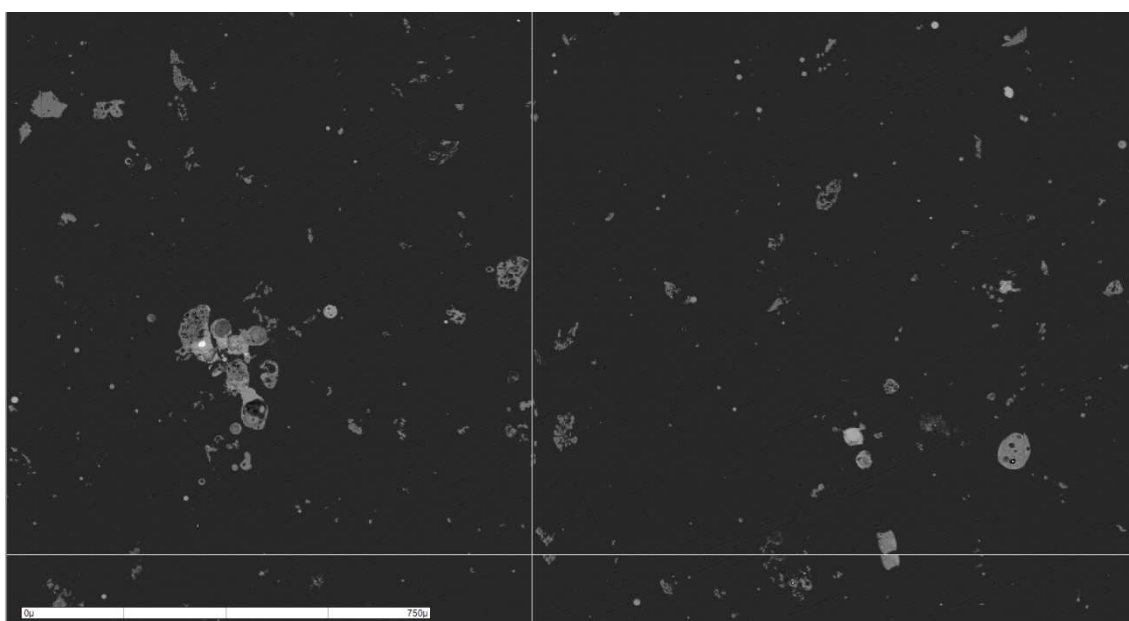


Figure 5-33: Electron micrograph of DTF South African (Koornfontein) Ash
(1450°C, 5%O₂, 600 ms)

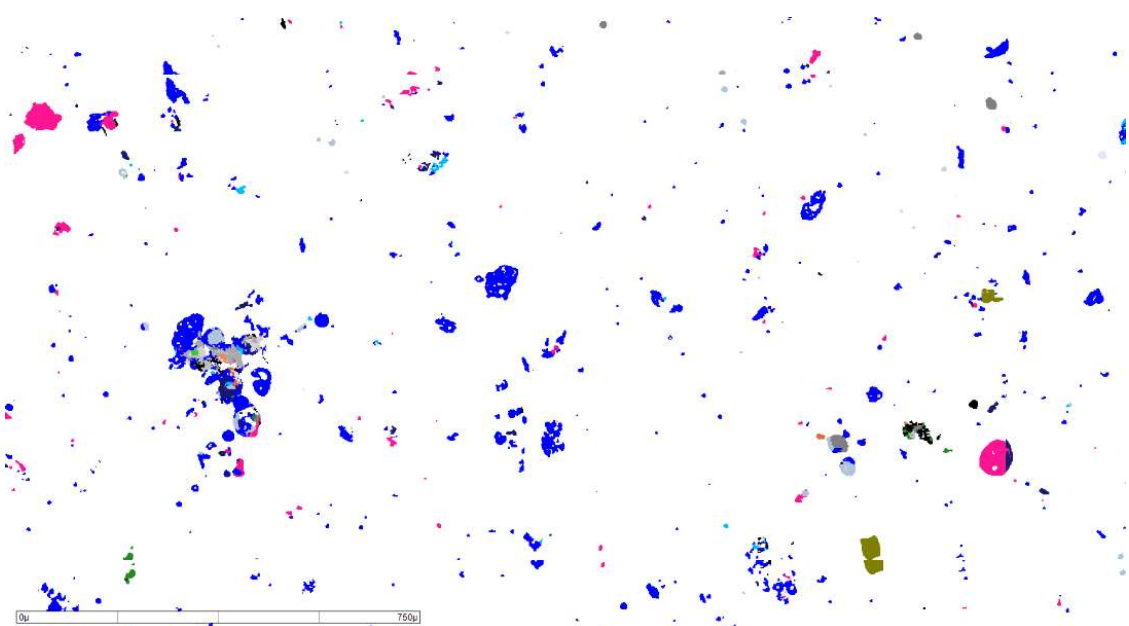


Figure 5-34: MLA coloured mosaic of DTF South African (Koornfontein) Ash
(1450°C, 5%O₂, 600 ms)

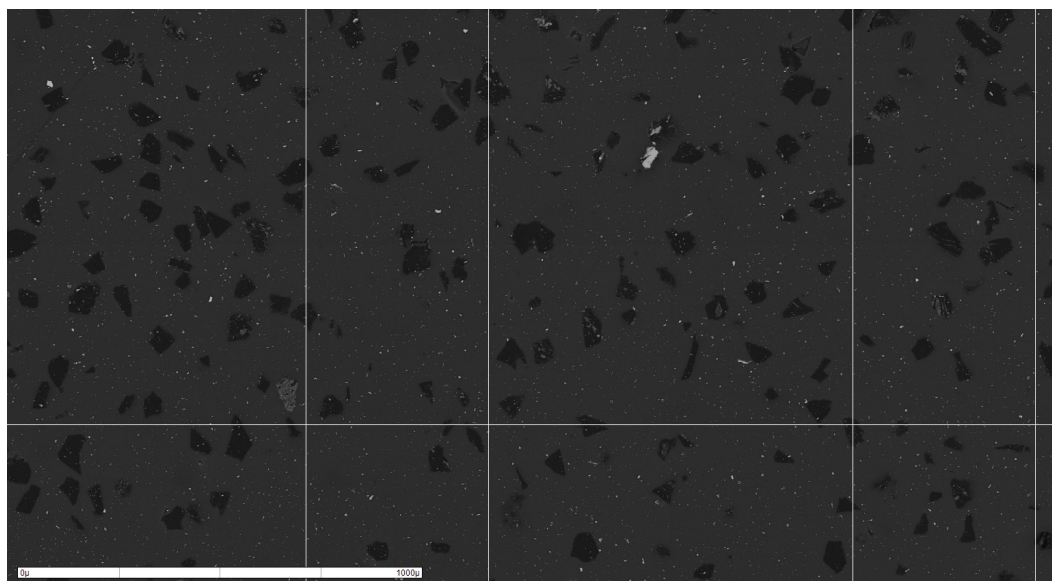


Figure 5-35: Electron micrograph of USA Illinois 53-75 µm coal fraction

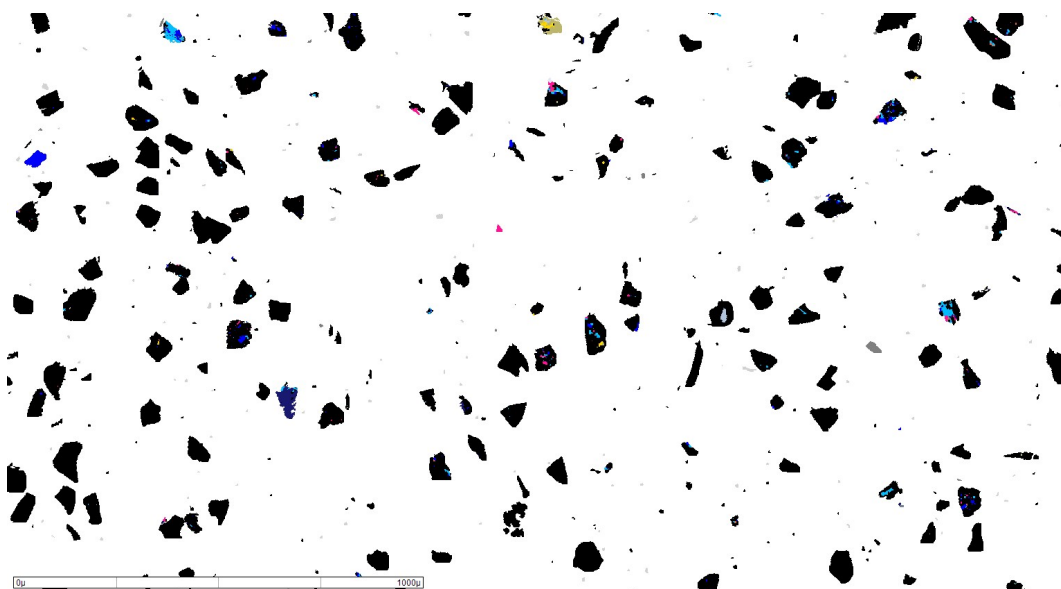


Figure 5-36: MLA coloured mosaic of USA Illinois 53-75 µm coal fraction

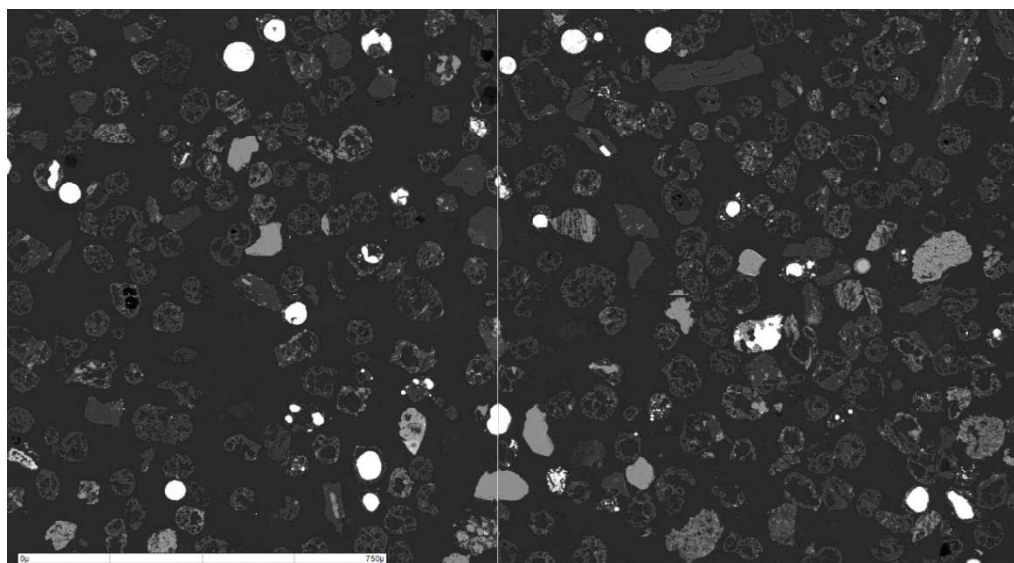


Figure 5-37: Electron micrograph of DTF USA Illinois Char (1450°C, 200 ms)

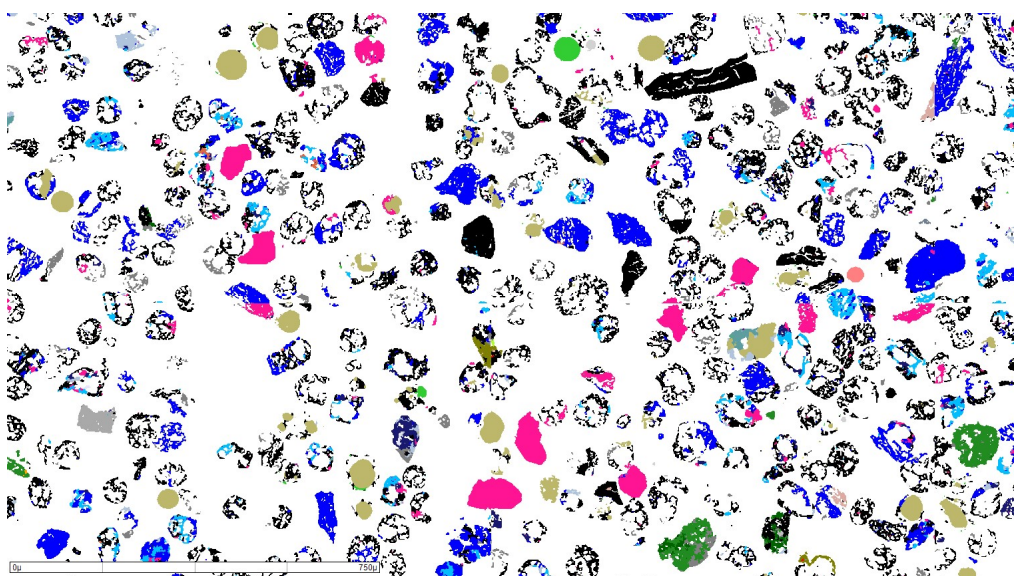


Figure 5-38: MLA coloured mosaic of DTF USA Illinois Char (1450°C, 200 ms)

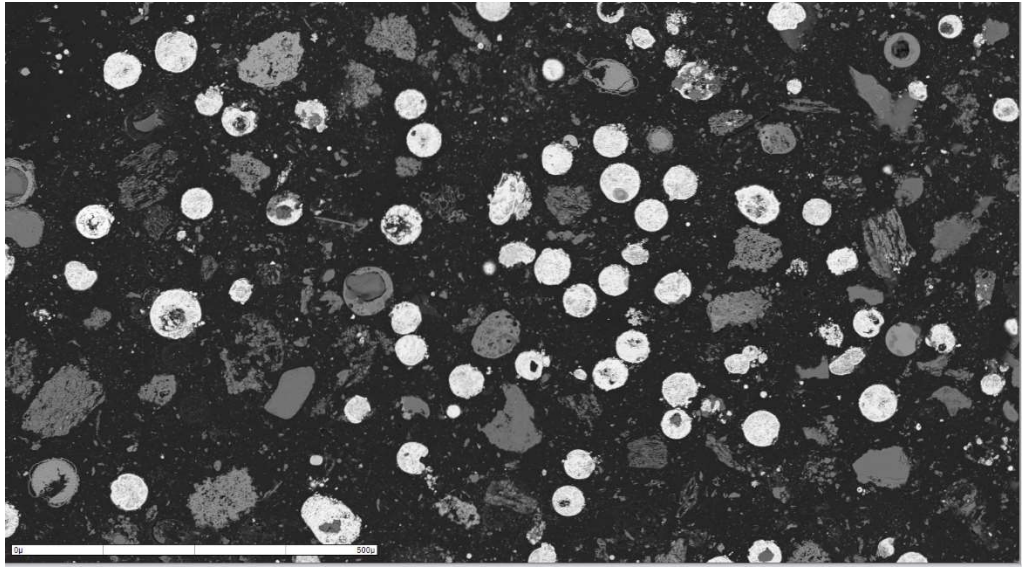


Figure 5-39: Electron micrograph of USA Illinois Ash (500°C muffle furnace)

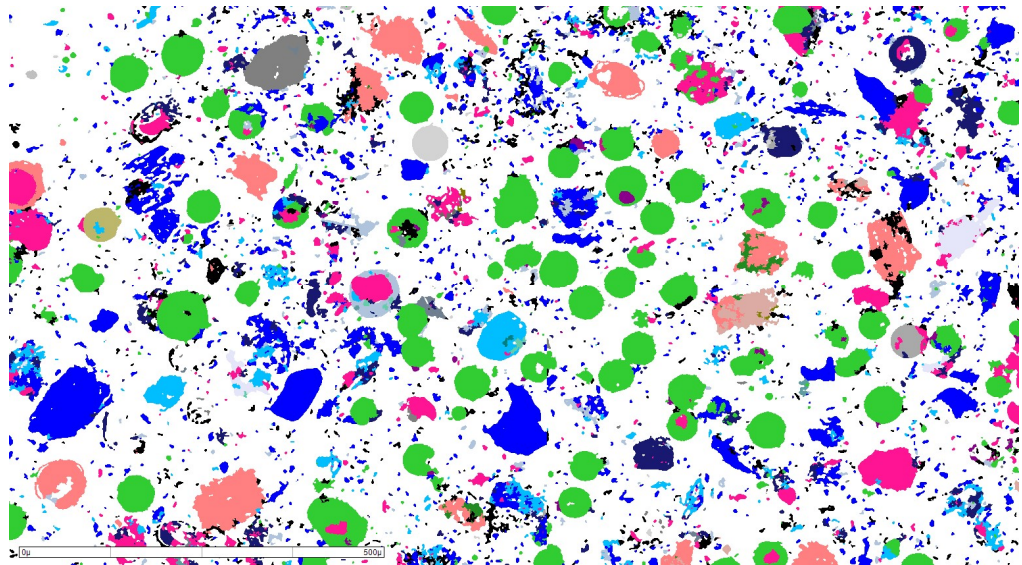


Figure 5-40: MLA coloured mosaic of USA Illinois Ash (500°C muffle furnace)

5.4.5 Evolution of Particle Sizes during Devolatilisation of Coal and Biomass Samples

Assessing the changes in the particle size distribution of coal and biomass particles during devolatilisation and char burnout are considered the most important parameters in combustion models[266]. The most widely used codes such as ANSYS Fluent include functions to account for particle diameter increases from swelling, but do not include the decrease of particle diameter due to fragmentation. Therefore, improved fragmentation models need to be included in existing combustion models[267].

Pyrolysis experiments were setup using the non-swelling South African (Koorfontein) coal, the swelling high volatile USA (Illinois) coal and olive cake biomasses. All samples were milled, dried and sieved for the 53-75 μm fraction. The proximate and ultimate analyses are presented in Table 3-1. The DTF was operated under a pure nitrogen atmosphere at 1450°C and 200 ms residence time for char production. Further information on the DTF setup and conditions are available in 3.2.11.

Dynamic image analysis, as described in 3.2.10 was used to measure the particle size distribution of the coals, biomass and resultant DTF chars. Each measurement was repeated in triplicate to guarantee reliable results. There is a research need to measure the particle size increase or reduction accurately due to the various size altering processes (such as burning and fragmentation) occurring simultaneously during combustion. The particle size rate changes are usually calculated using models or determined incorrectly through experiments[268].

This investigation into the particle size variations during coal and biomass devolatilisation for these three different types of solid fuels should provide an insight into the reliability of dynamic image analysis to measure particle size parameters for combustion models. Swelling and shrinkage phenomenon occurring during devolatilisation has been studied using 2D image analysis techniques such as optical microscopy and SEM for decades. Recent advances in 3D dynamic image analysis allows larger numbers of particles to be analysed simultaneously to determine the swelling or shrinkage ratios of coal samples. Bituminous coals usually undergo softening upon heating resulting in different types of char morphologies forming which significantly influences the subsequent char combustion, kinetics and ash formation[269]

During coal combustion, the volatile release in the early devolatilisation stage usually leads to swelling in bituminous coals[270] or fragmentation in lower rank coals[271]. However, the larger the amount of volatile matter the coal contains, the greater the probability it will fragment in the devolatilisation stage due to high stress induced from the expulsion of the volatiles, especially at high heating rates. Fragmentation models have been developed specifically for stress-induced fragmentation which occurs during devolatilisation[272, 273]:

$$n_d(d) = Kd^{-a}$$

Where d is the diameter of the fragments which are assumed to be spherical, $n_d(d)$ is the number of fragments at the size d . K and a are constants of the fragmentation system. Once the value a representing the fragmentation extent

is fixed, K can be determined using the conservation of mass assumption in the fragmentation process[274].

Dynamic image analysis can be used to assess the number of particles or fragments within a specific size range. Although there are limitations in terms of the lower particle size detection limits of the Camsizer P4, with particles below 30 μm unable to be identified, an attempt has been made to calculate the volumetric swelling and shrinkage ratios using the following formula[275]:

$$R = \frac{(V_t - V_0)}{V_0} \times 100\%$$

Where R is the volumetric swelling and shrinkage ratio (%), V_t is the volume of the particles at the final temperature and V_0 is the volume of the particles at the initial temperature. This formula can be translated into a more workable format using the D_{50} particle diameter, at which 50% of the samples mass is comprised of smaller particles, otherwise known as the mass median diameter. Following the same principles, this leads to the following formula:

$$R = \frac{(D_{50,\text{char}} - D_{50,\text{coal}})}{D_{50,\text{coal}}} \times 100\%$$

Table 5-18 shows that the volume-weighted particle sizes (D_{10} , D_{50} and D_{90}) of the two coals and biomass exhibit varying degrees of particle reduction or shrinkage and swelling after devolatilisation. The particle size distribution curves are shown in Figure 5-41, Figure 5-42 and Figure 5-43. The South African coal (VM 29.53% daf), has a very similar particle size to the char formed, with a small amount of fragmentation as the particles decrease by

approximately 0.3% for the D_{50} values, however this is of no statistical significance. In comparison, the USA Illinois coal (VM 39.37 %daf) experiences severe particle fragmentation as the shrinkage ratio exceeds 20%. This corresponds with previous studies that higher volatile matter content coals undergo larger amounts of fragmentation and particle size reduction as a result of thermal stress and internal over-pressure from volatile release[275-277].

Finally, the biomass char behaviour under high heating rate pyrolysis conditions was completely different to the coal chars formed. For olive cake (VM 77.73 %daf) there was 16% swelling of the char particles under nitrogen devolatilisation conditions. This correlates with previous studies which report that raw olive stone releases volatiles through the elongated, cellular pores during devolatilisation leading to swelling[246, 278].

Table 5-18: Particle size parameters before and after devolatilisation

	Size parameter (μm)	South African	USA Illinois	Olive Cake
Coal/Biomass (53-75 μm)	D_{10}	47	54	46
	D_{50}	60	77	62
	D_{90}	80	135	96
DTF Char (200 ms)	D_{10}	46	46	42
	D_{50}	59	61	72
	D_{90}	77	89	136
Swelling/shrinkage ratio	R (%)	-0.34	-20.73	16.22

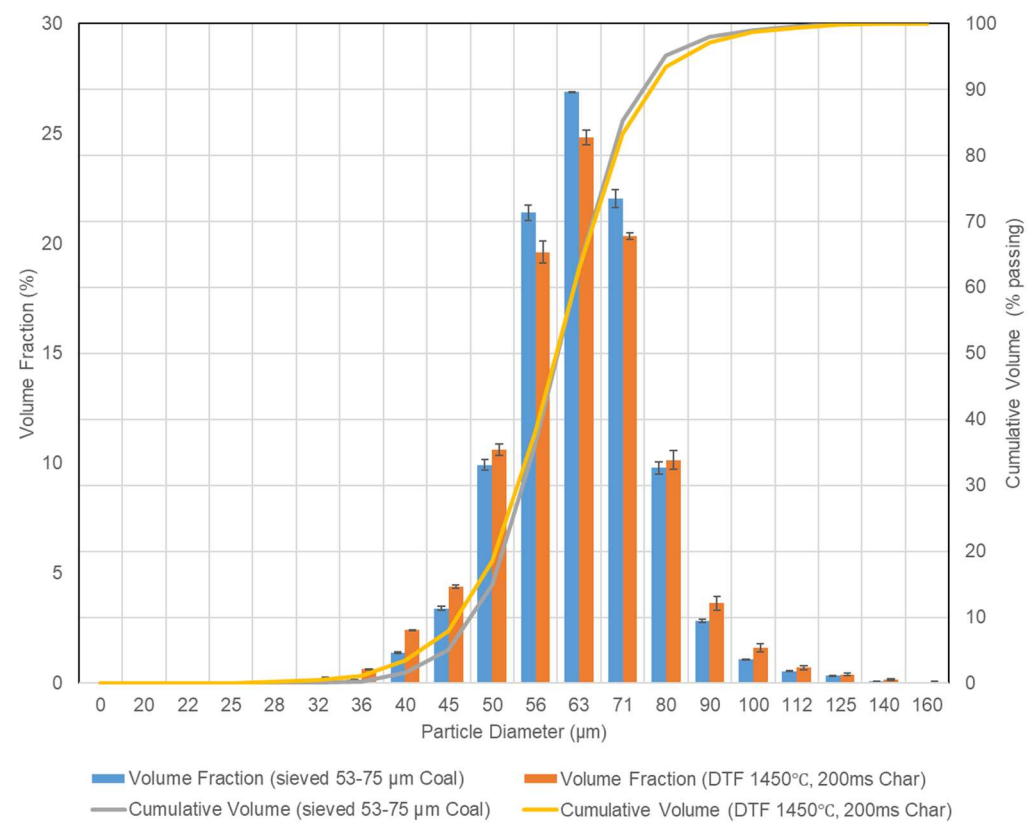


Figure 5-41: Particle size distribution of South African coal and DTF char

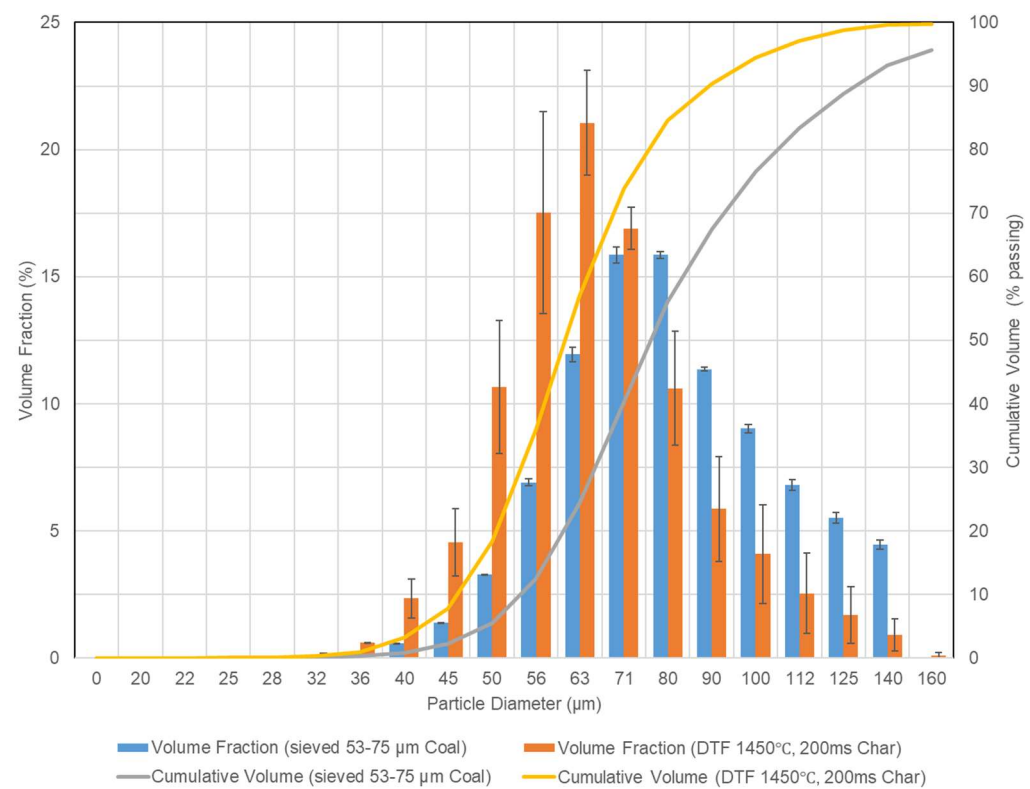


Figure 5-42: Particle size distribution of USA Illinois coal and DTF char

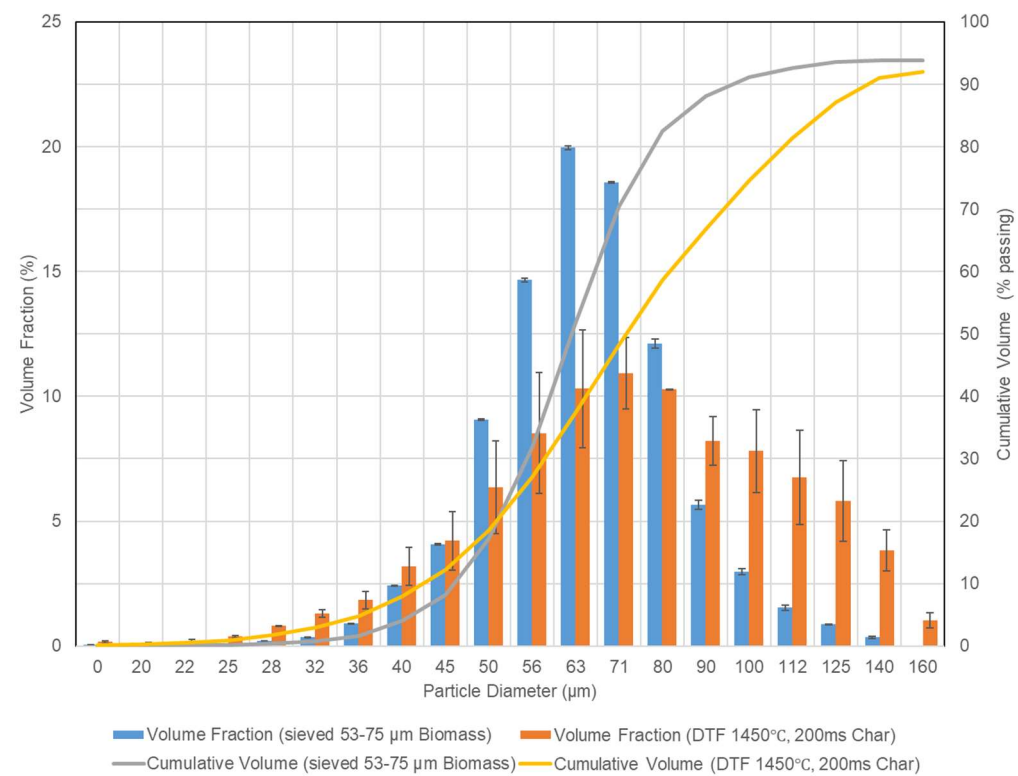


Figure 5-43: Particle size distribution of olive cake biomass and DTF char

5.4.6 Ternary Phase Diagrams during Combustion

This section provides the ternary phase diagrams of the South African raw coal, the coal char produced under devolatilisation conditions (1450°C, 200 ms) in the DTF and resultant ashes formed under 5 % O₂ with 200 and 600 ms residence times. The objective is to investigate how these furnace operating conditions influence the mineral transformations through examining the SiO₂ – Al₂O₃ – CaO phase diagrams with reference to Figure 4-18, particularly considering that South African coals contain a high amount of calcium-containing species.

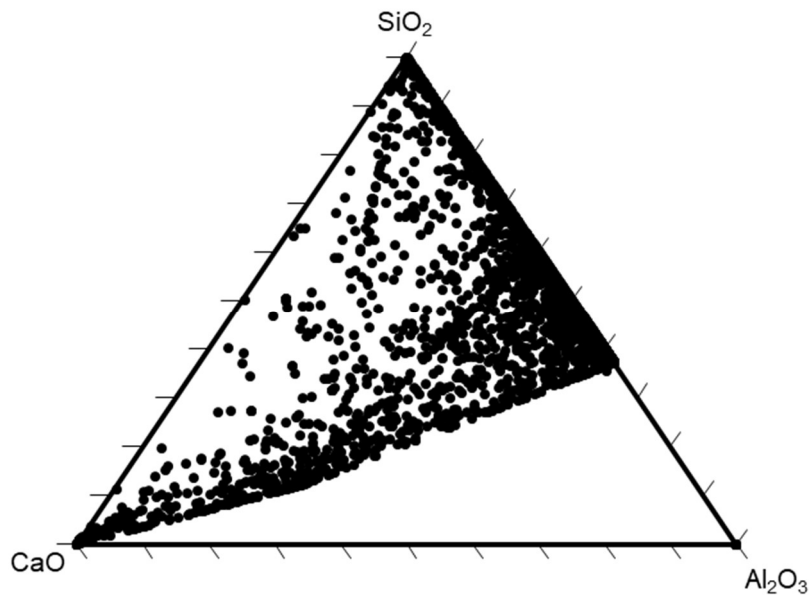


Figure 5-44: SiO₂ - Al₂O₃ - CaO ternary phase diagram of raw South African coal (53-75 μm)

Figure 5-44 shows that there is a wide variety of calcium-containing minerals, including $2\text{CaO} \cdot \text{SiO}_2$, $3\text{CaO} \cdot 2\text{SiO}_2$, Anorthite ($\text{CaO} \cdot \text{Al}_2\text{O}_3 \cdot 2\text{SiO}_2$) and mullite equidistant between the $\text{SiO}_2 - \text{Al}_2\text{O}_3$. The results show that there is a clear central divide with no particles approaching the Al_2O_3 apex. This corresponds with Figure 4-18 in that alumina is formed at temperatures exceeding 1450°C . It has recently been reported that the optimum combustion temperature for high alumina coal ash is below 1000°C [279] which supports this observation. Additionally, the MLA mineral database was developed with an aluminium oxide (Al_2O_3) spectra to identify such phases.

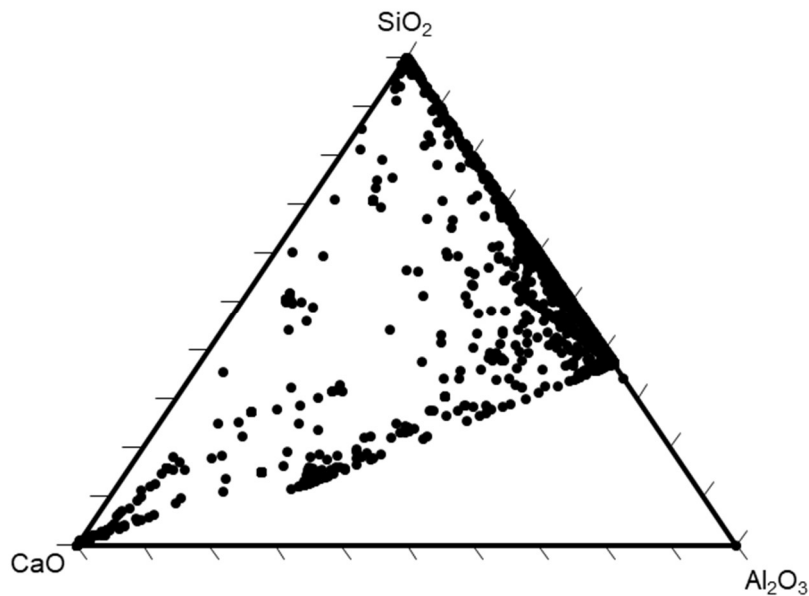


Figure 5-45: $\text{SiO}_2 - \text{Al}_2\text{O}_3 - \text{CaO}$ ternary phase diagram of DTF South African char (1450°C , 200 ms, N_2)

Contrary to the initial raw coal, the DTF char produced in Figure 5-45 shows that there are significantly less calcium-containing minerals positioned towards the CaO apex. Although a large proportion will remain trapped within the

aluminosilicate phases, there is likely to be a significant amount which will have vaporised at the high temperatures in the DTF.

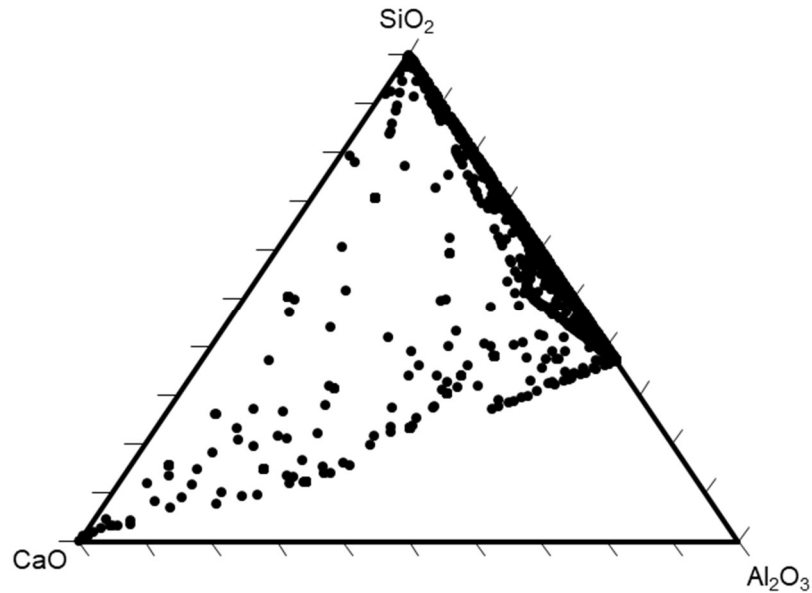


Figure 5-46: SiO₂ - Al₂O₃ - CaO ternary phase diagram of DTF South African ash (1450°C, 200 ms, 5% O₂)

Finally, Figure 5-46 shows that the number of calcium-containing phases has decreased further still during char oxidation and the vast majority of minerals are mullite phases with varying Si:Al ratios. This confirms that the ashes produced contain predominately Si and Al species, which may be able to capture fluxing elements such as K. This is investigated further in the next chapter.

5.5 Chapter Conclusions

Surface area analysis, cumulative pore volume and pore width analysis of the coal chars has confirmed the equivalent surface area reduces as a function of the residence time in the drop tube furnace. However, the higher volatile biomass chars exhibit higher specific surface areas than the coal chars, with the sunflower husk containing the highest surface area followed by miscanthus and olive cake respectively.

The TGA coal burnout and reactivity study confirmed that the least reactive coal was South African (Koorfontein) coal, attributed to the high inertinite content and longest char burnout time. A thermal annealing study suggested that the lowest DTF residence time of 200 ms should be applied to the proceeding mineral transformation study as confirmed by char burnout profiles and the depleted elemental hydrogen content in the char produced at 600 ms relative to 200 ms.

The MLA system was shown to have limited statistical variation between coal sample runs for a broad coal fraction of 0-75 μm and that the major minerals identified using XRD corresponded to the MLA. It was shown that circularity of particles progressively increased during coal devolatilisation and char combustion, and that the sphericity of the particles provides insights into the melting behaviour.

Dynamic image analysis was used to investigate the particle size distributions of DTF coal and biomass chars to determine the swelling/shrinkage ratios during devolatilisation. It was reported that whilst the coal chars experienced shrinkage under reducing conditions, the biomass swelled excessively.

Ternary phase diagrams, typically used to predict slagging and fouling phenomena showed that during DTF char combustion the proportion of mullite phases increased with residence time. This study confirmed that the South African coal has the high Si:Al ratios required to capture fluxing elements prevalent in biomass minerals.

Chapter 6: Coal Char Re-firing with Biomass Ash in a Drop Tube Furnace and Characterisation of Associated Mineral Transformations

6.1 General Introduction

This chapter presents the results of the experiments performed on the drop tube furnace (DTF) for the co-firing of DTF coal char with biomass ashes. These three biomasses were ashed in a muffle furnace at 500°C to remove the carbonaceous matter, leaving the mineral matter intact. The unreactive DTF derived South African (Koorfontein) coal char (produced at 1450°C, 200 ms and under a nitrogen atmosphere) was blended with the biomass ash and fired in the DTF under combustion conditions of 5 vol% O₂ in nitrogen. The coal chars were doped with biomass ash to investigate mineral transformations. Biomass ash was used due to the low ash content of raw biomass to provide sufficient quantities of biomass minerals into the coal char.

The experiments aimed to investigate the mineral changes that occur and the formation of ash deposits, from a morphological and chemical perspective. For the initial investigation, thermogravimetric analysis was performed on the DTF coal char and biomass ash mixtures at 10, 30 and 50 wt% to determine the influence of co-firing on the ignition temperature. This is an important parameter, providing an indication as to the temperature at which combustion commences.

In the second section, the mineral species are qualitatively identified in the biomass ashes using x-ray diffraction (XRD) to determine the presence of the

alkali and alkaline earth minerals, and compared to those determined by SEM-MLA. The mineral composition and coloured mosaic data of the fed and resultant ash are then compared for a restricted number of DTF ashes to investigate the interaction between the coal char and biomass ash mineral species as a function of DTF residence time. This provides an indication as to alkali and alkaline earth metal aluminosilicate phases involved in deposit formation during biomass co-firing.

6.2 Experimental Matrix

Table 6-1: Coal char and biomass ash combustion study using the drop tube

furnace

Sample	Carrier gas (vol %)	Temperature (°C)	Residence time (milliseconds)	Particle size (µm)
SAC	N/A	N/A	N/A	53-75
SAC (200ms) char	N ₂	1450	200	53-75
SAC (200ms) char / OC (500°C) Ash (50:50 wt%)	5% O ₂ /N ₂	1450	200	53-75
SAC (200ms) char / OC (500°C) Ash (50:50 wt%)	5% O ₂ /N ₂	1450	600	53-75
SAC (200ms) char / SUN (500°C) Ash (50:50 wt%)	5% O ₂ /N ₂	1450	600	53-75
SAC (200ms) char / MIS (500°C) Ash (50:50 wt%)	5% O ₂ /N ₂	1450	600	53-75

Table 6-2: Muffle furnace experiments on raw biomasses

Sample	Carrier gas	Temperature (°C)	Residence time (hours)	Particle size (µm)
OC	Air	500	12	53-75
SUN	Air	500	12	53-75
MIS	Air	500	12	53-75

6.3 TGA Study of Co-firing Coal Char with Biomass Ash

Previous studies have investigated the pyrolysis and combustion behaviour of co-firing biomass and coals using thermogravimetric analysis[236, 280-284]. These studies concluded that the biomass derived minerals, particularly those containing Na, K and Ca may contribute towards a catalytic effect which reduces the ignition temperature and lowers the apparent activation energy for the pyrolysis and combustion reactions to commence. However, these studies do not separate the carbonaceous volatile matter from the mineral species, which creates uncertainty as to whether it is the volatile or mineral components causing the catalytic effect. As such, few studies have investigated the influence that blending 500°C biomass ash and DTF coal char, with significantly reduced carbonaceous volatile components have on the ignition temperature. Further detail on the experimental method is presented in section 3.2.5.

Table 6-3 shows the effect of the biomass ash additions at various ratios on the char burnout. This data shows there are consistent reductions in ignition temperature as the blend ratio increases from 10, 30 and 50 wt % biomass ash addition compared to the DTF South African (Koorfontein) coal char. As shown in Table 6-3, the highest reduction in ignition temperature through doping biomass ash were observed with the olive cake ash, with reductions of 9, 30 and 80°C for 10, 30 and 50 wt% biomass ash addition respectively. This suggests that increasing the biomass ash content within the coal char reduces the ignition temperature. However, for the miscanthus biomass additions the results indicate there was no added benefit on the ignition temperature exceeding 30 wt%. Additionally, Table 6-4 showing the XRF data confirms that

the olive cake biomass ash contained the largest weight percentage of K and Na combined compared to sunflower and miscanthus ashes, totalling 57.68 wt%. This suggests there are synergistic effects between the coal char and biomass ash, and signifies the presence of a catalytic effect. This data is graphically represented in Figure 6-1, Figure 6-2 and Figure 6-3.

Table 6-3: Ignition temperature as a function of blend ratio

DTF Coal char / biomass ash	Blend ratio (coal char:biomass ash wt%)	Minimum value of d(weight)/d(Time) (%/min)	Ignition temperature (°C)	Ignition temperature reduction (°C)
DTF South African coal char	100:0	-3.1	556	N/A
DTF south African Char / Miscanthus 500°C Ash	50:50	-4.8	528	28
	70:30	-3.8	527	29
	90:10	-3.2	546	10
DTF south African Char / Olive Cake 500°C Ash	50:50	-2.4	476	80
	70:30	-3.9	526	30
	90:10	-3.9	547	9
DTF south African Char / Sunflower 500°C Ash	50:50	-2.9	526	30
	70:30	-3.6	540	16
	90:10	-3.9	545	11

The ignition temperatures of the DTF coal char and biomass ash blended samples (i.e. the temperature at which the onset of combustion starts) is analogous with the apparent activation energy, where the higher the apparent activation energy, the higher the ignition temperature. The order of reactivity follows olive cake > sunflower husk > miscanthus, which has been confirmed by other workers on the raw biomass samples[285]. It has been suggested that the high reactivity of the olive cake is due to the evaporation of oil at low temperatures[285]. However, for this study the ashing at 500°C should have cracked these low temperature oils.

Figure 6-4 shows the XRD minerals identified which may contribute to this catalytic effect, namely fairchildite ($\text{K}_2\text{Ca}(\text{CO}_3)_2$), polyhalite ($\text{K}_2\text{Ca}_2\text{Mg}(\text{SO}_4)_4 \cdot 2\text{H}_2\text{O}$), sylvite (KCl) and calcium sodium aluminosilicate ($\text{Ca}_{0.9}\text{Na}_{0.1}\text{Al}_{1.8}\text{Si}_{2.2}\text{O}_8$) that were found in the biomass ashes. This research supports previous studies which have investigated potassium-based catalysts such as potassium carbonate (K_2CO_3) blended with coal[114]. These previous studies suggested that the coal-derived calcium can attach onto potassium carbonate additives, producing fairchildite[286], and that there is a trade-off between the catalytic effect of the potassium and the influence on ash agglomeration. Whilst potassium containing species such as fairchildite reduce the activation energy when blended with unreactive coal, the potassium can react with other minerals forming low melting point eutectics, leading to more severe ash sintering[287, 288]. In this study, it is evident that these potassium-containing compounds derived from the biomass are exhibiting a similar effect.

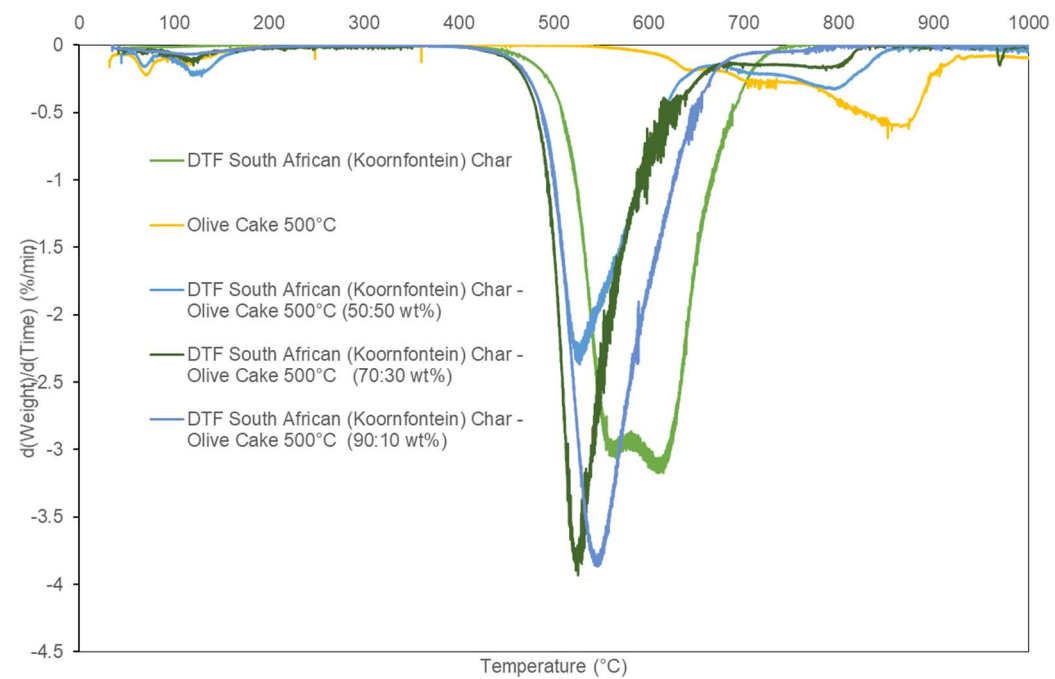


Figure 6-1: TGA char burnout profiles of South African Koornfontein DTF Coal Char (1450 $^{\circ}\text{C}$, 200 ms) and 500 $^{\circ}\text{C}$ Olive Cake Ash at 5 $^{\circ}\text{C}$ min $^{-1}$ to 1000 $^{\circ}\text{C}$

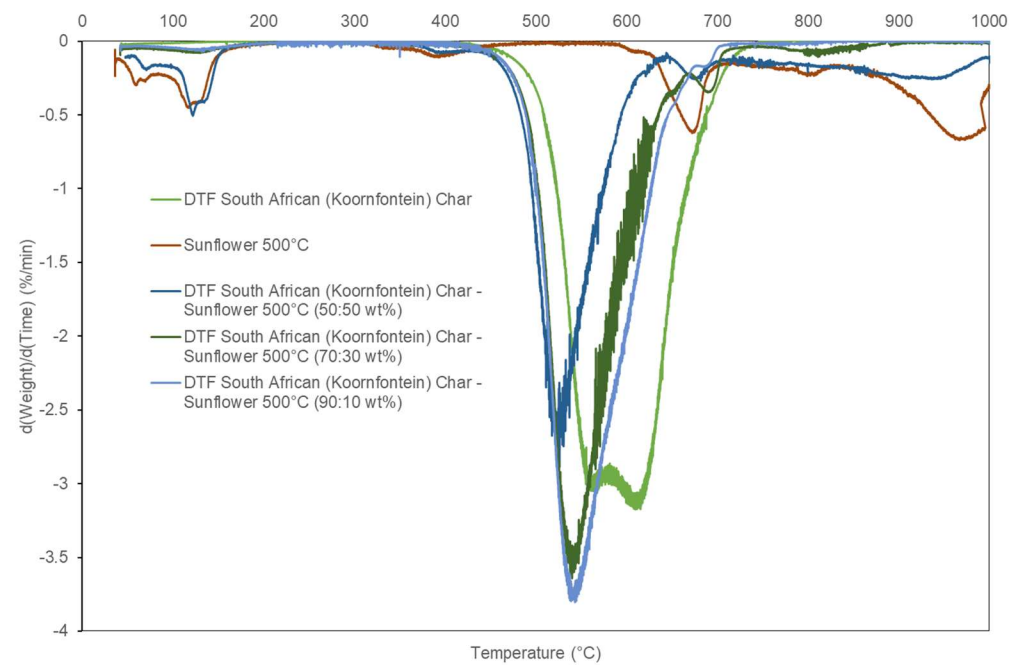


Figure 6-2: TGA char burnout profiles of South African Koorfontein DTF Coal Char (1450°C, 200 ms) and 500°C Sunflower Ash at 5°C min⁻¹ to 1000°C

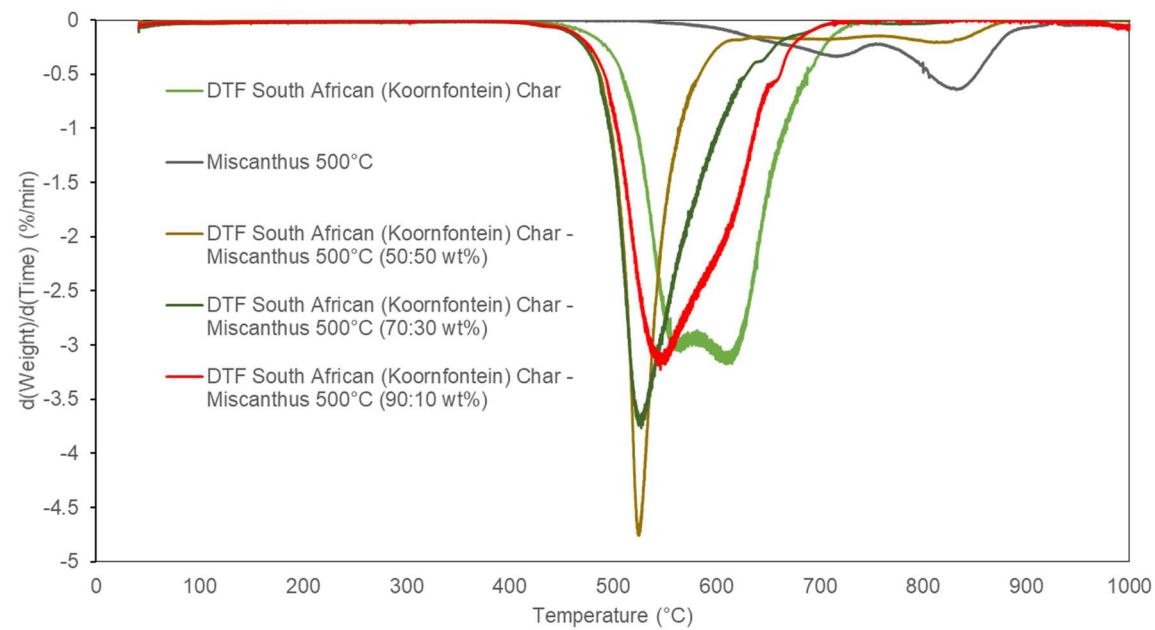


Figure 6-3: TGA char burnout profiles of South African Koorfontein DTF Coal Char (1450°C, 200 ms) and 500°C Miscanthus Ash at 5°C min⁻¹ to 1000°C

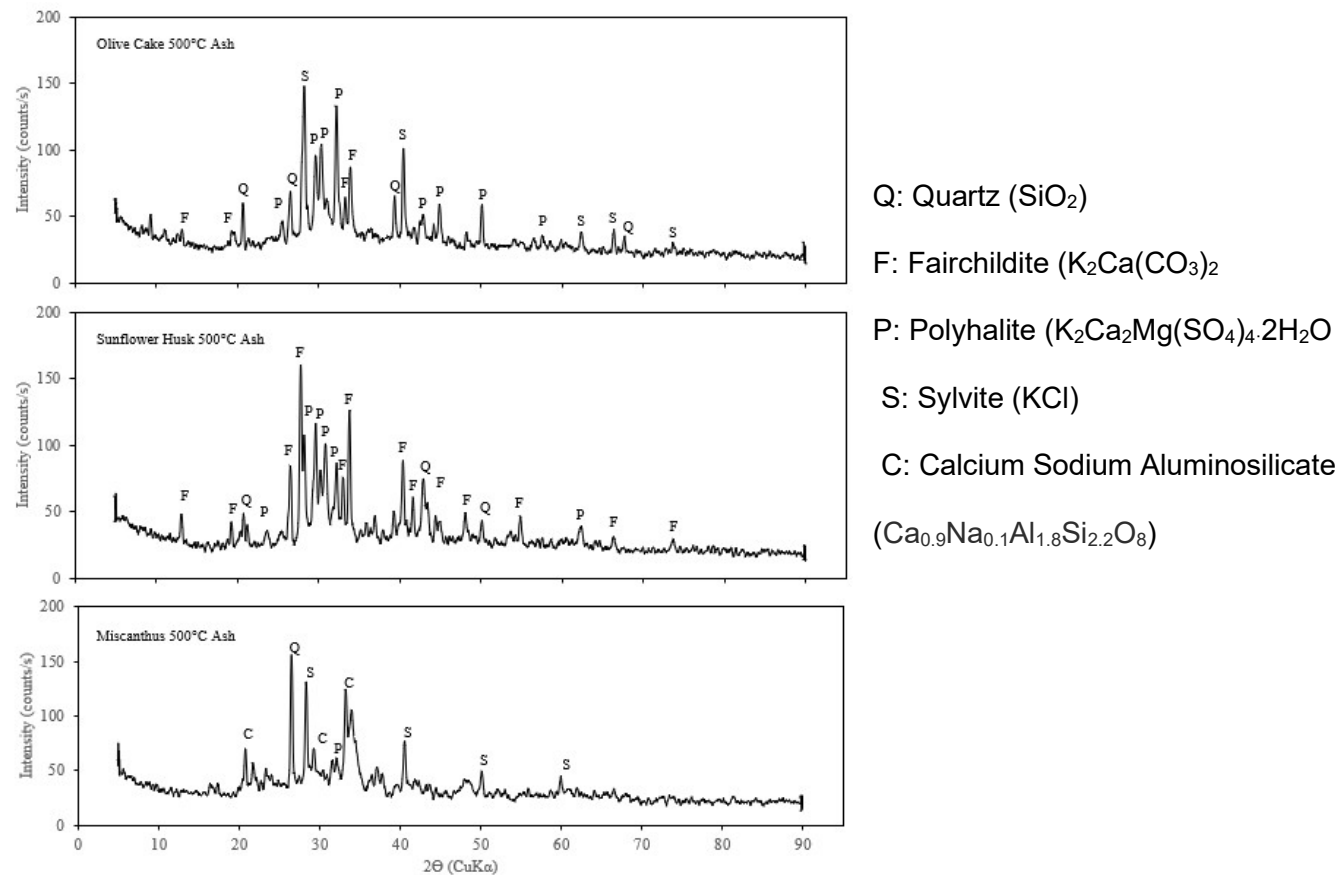


Figure 6-4: XRD of muffle furnace biomass ashes (500C, air)

Table 6-4: XRF data of 500°C biomass ashes

Oxides	500°C Miscanthus Ash	500°C Sunflower Husk Ash	500°C Olive Cake Ash
SiO ₂	20.02	2.80	6.42
Al ₂ O ₃	2.13	1.04	2.18
Fe ₂ O ₃	2.74	3.69	4.79
CaO	9.28	14.29	10.35
MgO	1.47	6.31	4.67
TiO ₂	0.12	0.05	0.11
Na ₂ O	33.44	0.48	1.53
K ₂ O	20.01	56.27	56.15
P ₂ O ₅	5.04	7.59	7.21
SO ₃	2.28	4.63	1.99
SrO	0.02	0.06	0.03
ClO ₂	3.30	2.60	4.41
ZnO	0.04	0.06	0.06
MnO ₂	0.10	0.07	0.06
CuO	0.01	0.05	0.05
SiO ₂ : Al ₂ O ₃	9.41	2.68	2.94
SiO ₂ : Fe ₂ O ₃	7.32	0.76	1.34
SiO ₂ - 1.5 Al ₂ O ₃	16.83	1.23	3.14
B:A ratio	3.23	22.77	9.72

6.4 Mineral Transformations and Particle Size Distributions of Co-fired Blends and DTF Ashes

The mineral transformations during pulverised combustion have been studied extensively in the literature. Previous workers have investigated the main mineral species that contribute towards slagging and fouling in pulverised boilers using CCSEM technology[262, 289, 290] such as illite, kaolinite and pyrite, and used some of this information to develop ash formation and deposition models[127]. However, the influence of the biomass derived minerals and coal char minerals during co-combustion have not been adequately investigated. The purpose of this section is to investigate the mineral groups that are consumed and formed, and highlight specific physical interactions that are apparent during the evolution of pulverised combustion.

From Table 6-6 showing the mineral composition data for the 500°C biomass ashes and South African Koornfontein DTF Char (1450°C, 200 ms), the blends of biomass ash and DTF coal char were calculated as shown in Table 6-7. This constituted the initial fed DTF coal char and biomass blends (50:50 weight %) composition fed into the DTF at the specified combustion conditions. The 50:50 weight % ratio for all the biomass ashes was investigated further as there were synergistic effects and reductions in ignition temperature observed in section 6.3. Table 6-8 shows the final mineral compositions of the DTF generated blended ashes.

The following graphs show the changes in mineral groups during DTF blend combustion by comparing the minerals species in the DTF ash to the DTF coal

char and biomass ash (50:50 wt%) calculated blend. Table 6-5 shows the possible mineral transformations which may have occurred to explain the compositional changes during combustion.

The XRD data of the South African (Koorfontein) muffle furnace 500°C ash shown in Figure 5-4 highlights that the dominant minerals after combustion were quartz, dolomite, calcite, illite, kaolinite and anhydrite. In the SAC DTF char shown in Table 6-6, the only minerals remaining after the high temperature decomposition in the DTF were mullite (reported as kaolinite), quartz and a small amount of minor minerals such as montmorillonite and calcium aluminosilicates (with traces of phosphorus). As expected, due to the high temperature of 1450°C and nitrogen atmosphere conditions for devolatilisation, there were minimal alkali and alkaline earth metals present within the DTF coal char for the subsequent biomass ash blending runs. Furthermore, the majority of these were excluded minerals, as shown in Figure 5-20, available for mineral reactions.

The XRD data of the miscanthus biomass ash in Figure 6-4 shows that there is predominantly quartz, sylvite, calcium sodium aluminosilicate and polyhalite present within the ash. The mineral compositions of the miscanthus muffle furnace 500°C ash in Figure 6-5 show that the dominant minerals are Ca/Na Al-silicate (32.95 wt%) and K/Fe/Ca/Na Al-silicate (5.88 wt%) with small amounts of fairchildite and sylvite. After combustion, Table 6-8 shows that the resultant DTF ash had undergone significant transformation, with the Ca/Na Al-silicate trapping the fluxing element K^+ within the Ca/Na/K Al-silicate mineral phase. This K^+ is likely to have originated from the fairchildite and sylvite which

as Table 6-5 indicates, would have fully decomposed under the 1450°C and 5% O₂ operating conditions of the DTF.

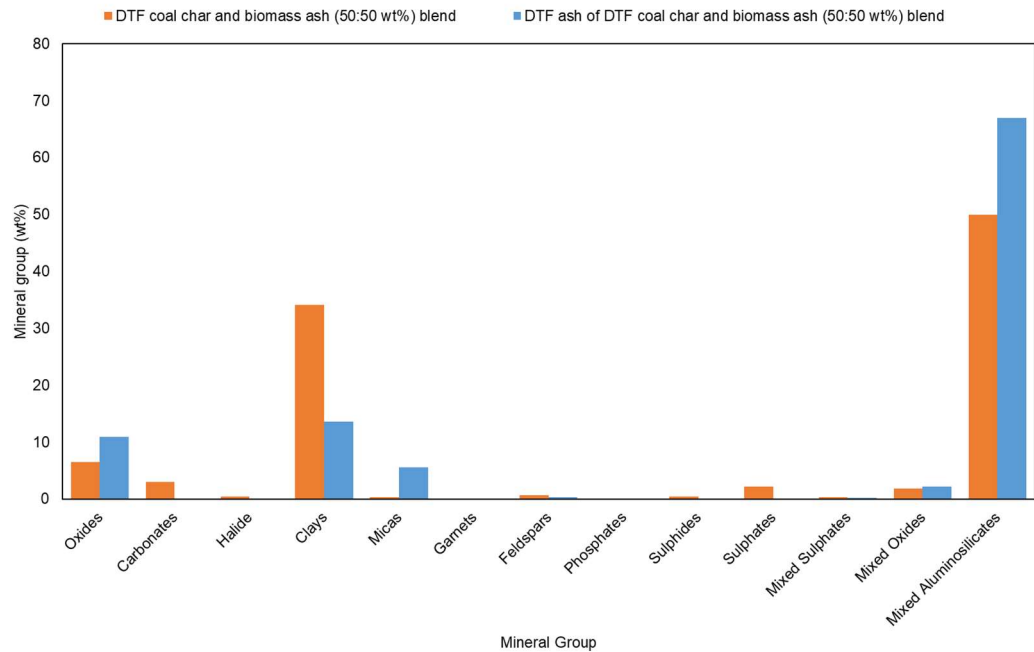


Figure 6-5: Mineral group changes of DTF South African (Koorfontein) Char (1450°C, N₂, 200 ms) / Miscanthus 500°C Ash (50:50 weight %) fired at 1450°C, 5% O₂ and 600 ms in a DTF

The XRD data of the sunflower biomass ash (Figure 6-4) confirms the presence of fairchildite, polyhalite and a small amount of quartz. Figure 6-6 shows that fairchildite constitutes the bulk, comprising 41.88 wt%, with 4.76 wt% of polyhalite and the bulk of the clay minerals from the char, with 24.85 wt% mullite. Examination of the DTF ash in Table 6-8, shows that the fairchildite has fully decomposed and there is the formation of polyhalite (14.31 wt%), which is likely to be a K-Mg-Ca phase as a result of the illite and carbonate decomposition. Due to the sensitivity of the MLA mineral database, it is possible

that this phase could be a mixed aluminosilicate with a similar composition to the Ca/K/P/Mg Al-silicate (46.60 wt%) and Ca/K/Mg/Fe Al-silicate (21.88 wt%) formed.

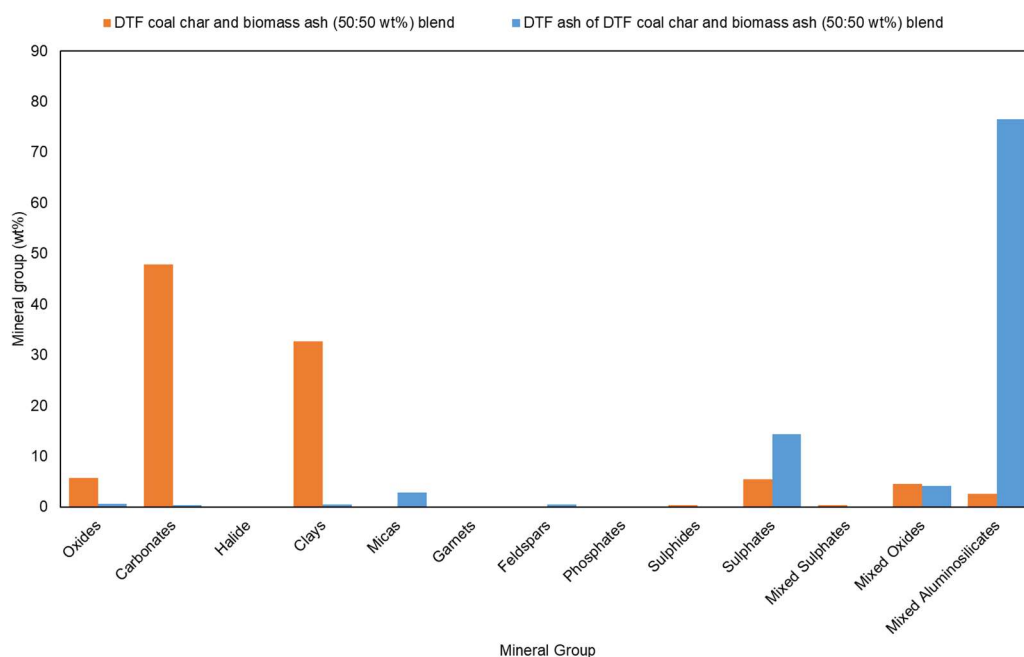


Figure 6-6: Mineral group changes of DTF South African (Koorfontein) Char (1450°C, N₂, 200 ms) / Sunflower Husk 500°C Ash (50:50 weight %) fired at 1450°C, 5% O₂ and 600 ms in a DTF

The XRD data shown in Figure 6-4 of the olive cake biomass ash suggests there are multiple peaks of fairchildite, polyhalite, sylvite and quartz minerals present in the sample. With reference to the 5% O₂ and 200 ms conditions (Figure 6-7), the majority of the mullite (24.86 wt%) has been consumed and the fairchildite has decomposed considerably. Similar to the blend with sunflower husk, the main mixed aluminosilicate formed is Ca/K/Mg/Fe Al-silicate (16.19 wt%). The second and third most abundant are K/Fe/Ca/Na Al-

silicate (13.88 wt%) and Ca/Mg Al-silicate (5.51 wt%). However, the polyhalite has only decomposed fractionally from 19.81 wt% to 16.79 wt%.

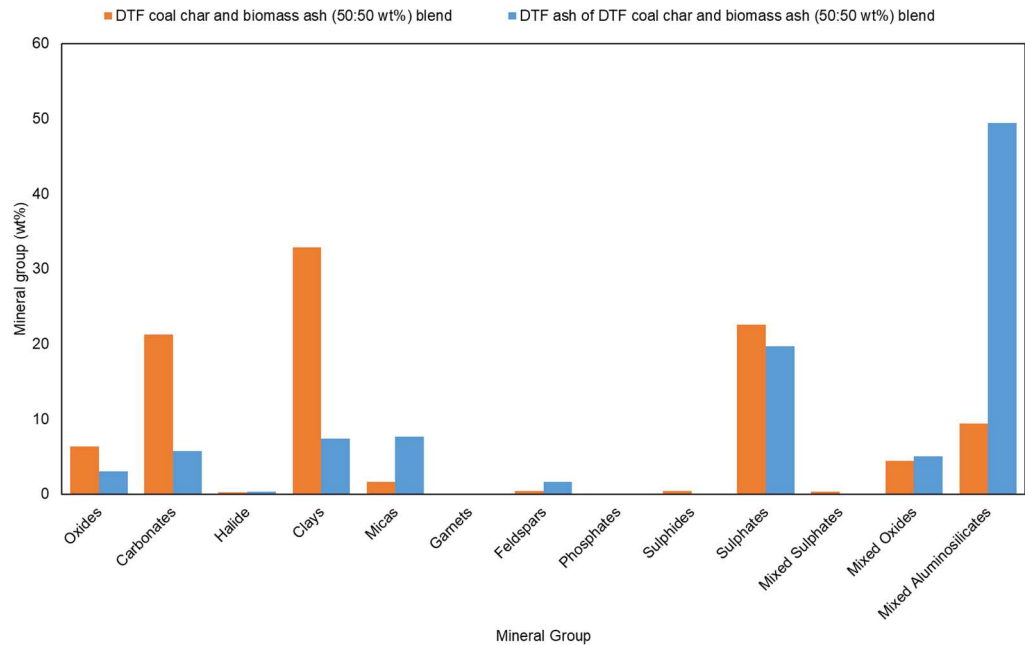


Figure 6-7: Mineral group changes of DTF South African (Koorfontein) Char (1450°C, N₂, 200 ms) / Olive Cake 500°C Ash (50:50 weight %) fired at 1450°C, 5% O₂ and 200 ms in a DTF

The DTF coal char and olive cake blend was repeated at a residence time of 600 ms (Figure 6-8) to investigate how the mineral composition and morphology of the particles changed compared to 200 ms. It can be seen that a greater proportion of mixed aluminosilicates and mixed oxides were formed, particularly Fe/K oxide (6.83 wt%), Ca/K/Mg/Fe Al-silicate (29.09 wt%) and K/Fe/Ca/Na Al-silicate (16.86 wt%). This suggests that the higher residence time in the combustion zone increases the uptake of metal fluxing elements into the

aluminosilicate phases. As expected, there is a lower fixed/volatile carbon fraction and similarly the polyhalite has not decomposed.

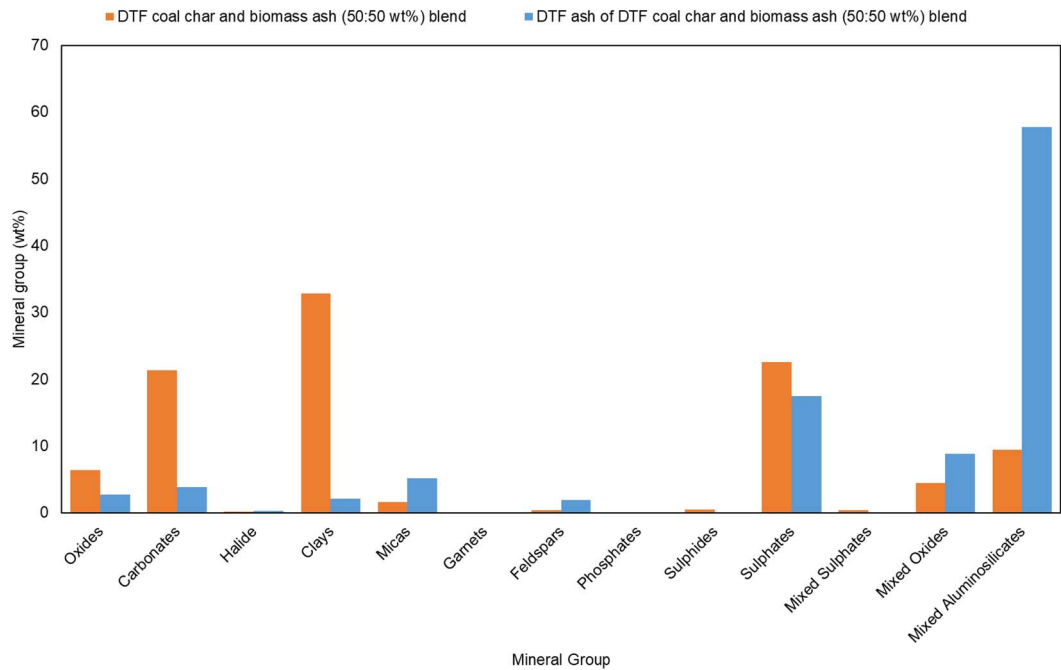


Figure 6-8: Mineral group changes of DTF South African (Koorfontein) Char (1450°C, N₂, 200 ms) / Olive Cake 500°C Ash (50:50 weight %) fired at 1450°C, 5% O₂, 600 ms in a DTF

The results indicate that the addition of the DTF coal char will improve the deposition behaviour through capturing the fluxing elements in the DTF coal char aluminosilicate phases. However, Figure 6-9 and Figure 6-10 show that the mixed aluminosilicates derived from the biomass species, such as Ca/K/Mg/Fe Al-silicate and K/Fe/Ca/Na Al-silicate are acting as binders, attaching to the coal char particles to form long chains. These chains are likely the initial stages of forming larger deposits. These visual observations show that the mixed aluminosilicates are engulfing the coal char particles. Although

these Al-silicate phases have been identified as the main binders, as discussed previously, other studies have suggested that potassium carbonates promote ash agglomeration[114]. Figure 6-11 and Figure 6-12 show that at the 600 ms residence time, these long chains initially formed at the 200 ms residence time, are agglomerating further and coalescing to form larger sintered deposits.

In general, each resultant DTF ash shows that there are reductions in fixed/volatile carbon, clay minerals and carbonate minerals and increases in the mixed aluminosilicate phases formed. The efficient transfer of the metal fluxing elements into the aluminosilicate phase is likely due to the high content of aluminium and silicon in the DTF coal char[291], which derives from the mullite (originally kaolinite in coal) and illite minerals. It is understood that the strength of association with aluminium increases in accordance with the ionisation potential $Mg^{2+} > Ca^{2+} > Na^{+} > K^{+}$ [292] Therefore, these metal fluxing elements may be only transiently associated with the aluminosilicate before being replaced by a higher ionisation potential element.

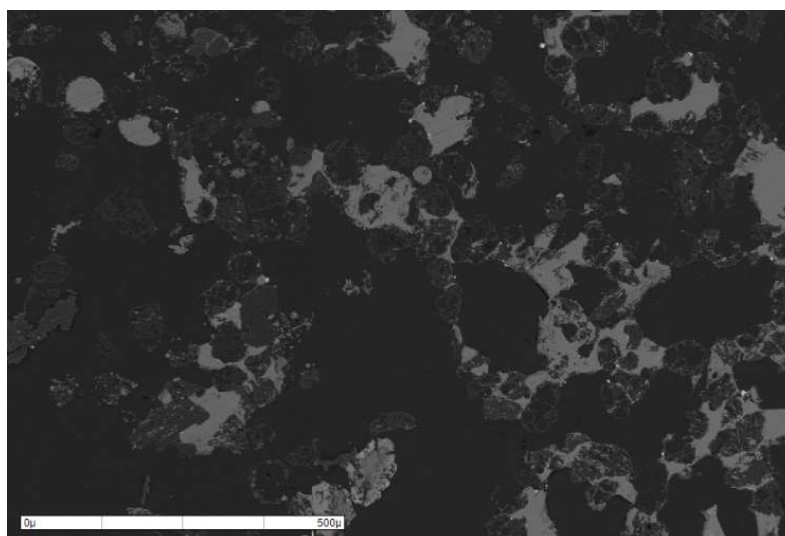


Figure 6-9: Electron micrograph of DTF ash of South African (Koorfontein) DTF Char (1450°C, 200 ms) and 500°C Olive Cake ash (50:50 weight %) fired at 1450°C, 5% O₂ and 200 ms

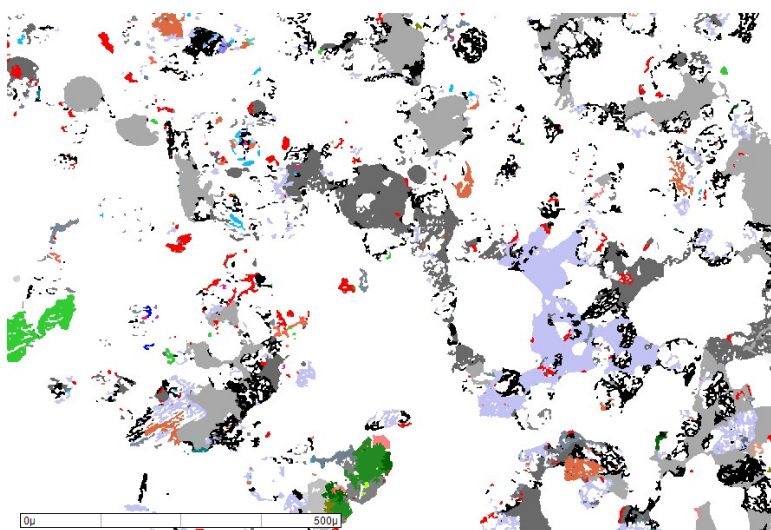


Figure 6-10: MLA coloured mosaic of DTF ash of South African (Koorfontein) DTF Char (1450°C, 200 ms) and 500°C Olive Cake ash (50:50 weight %) fired at 1450°C, 5% O₂ and 200 ms

Table 6-5: Possible mineral transformations during co-firing of DTF coal char and biomass ashes

Mineral/phase	Chemical formula	Melting point (°C)	Decomposition/ Formation reactions	Reference
Coal Char	Carbon-containing	-	Decomposition/oxidation 500-900°C, DTF SAC char starts at 556°C	[93]
Mullite	$\text{Al}_6\text{Si}_2\text{O}_{13}$	1810	$2(2\text{Al}_2\text{O}_3 \cdot 3\text{SiO}_2) \rightarrow 2(3\text{Al}_2\text{O}_3 \cdot 2\text{SiO}_2) + 5\text{SiO}_2$ (1150°C) Formation of molten ash, metal migration (1400-1500°C)	[93, 293]
Illite	$\text{KH}_2\text{O})\text{Al}_2(\text{AlSi})\text{Si}_3\text{O}_{10}(\text{OH})_2$	1200-1300	Dehydration at 50-200°C Crystal lattice destruction at 700-1100°C	[93]
Kaolinite	$\text{Al}_2\text{Si}_2\text{O}_5(\text{OH})_4$	1650-1810	Kaolinite ($\text{Al}_2\text{Si}_2(\text{OH})_4$) \rightarrow metakaolinite ($\text{Al}_2\text{O}_3 \cdot 2\text{SiO}_2$) + $2\text{H}_2\text{O}$ (at 450°C)	[93]
Metakaolinite	$\text{Al}_2\text{Si}_2\text{O}_5$	1650-1810	Metakaolinite ($\text{Al}_2\text{O}_3 \cdot 2\text{SiO}_2$) \rightarrow mullite ($3\text{Al}_2\text{O}_3 \cdot 2\text{SiO}_2$) + cristobalite (SiO_2) (at 1000-1400°C)	[93]
Calcite	CaCO_3	500-900	Ankerite decarbonation at 500-800°C, calcite and dolomite decarbonation at 500-900°C: $\text{CaCO}_3 \rightarrow \text{CaO} + \text{CO}_2$	[93]
Dolomite	$\text{CaMg}(\text{CO}_3)_2$	500-900		
Ankerite	$(\text{Ca}, (\text{Mg}, \text{Fe}))(\text{CO}_3)_2$	500-800		

			Anhydrite desulphation at 800-1300°C: $\text{CaSO}_4 \rightarrow \text{CaO} + \text{SO}_3$ Carbonates form calcium silicates	
Quartz	SiO_2	1713	Crystallisation at 400-1000°C Dissolution in melt (1100-1600°C)	[99]
Hematite	Fe_2O_3	1538	Pyrite (FeS_2) \rightarrow hematite (400-700°C in oxidising atmosphere) Pyrite \rightarrow pyrrhotite (Fe_{1-x}S) (325-750°C in inert atmosphere) Pyrrhotite (Fe_{1-x}S) \rightarrow hematite (Fe_2O_3) (600°C)	[294, 295]
Fairchildite	$\text{K}_2\text{Ca}(\text{CO}_3)_2$	815	$\text{K}_2\text{Ca}(\text{CO}_3)_2 \rightarrow \text{CaO} + \text{K}_2\text{O} + 2\text{CO}_2$ $\text{SiO}_2 + \text{CaO} + 5\text{C} \rightarrow \text{CaSi}_2 + 5\text{CO}$ or: $\text{SiO}_2 + \text{CaCO}_3 + 5\text{C} \rightarrow \text{CaSi}_2 + \text{CO}_2 + 5\text{CO}$ (at 600°C)	[296-298]
Polyhalite	$\text{K}_2\text{Ca}_2\text{Mg}(\text{SO}_4)_4$	225-380	$\text{K}_2\text{SO}_4 + 2\text{CaSO}_4 + \text{MgSO}_4 \rightarrow \text{K}_2\text{Ca}_2\text{Mg}(\text{SO}_4)_4$ (at 25°C) decomposition releases water and forms anhydrous langbeinite ($\text{K}_2\text{Mg}_2(\text{SO}_4)_3$) at 225-380°C	[299, 300]

Sylvite	KCl	770-790	$2\text{KCl} + \text{Al}_2\text{O}_3 \cdot 2\text{SiO}_2 + \text{H}_2\text{O} \rightarrow 2\text{KAlSiO}_4 + 2\text{HCl}$ (at 815°C, forming zeolite)	[135, 301, 302]
Muscovite	$\text{KAl}_2\text{AlSi}_3\text{O}_{10}(\text{OH}, \text{F})_2$	~1200	Kaolinite + sylvite → muscovite (at 700-800°C)	[303]
Ca – Na Aluminosilicate	$\text{Ca}_{0.9}\text{Na}_{0.1}\text{Al}_{1.8}\text{Si}_{2.2}\text{O}_8$	530°C (crystallises)	Quartz + calcite → Ca silicates (at 400-800°C) Quartz + anhydrite → Ca silicates (400-1300°C)	[294, 295]

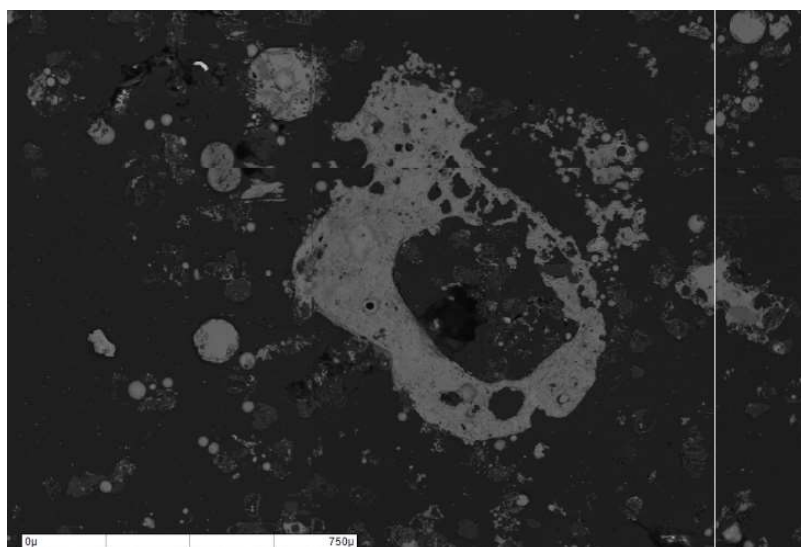


Figure 6-11: Electron micrograph of DTF ash of South African Koornfontein
DTF Char (1450°C, 200 ms) and 500°C Olive Cake ash (50:50 weight %) fired
at 1450°C, 5% O₂ and 600 ms

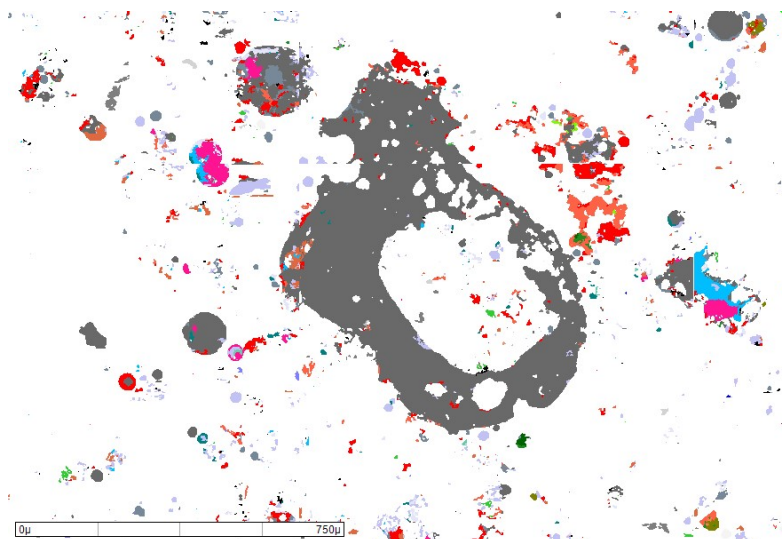


Figure 6-12: MLA coloured mosaic of DTF ash of South African Koornfontein
DTF Char (1450°C, 200 ms) and 500°C Olive Cake ash (50:50 weight %) fired
at 1450°C, 5% O₂ and 600 ms

Table 6-6: Mineral compositions of DTF South African (Koorfontein) Char
and 500°C biomass ashes

Mineral Groups	Mineral Species	SAC DTF Char (1450°C, 200 ms)	Miscanthus 500°C Ash	Sunflower 500°C Ash	Olive Cake 500°C Ash
Fixed/volatile carbon	C/H/O/S	24.34%	6.82%	0.16%	0.13%
Oxides	Quartz	9.80%	0.96%	0.02%	1.13%
	Hematite	0.00%	0.00%	0.00%	0.00%
	Rutile	0.19%	0.00%	0.00%	0.00%
Carbonates	Calcite	0.00%	0.00%	0.00%	0.00%
	Dolomite	0.18%	0.00%	0.00%	0.00%
	Ankerite	0.01%	0.00%	0.00%	0.00%
	Fairchildite	0.01%	4.97%	83.74%	37.16%
Halide	Sylvite	0.00%	0.79%	0.01%	0.37%
Clays	Kaolinite	49.70%	0.17%	0.00%	0.02%
	Montmorillonite	2.65%	0.00%	0.00%	0.00%
	Illite	5.11%	0.02%	0.00%	0.15%
Micas	Muscovite	0.10%	0.00%	0.00%	0.04%
	Biotite	0.00%	0.36%	0.01%	2.71%
Garnets	Almandine	0.08%	0.00%	0.00%	0.00%
	Pyrope	0.00%	0.00%	0.00%	0.00%
Feldspars	Plagioclase	0.00%	0.00%	0.00%	0.00%
	Sanidine	0.00%	0.33%	0.00%	0.18%
	Orthoclase	0.00%	0.66%	0.00%	0.45%
	Albite	0.07%	0.00%	0.00%	0.00%
Phosphates	Apatite	0.17%	0.02%	0.00%	0.00%

Sulphides	Pyrite	0.00%	0.00%	0.00%	0.00%
	Pyrrhotite	0.76%	0.00%	0.01%	0.00%
	Sphalerite	0.00%	0.00%	0.00%	0.00%
Sulphates	Barite	0.00%	0.00%	0.00%	0.00%
	Anhydrite	0.00%	0.00%	0.00%	0.00%
	Gypsum	0.00%	0.00%	0.00%	0.00%
	Polyhalite	0.09%	3.58%	9.43%	39.53%
Mixed Sulphates	Ca sulphate	0.00%	0.00%	0.00%	0.00%
	Ca/Mg sulphate	0.60%	0.00%	0.00%	0.00%
Mixed Oxides	K oxide	0.00%	0.00%	0.11%	1.23%
	Fe/K Oxide	0.83%	0.75%	5.26%	2.82%
	K/P/Mg/Ca oxide	0.00%	0.16%	0.46%	1.08%
	Ca oxide	0.64%	0.22%	0.00%	0.00%
	Ca/K/S/P oxide	0.00%	0.04%	0.00%	0.03%
	Cr oxide	0.00%	0.00%	0.00%	0.00%
	Al oxide	0.01%	0.00%	0.00%	0.01%
	Mg/Ca/K/Fe oxide	0.24%	0.13%	0.58%	0.86%
Mixed Aluminosilicates	Fe/Ca Al-silicate	0.01%	0.00%	0.00%	0.00%
	Ca Al-silicate	0.03%	0.00%	0.00%	0.00%
	Ca/Mg/Na Al-silicate	0.16%	0.01%	0.00%	0.00%
	Ca/Mg Al-silicate	0.29%	0.01%	0.00%	0.02%
	Ca/P Al-silicate	2.20%	0.03%	0.00%	0.01%
	Ca/K/Mg/Fe Al-silicate	0.01%	0.05%	0.04%	2.54%
	Ca/K/P/Mg Al-silicate	0.03%	1.73%	0.09%	4.86%
	Ca/Na Al-silicate	0.14%	65.76%	0.01%	0.05%
	Ca/Na/K Al-silicate	1.16%	0.02%	0.00%	0.04%
	Ca/P/Mg Al-silicate	0.34%	0.03%	0.00%	0.06%
	K/Na Al-silicate	0.00%	0.64%	0.00%	0.08%
	K/Fe/Ca/Na Al-silicate	0.02%	11.74%	0.06%	4.43%

Table 6-7: Mineral Composition of DTF South African (Koorfontein) coal char
and 500°C Biomass Ashes (50:50 weight %) – Calculated

Mineral Groups	Mineral Species	SAC DTF Char (1450°C, 200 ms) / Miscanthus 500°C Ash	SAC DTF Char (1450°C, 200 ms) / Sunflower Husk 500°C Ash	SAC DTF Char (1450°C, 200 ms) / Olive Cake 500°C Ash
Fixed/volatile carbon	C/H/O/S	15.58%	12.25%	12.24%
Oxides	Quartz	5.38%	4.91%	5.47%
	Hematite	0.00%	0.00%	0.00%
	Rutile	0.10%	0.10%	0.10%
Carbonates	Calcite	0.00%	0.00%	0.00%
	Dolomite	0.09%	0.09%	0.09%
	Ankerite	0.01%	0.01%	0.01%
	Fairchildite	2.49%	41.88%	18.59%
Halide	Sylvite	0.40%	0.01%	0.19%
Clays	Kaolinite	24.94%	24.85%	24.86%
	Montmorillonite	1.33%	1.33%	1.33%
	Illite	2.57%	2.56%	2.63%
Micas	Muscovite	0.05%	0.05%	0.07%
	Biotite	0.18%	0.01%	1.36%
Garnets	Almandine	0.04%	0.04%	0.04%
	Pyrope	0.00%	0.00%	0.00%
Feldspars	Plagioclase	0.00%	0.00%	0.00%
	Sanidine	0.17%	0.00%	0.09%
	Orthoclase	0.33%	0.00%	0.23%
	Albite	0.04%	0.04%	0.04%
Phosphates	Apatite	0.10%	0.09%	0.09%

Sulphides	Pyrite	0.00%	0.00%	0.00%
	Pyrrhotite	0.38%	0.39%	0.38%
	Sphalerite	0.00%	0.00%	0.00%
Sulphates	Barite	0.00%	0.00%	0.00%
	Anhydrite	0.00%	0.00%	0.00%
	Gypsum	0.00%	0.00%	0.00%
	Polyhalite	1.84%	4.76%	19.81%
Mixed Sulphates	Ca sulphate	0.00%	0.00%	0.00%
	Ca/Mg sulphate	0.30%	0.30%	0.30%
Mixed Oxides	K oxide	0.00%	0.06%	0.62%
	Fe/K Oxide	0.79%	3.05%	1.83%
	K/P/Mg/Ca oxide	0.08%	0.23%	0.54%
	Ca oxide	0.43%	0.32%	0.32%
	Ca/K/S/P oxide	0.02%	0.00%	0.02%
	Cr oxide	0.00%	0.00%	0.00%
	Al oxide	0.01%	0.01%	0.01%
	Mg/Ca/K/Fe oxide	0.19%	0.41%	0.55%
Mixed Aluminosilicates	Fe/Ca Al-silicate	0.01%	0.01%	0.01%
	Ca Al-silicate	0.02%	0.02%	0.02%
	Ca/Mg/Na Al-silicate	0.09%	0.08%	0.08%
	Ca/Mg Al-silicate	0.15%	0.15%	0.16%
	Ca/P Al-silicate	1.12%	1.10%	1.11%

	Ca/K/Mg/Fe Al-silicate	0.03%	0.03%	1.28%
	Ca/K/P/Mg Al-silicate	0.88%	0.06%	2.45%
	Ca/Na Al- silicate	32.95%	0.08%	0.10%
	Ca/Na/K Al- silicate	0.59%	0.58%	0.60%
	Ca/P/Mg Al-silicate	0.19%	0.17%	0.20%
	K/Na Al- silicate	0.32%	0.00%	0.04%
	K/Fe/Ca/Na Al-silicate	5.88%	0.04%	2.23%

Table 6-8: Mineral Composition of DTF Ash from Co-firing Coal Char with
Biomass Ash

Mineral Groups	Mineral Species	SAC DTF Char (1450°C, 200 ms) / Miscanthus 500°C Ash	SAC DTF Char (1450°C, 200 ms) / Sunflower Husk 500°C Ash	SAC DTF Char (1450°C, 200 ms) / Olive Cake 500°C Ash	SAC DTF Char (1450°C, 200 ms) / Olive Cake 500°C Ash
		1450°C, 5%O ₂ , 600 ms	1450°C, 5%O ₂ , 600 ms	1450°C, 5%O ₂ , 200 ms	1450°C, 5%O ₂ , 600 ms
Fixed/volatile carbon	C/H/O/S	6.37%	0.57%	14.53%	3.57%
Oxides	Quartz	10.21%	0.66%	2.54%	2.63%
	Hematite	0.01%	0.00%	0.02%	0.01%
	Rutile	0.02%	0.00%	0.00%	0.00%
Carbonates	Calcite	0.01%	0.00%	0.01%	0.09%
	Dolomite	0.01%	0.00%	0.03%	0.04%
	Ankerite	0.00%	0.00%	0.01%	0.00%
	Fairchildite	0.00%	0.44%	4.85%	3.52%
Halide	Sylvite	0.01%	0.03%	0.26%	0.29%
Clays	Kaolinite	9.61%	0.00%	2.40%	0.29%
	Montmorillonite	0.55%	0.00%	0.26%	0.05%
	Illite	2.55%	0.45%	3.66%	1.66%
Micas	Muscovite	5.17%	0.07%	5.79%	4.76%
	Biotite	0.01%	2.76%	0.73%	0.18%
Garnets	Almandine	0.01%	0.00%	0.00%	0.00%
	Pyrope	0.00%	0.00%	0.00%	0.00%
Feldspars	Plagioclase	0.00%	0.00%	0.00%	0.00%

	Sanidine	0.08%	0.31%	0.87%	0.69%
	Orthoclase	0.07%	0.15%	0.49%	1.14%
	Albite	0.20%	0.00%	0.03%	0.00%
Phosphates	Apatite	0.01%	0.00%	0.05%	0.03%
Sulphides	Pyrite	0.00%	0.00%	0.00%	0.00%
	Pyrrhotite	0.01%	0.00%	0.05%	0.00%
	Sphalerite	0.00%	0.00%	0.00%	0.00%
Sulphates	Barite	0.00%	0.00%	0.00%	0.00%
	Anhydrite	0.00%	0.00%	0.00%	0.00%
	Gypsum	0.00%	0.00%	0.00%	0.00%
	Polyhalite	0.09%	14.31%	16.79%	16.79%
Mixed Sulphates	Ca sulphate	0.00%	0.00%	0.06%	0.00%
	Ca/Mg sulphate	0.23%	0.00%	0.01%	0.04%
Mixed Oxides	K oxide	0.00%	0.02%	0.06%	0.11%
	Fe/K Oxide	0.73%	0.88%	3.20%	6.83%
	K/P/Mg/Ca oxide	0.00%	0.26%	0.12%	0.09%
	Ca oxide	0.16%	0.00%	0.19%	0.28%
	Ca/K/S/P oxide	0.10%	0.01%	0.08%	0.03%
	Cr oxide	0.01%	0.00%	0.01%	0.01%
	Al oxide	0.14%	0.00%	0.00%	0.00%
	Mg/Ca/K/Fe oxide	0.95%	2.96%	0.67%	1.16%
Mixed Aluminosilicates	Fe/Ca Al-silicate	0.02%	0.00%	0.01%	0.03%
	Ca Al-silicate	0.01%	0.00%	0.01%	0.00%
	Ca/Mg/Na Al-silicate	0.30%	0.00%	0.15%	0.13%

	Ca/Mg Al-silicate	0.35%	0.13%	5.51%	0.52%
	Ca/P Al-silicate	1.87%	0.00%	0.26%	0.23%
	Ca/K/Mg/Fe Al-silicate	0.28%	21.88%	16.19%	29.09%
	Ca/K/P/Mg Al-silicate	1.29%	46.60%	4.81%	6.17%
	Ca/Na Al-silicate	20.41%	0.10%	0.11%	0.05%
	Ca/Na/K Al-silicate	6.86%	0.13%	0.12%	0.05%
	Ca/P/Mg Al-silicate	0.51%	0.13%	0.53%	0.36%
	K/Na Al-silicate	0.46%	0.70%	0.63%	2.19%
	K/Fe/Ca/Na Al-silicate	30.33%	6.42%	13.88%	16.86%

Figure 6-13 shows the particle size distribution data of the DTF co-fired ashes at the 200 ms and 600 ms residence times. The results indicate that the particle size of the ash deposits formed at 600 ms are considerably larger (850 μm maximum) than the linkages of char particles partially fused with biomass ash at 200 ms (355 μm maximum). The transformation of the ash minerals during combustion are influenced by temperature, residence time and O_2 availability[304]. These results suggest that at the 200 ms residence time there are limited interactions and encounters between the coal-biomass and biomass-biomass particles with the combustion gases, and the equilibrium has not been reached. Figure 6-14 and Figure 6-15 provide further supporting evidence that the mixed aluminosilicate species are the dominant ash-deposition minerals, the mineral grain size distribution data clearly shows that the mixed aluminosilicates are the main contributors to the increased particle size distribution likely due to the melting of the oxides and clays.

As detailed in the literature review (section 2.3.3), potassium-containing compounds such as potassium carbonate (K_2CO_3), aside from their catalytic effect are considered to contribute towards sintering and ash agglomeration. Previous workers have reported that potassium silicate melts (K_2SiO_3 , $\text{K}_2\text{Si}_2\text{O}_5$ and $\text{K}_2\text{Si}_4\text{O}_9$) can be present on the surfaces of these agglomerates at 600°C[115, 305]. However, in this research it is likely that fairchildite ($\text{K}_2\text{Ca}(\text{CO}_3)_2$) and sylvite (KCl) are decomposing and reacting with the aluminosilicate phases at the higher 1450°C operating temperature of the DTF, and forming sticky bridging particles which enlarge the size of the ash particles.

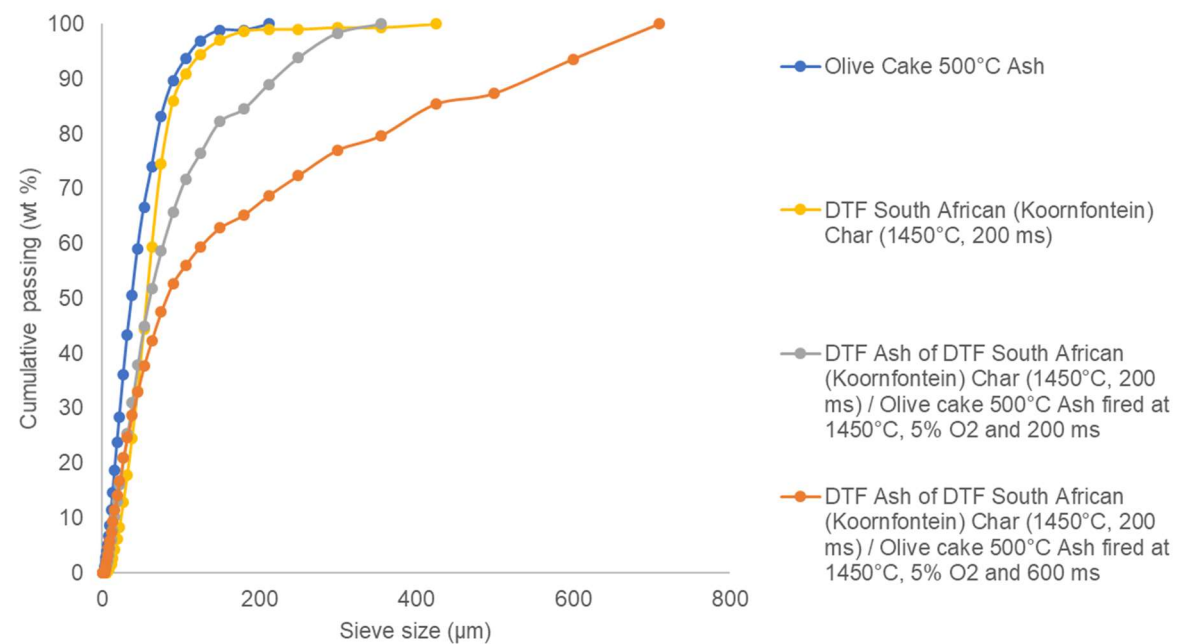


Figure 6-13: Cumulative particle size distribution of the DTF ash formed from firing DTF South African (Koorfontein) char and olive cake 500°C ash at two residence times.

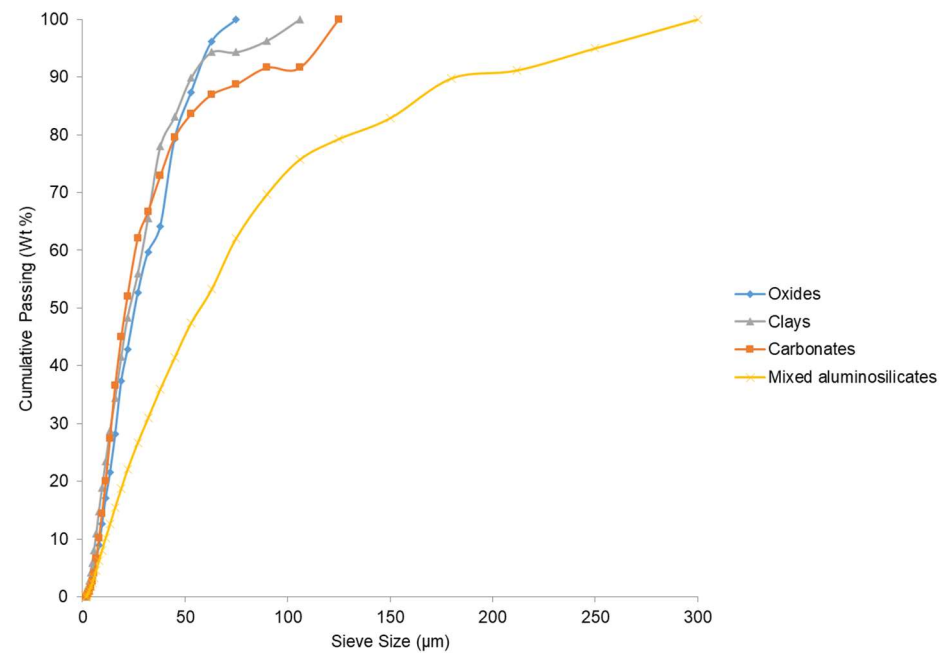


Figure 6-14: Cumulative mineral group size distribution of the DTF ash formed from firing DTF South African (Koorfontein) char and olive cake

500°C ash at 1450°C, 5% O₂ and 200 ms

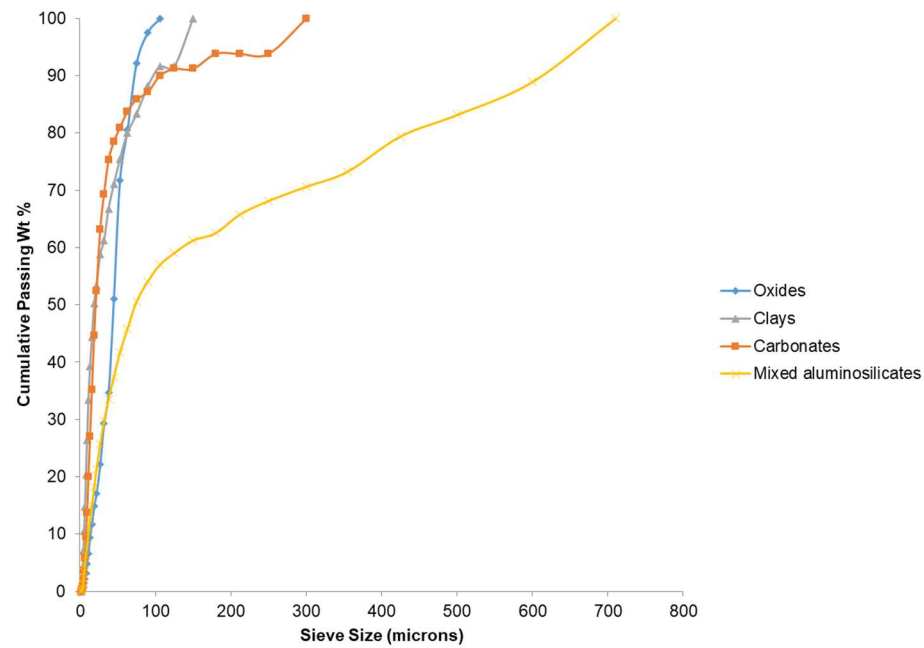


Figure 6-15: Cumulative mineral group size distribution of the DTF ash formed from firing DTF South African (Koorfontein) char and olive cake
500°C ash at 1450°C, 5% O₂ and 600 ms

6.5 Ternary Phase Diagrams of Biomass Ashes Co-fired with DTF Chars

This section investigates the mineral transformations during the co-firing of the DTF coal char with the muffle furnace biomass ashes, with particular attention to the capture of the inherent biomass potassium-containing compounds by the DTF char. Previous studies have used coal fly ash additives to capture the biomass-derived potassium, however limited studies have been conducted on the coal char exclusively, which usually constitutes a significant proportion of the unburned carbon within industrial coal fly ash.

Figure 6-16 shows the reference ternary phase diagram for the $\text{SiO}_2 - \text{Al}_2\text{O}_3 - \text{K}_2\text{O}$ system. The right-hand section along the intersection between SiO_2 and Al_2O_3 includes the formation of mullite ($3\text{Al}_2\text{O}_3 \cdot \text{SiO}_2$). For the MLA mineral database, the mullite contains a similar EDX spectra to the kaolinite ($\text{Al}_2\text{Si}_2\text{O}_5(\text{OH})_4$). These ternary phase diagrams are able to graphically show how the basic oxides (such as K_2O and CaO) are distributed within the individual mineral grains, which is usually not apparent from examining the mineral composition data alone. The phase diagrams are used to show the migration of the basic oxides into the aluminosilicate phases.

Figure 6-17 shows that the majority of the individual mineral grains within the DTF coal char are mullite (aluminosilicates) with negligible potassium-containing aluminosilicates close to the K_2O apex.

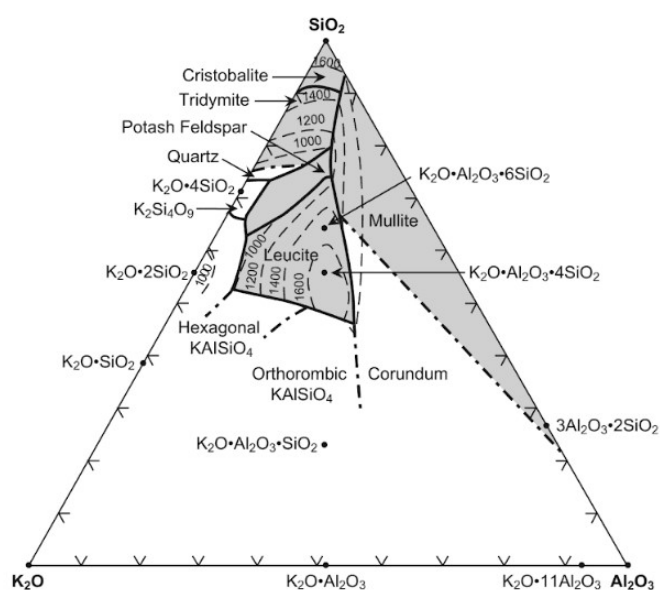


Figure 6-16: Ternary phase diagram of SiO_2 - Al_2O_3 - K_2O [306]

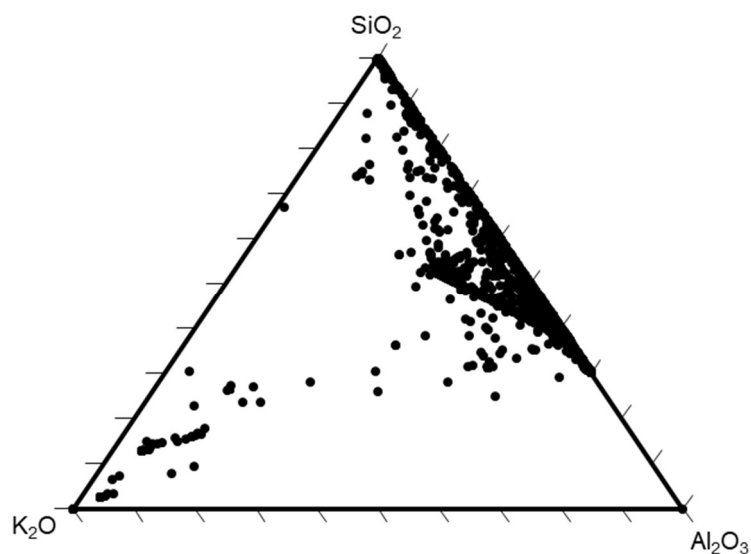


Figure 6-17: SiO_2 - Al_2O_3 - K_2O ternary phase diagram of DTF South African char (1450°C, 200 ms, N_2)

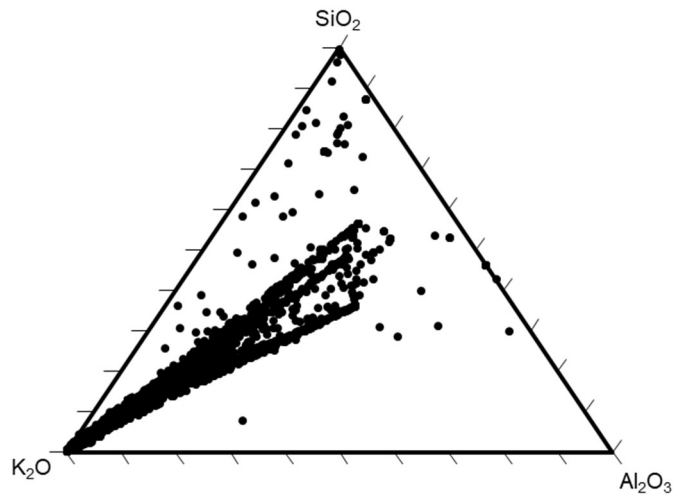


Figure 6-18: SiO_2 - Al_2O_3 - K_2O ternary phase diagram of muffle furnace olive cake ash (500°C, Air)

Figure 6-18 shows that there are significant $\text{K}_2\text{O}.\text{Al}_2\text{O}_3.\text{SiO}_2$ phases within the olive cake ash, with negligible mullite phases present. After combustion of the co-fired DTF coal char and olive cake ash, shown in Figure 6-19, the mineral grains are considerably more dispersed with the formation of $\text{K}_2\text{O}.\text{Al}_2\text{O}_3.\text{SiO}_2$ phases. These phases are likely to be the Ca/K/Mg/Fe Al-silicate and K/Fe/Ca/Na Al-silicate identified in the mineral composition data (Table 6-8). When the residence time increased to 600 ms, Figure 6-20 suggests that more of the mullite grains on the SiO_2 – Al_2O_3 line reacted with K^+ forming a greater concentration of the $\text{K}_2\text{O}.\text{Al}_2\text{O}_3.\text{SiO}_2$ in the centre of the phase diagram. This is further supported through the higher Ca/K/Mg/Fe Al-silicate and K/Fe/Ca/Na Al-silicate weight percentages in the 600 ms DTF ash in Table 6-8.

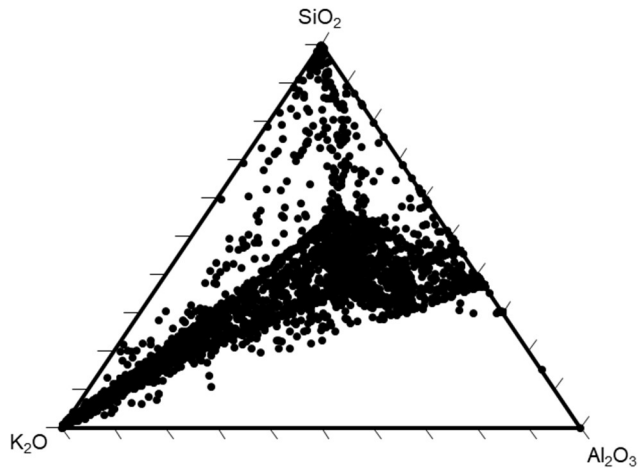


Figure 6-19: SiO₂ - Al₂O₃ - K₂O ternary phase diagram of DTF South African (Koorfontein) Char (1450°C, N₂, 200 ms) / Olive Cake 500°C Ash (50:50 weight %) fired at 1450°C, 5% O₂, 200 ms

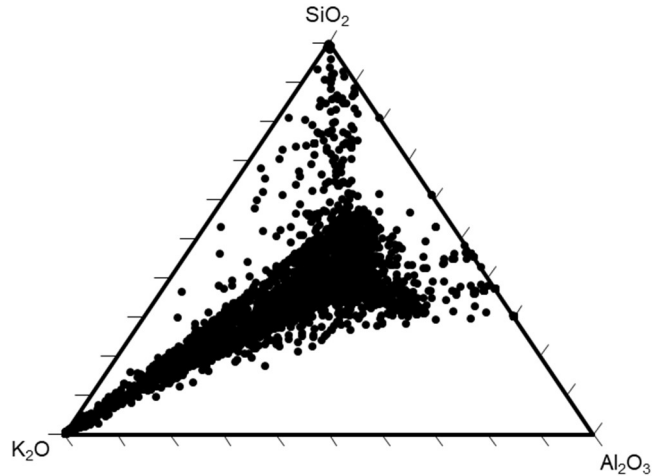


Figure 6-20: SiO₂ - Al₂O₃ - K₂O ternary phase diagram of DTF South African (Koorfontein) Char (1450°C, N₂, 200 ms) / Olive Cake 500°C Ash (50:50 weight %) fired at 1450°C, 5% O₂, 600 ms

6.6 MLA Coloured Mosaics of 500°C Biomass Muffle Furnace Ashes, Coal Chars and DTF Biomass Co-fired Ashes

The BSE images and MLA coloured mosaics of the biomass ash particles and the resultant biomass co-fired combustion ashes in the drop tube furnace are shown below. In the co-fired ash images the brighter particles are the ash particles whilst the darker particles are the DTF coal char particles. The MLA mineral legend has been shown previously in Figure 4-6. The physical characteristics of the ashes differ significantly, in Figure 6-34 there are more spherical particles formed whereas in Figure 6-30 the ash particles appear thinner and elongated.

The DTF coal char and biomass ash mixed blends show further morphological changes occurring during combustion. The blends containing olive cake, which were fired at 200 and 600 ms show there is a slight reduction in the number of spherical particles at the lower residence time, which could be attributed to the linkages between char particles formed, and then a significant increase in molten spherical particles formed at the higher residence time.

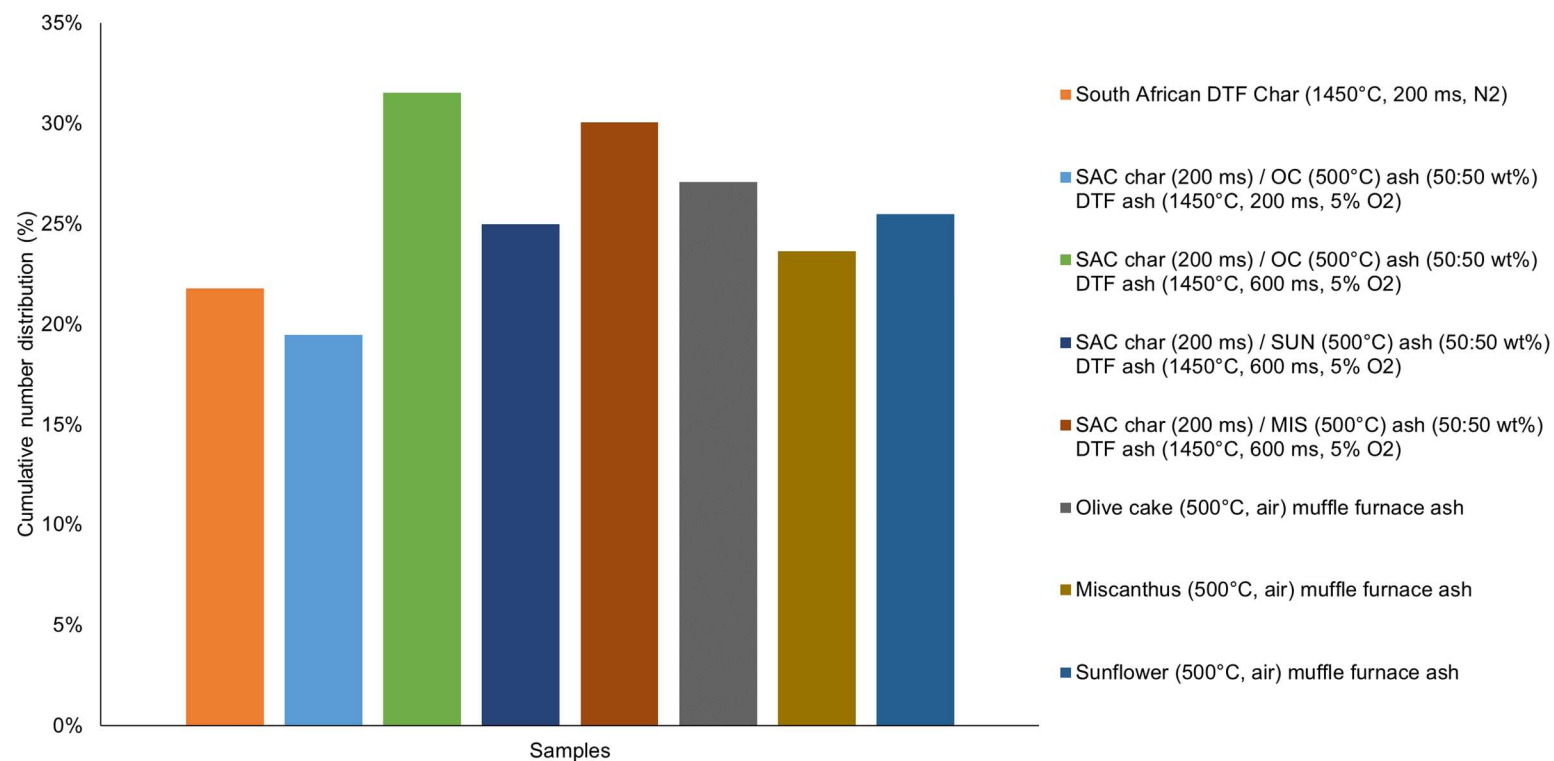


Figure 6-21: Cumulative number distribution (%) of the percentage of particles with a circularity between 0.6 - 1.0 within each biomass co-fired sample

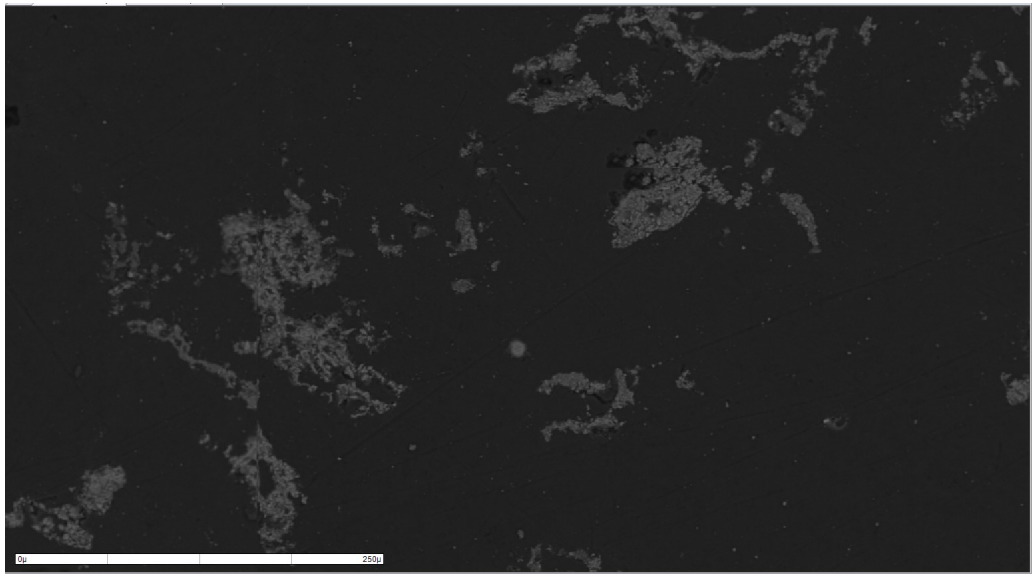


Figure 6-22: Electron micrograph of muffle furnace Miscanthus ash (500°C, air)

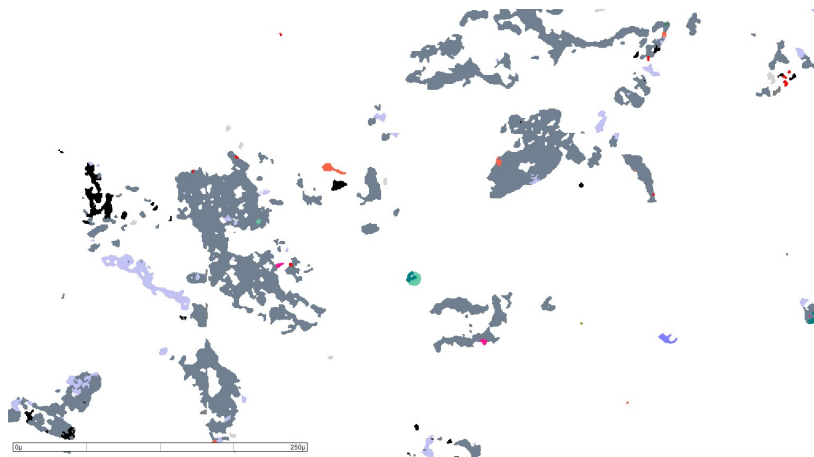


Figure 6-23: MLA coloured mosaic of muffle furnace Miscanthus ash (500°C, air)

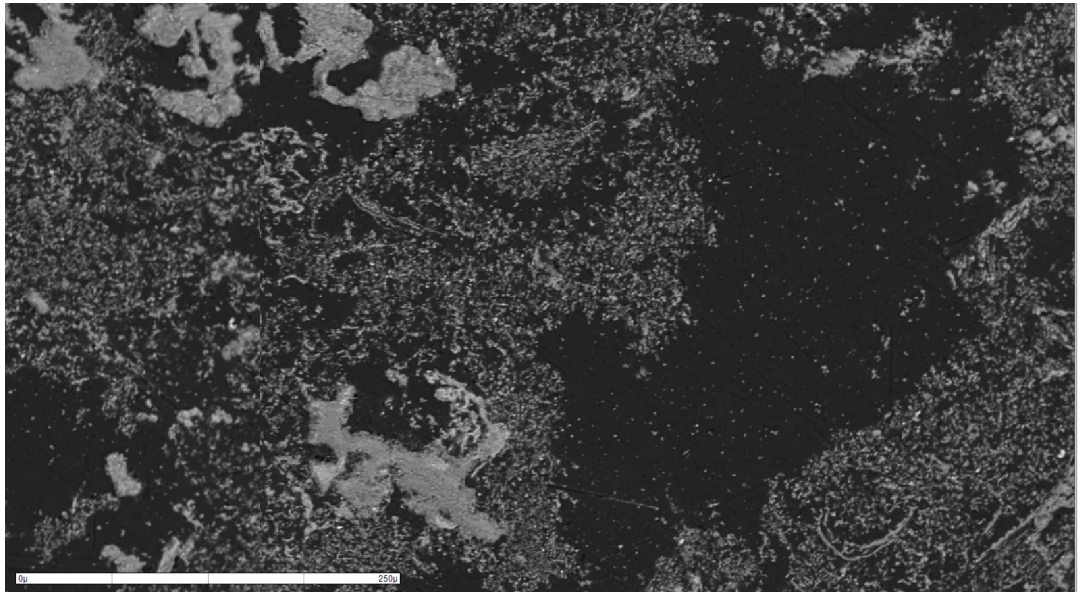


Figure 6-24: Electron micrograph of muffle furnace Sunflower ash (500°C, air)



Figure 6-25: MLA coloured mosaic of muffle furnace Sunflower ash (500°C,
air)

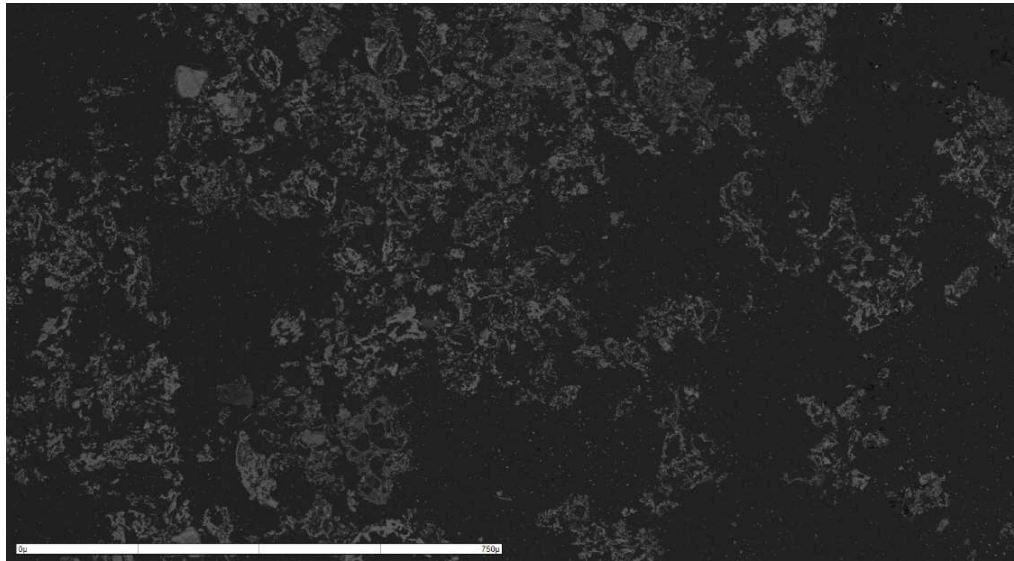


Figure 6-26: Electron micrograph of muffle furnace Olive Cake ash (500°C, air)

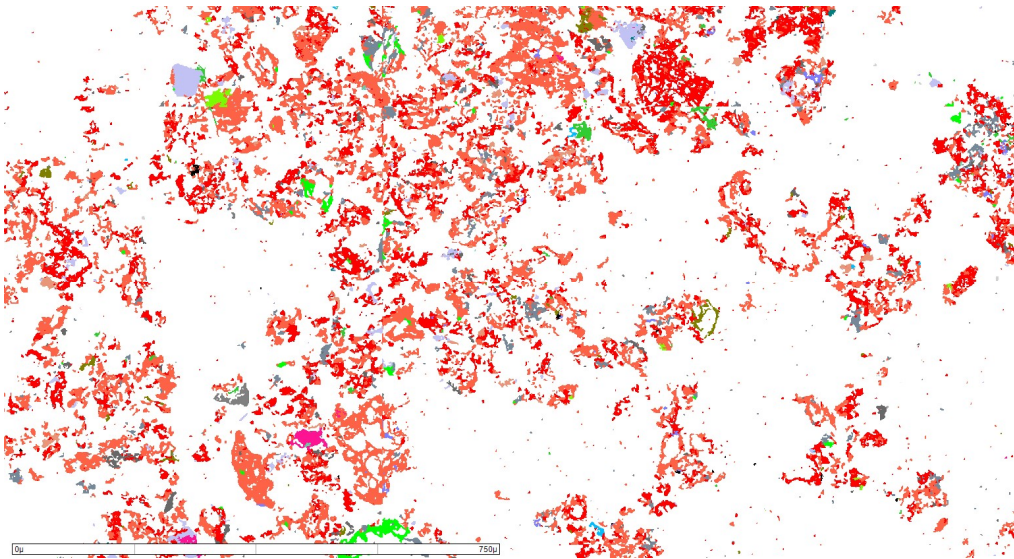


Figure 6-27: MLA coloured mosaic of muffle furnace Olive Cake ash (500°C, air)

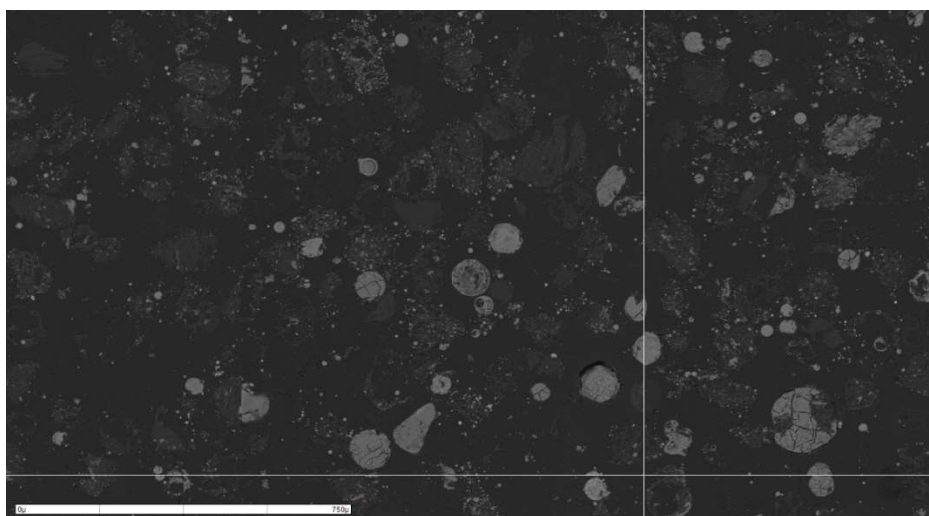


Figure 6-28: Electron micrograph of DTF South African (Koorfontein) Char (1450°C, N₂, 200 ms) / Miscanthus 500°C Ash (50:50 weight %) fired at 1450°C, 5% O₂, 600 ms

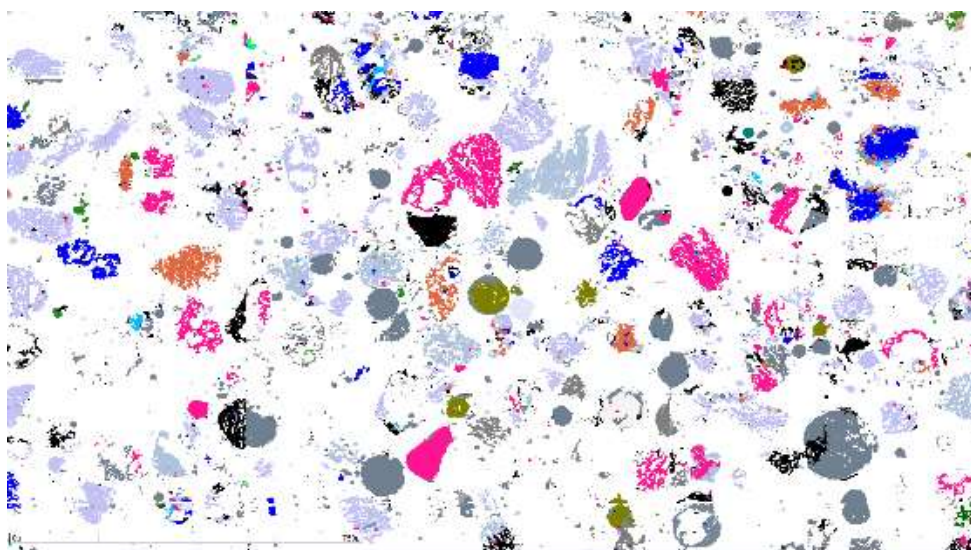


Figure 6-29: MLA coloured mosaic of of DTF South African (Koorfontein) Char (1450°C, N₂, 200 ms) / Miscanthus 500°C Ash (50:50 weight %) fired at 1450°C, 5% O₂, 600 ms

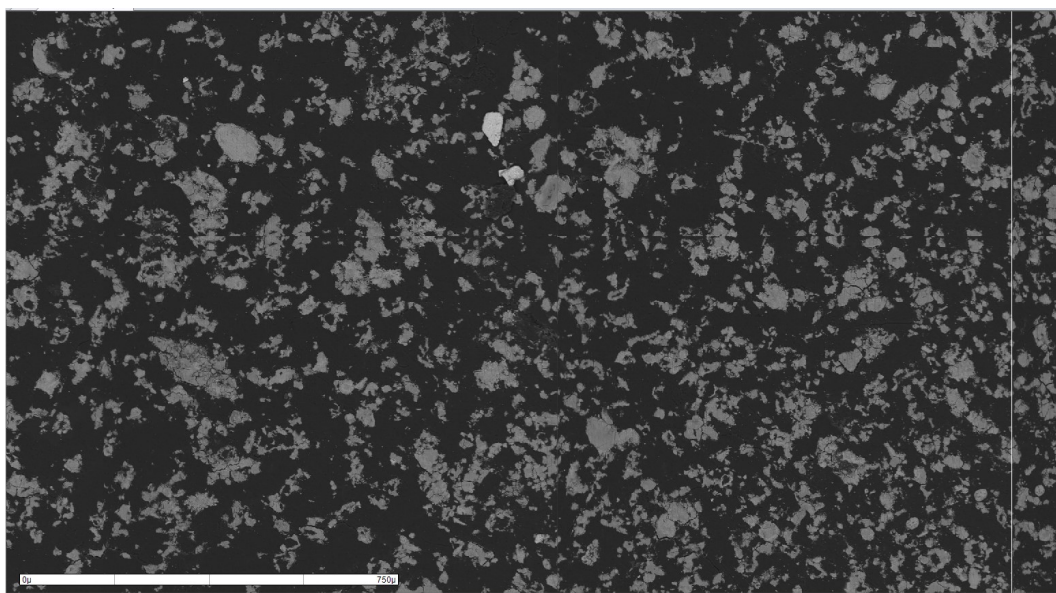


Figure 6-30: Electron micrograph of DTF South African (Koorfontein) Char (1450°C, N₂, 200 ms) / Sunflower Husk 500°C Ash (50:50 weight %) fired at 1450°C, 5% O₂, 600 ms

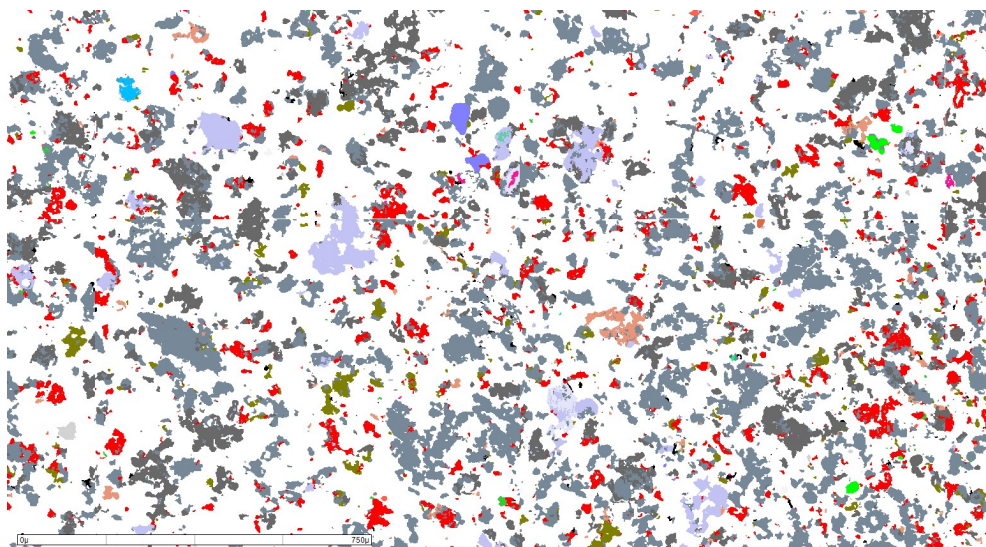


Figure 6-31: MLA coloured mosaic of DTF South African (Koorfontein) Char (1450°C, N₂, 200 ms) / Sunflower Husk 500°C Ash (50:50 weight %) fired at 1450°C, 5% O₂, 600 ms

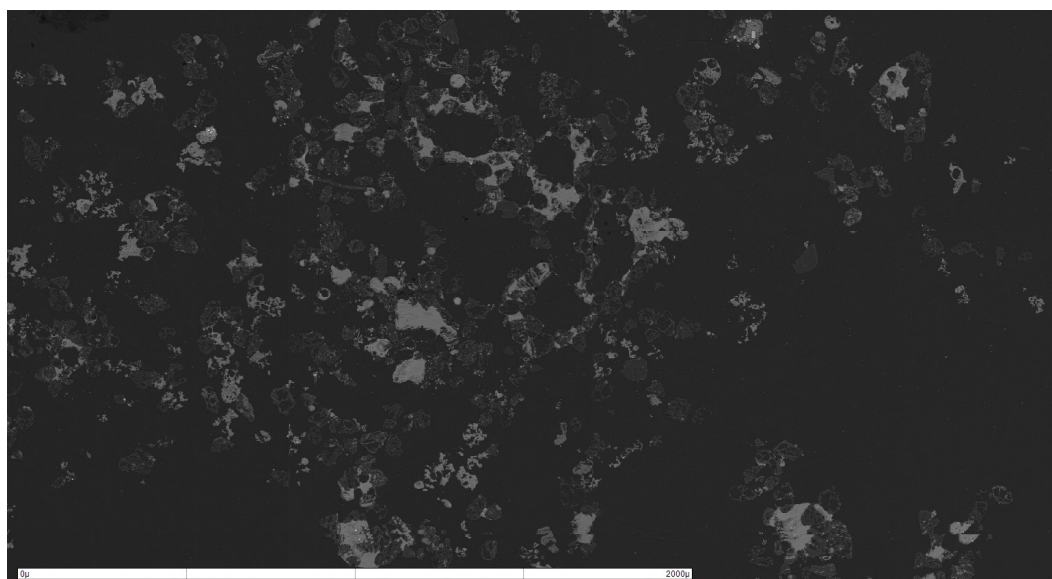


Figure 6-32: Electron micrograph of DTF South African (Koorfontein) Char
(1450°C, N₂, 200 ms) / Olive Cake 500°C Ash (50:50 weight %) fired at
1450°C, 5% O₂, 200 ms

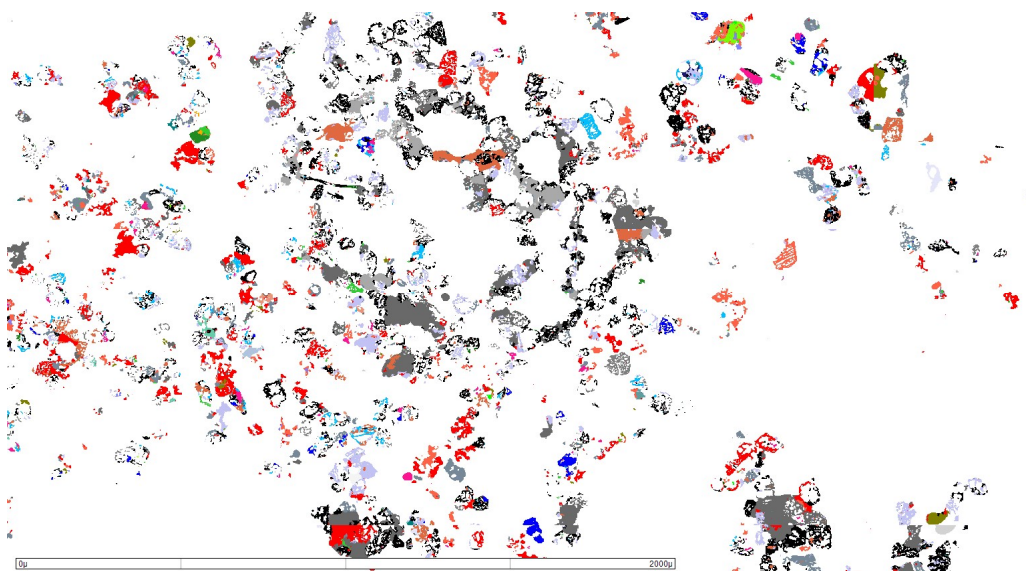


Figure 6-33: MLA coloured mosaic of DTF South African (Koorfontein) Char
(1450°C, N₂, 200 ms) / Olive Cake 500°C Ash (50:50 weight %) fired at
1450°C, 5% O₂, 200 ms

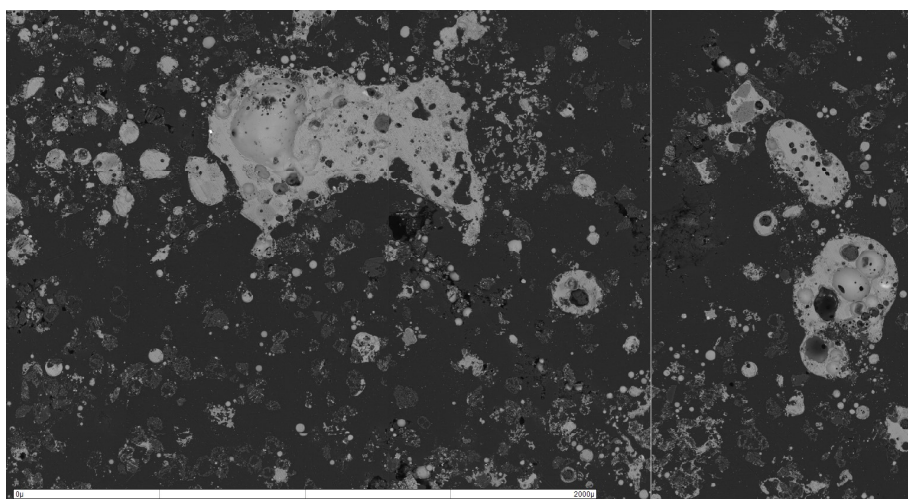


Figure 6-34: Electron micrograph of DTF South African (Koorfontein) Char (1450°C, N₂, 200 ms) / Olive Cake 500°C Ash (50:50 weight %) fired at 1450°C, 5% O₂, 600 ms

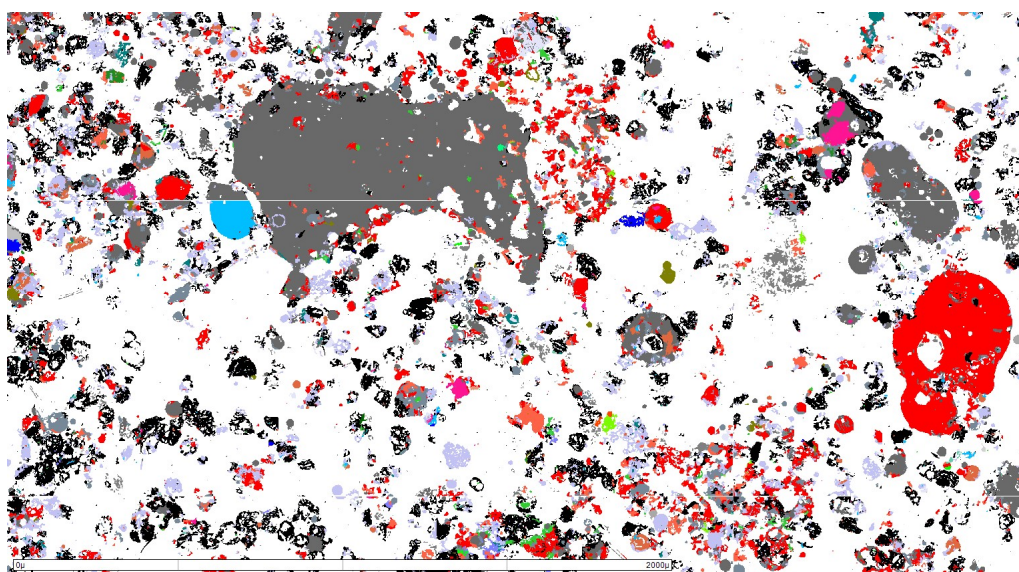


Figure 6-35: MLA coloured mosaic of DTF South African (Koorfontein) Char (1450°C, N₂, 200 ms) / Olive Cake 500°C Ash (50:50 weight %) fired at 1450°C, 5% O₂, 600 ms

6.7 Mineral Associations of DTF Ash from Co-firing Coal Char with Biomass Ash

The mineral association graphs are shown for the DTF South African (Koorfontein) char (1450°C, 200 ms) blended with the miscanthus, sunflower husk and olive cake 500°C ashes respectively at 1450°C, 5%O₂ at the various residence times. Figure 5-20 showing the DTF coal char mineral association graph in section 5.4.3 showed that during coal devolatilisation there was minimal interactions between the various mineral groups containing metal fluxing elements such as Ca, Mg, Na and K, and that the majority of mineral groups were excluded minerals. However, for the DTF coal char and biomass ash interactions this is not the case. Figure 6-36 at the 200 ms residence time suggests that there are limited interactions between mineral groups, but as the residence time is increased to 600 ms in Figure 6-37 there is a higher volume percentage of the mixed aluminosilicates interacting with the various mineral groups as the reactions approach equilibrium. The increase of residence time by 400 ms was found to lead to more metal fluxing elements such as Ca, Mg, Fe, Na and K being transformed into aluminosilicate phases in the DTF coal char.

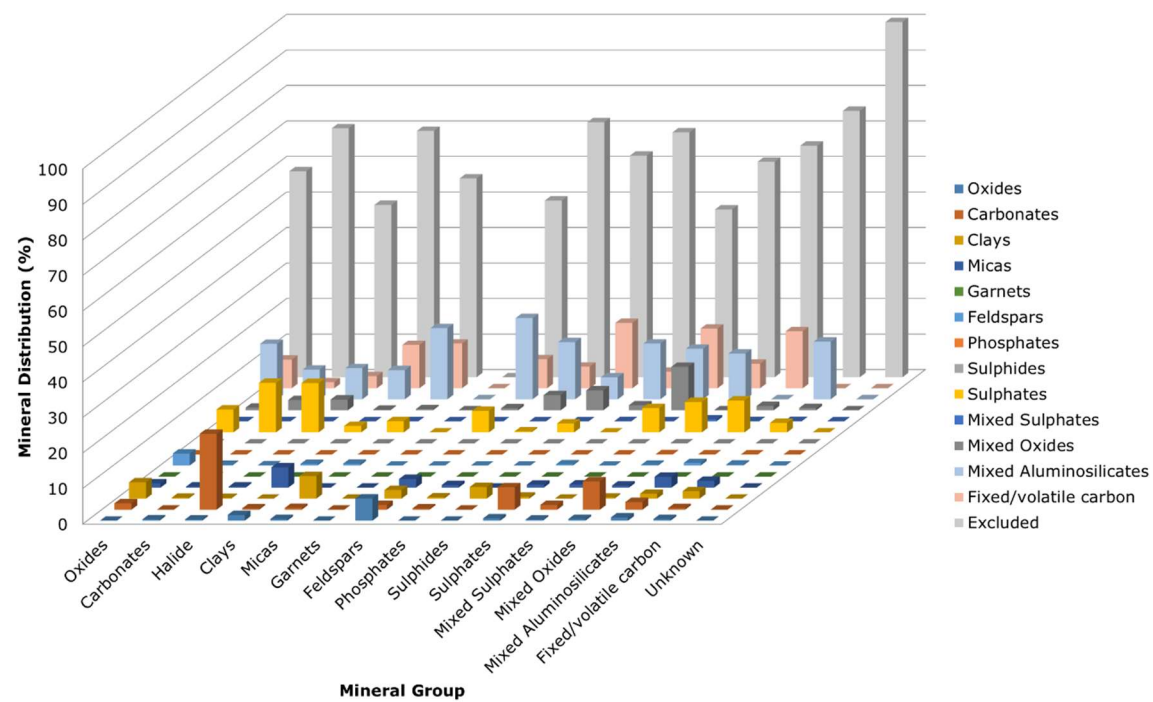


Figure 6-36: DTF Ash of DTF South African (Koorfontein) Char (1450°C, 200 ms) / Olive cake 500°C Ash under 1450°C, 5% O₂ and 200 ms

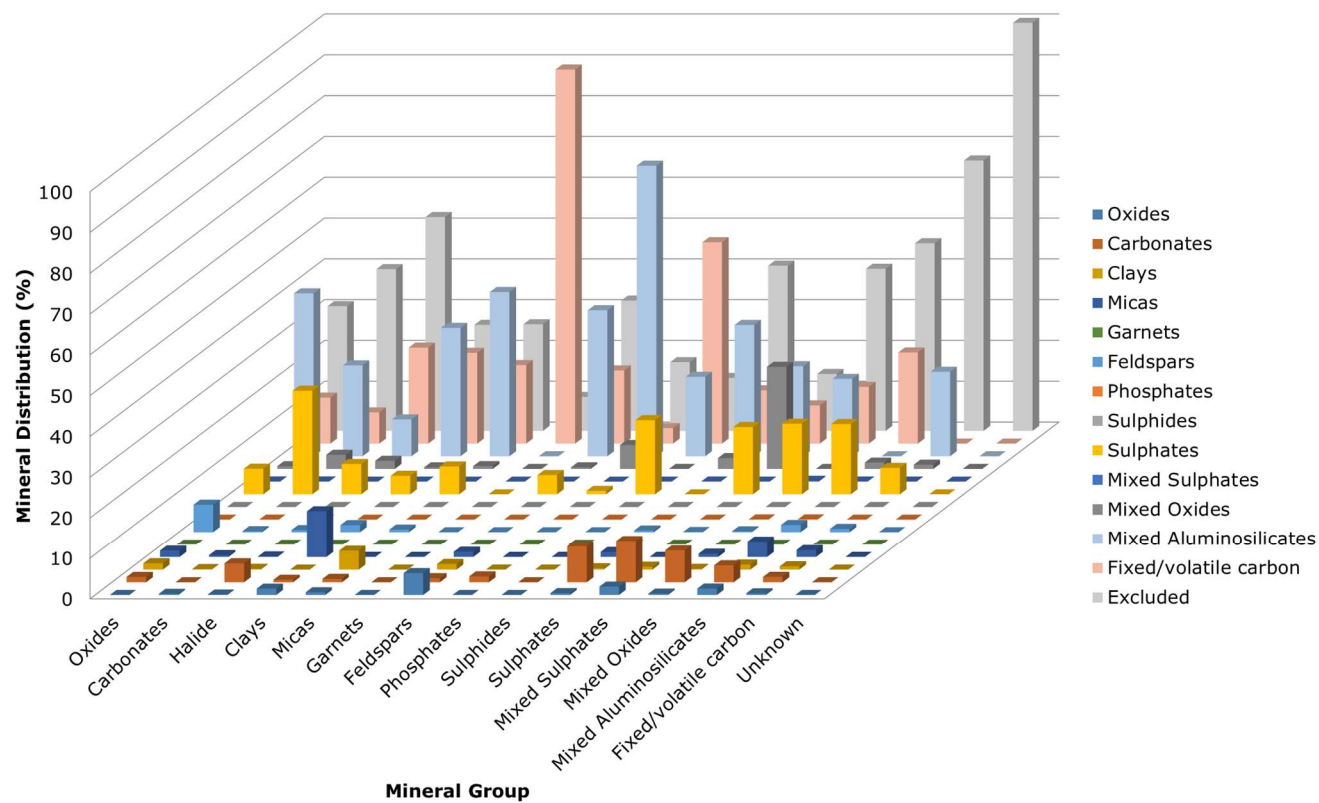


Figure 6-37: DTF Ash of DTF South African (Koorfontein) Char (1450°C, 200 ms) / Olive cake 500°C Ash under 1450°C, 5% O₂ and 600 ms

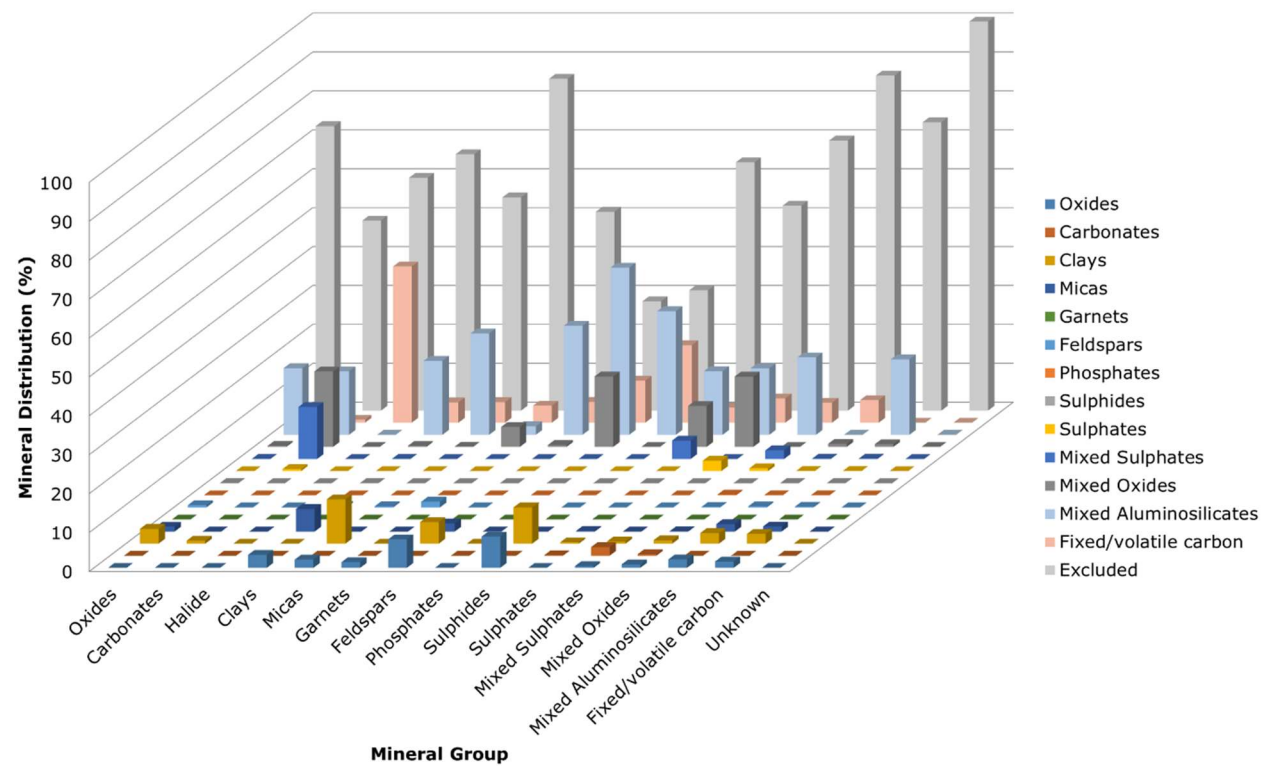


Figure 6-38: DTF Ash of DTF South African (Koorfontein) Char (1450°C, 200 ms) / Miscanthus 500°C Ash under 1450°C, 5% O₂ and 600 ms

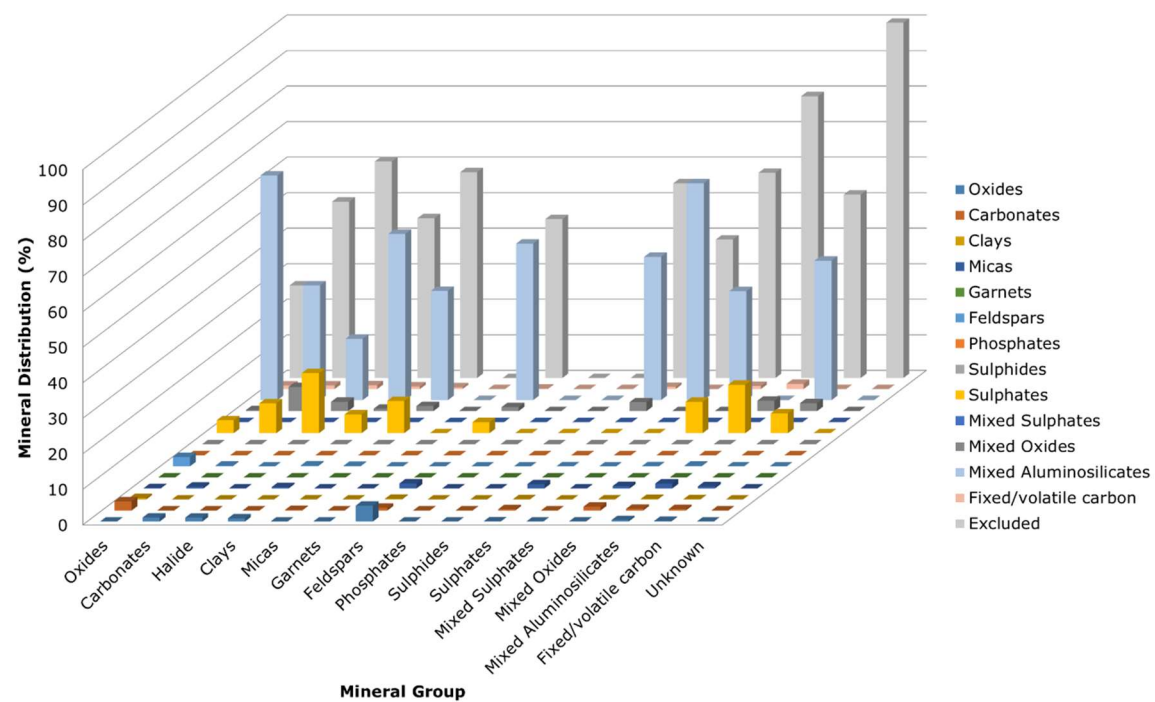


Figure 6-39: DTF Ash of DTF South African (Koorfontein) Char (1450°C, 200 ms) / Sunflower 500°C Ash under 1450°C, 5% O₂ and 600 ms

6.8 Chapter Conclusions

The thermogravimetric study of the DTF coal char mixed with muffle furnace biomass ashes at 10, 30 and 50 wt % suggested the presence of synergistic or catalytic effects. The addition of olive cake ash had the most significant impact on reducing the ignition temperature of the DTF coal char

The phase diagram of $K_2O - Al_2O_3 - SiO_2$ shows that the aluminosilicate phases consisting of various ratios of Al to Si, have the effect of entrapping the K containing species during devolatilisation and char combustion. This invariably has the effect of reducing the extent of K vaporisation which causes corrosion issues within boiler furnaces. However, the reaction of these fluxing elements with the aluminosilicates produces mixed aluminosilicates which cause structural bridging between the coal char particles, leading to an increase in the particle size of the deposits formed during the co-firing of coal char and biomass ash.

Finally, the South African Koornfontein coal char was selected to be co-fired with 500°C biomass ash at 50:50 weight percent at 1450°C under 5% O_2 in the drop tube furnace at residence times of 200 ms and 600 ms. The purpose was to determine the influence of the biomass ash minerals on the mineral transformations and identify any ash-deposition related minerals. A summary of the conclusions for this chapter are as follows:

- 1) The thermogravimetric char burnout profiles at $5^{\circ}\text{C min}^{-1}$ to 1000°C performed on the biomass ash and DTF coal char at 10, 30 and 50 wt % showed that for all the biomasses there was a reduction in the ignition temperature without the presence of volatile and fixed carbon components. This infers that there are catalytic or synergistic effects associated with the Na, K and Ca minerals present within the biomass ashes. X-ray diffraction of the biomass ashes show that the major minerals present within the samples are fairchildite ($\text{K}_2\text{Ca}(\text{CO}_3)$), the salt polyhalite ($\text{K}_2\text{Ca}_2\text{Mg}(\text{SO}_4)_4$), sylvite (KCl) and calcium sodium silicate species.
- 2) The coloured mosaics of the resultant DTF co-fired ashes, specifically for the DTF coal char and 500°C olive cake ash (Figure 6-33 and Figure 6-35) show that the mixed aluminosilicates contribute significantly to the development of ash deposits, and the deposit size increases with residence time from 200 ms to 600ms. This is further supported from the increased particle size distribution data and the mineral grain size analysis (Figure 6-13 and Figure 6-14). For this blend, it was shown that the number of spherical particles was less at the 200 ms residence time compared to 600 ms. This could be due to the biomass ash linking the char particles at 200 ms and then spherical agglomerating particles forming at 600 ms.

- 3) Mineral association data showed that the mineral groups were considerably distributed with the mixed aluminosilicate phases, and it is suggested that these interactions increased as a function of residence time as the DTF coal char and biomass ash reactions reached equilibrium.

Chapter 7: Conclusions and Future Work

The major aim of this research was to generate experimental data to aid the development of ash formation modelling in industrial-scale boilers, using conventional and advanced analytical techniques. Analysis of the boiler fly ashes enabled correlations to be developed relating mineral grain size distribution with erosive wear and confirmed that the angularities of individual mineral grains played a limited role on erosion potential. A novel MLA mineral database was developed which can be applied to coals and biomasses and their respective chars and ashes. This database provided detailed characterisation of the mixed aluminosilicate phases, which are important during slagging, fouling and ash deposit formation.

7.1 Automated Mineralogy and Erosion Test Rig Experiments

In this part of the project, characterisation was performed on a selection of power station fly ashes from the convective sections of pulverised coal-fired industrial scale boilers after shutdown. The main objective was to verify and validate a mineral species library or database for computer-controlled scanning electron microscopy (CCSEM) or mineral liberation analysis (MLA) and to compare to the minerals identified using traditional chemical analyses, XRF and XRD. This initial step in the project also served to identify the aluminosilicate species present in industrial ashes, particularly those that contribute to deposition behaviour. In particular, this study investigated the types of ash

morphologies, with respect to mineral composition formed during the pulverised combustion process.

The conclusions drawn from the analysis of the industrial ashes and the correlations of their mineral properties with traditional chemical analyses can be summarised as follows:

- 1) A unique mineral database has been developed using mineral standards collected from the Clay Minerals Society in the USA. Compared to mineral databases reported in the literature, this database provides more detailed EDX spectra to identify the metal fluxing aluminosilicate species (mixed aluminosilicates) which are important during the ash mineral transformations to aid understanding of slagging and fouling, erosion and corrosion behaviour.
- 2) The erosion test rig results confirmed that the Ratcliffe fly ash had the highest erosion rate compared to Drax and Longannet fly ashes. This has been attributed to the higher particle size of the fly ash, as determined through sieve analysis, laser light scattering and particle size distributions from the MLA.
- 3) Mineral grain size distribution graphs were generated using MLA for the fly ashes, and suggested that the particle size of quartz is a more dominant factor in the erosion rate than hematite.
- 4) X-ray diffraction patterns of the fly ashes showed the presence of a selection of minerals that were identified and semi-quantified using MLA, such as illite, kaolinite and quartz.

- 5) The limited quantitative data available in the literature regarding the impact of fly ash angularity on the erosion rate has been studied on the suite of fly ashes. It was confirmed that angularity has a negligible effect considering the large difference in erosion rates between the Ratcliffe and Longannet fly ashes, despite the similar mean angularities.

7.2 Drop Tube Furnace Experiments

In this part of the project, initial experiments were performed on the drop tube furnace to investigate the devolatilisation characteristics of the coals and biomasses. A selection of the DTF coal chars were fired under a combustion environment to determine the char burnout as a function of residence time. The primary aim of this chapter was to report the mineral transformation changes during devolatilisation and char combustion in the drop tube furnace using a mineral liberation analyser (MLA). The purpose being to predict the type of mineral species formed, in particular the mixed aluminosilicate phases containing alkali and alkaline earth metals which contribute to ash deposition in industrial scale boiler systems.

A summary of the conclusions for this chapter are as follows:

- 1) Surface area analysis of the coal and biomass chars produced in the drop tube furnace under the 200 and 600 millisecond residence times was conducted. The coal chars experienced a reduction in D-R equivalent surface area with increased residence time in contrast to the higher volatile biomass chars.
- 2) South African Koornfontein has the highest activation energy and is the most unreactive coal, likely due to the higher relative inertinite content. TGA burnout profiles of DTF char suggest that devolatilisation at the higher 600ms residence time contributes to lower reactivity due to greater loss of residual hydrogen.

- 3) The mineral compositions and associations show that as the South African Koorfontein coal undergoes devolatilisation there is an increase in the proportion of excluded minerals, with the majority of the inherent char minerals released. Then, upon char combustion the 5% O₂ provides a suitable environment for further minerals to become associated with one another as complex melt phases.
- 4) The average char ash contents (wt% dry basis) of the coal and biomass samples increases as a function of residence time in the drop tube furnace, albeit with limited statistical significance. It was found that the biomasses generally contained higher standard deviations owing to the greater proportion of volatile matter compared to the coals.
- 5) The collection efficiencies of the pyrolysed chars, as determined using the ash tracer technique, showed that there was a reduction in the average amount of char collected as the residence time increased from 200 ms to 600ms. These losses can be attributed to the high temperature conditions resulting in ash devolatilisation.

7.3 Coal Char Re-firing with Biomass Ash in a Drop Tube Furnace

The final part of the project involved the co-firing of unreactive DTF coal char with biomass ashes. Three biomass ashes produced at 500°C in a muffle furnace were blended at 50:50 weight percent with South African DTF coal char and fired at two residence times, 200 ms and 600 ms in the drop tube furnace. The purpose of the investigation was to assess the mineral changes and transformations that occur in the formation of blended ash deposits. A TGA study was conducted to assess the influence of co-firing on the ignition temperatures when the DTF coal char was blended with 10, 30 and 50 wt% of biomass ashes.

A summary of conclusions for this chapter are as follows:

- 1) The TGA study confirmed that the addition of biomass ash to the DTF coal char suggested the presence of a catalytic effect. The reduction in ignition temperature increased as the blend ratio (coal char to biomass ash weight %) increased. The olive cake ash contained the greatest ignition temperature reduction which has been attributed to the highest proportion of K and Na species in this biomass ash. XRD analysis confirmed that the major minerals determined to be contributing to this catalytic effect were fairchildite, polyhalite, sylvite and calcium sodium silicate species.

- 2) The mineral transformations during the devolatilisation and char combustion of DTF coal char doped with biomass ash showed the general trend that fluxing elements present with the clays and carbonate species were transforming into mixed aluminosilicates of varying composition, and that these biomass-derived species were acting as binders and attaching to the coal char particles to form longer chains. At the highest residence time these chains coalesced into larger sintered agglomerates.
- 3) The coloured mosaics of the DTF co-fired ashes showed that the addition of the biomass significantly increased the particle size distribution of the resultant DTF ashes, and that these deposits increase in size as a function of residence time.

7.4 Recommendations for Future Work

Mineral liberation analysis (MLA) can provide useful information relating to the ash deposition behaviour encountered during co-combustion, such as detailed examination of the aluminosilicate minerals and deposit-related minerals, which cannot be determined using traditional analytical techniques such as XRD and XRF.

The considerable amount of data collected during this research relating to the erosion potential of fly ashes, and the coal and biomass co-firing mineral transformations during devolatilisation and combustion could be used to develop a more robust devolatilisation and combustion model. This CFD model would include the MLA experimental results related to mineralogy, particle size distributions and morphological characteristics to predict important slagging and fouling indices. Additional sub-routines related to erosive wear and corrosion could be developed to predict the lifetime of boiler components and predict shutdown times.

As it is widely accepted that potassium-containing minerals contribute to the accelerated corrosion of boiler components, a further project could investigate the influence of DTF coal char or other additives to capture the vapour phase potassium within the aluminosilicate phases and the impact on the catalytic effect. The objective would be to determine an optimum blending ratio at which potassium and other fluxing metals are captured to reduce corrosion whilst minimising the ignition temperature or char burnout time during combustion.

Chapter 8: References

1. IEA, *Coal Information Overview Statistics*. 2019.
2. IEA, *Global Energy & CO₂ Status Report 2019*.
3. Demirbas, A., *Fuelwood characteristics of six indigenous wood species from the Eastern Black Sea region*. *Energy Sources*, 2003. **25**(4): p. 309-316.
4. Baxter, L., *Biomass-coal co-combustion: opportunity for affordable renewable energy*. *Fuel*, 2005. **84**(10): p. 1295-1302.
5. Tillman, D.A., *Biomass cofiring: the technology, the experience, the combustion consequences*. *Biomass and Bioenergy*, 2000. **19**(6): p. 365-384.
6. Roni, M.S., et al., *Biomass co-firing technology with policies, challenges, and opportunities: A global review*. *Renewable and Sustainable Energy Reviews*, 2017. **78**: p. 1089-1101.
7. van Ree, R., et al., *Biomass cofiring potential and experiences in the Netherlands*. Report ECN BM: ECN-RX—00-035, 2000: p. 1-18.
8. Association, W.C., *A Global Platform for Accelerating Coal Efficiency*. 2014.
9. Morris, L.E., *Sulphur Trioxide Behaviour in CO₂ Rich Atmospheres*. 2013, University of Nottingham.
10. Smoot, L.D., *Fundamentals of coal combustion : for clean and efficient use*. 1993.
11. van Krevelen, D.W., *Coal: Typology, Chemistry, Physics, Constitution*. 1961: Elsevier Publishing Company.
12. Bartok, W. and A.F. Sarofim, *Fossil fuel combustion : a source book*. 1991, New York: Wiley.
13. Stopes, M.C., *On the petrology of banded bituminous coals*. 1935, *Fuel*. p. 4-13.

14. Taylor, G.H., *Organic petrology: a new handbook incorporating some revised parts of Stach's Textbook of coal petrology*. 1998: Gebrüder Borntraeger.
15. Zhang, X., W. Yang, and W. Blasiak, *Modeling Study of Woody Biomass: Interactions of Cellulose, Hemicellulose, and Lignin*. Energy & Fuels, 2011. **25**(10): p. 4786-4795.
16. IEA, *Coal Information 2017*.
17. Association, R.E., *Bioenergy Strategy 2019*.
18. Smoot, L.D. and P.J. Smith, *Coal combustion and gasification*. 1985, United States: Plenum Press, New York, NY.
19. D. Smoot, L. and D. T. Pratt, *Pulverized-coal combustion and gasification: Theory and applications for continuous flow processes*. Vol. -1. 1979.
20. Simons, G.A., *Enhanced char reactivity via a tailored pore structure*. Combustion and Flame, 1983. **50**: p. 275-285.
21. Bailey, J.G., et al., *A char morphology system with applications to coal combustion*. Fuel, 1990. **69**(2): p. 225-239.
22. Guo, L., et al., *Comparison of bituminous coal and lignite during combustion: Combustion performance, coking and slagging characteristics*. Journal of the Energy Institute, 2019. **92**(3): p. 802-812.
23. Mlonka-Mędrala, A., et al., *Laboratory studies on the influence of biomass particle size on pyrolysis and combustion using TG GC/MS*. Fuel, 2019. **252**: p. 635-645.
24. Yu, D., et al., *Effect of coal particle size on the proximate composition and combustion properties*. Thermochemica Acta, 2005. **439**(1): p. 103-109.
25. Yi, B., et al., *Effect of the particle size on combustion characteristics of pulverized coal in an O₂/CO₂ atmosphere*. Fuel Processing Technology, 2014. **128**: p. 17-27.
26. Jayaraman, K., M.V. Kok, and I. Gokalp, *Pyrolysis, combustion and gasification studies of different sized coal particles using TGA-MS*. Applied Thermal Engineering, 2017. **125**: p. 1446-1455.

27. Lemaire, R., D. Menage, and P. Seers, *Study of the high heating rate devolatilization of bituminous and subbituminous coals—Comparison of experimentally monitored devolatilization profiles with predictions issued from single rate, two-competing rate, distributed activation energy and chemical percolation devolatilization models*. Journal of Analytical and Applied Pyrolysis, 2017. **123**: p. 255-268.
28. Farrow, S.T., et al., *Comparative study of the inherent combustion reactivity of sawdust chars produced by TGA and in the drop tube furnace*. Fuel Processing Technology, 2020. **201**: p. 106361.
29. Tremel, A. and H. Spliethoff, *Gasification kinetics during entrained flow gasification – Part I; Devolatilisation and char deactivation*. Fuel, 2013. **103**: p. 663-671.
30. Senneca, O. and P. Salatino, *A semi-detailed kinetic model of char combustion with consideration of thermal annealing*. Proceedings of the Combustion Institute, 2011. **33**(2): p. 1763-1770.
31. Lu, L., et al., *Char structural ordering during pyrolysis and combustion and its influence on char reactivity*. Fuel, 2002. **81**(9): p. 1215-1225.
32. Guerrero, M., et al., *Pyrolysis of eucalyptus at different heating rates: studies of char characterization and oxidative reactivity*. Journal of Analytical and Applied Pyrolysis, 2005. **74**(1): p. 307-314.
33. Di Blasi, C., *Combustion and gasification rates of lignocellulosic chars*. Progress in Energy and Combustion Science, 2009. **35**(2): p. 121-140.
34. Su, S., et al., *A proposed maceral index to predict combustion behavior of coal*. Fuel, 2001. **80**(5): p. 699-706.
35. Cloke, M. and E. Lester, *Characterization of coals for combustion using petrographic analysis: a review*. Fuel, 1994. **73**(3): p. 315-320.
36. Lee, G.K. and H. Whaley, *Modification of combustion and fly-ash characteristics by coal blending*. Journal of the Institute of Energy, 1983. **56**: p. 190-7.
37. Cloke, M., et al., *Automated maceral analysis using fluorescence microscopy and image analysis*. Fuel, 1995. **74**(5): p. 659-669.

38. Cloke, M., et al., *Repeatability of maceral analysis using image analysis systems*. Fuel, 1995. **74**(5): p. 654-658.
39. Lester, E., D. Watts, and M. Cloke, *A novel automated image analysis method for maceral analysis*. Fuel, 2002. **81**(17): p. 2209-2217.
40. Liu, Y., et al., *Mineral matter–organic matter association characterisation by QEMSCAN and applications in coal utilisation*. Fuel, 2005. **84**(10): p. 1259-1267.
41. Williams, A., M. Pourkashanian, and J.M. Jones, *Combustion of pulverised coal and biomass*. Progress in Energy and Combustion Science, 2001. **27**(6): p. 587-610.
42. Saeed, M.A., et al., *Global kinetics of the rate of volatile release from biomasses in comparison to coal*. Fuel, 2016. **181**: p. 347-357.
43. Vamvuka, D., et al., *Kinetic Modeling of Coal/Agricultural By-Product Blends*. Energy & Fuels, 2003. **17**(3): p. 549-558.
44. Munir, S., et al., *Thermal analysis and devolatilization kinetics of cotton stalk, sugar cane bagasse and shea meal under nitrogen and air atmospheres*. Bioresource Technology, 2009. **100**(3): p. 1413-1418.
45. Haykiri-Acma, H. and S. Yaman, *Effect of co-combustion on the burnout of lignite/biomass blends: A Turkish case study*. Waste Management, 2008. **28**(11): p. 2077-2084.
46. Benson, S.A., *Ash Formation and Deposition, Chapter 4*. Coal Sci. and Tech. 20, Fundamentals of Coal Combustion, 1993: p. 299-373.
47. Benson, S.A. and P.L. Holm, *Comparison of Inorganic Constituents in Three Low Rank Coals*. 1985. p. 145.
48. Given, P.H., *An Essay on the Organic Geochemistry of Coal*, ed. M.L. Gorbaty, J.W. Larsen, and I. Wender. Vol. 3. 1984: Coal Science. 137.
49. Bool, L.E. and J.J. Helble, *A laboratory study of the partitioning of trace elements during pulverized coal combustion*. 1995, Energy & Fuels. p. 880-997.

50. Quann, R.J., M. Neville, and A.F. Sarofim, *A laboratory study of the effect of coal selection on the amount and composition of combustion generated submicron particles*. 1990, Combust. Sci. and Tech. p. 245-265.
51. Benson, S.A., et al., *Predicting ash behavior in utility boilers*. Energy & Fuels, 1993. **7**(6): p. 746-754.
52. Gräbner, M. and E. Lester, *Proximate and ultimate analysis correction for kaolinite-rich Chinese coals using mineral liberation analysis*. Fuel, 2016. **186**: p. 190-198.
53. Couch, G. and I.E.A.C. Research, *Understanding slagging and fouling in pf combustion*. 1994, London: IEA Coal Research.
54. Bryers, R.W., *Fireside slagging, fouling, and high-temperature corrosion of heat-transfer surface due to impurities in steam-raising fuels*. Progress in Energy and Combustion Science, 1996. **22**(1): p. 29-120.
55. Srinivasachar, S., et al., *Mineral behavior during coal combustion 2. Illite transformations*. Progress in Energy and Combustion Science, 1990. **16**(4): p. 293-302.
56. Wang, J., K. Morishita, and T. Takarada, *High-Temperature Interactions between Coal Char and Mixtures of Calcium Oxide, Quartz, and Kaolinite*. Energy & Fuels, 2001. **15**(5): p. 1145-1152.
57. McLennan, A.R., et al., *Ash Formation Mechanisms during pf Combustion in Reducing Conditions*. Energy & Fuels, 2000. **14**(1): p. 150-159.
58. Srinivasachar, S., J.J. Helble, and A.A. Boni, *Mineral Behavior During Coal Combustion: 1. Pyrite Transformations*. 1990, Prog. Energy Combust. Sci. p. 281-292.
59. Brink, H.M.t., et al., *Flame transformations and burner slagging in a 2.5 MW furnace firing pulverized coal: 1. Flame transformations*. Fuel, 1994. **73**(11): p. 1706-1711.
60. Srinivasachar, S. and A.A. Boni, *A kinetic model for pyrite transformations in a combustion environment*. Fuel, 1989. **68**(7): p. 829-836.
61. Yan, L., R. Gupta, and T. Wall, *Fragmentation Behavior of Pyrite and Calcite during High-Temperature Processing and Mathematical Simulation*. Energy & Fuels, 2001. **15**(2): p. 389-394.

62. Wen, C., X.P. Gao, and M.H. Xu, *A CCSEM study on the transformation of included and excluded minerals during coal devolatilization and char combustion*. Fuel, 2016. **172**: p. 96-104.
63. Arvelakis, S., P.A. Jensen, and K. Dam-Johansen, *Simultaneous Thermal Analysis (STA) on Ash from High-Alkali Biomass*. Energy & Fuels, 2004. **18**: p. 1066-1076.
64. Arvelakis, S., et al., *Effect of leaching on the ash behavior of wheat straw and olive residue during fluidized bed combustion*. Biomass and Bioenergy, 2001. **20**(6): p. 459-470.
65. Kleinhans, U., et al., *Ash formation and deposition in coal and biomass fired combustion systems: Progress and challenges in the field of ash particle sticking and rebound behavior*. Progress in Energy and Combustion Science, 2018. **68**: p. 65-168.
66. Sarofim, A.F., J.B. Howard, and A.S. Padia, *The Physical Transformation of the Mineral Matter in Pulverized Coal Under Simulated Combustion Conditions*. Combustion Science and Technology, 1977. **16**(3-6): p. 187-204.
67. Field, M.A., et al., *Combustion of Pulverized Coal*. 1967, BCURA: Leatherhead. p. 186.
68. Backreedy, R.I., et al., *Burn-out of pulverised coal and biomass chars ☆*. Fuel, 2003. **82**(15–17): p. 2097-2105.
69. Kurose, R., M. Ikeda, and H. Makino, *Combustion characteristics of high ash coal in a pulverized coal combustion*. Fuel, 2001. **80**(10): p. 1447-1455.
70. Lunden, M.M., et al., *Mineral-char interactions during char combustion of a high-volatile coal*. Symposium (International) on Combustion, 1998. **27**(2): p. 1695-1702.
71. Jones, J.M., et al., *Porphyrin- and metalloporphyrin-derived carbons as models for coal char combustion and pyrolysis*. Fuel, 1997. **76**(13): p. 1235-1240.
72. Backreedy, R., et al., *A study of the reaction of oxygen with graphite: Model chemistry*. Faraday Discussions, 2002. **119**(0): p. 385-394.
73. Huang, H.Y. and R.T. Yang, *Catalyzed Carbon–NO Reaction Studied by Scanning Tunneling Microscopy and ab Initio Molecular Orbital Calculations*. Journal of Catalysis, 1999. **185**(2): p. 286-296.

74. Baker, R.T.K., J.J. Chludzinski, and R.D. Sherwood, *A comparison of the catalytic influence of nickel, iron and nickel-iron on the gasification of graphite in various gaseous environments*. Carbon, 1985. **23**(3): p. 245-254.
75. Howard, J.B. and W.J. Kausch, *Soot control by fuel additives*. Progress in Energy and Combustion Science, 1980. **6**(3): p. 263-276.
76. Du, S., et al., *Fusion and transformation properties of the inorganic components in biomass ash*. Fuel, 2014. **117**: p. 1281-1287.
77. Munir, S., W. Nimmo, and B.M. Gibbs, *Potential slagging and fouling problems associated with biomass-coal blends in coal-fired boilers*. Journal of Pakistan Institute of Chemical Engineers. Vol. 38, 1, 2010. **26**.
78. Centre, I.C.C., *Pulverised Coal Combustion (PCC)* 2018.
79. Matthews, C., *I4 - Power boilers – remnant life assessment*, in *Case Studies in Engineering Design*, C. Matthews, Editor. 1998, Butterworth-Heinemann: London. p. 142-156.
80. Jenkins, B.M., et al., *Combustion properties of biomass*. Fuel Processing Technology, 1998. **54**(1): p. 17-46.
81. Demirbas, A., *Potential applications of renewable energy sources, biomass combustion problems in boiler power systems and combustion related environmental issues*. Progress in Energy and Combustion Science, 2005. **31**(2): p. 171-192.
82. Obernberger, I., et al., *Concentrations of inorganic elements in biomass fuels and recovery in the different ash fractions*. Biomass and Bioenergy, 1997. **12**(3): p. 211-224.
83. Werther, J., et al., *Combustion of agricultural residues*. Progress in Energy and Combustion Science, 2000. **26**(1): p. 1-27.
84. Pronobis, M., *Evaluation of the influence of biomass co-combustion on boiler furnace slagging by means of fusibility correlations*. Biomass and Bioenergy, 2005. **28**(4): p. 375-383.
85. Wen, X., Y. Xu, and J. Wang, *Assessing slagging propensity of coal from their slagging indices*. Journal of the Energy Institute, 2018. **91**(5): p. 646-654.

86. Miles, T.R., et al., *Boiler deposits from firing biomass fuels*. Biomass and Bioenergy, 1996. **10**(2): p. 125-138.
87. Yu, L.Y., L.W. Wang, and P.S. Li, *Study on prediction models of biomass ash softening temperature based on ash composition*. Journal of the Energy Institute, 2014. **87**(3): p. 215-219.
88. García, R., et al., *Study of biomass combustion wastes*. Fuel, 2015. **148**: p. 152-159.
89. Fernández Llorente, M.J. and J.E. Carrasco García, *Comparing methods for predicting the sintering of biomass ash in combustion*. Fuel, 2005. **84**(14): p. 1893-1900.
90. Teixeira, P., et al., *Evaluation of slagging and fouling tendency during biomass co-firing with coal in a fluidized bed*. Biomass and Bioenergy, 2012. **39**: p. 192-203.
91. Van Loo, S. and J. Koppejan, *The Handbook of Biomass Combustion and Co-firing*. 2012: Earthscan LLC.
92. Cuiping, L., et al., *Chemical elemental characteristics of biomass fuels in China*. Biomass and Bioenergy, 2004. **27**(2): p. 119-130.
93. Vassilev, S.V., et al., *An overview of the composition and application of biomass ash. Part 1. Phase-mineral and chemical composition and classification*. Fuel, 2013. **105**(0): p. 40-76.
94. Nordin, A., *Chemical elemental characteristics of biomass fuels*. 1994, Biomass and Bioenergy. p. 339-347.
95. Wigley, F., et al., *Ash deposition at higher levels of coal replacement by biomass*. Fuel Processing Technology, 2007. **88**(11): p. 1148-1154.
96. Li, Q.H., et al., *Study on ash fusion temperature using original and simulated biomass ashes*. Fuel Processing Technology, 2013. **107**: p. 107-112.
97. Lolja, S.A., et al., *Correlation between ash fusion temperatures and chemical composition in Albanian coal ashes*. Fuel, 2002. **81**(17): p. 2257-2261.
98. Liu, B., et al., *Relationship between coal ash composition and ash fusion temperatures*. Fuel, 2013. **105**: p. 293-300.

99. Vassilev, S.V., D. Baxter, and C.G. Vassileva, *An overview of the behaviour of biomass during combustion: Part I. Phase-mineral transformations of organic and inorganic matter*. Fuel, 2013. **112**: p. 391-449.
100. Capareda, S., *Introduction to biomass energy conversions*. 2013: CRC press.
101. Tortosa Masiá, A.A., et al., *Characterising ash of biomass and waste*. Fuel Processing Technology, 2007. **88**(11): p. 1071-1081.
102. Niu, Y., et al., *Experimental study on the coexistent dual slagging in biomass-fired furnaces: Alkali-and silicate melt-induced slagging*. Proceedings of the Combustion Institute, 2015. **35**(2): p. 2405-2413.
103. Öhman, M., et al., *Slagging tendencies of wood pellet ash during combustion in residential pellet burners*. Biomass and Bioenergy, 2004. **27**(6): p. 585-596.
104. Gilbe, C., et al., *Slagging characteristics during residential combustion of biomass pellets*. Energy & Fuels, 2008. **22**(5): p. 3536-3543.
105. Öhman, M., et al., *Reasons for slagging during stemwood pellet combustion and some measures for prevention*. Biomass and Bioenergy, 2004. **27**(6): p. 597-605.
106. Vega-Nieva, D., C. Alvarez, and L. Ortiz. *Results of new laboratory methods and slagging classification systems for the prediction and quantification of ash slagging in woody and herbaceous biomass fuels*.
107. Vega-Nieva, D., R. Dopazo, and L. Ortiz, *Strategies for minimizing ash slagging in combustion of mediterranean biomasses*. World Bioenergy, 2012. **2012**.
108. Somoza, L., D. Vega-Nieva, and L. Ortiz, *Quality control of wood chips and wood pellet from the biomass logistic center of Biopalas*. FEADER-Xunta Project Report, 2014.
109. Atlas, S., ed. by Verein Deutscher Eisenhüttenleute. Verlag Stahleisen GmbH, Düsseldorf, 1995. **48**.
110. Qiu, J.R., et al., *The influences of mineral behaviour on blended coal ash fusion characteristics*. Fuel, 1999. **78**(8): p. 963-969.
111. Zhou, H., et al., *Effect of biomass ashes on sintering characteristics of high/low melting bituminous coal ash*. Fuel Processing Technology, 2019. **189**: p. 62-73.

112. Saikia, B.K. and Y. Ninomiya, *An investigation on the heterogeneous nature of mineral matters in Assam (India) coal by CCSEM technique*. Fuel Processing Technology, 2011. **92**(5): p. 1068-1077.
113. Gupta, S.K., et al., *The effect of potassium on the fusibility of coal ashes with high silica and alumina levels*. Fuel, 1998. **77**(11): p. 1195-1201.
114. Wang, J., et al., *Steam gasification of coal char catalyzed by K₂CO₃ for enhanced production of hydrogen without formation of methane*. Fuel, 2009. **88**(9): p. 1572-1579.
115. Anicic, B., et al., *Agglomeration mechanism in biomass fluidized bed combustion – Reaction between potassium carbonate and silica sand*. Fuel Processing Technology, 2018. **173**: p. 182-190.
116. Garcia-Maraver, A., et al., *Critical review of predictive coefficients for biomass ash deposition tendency*. Journal of the Energy Institute, 2017. **90**(2): p. 214-228.
117. Flagan, R. and S. Friedlander, *Particle formation in pulverized coal combustion—a review*. Recent Developments in Aerosol Science, 1978. **2**: p. 25-59.
118. Dacombe, P.J., E. Hampartsoumian, and M. Pourkashanian, *Fragmentation of large coal particles in a drop-tube furnace*. Fuel, 1994. **73**(8): p. 1365-1367.
119. Wilemski, G. and S. Srinivasachar. *Prediction of ash formation in pulverized coal combustion with mineral distribution and char fragmentation models (pp. 151–164)*. in *Proceeding of the engineering foundation conference, England*. 1993.
120. S. Monroe, L., *An experimental and modeling study of residual fly ash formation in combustion of a bituminous coal*. 2005.
121. Barta, L.E., et al., *Variation of mineral matter distribution in individual pulverized coal particles: Application of the “URN” model*. Symposium (International) on Combustion, 1991. **23**(1): p. 1289-1296.
122. Barta, L.E., et al., *Prediction of fly ash size and chemical composition distributions: The random coalescence model*. Symposium (International) on Combustion, 1992. **24**(1): p. 1135-1144.

123. Straszheim, W.E. and R. Markuszewski, *SEM-AIA measurement of the association of mineral matter with the organic coal matrix for predicting fine coal cleanability*. Coal Preparation, 1992. **10**(1-4): p. 59-75.
124. Wigley, F., J. Williamson, and W.H. Gibb, *The distribution of mineral matter in pulverised coal particles in relation to burnout behaviour*. Fuel, 1997. **76**(13): p. 1283-1288.
125. Wigley, F. and J. Williamson, *Modelling fly ash generation for pulverised coal combustion*. Progress in Energy and Combustion Science, 1998. **24**(4): p. 337-343.
126. Gupta, R.P., et al., *Computer-controlled scanning electron microscopy of minerals in coal—Implications for ash deposition*. Progress in Energy and Combustion Science, 1998. **24**(6): p. 523-543.
127. Yan, L., R.P. Gupta, and T.F. Wall, *The implication of mineral coalescence behaviour on ash formation and ash deposition during pulverised coal combustion*. Fuel, 2001. **80**(9): p. 1333-1340.
128. Yan, L., R.P. Gupta, and T.F. Wall, *A mathematical model of ash formation during pulverized coal combustion*. Fuel, 2002. **81**(3): p. 337-344.
129. Wang, H. and J.N. Harb, *Modeling of ash deposition in large-scale combustion facilities burning pulverized coal*. Progress in Energy and Combustion Science, 1997. **23**(3): p. 267-282.
130. Zygarlicke, C.J., M. Ramanathan, and T.A. Erickson, *Fly ash particle-size distribution and composition: experimental and phenomenological approach*. Inorganic Transformations and Ash Deposition During Combustion, 1992: p. 525-544.
131. Erickson, T.A., et al., *Modelling of fouling and slagging in coal-fired utility boilers*. Fuel Processing Technology, 1995. **44**(1): p. 155-171.
132. Johansen, J.M., et al., *Release of K, Cl, and S during combustion and co-combustion with wood of high-chlorine biomass in bench and pilot scale fuel beds*. Proceedings of the Combustion Institute, 2013. **34**(2): p. 2363-2372.
133. Damoe, A.J., et al., *Fly ash formation during suspension firing of biomass: Effects of residence time and fuel type*. Energy & Fuels, 2016. **31**(1): p. 555-570.

134. Wang, G., L. Shen, and C. Sheng, *Characterization of biomass ashes from power plants firing agricultural residues*. Energy & Fuels, 2011. **26**(1): p. 102-111.
135. Nielsen, H.P., et al., *The implications of chlorine-associated corrosion on the operation of biomass-fired boilers*. Progress in Energy and Combustion Science, 2000. **26**(3): p. 283-298.
136. Nielsen, H.P., et al., *Deposition of potassium salts on heat transfer surfaces in straw-fired boilers: a pilot-scale study*. Fuel, 2000. **79**(2): p. 131-139.
137. Hansen, L.A., et al., *Influence of deposit formation on corrosion at a straw-fired boiler*. Fuel Processing Technology, 2000. **64**(1): p. 189-209.
138. Zheng, Y., A.D. Jensen, and J.E. Johnsson, *Deactivation of V₂O₅-WO₃-TiO₂ SCR catalyst at a biomass-fired combined heat and power plant*. Applied Catalysis B: Environmental, 2005. **60**(3): p. 253-264.
139. Zheng, Y., et al., *Deactivation of V₂O₅-WO₃-TiO₂ SCR catalyst at biomass fired power plants: Elucidation of mechanisms by lab- and pilot-scale experiments*. Applied Catalysis B: Environmental, 2008. **83**(3): p. 186-194.
140. Li, L., et al., *Study on the deposits derived from a biomass circulating fluidized-bed boiler*. Energy & Fuels, 2012. **26**(9): p. 6008-6014.
141. Lindberg, D., R. Backman, and P. Chartrand, *Thermodynamic evaluation and optimization of the (NaCl+Na₂SO₄+Na₂CO₃+KCl+K₂SO₄+K₂CO₃) system*. The Journal of Chemical Thermodynamics, 2007. **39**(7): p. 1001-1021.
142. Aho, M., et al., *Effective new chemicals to prevent corrosion due to chlorine in power plant superheaters*. Fuel, 2008. **87**(6): p. 647-654.
143. Wang, G., et al., *KOH capture by coal fly ash*. Fuel, 2019. **242**: p. 828-836.
144. Xu, L., et al., *Safely burning high alkali coal with kaolin additive in a pulverized fuel boiler*. Energy & Fuels, 2014. **28**(9): p. 5640-5648.
145. Fuller, A., et al., *The impact of an additive on fly ash formation/transformation from wood dust combustion in a lab-scale pulverized fuel reactor*. Renewable energy, 2019. **136**: p. 732-745.
146. Zheng, Y., et al., *Ash transformation during co-firing coal and straw*. Fuel, 2007. **86**(7): p. 1008-1020.

147. Dayton, D.C., et al., *Release of inorganic constituents from leached biomass during thermal conversion*. Energy & Fuels, 1999. **13**(4): p. 860-870.
148. Turn, S., et al., *Leaching of Alkalis in Biomass Using Banagrass as a Prototype Herbaceous Species: Final Report, February 1997*. 1997, National Renewable Energy Lab., Golden, CO.(US).
149. Davidsson, K.O., et al., *The effects of fuel washing techniques on alkali release from biomass*. Fuel, 2002. **81**(2): p. 137-142.
150. Damoe, A.J., et al., *Impact of coal fly ash addition on combustion aerosols (PM_{2.5}) from full-scale suspension-firing of pulverized wood*. Energy & Fuels, 2014. **28**(5): p. 3217-3223.
151. Wu, H., et al., *Impact of coal fly ash addition on ash transformation and deposition in a full-scale wood suspension-firing boiler*. Fuel, 2013. **113**: p. 632-643.
152. Zheng, Y., P.A. Jensen, and A.D. Jensen, *A kinetic study of gaseous potassium capture by coal minerals in a high temperature fixed-bed reactor*. Fuel, 2008. **87**(15): p. 3304-3312.
153. Liu, Y., et al., *Experimental study on adsorption of potassium vapor in flue gas by coal ash*. Powder Technology, 2017. **318**: p. 170-176.
154. Wang, G., et al., *Potassium Capture by Kaolin, Part 2: K₂CO₃, KCl, and K₂SO₄*. Energy & fuels, 2018. **32**(3): p. 3566-3578.
155. Raask, E., *Erosion wear in coal utilization*. 1988: Hemisphere Pub. Corp.
156. Livingston, W.R., et al., *Design guidelines for corrosion, erosion and steam oxidation of boiler tubes in pulverized coal-fired boilers*. 2014, ASME Standards Technology, LLC.
157. Finnie, I., *Some observations on the erosion of ductile metals*. Wear, 1972. **19**(1): p. 81-90.
158. Finnie, I. and D.H. McFadden, *On the velocity dependence of the erosion of ductile metals by solid particles at low angles of incidence*. Wear, 1978. **48**(1): p. 181-190.
159. Finnie, I. and Y.H. Kabil, *On the formation of surface ripples during erosion*. Wear, 1965. **8**(1): p. 60-69.

160. Goodwin, J., W. Sage, and G. Tilly, *Study of erosion by solid particles*. Proceedings of the Institution of Mechanical Engineers, 1969. **184**(1): p. 279-292.
161. Winter, R.E. and I.M. Hutchings, *Solid particle erosion studies using single angular particles*. Wear, 1974. **29**(2): p. 181-194.
162. Srinivasan, S. and R.O. Scattergood, *Effect of erodent hardness on erosion of brittle materials*. Wear, 1988. **128**(2): p. 139-152.
163. Levy, A.V. and P. Chik, *The effects of erodent composition and shape on the erosion of steel*. Wear, 1983. **89**(2): p. 151-162.
164. Hutchings, I. and P. Shipway, *Tribology: friction and wear of engineering materials*. 2017: Butterworth-Heinemann.
165. Stachowiak, G. and A.W. Batchelor, *Engineering tribology*. 2013: Butterworth-Heinemann.
166. Palasamudram, S.L. and S. Bahadur, *Particle characterization for angularity and the effects of particle size and angularity on erosion in a fluidized bed environment*. Wear, 1997. **203-204**: p. 455-463.
167. Levy, A.V. and M. Yong-Fa, *Effect of particle variables on the erosion-corrosion of 9cr1Mo steel*. Wear, 1989. **131**(1): p. 53-69.
168. Lindsley, B.A., A.R. Marder, and J.J. Lewnard, *The effect of circulating fluidized bed particle characteristics on erosion of 1020 carbon steel*. Wear, 1995. **188**(1): p. 33-39.
169. Buqian, W., G. Gangqiang, and A.V. Levy, *Erosivity of particles from operating fluidized bed combustors*. Wear, 1991. **150**(1-2): p. 107-124.
170. Suckling, M. and C. Allen, *Critical variables in high temperature erosive wear*. Wear, 1997. **203**: p. 528-536.
171. Foley, T. and A. Levy, *The erosion of heat-treated steels*. Wear, 1983. **91**(1): p. 45-64.
172. Naim, M. and S. Bahadur, *Effect of microstructure and mechanical properties on the erosion of 18 Ni (250) maraging steel*. Wear, 1986. **112**(2): p. 217-234.

173. Wells, J.J., et al., *The nature of mineral matter in a coal and the effects on erosive and abrasive behaviour*. Fuel Processing Technology, 2005. **86**(5): p. 535-550.
174. G, M.J., S.T. J, and S. R, *A model to predict erosion on mild steel surfaces impacted by boiler fly ash particles*. 2004: School of Mechanical, Industrial and Aeronautical Engineering, University of the Witwatersrand, Johannesburg, South Africa. p. 612-624.
175. Raask, E., *Mineral Impurities in Coal Combustion*. 1985, Hemisphere Publishing Company: Washington.
176. Aboustait, M., et al., *Physical and chemical characteristics of fly ash using automated scanning electron microscopy*. Vol. 106. 2016. 1-10.
177. Poelt, P., et al., *Automated analysis of submicron particles by CCSEM/EDXS - Where are the limits?* Electron Microscopy and Analysis 2001, 2001(168): p. 81-84.
178. van Alphen, C., *Automated mineralogical analysis of coal and ash products - Challenges and requirements*. Minerals Engineering, 2007. **20**(5): p. 496-505.
179. Wen, C., X. Gao, and M. Xu, *A CCSEM study on the transformation of included and excluded minerals during coal devolatilization and char combustion*. Fuel, 2016. **172**: p. 96-104.
180. Gupta, R., *Advanced Coal Characterization: A Review*. Energy & Fuels, 2007. **21**(2): p. 451-460.
181. O'Brien, G., et al., *The use of optical reflected light and SEM imaging systems to provide quantitative coal characterisation*. Minerals Engineering, 2011. **24**(12): p. 1299-1304.
182. Kwitko-Ribeiro, R., *New Sample Preparation Developments to Minimize Mineral Segregation in Process Mineralogy*. 2012.
183. Pearce, B.C., J.W.F. Hill, and I. Kerry, *Use of X-Ray-Fluorescence Spectrometry for the Direct Multielement Analysis of Coal Powders*. Analyst, 1990. **115**(11): p. 1397-1403.
184. Ward, C.R., *Analysis and significance of mineral matter in coal seams*. International Journal of Coal Geology, 2002. **50**(1-4): p. 135-168.

185. Wen, C., et al., *The melting potential of various ash components generated from coal combustion: Indicated by the circularity of individual particles using CCSEM technology*. Fuel Processing Technology, 2015. **133**: p. 128-136.
186. Liu, Y.H., et al., *Mineral matter-organic matter association characterisation by QEMSCAN and applications in coal utilisation*. Fuel, 2005. **84**(10): p. 1259-1267.
187. Liu, Y., et al., *Mineral-mineral associations in pulverized Australian coals*. 2005.
188. Galbreath, K., et al., *Collaborative study of quantitative coal mineral analysis using computer-controlled scanning electron microscopy*. Fuel, 1996. **75**(4): p. 424-430.
189. Gupta, R.P., et al., *System Accuracy for CCSEM Analysis of Minerals in Coal, in Impact of Mineral Impurities in Solid Fuel Combustion*, R.P. Gupta, T.F. Wall, and L. Baxter, Editors. 1999, Springer US: Boston, MA. p. 225-235.
190. Liu, Y., R. Gupta, and T. Wall, *Ash Formation from Excluded Minerals Including Consideration of Mineral–Mineral Associations*. Energy & Fuels, 2007. **21**(2): p. 461-467.
191. Gu, Y., *Automated Scanning Electron Microscope Based Mineral Liberation Analysis An Introduction to JKMRC/FEI Mineral Liberation Analyser*. Journal of Minerals and Materials Characterization and Engineering, 2003. **Vol.02No.01**: p. 9.
192. Keulen, N., M.T. Hutchison, and D. Frei, *Computer-controlled scanning electron microscopy: A fast and reliable tool for diamond prospecting*. Journal of Geochemical Exploration, 2009. **103**(1): p. 1-5.
193. Mitsche, S., P. Poelt, and J. Wagner, *Analysis of submicron particles by scanning electron microscopy-energy-dispersive X-ray spectrometry—accuracy of size measurement*. Scanning, 2006. **28**(5): p. 282-288.
194. Benson, S., et al., *Characterization of Particulate Matter with Computer-Controlled Scanning Electron Microscopy*. 2002. 29-42.
195. Katrinak, K.A. and C.J. Zygarlicke, *Size-related variations in coal fly ash composition as determined using automated scanning electron microscopy*. Fuel Processing Technology, 1995. **44**(1): p. 71-79.

196. Chen, Y., et al., *Investigation of primary fine particulate matter from coal combustion by computer-controlled scanning electron microscopy*. Fuel Processing Technology, 2004. **85**(6): p. 743-761.
197. Cprek, N., et al., *Computer-controlled scanning electron microscopy (CCSEM) investigation of quartz in coal fly ash*. Fuel Processing Technology, 2007. **88**(11-12): p. 1017-1020.
198. Sitzmann, B., et al., *Characterisation of airborne particles in London by computer-controlled scanning electron microscopy*. Science of The Total Environment, 1999. **241**(1): p. 63-73.
199. Watt, J., *Automated characterisation of individual carbonaceous fly-ash particles by computer controlled scanning electron microscopy: Analytical methods and critical review of alternative techniques*. Water Air and Soil Pollution, 1998. **106**(3-4): p. 309-327.
200. O'Keefe, C.A., T.M. Watne, and J.P. Hurley, *Development of advanced scanning electron microscopy techniques for characterization of submicron ash*. Powder Technology, 2000. **108**(2): p. 95-102.
201. Lui, Y., et al., *A comparison of CCSEM and QEMSCAN analysis of pulverized coal / authors: Yinghui Lui, Raj Gupta, Terry Wall*. Research report (Cooperative Research Centre for Coal in Sustainable Development (Australia)) ; 71. 2007, Pullenvale, Qld: QCAT Technology Transfer Centre.
202. Zhang, L., A. Sato, and Y. Ninomiya, *CCSEM analysis of ash from combustion of coal added with limestone*. Fuel, 2002. **81**(11-12): p. 1499-1508.
203. Institute, B.S., *BS EN ISO 17827-2:2016 Solid biofuels. Determination of particle size distribution for uncompressed fuels. Vibrating screen method using sieves with aperture of 3,15 mm and below*. 2016.
204. Institute, B.S., *BS ISO 14488:2007 Particle materials - Sampling and sample splitting for the determination of particulate properties*. 2007.
205. Mayoral, M.C., et al., *Different approaches to proximate analysis by thermogravimetry analysis*. Thermochimica Acta, 2001. **370**(1): p. 91-97.
206. Brown, R.C. and J. Dykstra, *Systematic-Errors in the Use of Loss-on-Ignition to Measure Unburned Carbon in Fly-Ash*. Fuel, 1995. **74**(4): p. 570-574.

207. Hower, J.C., et al., *Coal-derived unburned carbons in fly ash: A review*. International Journal of Coal Geology, 2017. **179**: p. 11-27.
208. Fan, M. and R.C. Brown, *Comparison of the Loss-on-Ignition and Thermogravimetric Analysis Techniques in Measuring Unburned Carbon in Coal Fly Ash*. Energy & Fuels, 2001. **15**(6): p. 1414-1417.
209. Duval, C.m., *Inorganic thermogravimetric analysis*. 2d and rev. ed. 1963, Amsterdam, New York,: Elsevier Pub. Co. 722 p.
210. Brown, R.C. and J. Dykstra, *Systematic errors in the use of loss-on-ignition to measure unburned carbon in fly ash*. Fuel, 1995. **74**(4): p. 570-574.
211. Institution, B.S., *BSI ISO 7404-4 2017: Methods for petrographic analysis of coals*. 2017.
212. Institute, B.S., *BS ISO 7404-2:2009 Methods for the petrographic analysis of coals. Methods of preparing coal samples*. 2009, BSI.
213. Suárez-Ruiz, I., et al., *Review and update of the applications of organic petrology: Part I, geological applications*. International Journal of Coal Geology, 2012. **99**: p. 54-112.
214. Corporation, M.I. *ASAP 2420 Multi-port Surface Area and Porosimetry Analyzer*. 2017.
215. Marsh, H., *Adsorption methods to study microporosity in coals and carbons—a critique*. Carbon, 1987. **25**(1): p. 49-58.
216. Brunauer, S., P.H. Emmett, and E. Teller, *Adsorption of Gases in Multimolecular Layers*. Journal of the American Chemical Society, 1938. **60**(2): p. 309-319.
217. Ward, C.R., et al., *Quantification of mineral matter in the Argonne Premium Coals using interactive Rietveld-based X-ray diffraction*. International Journal of Coal Geology, 2001. **46**(2): p. 67-82.
218. Renton, J.J., *Semiquantitative Determination of Coal Minerals by X-ray Diffractometry*, in *Mineral Matter and Ash in Coal*. 1986, American Chemical Society. p. 53-60.

219. Matjie, R.H., C. van Alphen, and P.C. Pistorius, *Mineralogical characterisation of Secunda gasifier feedstock and coarse ash*. Minerals Engineering, 2006. **19**(3): p. 256-261.
220. Matsuoka, K., et al., *CCSEM study of ash forming reactions during lignite gasification*. Fuel, 2006. **85**(17-18): p. 2371-2376.
221. Institute, B.S., *BS ISO 13322-2:2006*, in *Part 2: Dynamic image analysis methods*. 2006, BSI.
222. Badzioch, S. and P.G. Hawksley, *Kinetics of Thermal Decomposition of Pulverized Coal Particles*. Industrial & Engineering Chemistry Process Design and Development, 1970. **9**(4): p. 521-&.
223. Ballantyne, T.R., P.J. Ashman, and P.J. Mullinger, *A new method for determining the conversion of low-ash coals using synthetic ash as a tracer*. Fuel, 2005. **84**(14): p. 1980-1985.
224. Troiano, M., et al., *Impact experiments of char and ash particles relevant to entrained-flow coal gasifiers*. Fuel, 2017. **202**: p. 665-674.
225. Institute, B.S., *BS ISO 1332201:2014*. Part 1: Static image analysis methods, 2014.
226. Milford, M. *Noisy spectra recognition using a single-layer perception neural network*. 2002.
227. Society, T.C.M., *Available Source Clays*. 2017, United States, Chantilly, VA: The Clay Minerals Society.
228. Nagarajan, R., et al., *Development of predictive model for fly-ash erosion phenomena in coal-burning boilers*. Wear, 2009. **267**(1): p. 122-128.
229. Russell, N.V., F. Wigley, and J. Williamson, *The roles of lime and iron oxide on the formation of ash and deposits in PF combustion*. Fuel, 2002. **81**(5): p. 673-681.
230. Levin, E.M., et al., *Phase Diagrams for Ceramists Columbus*. OH: American Ceramic Society, 1964.
231. Jak, E., et al., *Thermodynamic modelling of the Al₂O₃-CaO-FeO-Fe₂O₃-PbO-SiO₂-ZnO system with addition of K and Na with metallurgical applications*. 2009.

232. Raask, E., *Mineral Impurities on Coal Combustion: Behaviour, Problems, and Remedial Measures*. 1985, Hemisphere Publishing: New York. p. 243-248.
233. Wells, J.J., et al., *The relationship between excluded mineral matter and the abrasion index of a coal*. 2004, Fuel. p. 358-364.
234. Henderson, C., *Co-firing of biomass in coal-fired power plants - European experience*. IEA Clean Coal Centre, 2015.
235. Institute, B.S., *BS ISO 11760:2005*. Classification of coals, 2005.
236. G. Li, X., et al., *Catalytic Effect of Metallic Oxides on Combustion Behavior of High Ash Coal*. Vol. 21. 2007.
237. Slegl, J. *Co-firing of Biomass and Coal: Capture and Tendering*. 2009.
238. Williams, O., et al., *Overcoming the caking phenomenon in olive mill wastes*. Industrial Crops and Products, 2017. **101**: p. 92-102.
239. Williams, O., et al., *Influence of mill type on densified biomass comminution*. Applied Energy, 2016. **182**: p. 219-231.
240. Barranco Melendez, R., *Characterisation and Combustion of South American Coals PhD thesis*, in *Faculty of Engineering*. 2001: University of Nottingham.
241. Farrow, T.S., *A fundamental study of biomass oxy-fuel combustion and co-combustion*, in *Faculty of Engineering*. 2013: University of Nottingham.
242. R. Gibbins, J., C. K. Man, and K. J. Pendlebury, *Determination of Rapid Heating Volatile Matter Contents as a Routine Test*. Combustion Science and Technology - COMBUST SCI TECHNOL. 1993. 349-361.
243. Kimber, G.M. and M.D. Gray, *Rapid devolatilization of small coal particles*. Combustion and Flame, 1967. **11**(4): p. 360-362.
244. Kobayashi, H., J.B. Howard, and A.F. Sarofim, *Coal devolatilization at high temperatures*. Symposium (International) on Combustion, 1977. **16**(1): p. 411-425.
245. Rathnam, R.K., et al., *Differences in reactivity of pulverised coal in air (O₂/N₂) and oxy-fuel (O₂/CO₂) conditions*. Fuel Processing Technology, 2009. **90**(6): p. 797-802.

246. Gil, M.V., et al., *Biomass devolatilization at high temperature under N₂ and CO₂: Char morphology and reactivity*. Energy, 2015. **91**: p. 655-662.
247. Gopalakrishnan, R. and C.H. Bartholomew, *Effects of CaO, High-Temperature Treatment, Carbon Structure, and Coal Rank on Intrinsic Char Oxidation Rates*. Energy & Fuels, 1996. **10**(3): p. 689-695.
248. Gupta, R., et al., *Impact of mineral impurities in solid fuel combustion*. 2002.
249. Cai, H.Y. and R. Kandiyoti, *Effect of changing inertinite concentration on pyrolysis yields and char reactivities of two South African coals*. Energy & fuels, 1995. **9**(6): p. 956-961.
250. Essenhigh, R.H., *In Chemistry of Coal Utilisation*. 1981, New York: John Wiley & Sons.
251. Smith, I.W., *The combustion rates of coal chars: A review*. Symposium (International) on Combustion, 1982. **19**(1): p. 1045-1065.
252. Zolin, A., et al., *Experimental study of char thermal deactivation*. Fuel, 2002. **81**(8): p. 1065-1075.
253. Hurt, R.H., *Structure, properties, and reactivity of solid fuels*. Symposium (International) on Combustion, 1998. **27**(2): p. 2887-2904.
254. Senneca, O., et al., *Relevance of structure, fragmentation and reactivity of coal to combustion and oxy-combustion*. Fuel, 2017. **201**(Supplement C): p. 65-80.
255. Senneca, O., P. Salatino, and S. Masi, *Heat treatment-induced loss of combustion reactivity of a coal char: the effect of exposure to oxygen*. Experimental Thermal and Fluid Science, 2004. **28**(7): p. 735-741.
256. Gale, T.K., C.H. Bartholomew, and T.H. Fletcher, *Effects of Pyrolysis Heating Rate on Intrinsic Reactivities of Coal Chars*. Energy & Fuels, 1996. **10**(3): p. 766-775.
257. Le Manquais, K., et al., *Evaluating the Combustion Reactivity of Drop Tube Furnace and Thermogravimetric Analysis Coal Chars with a Selection of Metal Additives*. Energy & Fuels, 2011. **25**(3): p. 981-989.
258. Babinski, P., M. Sciazko, and E. Ksepko, *Limitation of thermogravimetry for oxy-combustion analysis of coal chars*. Journal of Thermal Analysis and Calorimetry, 2018. **133**(1): p. 713-725.

259. Alonso, M.J.G., et al., *Pyrolysis behaviour of pulverised coals at different temperatures*. Fuel, 1999. **78**(13): p. 1501-1513.
260. Karunadasa, K.S.P., et al., *Thermal decomposition of calcium carbonate (calcite polymorph) as examined by in-situ high-temperature X-ray powder diffraction*. Journal of Physics and Chemistry of Solids, 2019. **134**: p. 21-28.
261. Senneca, O., P. Salatino, and S. Masi, *The influence of char surface oxidation on thermal annealing and loss of combustion reactivity*. Proceedings of the Combustion Institute, 2005. **30**(2): p. 2223-2230.
262. Van Dyk, J.C., et al., *Coal and coal ash characteristics to understand mineral transformations and slag formation*. Fuel, 2009. **88**(6): p. 1057-1063.
263. Combustion Working, G., *Atlas of Char Occurrences*. The International Committee for Coal and Organic Petrology (ICCP), CD-ROM, 2000.
264. Priyanto, D.E., et al., *Ash transformation by co-firing of coal with high ratios of woody biomass and effect on slagging propensity*. Fuel, 2016. **174**: p. 172-179.
265. Ulusoy, U., M. Yekeler, and C. Hiçyılmaz, *Determination of the shape, morphological and wettability properties of quartz and their correlations*. Minerals Engineering, 2003. **16**(10): p. 951-964.
266. Holland, T. and T.H. Fletcher, *Global Sensitivity Analysis for a Comprehensive Char Conversion Model in Oxy-fuel Conditions*. Energy & Fuels, 2016. **30**(11): p. 9339-9350.
267. Senneca, O., et al., *Fragmentation of pulverized coal in a laminar drop tube reactor: Experiments and model*. Proceedings of the Combustion Institute, 2019. **37**(3): p. 2849-2855.
268. Shah, K.V., M.K. Cieplik, and H.B. Vuthaluru, *A Review on Ash Formation During Pulverized Fuel Combustion: State of Art and Future Research Needs* 2016, Springer.
269. Yu, J., et al., *Swelling behaviour of individual coal particles in the single particle reactor*. Fuel, 2003. **82**(15): p. 1977-1987.
270. Zeng, D., et al., *Swelling properties and intrinsic reactivities of coal chars produced at elevated pressures and high heating rates*. Proceedings of the Combustion Institute, 2005. **30**(2): p. 2213-2221.

271. Salatino, P., F. Scala, and R. Chirone, *Fluidized-bed combustion of a biomass char: The influence of carbon attrition and fines postcombustion on fixed carbon conversion*. Symposium (International) on Combustion, 1998. **27**(2): p. 3103-3110.
272. Sahimi, M. and T. T. Tsotsis, *Dynamic scaling for the fragmentation of reactive porous media*. Vol. 59. 1987. 888-891.
273. K. Brown, W., *A theory of sequential fragmentation and its astronomical applications*. Vol. 10. 1989. 89-112.
274. Gao, Q., et al., *Mechanism on the contribution of coal/char fragmentation to fly ash formation during pulverized coal combustion*. Proceedings of the Combustion Institute, 2019. **37**(3): p. 2831-2839.
275. Fu, Z., et al., *Swelling and shrinkage behavior of raw and processed coals during pyrolysis*. Fuel, 2007. **86**(3): p. 418-425.
276. Senneca, O., M. Urciuolo, and R. Chirone, *A semidetalled model of primary fragmentation of coal*. Fuel, 2013. **104**: p. 253-261.
277. Senneca, O., et al., *Prediction of structure evolution and fragmentation phenomena during combustion of coal: Effects of heating rate*. Fuel Processing Technology, 2017. **166**: p. 228-236.
278. Lester, E., et al., *A proposed biomass char classification system*. Fuel, 2018. **232**: p. 845-854.
279. Zhu, S., et al., *Influence of combustion temperature and coal types on alumina crystal phase formation of high-alumina coal ash*. Proceedings of the Combustion Institute, 2019. **37**(3): p. 2919-2926.
280. Yan, J., et al., *Influence of minerals on the thermal processing of bamboo with a suite of carbonaceous materials*. Fuel, 2016. **180**: p. 256-262.
281. Yin, K., et al., *Thermogravimetric analysis of the catalytic effect of metallic compounds on the combustion behaviors of coals*. Vol. 106. 2012.
282. Ma, B.-G., et al., *Investigation on catalyzed combustion of high ash coal by thermogravimetric analysis*. Thermochimica Acta, 2006. **445**(1): p. 19-22.
283. Gil, M.V., et al., *Thermal behaviour and kinetics of coal/biomass blends during co-combustion*. Bioresource Technology, 2010. **101**(14): p. 5601-5608.

284. Ellis, N., et al., *Mineral matter interactions during co-pyrolysis of coal and biomass and their impact on intrinsic char co-gasification reactivity*. Chemical Engineering Journal, 2015. **279**: p. 402-408.
285. Jones, J.M., et al., *Low temperature ignition of biomass*. Fuel Processing Technology, 2015. **134**: p. 372-377.
286. Yao, X., et al., *Evaluation of the fusion and agglomeration properties of ashes from combustion of biomass, coal and their mixtures and the effects of K₂CO₃ additives*. Fuel, 2019. **255**: p. 115829.
287. Li, J., et al., *A new criterion for determination of coal ash sintering temperature using the pressure-drop technique and the effect of ash mineralogy and geochemistry*. Fuel, 2016. **179**: p. 71-78.
288. Yao, X., et al., *Systematic study on ash transformation behaviour and thermal kinetic characteristics during co-firing of biomass with high ratios of bituminous coal*. Renewable Energy, 2020. **147**: p. 1453-1468.
289. Slater, P.N., G.H. Richards, and J.N. Harb, *Pyrite and illite associations in two eastern US bituminous coals*. Fuel Processing Technology, 1995. **44**(1): p. 55-69.
290. Srinivasachar, S., J.J. Helble, and A.A. Boni, *Mineral behavior during coal combustion 1. Pyrite transformations*. Progress in Energy and Combustion Science, 1990. **16**(4): p. 281-292.
291. Wang, G., et al., *Potassium capture by coal fly ash: K₂CO₃, KCl and K₂SO₄*. Fuel Processing Technology, 2019. **194**: p. 106115.
292. Mysen, B. and P. Richet, *Chapter 8 - Properties of Aluminosilicate Systems*, in *Silicate Glasses and Melts (Second Edition)*, B. Mysen and P. Richet, Editors. 2019, Elsevier. p. 263-300.
293. Zheng, G. and J.A. Koziński, *Thermal events occurring during the combustion of biomass residue*. Fuel, 2000. **79**(2): p. 181-192.
294. Vassileva, C.G. and S.V. Vassilev, *Behaviour of inorganic matter during heating of Bulgarian coals: 2. Subbituminous and bituminous coals*. Fuel Processing Technology, 2006. **87**(12): p. 1095-1116.

295. Vassileva, C.G. and S.V. Vassilev, *Behaviour of inorganic matter during heating of Bulgarian coals: 1. Lignites*. Fuel Processing Technology, 2005. **86**(12): p. 1297-1333.
296. Llorente, M.J.F. and J.E.C. García, *Concentration of elements in woody and herbaceous biomass as a function of the dry ashing temperature*. Fuel, 2006. **85**(9): p. 1273-1279.
297. Llorente, M.J.F., et al., *Ash behaviour of lignocellulosic biomass in bubbling fluidised bed combustion*. Fuel, 2006. **85**(9): p. 1157-1165.
298. Niu, Y., et al., *Study on fusion characteristics of biomass ash*. Bioresource Technology, 2010. **101**(23): p. 9373-9381.
299. Guo, X. and H. Xu, *Enthalpies of formation of polyhalite: A mineral relevant to salt repository*. The Journal of Chemical Thermodynamics, 2017. **114**: p. 44-47.
300. Xu, H., X. Guo, and J. Bai, *Thermal behavior of polyhalite: a high-temperature synchrotron XRD study*. Physics and Chemistry of Minerals, 2017. **44**(2): p. 125-135.
301. Olanders, B. and B.-M. Steenari, *Characterization of ashes from wood and straw*. Biomass and Bioenergy, 1995. **8**(2): p. 105-115.
302. Van der Drift, A., et al., *Conversion of Biomass, {Private} Prediction and Solution Methods for Ash Agglomeration and Related Problems*. Project Report of ECN, Petten, The Netherlands, 1999: p. 89.
303. Steenari, B.M. and O. Lindqvist, *High-temperature reactions of straw ash and the anti-sintering additives kaolin and dolomite*. Biomass and Bioenergy, 1998. **14**(1): p. 67-76.
304. Boström, D., et al., *Ash Transformation Chemistry during Combustion of Biomass*. Energy & Fuels, 2012. **26**(1): p. 85-93.
305. Ma, T., et al., *Biomass ash induced agglomeration in fluidized bed. Part 2: Effect of potassium salts in different gas composition*. Fuel Processing Technology, 2018. **180**: p. 130-139.
306. Levin, E.M., et al., *Phase diagrams for ceramists*. 1964, Columbus, Ohio: American Ceramic Society.

Chapter 9: Appendices

Appendix 1: TGA Burnout Profiles of DTF Chars

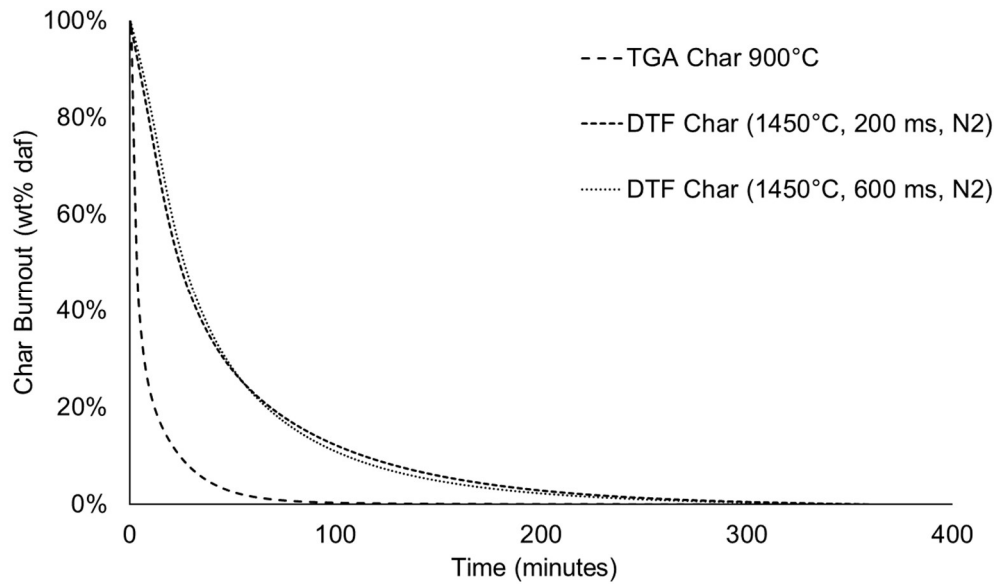


Figure 9-1: Char burnout profiles of TGA char and DTF char at different residence times for Cumberworth coal

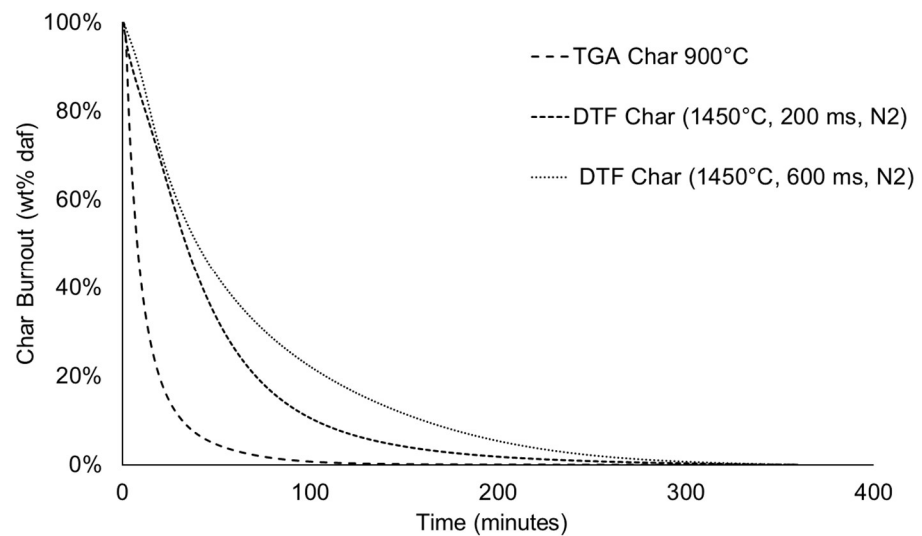


Figure 9-2: Char burnout profiles of TGA char and DTF char at different residence times for Kellingley coal

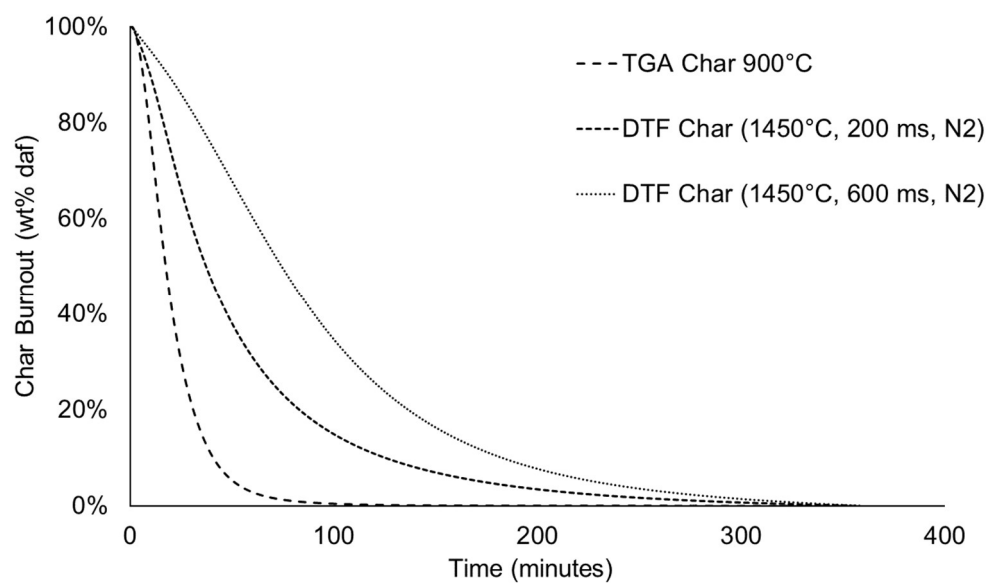


Figure 9-3: Char burnout profiles of TGA char and DTF char at different residence times for USA Illinois coal

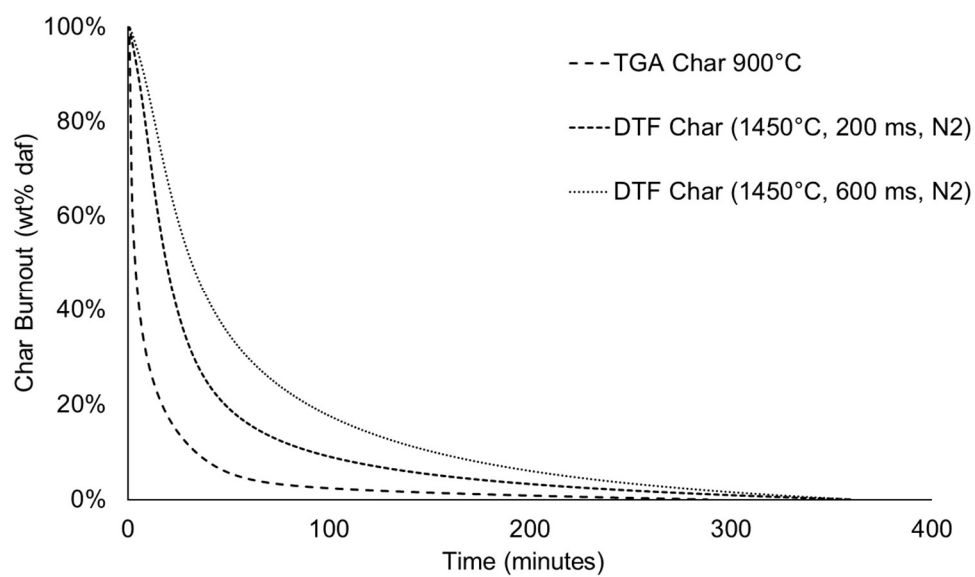


Figure 9-4: Char burnout profiles of TGA char and DTF char at different residence times for Roundwood coal

Appendix 2: Mineral Transformations during Devolatilisation and Char Combustion

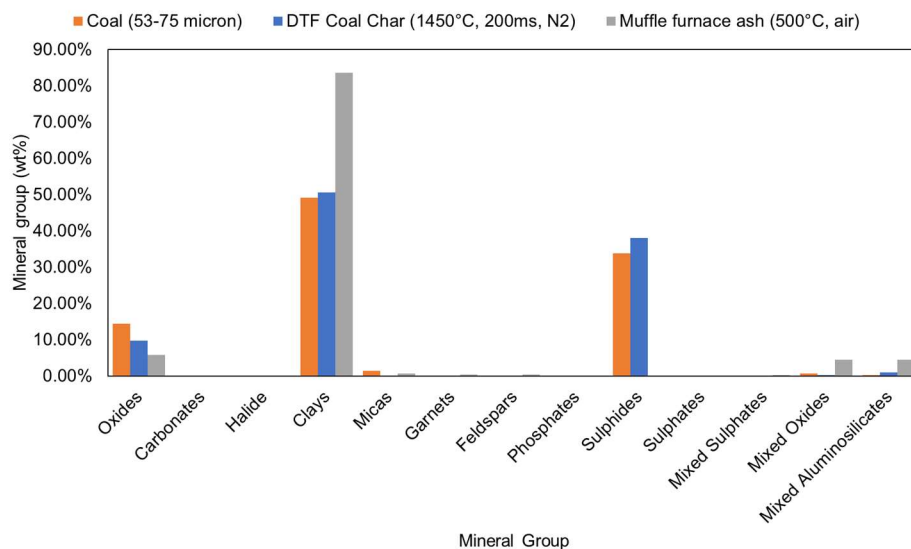


Figure 9-5: Mineral group changes of Kellingley coal during devolatilisation and char combustion

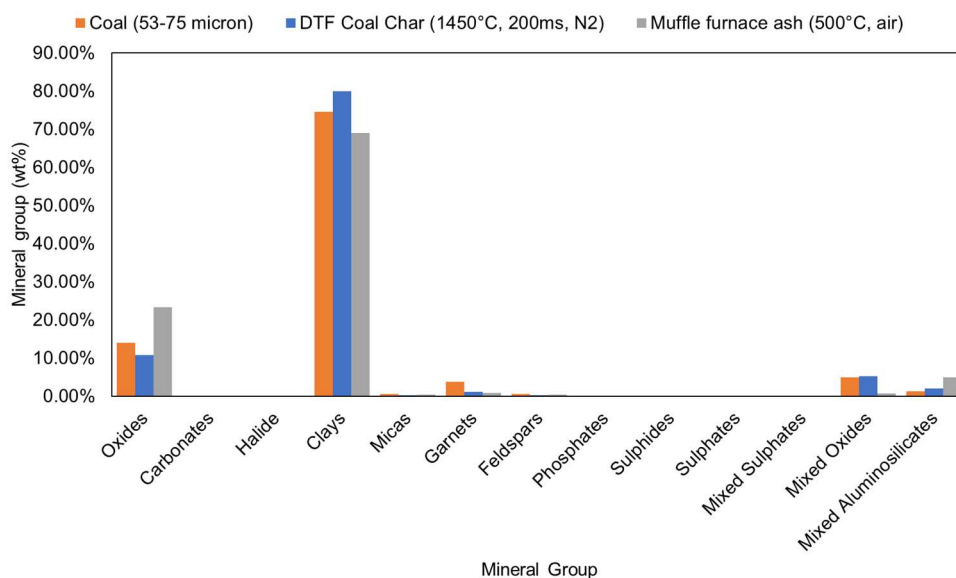


Figure 9-6: Mineral group changes of Cumberworth coal during devolatilisation and char combustion

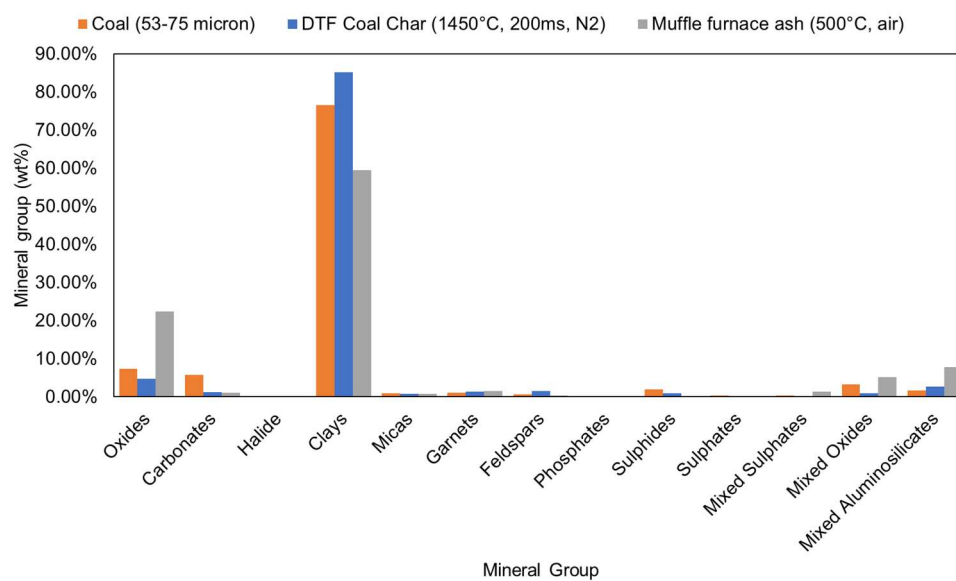


Figure 9-7: Mineral group changes of Roundwood coal during devolatilisation and char combustion